Fluid –Rock Characterization and Interactions in NMR Well Logging

Final Report

Reporting Period Start Date: August 1, 1999
Reporting Period End Date: August 31, 2002

George J. Hirasaki
Kishore K. Mohanty

Report Issued September 5, 2002

DOE Award Number: DE-AC26-99BC15201

Rice University
6100 Main Street
Houston, TX 77005-1892

Subcontractor
University of Houston
4800 Calhoun Road
Houston, TX 77204-4792

DISCLAIMER

"This report was prepared as an account of work sponsored by an agency of the United States Government. Neither the United States Government nor any agency thereof, nor any of their employees, makes any warranty, express or implied, or assumes any legal liability or responsibility for the accuracy, completeness, or usefulness of any information, apparatus, product, or process disclosed, or represents that its use would not infringe privately owned rights. Reference herein to any specific commercial product, process, or service by trade name, trademark, manufacturer, or otherwise does not necessarily constitute or imply its endorsement, recommendation, or favoring by the United States Government or any agency thereof. The views and opinions of authors expressed herein do not necessarily state or reflect those of the United States Government or any agency thereof."

ABSTRACT

Objective: To characterize the fluid properties and fluid-rock interactions that are needed for formation evaluation by NMR well logging.

This project is a partnership between Professor George J. Hirasaki at Rice University and Professor Kishore Mohanty at University of Houston. In addition to the DOE, a consortium of oil companies and service companies supports this project.

The advances made in the understanding of NMR fluid properties are summarized in a chapter written for an AAPG book on NMR well logging. This includes live oils, viscous oils, natural gas mixtures, and the relation between relaxation time and diffusivity.

Oil based drilling fluids can have an adverse effect on NMR well logging if it alters the wettability of the formation. The effect of various surfactants on wettability and surface relaxivity are evaluated for silica sand.

The relation between the relaxation time and diffusivity distinguishes the response of brine, oil, and gas in a NMR well log. A new NMR pulse sequence in the presence of a field gradient and a new inversion technique enables the T_2 and diffusivity distributions to be displayed as a two-dimensional map.

The objectives of pore morphology and rock characterization are to identify vug connectivity by using X-ray CT scan, and to improve NMR permeability correlation. Improved estimation of permeability from NMR response is possible by using estimated tortuosity as a parameter to interpolate between two existing permeability models.

EXECUTIVE SUMMARY

The fluid properties characterization is summarized as a chapter written for an AAPG book on NMR well logging. It describes the departure of live oils from correlations based on dead oils. Mixing rules are developed for gaseous mixtures of methane, ethane, propane, carbon dioxide, and nitrogen. The coupling between the relaxation time distribution and the diffusivity distribution is demonstrated with a binary mixture of hexane and squalene. Measurements of crude oils show that the $T_{1,\mathrm{LM}}$ and $T_{2,\mathrm{LM}}$ are equal at low viscosity but the $T_{1,\mathrm{LM}}$ approach a plateau that is a function of viscosity and Larmor frequency. The hydrogen index of live oils can be estimated from measurements on the stock tank oil and live oil PVT data.

Oil based drilling fluids can have an adverse effect on NMR well log interpretation if it alters the wettability from the natural condition of the reservoir. To gain an understanding of the effect of additives on NMR response, several surfactants were added to a base oil and its effect was evaluated on silica sand. A fatty acid, stearic acid, has no effect. However, a cationic surfactant and a commercial emulsifier alter wettability and increase the surface relaxivity of oil.

New down-hole nuclear magnetic resonance (NMR) measurement and interpretation techniques have substantially improved fluid and reservoir characterization. These techniques take advantage of the magnetic field gradient of the logging tools to make diffusion sensitive NMR measurements. New NMR pulse sequences called "diffusion-editing" (DE) are used to measure diffusivity and relaxation times for water, crude oil, refined oil, and a series of partially saturated core samples. A new inversion technique to obtain two-dimensional maps of diffusivity and relaxation times is demonstrated. Departure of the water diffusivity response from that of bulk water is an indication of restricted diffusion in small pores and/or internal field gradients. Bulk oil has a diffusivity distribution that correlates with the relaxation time distribution. Wettability alteration can result in oil surface relaxation. This becomes apparent as an oil relaxation time distribution that is shorter than that of bulk oil.

Estimation of permeability of vuggy carbonates has been problematic because NMR measures the pore body size distribution while the permeability is determined by the pore throat size distribution. One approach has been to assume that the vugs are not connected and thus do not contribute to permeability. This approach works for low permeability samples but underestimates permeability in high permeability samples. The permeability correlations were evaluated for a set of samples from a West Texas dolomite reservoir. The permeability of the samples ranged from 0.2 md to 2,321 md. Besides porosity and permeability, measurements of mercury capillary pressure, NMR T_2 distributions, and electrical resistivity were made. Photographs, thin sections, CT scans, and tracer floods characterized the pore structure. The vuggy porosity could be distinguished from the T_2 distribution. The electricial formation factor estimated from the Myers model compared well with the experimental measurements. The electricial tortousity was estimated from the estimated formation factor and porosity. The estimated tortousity was then used to interpolate between the SDR permeability model and the Chang *et al*. permeability model. The resulting permeability estimate was much improved compared to either of the original medels.

TABLE OF CONTENTS

Disclaimer 2

Abstract 3

Executive Summary 4

Table of Contents 6

Task 1 Fluid Properties,

- NMR Properties of Reservoir Fluids 7
- Effect of Drilling-Mud Base-Oil Contamination on Crude Oils T_2 Distributions 49
- Correlating Viscosity and NMR Relaxation Times for Drilling Fluid Base Oils and Cyclic Crude Oil Components 70

Task 2 Fluid-Rock Interactions

- Wettability alteration by surfactants and its effects on NMR surface relaxation 84
- Fluid and Rock Characterization Using New NMR Diffusion-Editing Pulse Sequences and Two Dimensional Diffusivity-T_2 Maps 98

Task 3 Pore Morphology/Rock Characterization 132

Task 1.0 Fluid Properties

The following chapter is a draft prepared as a chapter in the AAPG book , *A Practical Guide to NMR Well Logging.*

NMR Properties of Reservoir Fluids

George Hirasaki[1], Matthias Appel[2], Justin Freeman[2]

1 Rice University

2 Shell International E&P Co

NMR PROPERTIES OF RESERVOIR FLUIDS 7

RELAXATION 9

MECHANISMS 9
INTRA-MOLECULAR DIPOLE-DIPOLE INTERACTIONS 11
INTER-MOLECULAR DIPOLE-DIPOLE INTERACTIONS 13
SPIN-ROTATION INTERACTIONS 14
DEAD CRUDE OILS 16
LIVE CRUDE OILS 19
EFFECT OF DISSOLVED OXYGEN 21
BRINE AND WATER-BASED DRILLING FLUIDS 22
RESERVOIR GAS 23

DIFFUSION 26

CONTINUUM TRANSPORT: FICK'S LAWS OF DIFFUSION 26
SELF-DIFFUSION 27
DIFFUSION EQUATION 27
MEASUREMENT TECHNIQUES - DIFFUSION AND SELF-DIFFUSION 29
SELF DIFFUSION OF HYDROCARBON SYSTEMS 31
SELF-DIFFUSION MEASUREMENTS BY CPMG WITH CONSTANT MAGNETIC FIELD GRADIENTS 33
CONSTITUENT VISCOSITY MODEL 35

HYDROGEN INDEX 37

DEFINITION OF HYDROGEN INDEX 37
HI OF BRINES 39
HI OF GAS 39
CORRELATIONS FOR HYDROGEN INDEX 40
HI OF HEAVY OILS 41
HI FOR HYDROCARBON MIXTURES AND LIVE OILS 42

REFERENCES 45

INTRODUCTION

The response measured by NMR well logging tools is from the fluids in the pore space. The initial amplitude is a function of the total porosity, fluid saturation and the hydrogen index of the fluids. The relaxation of the response is a function of the surface relaxation, bulk relaxation, and diffusion in a field gradient. Surface relaxation is discussed elsewhere. Here we will discuss bulk fluid relaxation, self-diffusion of bulk fluids and hydrogen index (*HI*).

The estimation of porosity usually assumes that the initial response in a NMR well log is a measure of the total fluids in the pore space. However, if the wait time of the pulse sequence is not long enough compared to the longest T_1 of the fluids, then the fluids will not be completely polarized and the initial amplitude will need to be corrected for the effect of partial polarization. Also, a heavy oil may have a portion of its relaxation time distribution shorter than the echo spacing and thus not be detected by the CPMG echo sequence. This will result in an apparent *HI* that is less than the actual *HI*. In such cases, the *HI* of the oil should be measured in the laboratory with the same echo spacing as used in the well log.

The estimation of the bulk volume irreducible (*BVI*) requires that the T_2 distribution below the T_2 cut-off be distinguished between that due to water and that due to fast relaxing components of the crude oil. Also, estimation of the oil and/or gas saturation and the oil viscosity require that the contributions of the different fluids to the T_2 distribution be distinguished. Water, oil and gas generally have different diffusion coefficients and their contributions to the T_2 distribution can be estimated by performing a sequence of measurements with different echo spacing.

Laboratory measurements of fluid properties are often made at ambient conditions. However, petroleum reservoirs are often at elevated temperatures and pressures. The effect of reservoir temperature and dissolved gas on viscosity is generally recognized. However, methane, even when dissolved in the oil, relaxes by a different mechanism than the dead oil and thus it is

necessary to account for the gas/oil ratio in the estimation of the relaxation time. Also, dissolved gases can significantly lower the *HI* of live oils.

RELAXATION

Mechanisms

NMR relaxation describes the return of the magnetization to equilibrium after the Boltzmann population of oriented magnetic moments has been disturbed. A short duration or "pulse" of electromagnetic radiation at the Larmor frequency usually accomplishes the perturbation from equilibrium.

NMR relaxation processes can be categorized into two main classes: (i) dispersion of irradiated energy (T_1-relaxation), and (ii) the loss of phase coherence of spin groups caused by local variations of the Larmor frequency (T_2-relaxation).

The *spin-lattice* or *longitudinal* relaxation process (T_1) depends on the exchange of energy between the spin system and its surroundings to allow relaxation of the spin system towards its thermal equilibrium state (given by a certain temperature and magnetic field strength) after the population of the Zeeman energy levels have been disturbed by radio-frequency pulses. This energy exchange is realized through dynamics of the molecular lattice such as molecular rotation, diffusion, or vibration.

In contrast to this, the *spin-spin* or *transverse* relaxation process (T_2) does not require energy transitions but depends on local (on a molecular level) variations of the magnetic field strength which in turn lead to variations of the Larmor frequency of individual spins. The greater the dispersion of Larmor frequencies, the faster the phase coherence of precessing spins disappears.

All NMR relaxation processes require electromagnetic fields that fluctuate over molecular distances. For NMR relaxation, two types of fields are important: (i) a time varying magnetic field that interacts with the nuclear magnetic dipole moments and (ii) a gradient of the electric field that interacts with the electric quadrupole moment of the nucleus. In oil field applications,

only the magnetic resonance effect of protons is currently exploited. Therefore, this discussion needs only to focus on the dipolar interaction caused by time varying magnetic fields, since protons do not possess any quadrupole moment.

There are several possible sources for time varying magnetic fields. The strongest magnetic fields (on a molecular level) are caused by unpaired electrons as found in paramagnetic materials such as dissolved molecular oxygen and paramagnetic ions such as iron and manganese. The latter are primarily responsible for surface relaxation on the pore walls of rocks.

The tumbling motion of molecules is an additional source of time varying magnetic fields. The superposition of the magnetic fields of individual spins leads to interactions between magnetic moments and creates a randomly varying field at the site of the nucleus.

For our discussion of the NMR response of reservoir fluids, two kinds of interactions between magnetic moments are important. In liquids, the molecular distances between spin groups are small enough such that short-range dipolar interactions contribute significantly to spin relaxation. This process is known as a dipole-dipole interaction. This includes both *intra*molecular and *inter*molecular interactions. *Inter*molecular dipole-dipole interactions are a very strong function of the intermolecular distances i.e., the density. When the density of magnetic moments is reduced, as in the case in gases, this interaction becomes less important.

For liquid systems, dipolar interactions between the spins are the main source of the local magnetic field modifications that govern the T_2 relaxation process. Molecular rotation, diffusion, or vibrations of the lattice (that are the source for the T_1 relaxation process) also contribute to T_2 relaxation. For low viscosity liquids, the fast molecular tumbling averages out the dipolar fields from neighboring spins, the dipolar contribution to the T_2 relaxation process is minimized and the T_2 relaxation process will be as slow as the T_1 relaxation, i.e., $T_1=T_2$. This process is often referred to as motional narrowing.

However, for asphaltenes, resins and other structures of higher molecular weight, the molecular motion might not be fast enough to average

the dipolar field of neighboring spin systems. This leads to a spin-spin relaxation time, T_2, which is shorter than the spin-lattice relaxation time, T_1.

For gases where small spherical molecules are relatively free to rotate, spin rotation is another important interaction of the magnetic moments. This mechanism is between the nuclear spin and the molecular magnetic moment that arises from variations of the angular momentum of a rotating molecule.

Since any one of the various mechanisms can accomplish the relaxation to equilibrium, the net relaxation rate can be expressed as the sum of the individual rates:

$$\frac{1}{T_{1,2\,b}} = \frac{1}{T_{1,2\,d-dr}} + \frac{1}{T_{1,2\,d-dt}} + \frac{1}{T_{1,2\,sr}} \quad , \tag{1}$$

where 1,2 denotes either T_1 or T_2, *b* denotes bulk fluid, *d-dr* denotes intra-molecular dipole-dipole rotation, *d-dt* denotes intermolecular dipole-dipole translation, and *sr* denotes spin-rotation.

Intra-molecular dipole-dipole interactions

Molecular collisions of a molecule with its neighbors result in a time dependent change of the orientation of a pair of neighboring protons. This random motion has a characteristic time, called the correlation time, τ_c. This random change of orientation with time can also be described by a rotational diffusivity, D_r. The rotational diffusivity is a function of the viscosity of the medium, temperature and molecular size. The relation between the relaxation times and the rotational correlation time for intra-molecular, dipole-dipole interactions is as follows (Cowan, 1997),

$$\begin{aligned}
\frac{1}{T_1} &= M_2\,\tau_c \left[\frac{2/3}{1+(\omega_o\,\tau_c)^2} + \frac{8/3}{1+(2\omega_o\,\tau_c)^2} \right] \\
\frac{1}{T_2} &= M_2\,\tau_c \left[1 + \frac{5/3}{1+(\omega_o\,\tau_c)^2} + \frac{2/3}{1+(2\omega_o\,\tau_c)^2} \right] \\
M_2 &= \frac{9}{20}\left(\frac{\mu_o}{4\pi}\right)^2 \frac{\hbar^2\,\gamma^4}{r^6}, \quad \text{for a diatomic molecule}
\end{aligned} \tag{2}$$

where ω_o is the Larmor frequency, μ_o is the magnetic permeability of free space, $\hbar$ is Planck's constant divided by 2π, γ is the gyromagnetic ratio for the ^{1}H proton, and r is the distance between the nearest protons in the molecule. Only the nearest neighbors are considered because the coefficient, M_2, is a function of distance to the inverse sixth power.

Liquids with fast motions (e.g., low viscosity, high temperature, and small molecules) relative to the Larmor frequency have a relaxation rate that is proportional to the rotational correlation time. We can see this by taking the limit of short correlation time behaviour of the above equations:

$$\frac{1}{T_1} = \frac{1}{T_2} = \frac{10 M_2}{3} \tau_c , \qquad \omega_o \tau_c \ll 1 . \tag{3}$$

This limit where $T_1 = T_2$ is called the fast motion, adiabatic motional narrowing, or extreme narrowing approximation.

It is helpful to express the rotational correlation time in terms of measurable variables. This can be done by assuming that the molecule is a sphere undergoing rotation by Brownian motion (McConnell, 1987).

$$\begin{aligned}
&\tau_c = \frac{1}{6 D_r} \\
&D_r = \frac{k T}{8 \pi a^3 \eta}, \qquad \text{spherical molecule} \\
&\tau_c = \frac{4 \pi a^3 \eta}{3 k T}, \qquad \text{spherical molecule} \\
&\frac{1}{T_1} = \frac{1}{T_2} = \frac{40 \pi M_2 a^3 \eta}{9 k T}, \qquad \omega_o \tau_c \ll 1, \quad \text{spherical molecule}
\end{aligned} \tag{4}$$

where a is the radius, η is the viscosity, k is the Boltzmann constant, and T is the absolute temperature. The significant result here is that liquids of spherical molecules in the fast motion limit ('motional narrowing') have T_1 and T_2 equal to each other and inversely proportional to viscosity/temperature.

The dependence of the relaxation times on viscosity/temperature can be visualized by expressing the equation for relaxation by intramolecular dipole-dipole mechanisms in dimensionless variables.

$$T_{1,2\,D} = \frac{M_2}{\omega_o} T_{1,2}$$
$$\omega_o \, \tau_c = \frac{4\pi \, \omega_o \, a^3 \, \eta}{3 k \, T}, \qquad \text{spherical molecule} \tag{5}$$

The results are shown in Fig. 1. The relaxation times, T_{1D} and T_{2D} are equal to each other for short correlation times compared to the Larmor period, e.g., for low viscosity/temperature. When the correlation time is long compared to the Larmor period, e.g., for high viscosity fluids, or for highly asymmetrical fluid molecules, T_{1D} is larger than T_{2D}.

Exceptions to the dependence of relaxation time on viscosity occur for liquids at very high pressure (Benedek and Purcell, 1954). Benedek and Purcell's interpretation was, "If the free volume of the liquid is reduced by compressing the liquid, it is plausible that the freedom to migrate will be more drastically affected than the freedom to rotate."

Inter-molecular dipole-dipole interactions

Inter-molecular dipole-dipole interactions are usually less significant compared to the intra-molecular dipole-dipole interactions because these interactions depend on the distance between spins to the inverse sixth power. An exception is when one of the spins is due to the electronic spins of a paramagnetic ion, free radical, or oxygen molecule. Because the mass of an electron is much less than that of a proton, the gyromagnetic ratio of an electron is about 10^3 greater than that of a proton (McConnell, 1987). The spin-lattice or longitudinal relaxation rate of unlike spins in the extreme narrowing approximation is (Hennel and Klinowski, 1993),

$$\frac{1}{T_{1,d-dt}} = \frac{2\,\mu_o^2 \, \hbar^2 \, \gamma^2}{32} \frac{\eta}{kT} \left(\gamma_2^2 \, N_2 \right) \tag{6}$$

where γ_2 and N_2 are the gyromagnetic ratio and number concentration of the second species of molecule. Since the gyromagnetic ratio is raised to the second power, the contribution of a paramagnetic species may be significant even though its concentration N_2 is small.

Since dipolar interactions dominate the NMR relaxation for gas-free reservoir fluids, it is useful to combine the intra- and intermolecular contributions. For low viscosity fluids and temperatures above ambient, the motional narrowing condition is generally well fulfilled. Assuming further that intra- and intermolecular motions are uncorrelated, the dipolar relaxation rate can be expressed as

$$\frac{1}{T_2} = \frac{1}{T_1} = \frac{2\pi\,\gamma^4\,\hbar^2\,a^3}{k\,b^6}\left(1 + \frac{3\pi\,N\,b^6}{5a^3}\right)\frac{\eta}{T} \quad . \tag{7}$$

where *a* is the molecular radius and *b* is the distance between the nearest protons.

In reference to the first authors, the derivation of the above relation is often referred to as Bloembergen, Pound, Purcell (1948) ("BPP") theory.

Spin-rotation interactions

Spin-rotation interaction becomes a significant contribution to the relaxation of small molecules and/or gases where the motions are so fast that the dipole-dipole relaxation rate becomes small. The molecular collisions in dilute gases are assumed to be binary as the time between collisions becomes large compared to the time two molecules are interacting with each other. The relaxation times within the extreme narrowing approximation are as follows (Gordon, 1966):

$$\frac{1}{T_1} = \frac{1}{T_2} \propto \frac{k\,T}{\rho_N\,\langle v\,\sigma_J\rangle} \tag{8}$$

where, ρ_N is the number density of the gas, v is the velocity of the gas, and σ_J is the cross section for the transfer of angular momentum. The bracket represents the average of the product. Kinetic theory can be used to approximate the ensemble average molecular speed of a dilute gas.

$$\langle v\rangle = \sqrt{\frac{8\,k\,T}{\pi\,m}} \tag{9}$$

where m is the reduced mass of the collision pair. It is assumed that the average of the product of speed and cross-section is equal to the product of the respective average quantities. Thus the relaxation time can be expressed as a function of density and temperature.

$$\frac{1}{T_1} = \frac{1}{T_2} \propto \frac{\sqrt{k\,T}}{\rho_N\,\sigma_J(T)}$$
$$\frac{T_1}{\rho_N} = \frac{T_2}{\rho_N} \propto \frac{\sigma_J(T)}{\sqrt{T}} \propto \frac{1}{T^n} \tag{10}$$

where *n* is an empirical exponent equal to about 1.5 for methane (Jameson *et al*., 1991).

An alternate derivation (Hubbard, 1963b) expresses the spin-rotation relaxation rate in terms of viscosity and temperature.

$$\frac{1}{T_1} = \frac{1}{T_2} = \frac{2\,I\,k\,T\left(2\,C_\perp^2 + C_\parallel^2\right)}{3\hbar^2}\,\tau_1\,, \qquad \tau_1 << \tau_2,\ \left(\omega_o\,\tau_o\right)^2 \ll 1$$
$$\tau_o = \frac{2\,a^2}{D} \quad ,\tau_2 = \tau_o/9$$
$$\tau_1 = \frac{3\,I\,D}{4\,a^2\,k\,T} \tag{11}$$
$$D = \frac{k\,T}{6\,\pi\,a\,\eta}$$
$$\therefore\ \frac{1}{T_1} = \frac{1}{T_2} = \frac{I^2\left(2\,C_\perp^2 + C_\parallel^2\right)}{12\,\pi\,\hbar^2}\,\frac{k\,T}{a^3\,\eta}, \qquad \tau_1 << \tau_2,\ \left(\omega_o\,\tau_o\right)^2 \ll 1$$

where the τ are the various correlation times, $C_\parallel, C_\perp$ are the components of the spin-rotation coupling tensor, and *I* is the moment of inertia of the spherical molecule.

The significance of this expression is that the relaxation rate for the spin-rotation mechanism has a dependence on temperature, viscosity, and molecular size that is the inverse of the relationship for intra-molecular dipole-dipole interactions.

Dead Crude Oils

Dead crude oils relax primarily by intramolecular dipole-dipole interactions. Therefore, the direct correlation between NMR relaxation rates and fluid viscosity has often been exploited in formation evaluation. The original correlation for the relaxation time of dead crude oils and viscosity standards at ambient conditions was expressed only as a function of viscosity (Morriss *et al*., 1994). The correlation was modified to express it as a function of viscosity and temperature:

$$T_{2,\mathrm{LM}} = \frac{1.2}{\eta^{0.9}}\ ,\ \text{at ambient temperature.}\quad \text{Morriss } et\ al.\ (1997) \qquad (12)$$

$$T_{2,\mathrm{LM}} = \frac{1.2\,T}{298\,\eta},\qquad \text{Vinegar (1995)} \qquad (13)$$

$$T_{2,\mathrm{LM}} = \frac{1.2}{(298)^{0.9}}\left(\frac{T}{\eta}\right)^{0.9} = 0.0071\left(\frac{T}{\eta}\right)^{0.9},\quad \text{Zhang } et\ al.\ (1998) \qquad (14)$$

In these equations, $T_{2,\mathrm{LM}}$ is the log-mean value (in seconds) of the transverse relaxation time spectrum, η the viscosity in cp, and T the temperature in Kelvin.

Fig. 2 shows measured $T_{1,\mathrm{LM}}$ and $T_{2,\mathrm{LM}}$ relaxation times as a function of fluid viscosity over temperature for various alkanes, gas-free oils and viscosity standards. Lo *et al*. (1999) showed that the approximation developed by Morriss *et al*. underestimates the relaxation times of degassed normal alkanes. The NMR relaxation of such fluids might be enhanced because of the additional paramagnetic relaxation brought about by the dissolved oxygen. This effect is discussed in more detail below. Experimentally, Lo *et al*. quantified the impact of the dissolved oxygen on the relaxation behaviour of alkanes and derived the following correlation between the relaxation time and viscosity of oxygen-free alkanes:

$$T_{1,\mathrm{LM}} = 0.00956\frac{T}{\eta}\ . \qquad (15)$$

This correlation was based on measured $T_{1,LM}$ relaxation times. However, no significant difference was found between $T_{1,LM}$ and $T_{2,LM}$ measurements for these alkanes (Zega *et al.*, 1989; Lo, 1999). This correlation was compared with the base oil of an OBM as a function of temperature and pressure in Fig. 3. The experimental data for T_2 as a function of pressure show that temperature and pressure variations affect the relaxation behaviour of the gas-free OBM in different ways. While the variation of relaxation time with temperature at a given pressure can be adequately described with the correlation for oxygen-free alkanes, pressure variation results in different trends than that expected from the correlation. The reduction in relaxation time is much reduced compared to the increase in viscosity. This experiment illustrates the decoupling between viscosity and relaxation. The effect is related to molecular free volume. As outlined in the section on intramolecular dipolar interactions, increases in pressure will first reduce the free volume of the system, and hence reduce the intermolecular motion, before it reduces the intramolecular motions, i.e., the freedom of a molecule to rotate. Since the intramolecular term generally contributes more to relaxation than the intermolecular one, and viscosity is governed by intermolecular actions, pressure increases reduce relaxation time less than it reduces viscosity. The above equations based on crude oils and on alkanes have been widely used in formation evaluation. However, it needs to be emphasized that these equations are only valid for gas-free liquids.

Differences between T_1 and T_2 measurements have been found for viscous crude oils. This difference is a function of the Larmor frequency, Fig. 2, and may be due to heavy components of the crude oil not being in the fast motion limit. Fig. 2 shows that T_1/T_2 is larger for larger viscosity (i.e., longer correlation time) and higher Larmor frequency. The dependence of the T_1 on Larmor frequency can be correlated by normalizing the relaxation time and viscosity with the Larmor frequency in the manner suggested by the section on intramolecular dipole-dipole interactions.

$$T_{1,2\mathrm{N}} = \frac{2(\mathrm{MHz})}{\omega_0} T_{1,2}$$
$$\left(\frac{\eta}{T}\right)_{\mathrm{N}} = \frac{\omega_0}{2(\mathrm{MHz})}\left(\frac{\eta}{T}\right) \tag{16}$$

The normalized $T_{1,\mathrm{LM}}$ relaxation time as a function of the normalized viscosity is shown in Fig. 4. This normalization to 2 MHz collapses all $T_{1,\mathrm{LM}}$ data of crude oils to a single curve. For low viscosities, the measured $T_{1,\mathrm{LM}}$ data agree well with the correlation between viscosity and $T_{2,\mathrm{LM}}$ derived for gas-free crude oils, and therefore illustrate the validity of the fast motion approximation for this viscosity range. At higher viscosities, the measured $T_{1,\mathrm{LM}}$ values depart from the $T_{2,\mathrm{LM}}$ correlation. Furthermore, the experimental $T_{1,\mathrm{LM}}$ show a lower plateau value instead of the theoretically expected increase of T_1. In Fig. 4, a dashed line shows the theoretical prediction for T_1 of a system with a single molecular correlation time. Given that T_1 will reach its minimum when the inverse of the Larmor frequency is equal to the molecular correlation time, the observed lower plateau of the T_1 data illustrates that crude oils need to be characterized by a spectrum of molecular correlation times.

The relaxation time distribution of crude oils (Morriss *et al.*, 1997) is typically significantly broader than that of a pure hydrocarbon as illustrated in Fig. 5. Here the T_2 distribution of a 23 cp, 30°API gravity crude oil is compared with that of *n*-hexadecane. The shape of the distribution is important for fluid identification, e.g., for the distinction between crude oils and oil-based mud filtrates (Prammer *et al.*, 2001).

Heavy oils may have fast relaxing components that relax significantly before the first echo occurs and thus are not fully detected. This will not only result in a misinterpretation of the relaxation time distribution but also result in an underestimation of the hydrogen index (LaTorraca *et al.*, 1998 &1999; Mirotchnik *et al.*, 1999). In Fig. 6, the relaxation time distributions of a 302 cp, 19°API gravity oil are shown that are measured at 30° C by inversion recovery and CPMG with echo spacing of 0.24 ms and 2 ms. The T_2 distribution is truncated for short relaxation times at the longer echo spacing because of the

loss of information. Also, the difference between T_1 and T_2 is apparent even at a Larmor frequency of 2 MHz for this viscous crude oil.

The viscosity and thus the relaxation time of heavy oils are very strongly dependent on the temperature. Thus measurements at different temperature is a good test of the correlation of $T_{2,LM}$ with the ratio of viscosity and temperature. Fig. 7 shows a plot of $T_{2,LM}$ as a function of the ratio of viscosity and temperature for measurements at 40°, 70°, and 100° C. These results show that the correlations which were developed for alkanes at close to ambient conditions apply to viscous, heated oils until $T_{2,LM}$ becomes close to the echo spacing of the measurement. It was mentioned earlier that short relaxation times are truncated by lack of data shorter than the echo spacing.

Live Crude Oils

Live oils differ from dead oils in that they contain dissolved gas components. Methane is the primary, but not the only, dissolved component. Supercritical methane and methane vapour relax by the spin-rotation mechanism. Cryogenic liquid methane relaxes by intermolecular dipolar coupling. With decreasing viscosity, the contribution from spin rotation to the relaxation process of methane successively increases and leads to an opposite trend for the relaxation time-viscosity relation compared to higher alkanes. In Fig. 8, the contributions to the proton relaxation time of methane are plotted as a function of viscosity divided by temperature. In gaseous methane, the relaxation time is mainly accounted for by spin-rotation. However, both dipolar and spin-rotation interactions become significant with increasing viscosity. In cryogenic liquid methane, the relaxation mechanism is dominated by intermolecular dipolar coupling.

For formation fluids with a significant amount of solution gas, the relaxation behaviour will be governed by both dipolar interactions and spin rotation. The contribution from spin rotation increases with increasing gas-oil ratio and increasing hydrogen index of the gas phase. This is illustrated in Fig. 9, which includes methane-alkane mixtures, in addition to pure methane and pure higher alkanes.

Because of the opposite dependencies on the ratio of viscosity/temperature between dipolar interactions and spin rotation, prediction of the NMR relaxation times from PVT data for live oils is complicated. Generally speaking, live fluids will have shorter relaxation times than gas-free fluids of similar viscosity because of the additional contributions to the relaxation from spin rotation.

Figure 10 shows measured relaxation times for live reservoir fluids as a function of viscosity divided by temperature. Gas-free oils and oils with a relatively low solution gas-oil ratio are closely represented by the correlations developed for dead oils and alkanes. In contrast to this, the experimental data show that the relaxation times of oils with high solution gas-oil ratios are significantly shorter than those predicted by the correlations developed for gas-free systems. The measurements indicate that the difference between live oil data and the dead oil correlation can be greater factor of 2 for oils with solution gas-oil ratios larger than about 825 Scf/STB (standard cubic feet/stock tank barrel) (or 150 m^3/m^3) and can approach a factor of 5 for samples with as much as 2200 Scf/STB (or 400 m^3/m^3) solution gas oil ratios.

A comparison of the NMR response of live crude oils with those of live and dead oil-based mud filtrates (Fig. 11) illustrates that the relaxation times of both fluid types cover a similar range. Therefore, when approximating the relaxation spectra with a single relaxation time value, such as the logarithmic-mean value, it may be difficult to unambiguously distinguish between native oils and invaded oil-based mud filtrates. However, the measurements show that even live oil-based mud filtrates have a significantly narrower relaxation time distribution than those of live and dead crude oils. This effect should be exploited for downhole fluid identification (Prammer *et al*., 2001).

Lo *et al*. (1999) have shown that the relaxation times of methane-alkane mixtures show a significant deviation from the straight-line correlation for pure liquid alkanes. This departure is not exclusively due to the system being a mixture, since the log-mean relaxation of n-hexane and n-hexadecane mixtures followed the correlation for pure liquid alkanes. The deviation of the methane-alkane mixtures from the correlation for the liquid alkanes correlates with the methane content of the mixture or the gas/oil ratio, *GOR*, (in m^3/m^3)

(Lo *et al*, 2000). The correlation of the measurements resulted in the following expression:

$$\begin{aligned} deviation &= \mathrm{Log}_{10}\left(T_{1,linear}/T_1\right) = \mathrm{Log}_{10}\left[f\left(GOR\right)\right] \\ \mathrm{Log}_{10}\left(deviation\right) &= \mathrm{Log}_{10}\left\{\mathrm{Log}_{10}\left[f\left(GOR\right)\right]\right\} \\ &= -0.127\left[\mathrm{Log}_{10}\left(GOR\right)\right]^2 + 1.25\,\mathrm{Log}_{10}\left(GOR\right) - 2.80 \end{aligned} \tag{17}$$

The relaxation of the live oil can thus be estimated from the correlation in the absence of methane, denoted $T_{1,linear}$, and the function of the *GOR*:

$$T_1 = \frac{T_{1,linear}}{f(GOR)} \tag{18}$$

The correlation of the relaxation time as a function of viscosity/temperature and *GOR* is shown in Fig. 9. The contour lines of constant *GOR* are straight lines that are parallel to the line for dead oils.

The above correlation was developed from binary mixtures of methane and higher alkanes. Fig. 12 shows the deviation of live oil and OBM T_2 relaxation time as a function of the GOR. The correlation of the deviation developed from methane-alkane measurements is shown for comparison.

Effect of Dissolved Oxygen

The previous section explained that molecular oxygen is paramagnetic and thus will contribute to the bulk relaxation of fluids even if it is present in small quantities. The effect of dissolved oxygen is best demonstrated by comparing the relaxation times of oils saturated with air with those of oils that have been degassed by freezing and vacuum. Measured relaxation time for alkanes from *n*-pentane to *n*-hexadecane are shown in Fig. 13. The relaxation time is clearly shorter for the samples that had not been degassed. The line in the figure is the correlation (Morriss *et al*., 1994) for crude oils that

were not degassed. These results show that dissolved oxygen has the greatest effect for light oils and is nearly insignificant for *n*-hexadecane. Removal of oxygen is critical for measurements with hydrocarbon gases (Johnson and Waugh, 1961, Sandhu, 1966).

Air dissolved in water affects the bulk relaxation time of water. The measured relaxation time of air-saturated, deionized water at 30° C is in the range of 2-3 seconds. The measured T_1 of carefully degassed, pure water at 30° C is 4.03 seconds (Krynicki, 1966).

Brine and Water-Based Drilling Fluids

Whole water-based drilling mud will have a short relaxation time because of the surface relaxation on the mud solids. If the mud filter cake is effective in filtering out the solids, the bulk fluid relaxation time of the filtrate is primarily a function of temperature and the dissolved components in the filtrate.

Drilling mud contains a number of additives that can affect the relaxation time of water. The effect of temperature on pure, degassed water is shown in Fig. 14. Figure 15 and 16 illustrate the effect of some additives.

When estimating the residual oil saturation, it is convenient to add a paramagnetic additive to make the relaxation time of water so short that it either will not be measured by the logging tool or is short enough to be distinguished from the oil signal. Horkowitz *et al*., 1997 added manganese chloride to the drilling fluid to "kill" the water signal so that only oil was detected. $MnCl_2$ could be used in that application because the formation was carbonate. Sandstone formations often have a significant amount of clay that can retard the propagation of manganese ions into the formation. Thus sandstone formations usually require the use of a chealated Mn-EDTA. The relaxation times as a function of concentration of these two forms of manganese ions are shown in Fig. 17.

Reservoir Gas

The primary component of natural gas is methane. Supercritical methane relaxes by the spin rotation mechanism and the relaxation time can be correlated with density and temperature. The relaxation time data of Gerritsma *et al*. (1970) and Lo (1999) are shown in Fig. 18.

The data of Gerritsma *et al*. are given along five isochors (constant density) and one isotherm. The data of Lo are at two temperatures and various pressures. The density corresponding to Lo's conditions were calculated with the NIST program, SUPERTRAPP. The data were fitted by linear regression and the fit shown by the heavy line. Also shown are the correlations reported by Prammer *et al*. (1995) and Lo (1999). The correlation of Prammer appears to have been fitted to the data corresponding to the highest density. The correlation of Lo and the linear regression are hardly distinguishable. The correlations of T_1 relaxation time with mass density and temperature are given by the following equations:

$$\begin{aligned} \frac{T_1}{\rho} &= \frac{1.19\times10^5}{T^{1.45}} \quad \text{regression} \\ \frac{T_1}{\rho} &= \frac{1.57\times10^5}{T^{1.50}} \quad \text{Lo}\left(1999\right) \\ \frac{T_1}{\rho} &= \frac{2.5\times10^4}{T^{1.17}} \quad \text{Prammer,et al.}\left(1995\right) \end{aligned} \tag{19}$$

Although methane is usually the primary component of natural gas, other light hydrocarbons and non-hydrocarbons are usually present. Pure ethane and propane gas have relaxation times that are longer than that of methane, especially when correlated with molar density (Fig. 19).

A mixing rule can be developed for T_1 in the gas mixtures with *n* components based on the kinetic model for spin rotation interaction (Bloom *et al*., 1967; Gordon, 1966). It is assumed that spin rotation interaction is dominant for all components in the mixture. For an *n*-component gas mixture, there may be *n* contributions to T_1. The logarithmic mean T_1 may be described as

$$T_{1,\text{logmean}} = T_{1,1}^{f_1} \cdot \cdot \cdot \cdot \cdot T_{1,i}^{f_i} \cdot \cdot \cdot \cdot \cdot T_{1,n}^{f_n} , \tag{20}$$

where f_i is the resonant nucleus fraction of the *i*-th component in the mixture and $T_{1,i}$ is the individual relaxation time of the *i*-th component in the mixture.

The relaxation by the spin rotation interaction for the *i*-th component is caused by the collisions of the *i*-th molecule with various collision partners in the mixture. It has been empirically established that the contributions of various collision partners are additive (Jameson and Jameson, 1990; Jameson *et al*., 1987a; Jameson *et al*., 1991; Jameson *et al*., 1987b; Rajan and Lalita, 1975)

$$T_{1,i} = \sum_{j=1}^{n} \rho_j \left(\frac{T_1}{\rho} \right)_{i\text{-}j} , \tag{21}$$

where ρ_j is the partial molar density of the *j*-th component. In addition, Gordon has derived this additivity theoretically as a result of neglect of correlations between the effects of successive collisions and the assumption of binary collisions (Gordon, 1966). By assuming that all components have the inverse temperature to the 1.5 power, the coefficients for the interactions between like and unlike molecules can be estimated (Zhang *et al*., 2002).

$$\left(\frac{T_1}{\rho} \right)_{i-j} = \frac{B_{ij}}{T^{1.5}} \tag{22}$$

The coefficient B_{ij} describes the interaction between probe molecule *i* and molecule *j*. Natural gas is composed primarily of methane. In addition, ethane, propane, CO_2 and N_2 are usually present. It is meaningful to calculate the coefficients B_{ij} for various collision partners in natural gas. The coefficients B_{ij} for the gas mixtures containing methane, ethane, propane, CO_2 and N_2 were calculated and summarized in Table 1. The details of the calculation can be found in (Zhang, 2002). The calculations for the pure components correspond to the dashed line in Figure 19.

Table 1: Values of the coefficients B_{ij} for proton relaxation in the gas mixture of CH_4, C_2H_6, C_3H_8, CO_2, and N_2

$j \rightarrow$ / $i \downarrow$	CH_4	C_2H_6	C_3H_8	CO_2	N_2
CH_4	2.41×10^{6} [a] 2.52×10^{6} [b]	3.77×10^{6}	4.06×10^{6}	3.55×10^{6}	1.90×10^{6}
C_2H_6	1.06×10^{7}	1.58×10^{7}	1.66×10^{7}	1.45×10^{7}	8.02×10^{6}
C_3H_8	3.09×10^{7}	4.47×10^{7}	4.60×10^{7}	2.84×10^{7}	2.28×10^{7}
CO_2	0	0	0	0	0
N_2	0	0	0	0	0

[a] Estimated from experimental data of methane (Lo, 1999)

[b] Calculated from the theoretical equation for spin rotation interaction using the molecular constants of methane

Carbon dioxide and nitrogen do not have protons but their presence in mixtures with methane results in a reduction of the relaxation time of methane compared to the correlation for pure methane based on mass density (Rajan *et al*., 1975). However, if the molar density rather than the mass density is used in the correlation, the methane relaxation in mixtures with CO_2 or nitrogen will approximately correlate with that of pure methane. The symbols in Fig. 20 are the relaxation times of methane in mixtures with either CO_2 or nitrogen compared with the correlation for pure methane. The departure is apparently due to the collision cross-section of methane with these other gases being different from the methane-methane collision cross-section.

The dependence of the relaxation time of methane as a function of temperature and pressure (Kleinberg and Vinegar, 1996; Gerritsma et al., 1971) is shown in Fig. 21. It should be noted that the gas density was calculated for something slightly heavier than methane but it is unlikely that the contribution of any component other than methane to the relaxation time was included.

DIFFUSION

The subjects of viscosity and diffusion are parts of the general phenomena of transport in gases and liquids. Viscosity is concerned with momentum transport and governs both the motion of fluids and the motion of particles in a fluid under the influence of external forces (e.g. shear or gravitational forces). However, molecular migration can be observed even without the existence of external forces. This is the subject of Brownian motion, i.e. the statistical movement of atoms or molecules. Brownian motion has been extensively studied, beginning with the observations of random incessant motions of dust pollen in solution by Robert Brown in 1853. In the following section the basic principles of Brownian motion and its two major categories, diffusion and self-diffusion, will be explained.

Continuum Transport: Fick's Laws of Diffusion

The term *diffusion* describes the process of molecular transport within systems caused by the statistical movement of atoms or molecules. The relation between a concentration gradient a particle flux can be described with Fick's first law.

$$\vec{j}_i = -D_i \nabla c_i \tag{23}$$

The proportionality constant between the particle flux density, $\vec{j}_i$, and the concentration gradient, ∇c_i, is the *diffusion coefficient,* D_i of the *i*th component of a mixture. D_i is a unit of measurement of the velocity of molecular rearrangement.

The time derivative of the concentration of a component *i* in a volume element has to be equal to the total flux of this component through the surface of the volume for conservation of particles.

$$\frac{\partial c_i}{\partial t} = -\nabla \bullet \vec{j}_i \tag{24}$$

Combining the last two equations, Fick's second law

$$\frac{\partial c_i}{\partial t} = \nabla \bullet \left(D_i \nabla c_i \right) \tag{25}$$

describes the time derivative of the concentration for systems that are not in their equilibrium state. Generally speaking, the diffusion coefficient D_i of a component is also a function of its concentration. This process might be also referred to as *mutual diffusion* or *transport diffusion.*

Self-Diffusion

According to Fick's first law, motion will always occur in systems that have a concentration gradient. However, particles move even without the existence of such a gradient. This process is called *self-diffusion* and is caused by the thermal energy of the particles. The self-diffusion coefficient D_S is a unit of measurement of the velocity of the Brownian movement under equilibrium conditions. Although no macroscopic particle fluxes are possible under such conditions, Fick's first and second laws can still be used to describe the process of self-diffusion. In this approach one assumes that a portion of the molecules are labeled, making it possible to observe their displacement within the system.

Diffusion Equation

In homogenous systems, the Brownian motion is determined by the coefficient of self-diffusion only. Since in such systems the self-diffusivity is independent of the spatial position of the molecules, Fick's second law simplifies to

$$\frac{\partial c^* \left(\vec{r}, t \right)}{\partial t} = D_s \nabla^2 c^* \tag{26}$$

In this equation c^* is the concentration of labeled molecules, and therefore the probability of finding a labeled particle in a certain position. The above equation is commonly referred to as the *diffusion equation* since the differential equation gives the probability of finding a molecule at time t at

position $\vec{r}$, if it initially was located at the position $\vec{r}_o$. With the initial condition that the concentration of the labelled molecules follows Dirac's delta function, $c^*(\vec{r},0) = \delta(\vec{r} - \vec{r}_o)$, the solution of the diffusion equation is found to be a Gaussian distribution of the form

$$c^*\left(\vec{r},\vec{r}_{0,}t\right) = \frac{1}{\sqrt{(4\pi\, Dt)^3}} \exp\left\{-\frac{\left(\vec{r} - \vec{r}_0\right)^2}{4Dt}\right\} = P\left(\vec{r}\,|\vec{r}_0\,,t\right)$$

(27)

This equation is commonly referred to as the *propagator,* $P(\vec{r},t)$*,* or the *fundamental solution of the diffusion equation* since it allows the calculation of the mean square value of molecular displacement during the observation time, t:

$$\left\langle \vec{r}^{\,2}(t) \right\rangle = \int_{-\infty}^{+\infty} P(\vec{r},t)\,\vec{r}^{\,2} d\vec{r} = 6Dt$$

(28)

The above relation is referred to as Einstein's equation of diffusion and provides a straightforward definition of molecular diffusivity. In general, Einstein's equation depends on the dimension, *k*, of molecular migration

$$\left\langle x^2(t) + y^2(t) + z^2(t) \right\rangle = 2\,k\,Dt$$

(29)

The expression above coincides with Einstein's equation in isotropic systems where $\left\langle \vec{r}^{\,2}(t) \right\rangle = \left\langle x^2(t) + y^2(t) + z^2(t) \right\rangle$ and the dimension of diffusion, *k*, is equal to 3.

The mean square displacement is thus found to be directly proportional to the total observation (or diffusion) time. Molecular propagation which follows this relation is generally called *normal diffusion*. Any confinements interfering with the diffusion process lead to a correlation of subsequent elementary jumps, and the direct proportionality between mean square displacement and diffusion time breaks down. This process is called *anomalous diffusion* or *restricted diffusion*. Depending on the nature of the

confinement, different patterns of deviations from normal diffusion may be observed.

The single most important relation between viscosity and diffusion in liquids is the Stokes-Einstein equation. It has been found to be an accurate equation down to the molecular length scale and it finds wide application in relating molecular diffusion to fluid viscosity.

$$D_0 \equiv \int_0^\infty \langle U(0)U(t)\rangle dt = \frac{k_B T}{6\pi\eta R} \tag{30}$$

According to the Stokes-Einstein equation, the self-diffusivity D_0 is defined via the velocity autocorrelation function, $\langle U(0)U(t)\rangle$, and is related to the thermal energy, $k_B T$, and the viscous drag on a sphere of radius R.

Measurement Techniques - Diffusion and Self-Diffusion

Diffusion Measurements

In systems that are not in their equilibrium state, concentration gradients lead to particle fluxes that can be observed macroscopically. According to Fick's first law, a determination of the diffusion coefficient of a certain species of molecules can be based either on measurements of both the flux density and the gradients of the concentration or on measurements of the particle distribution at different times.

Molecular concentrations can be determined by chemical as well as various physical methods, since numerous properties such as weight, refraction index, birefringence, radioactivity, spectral absorbance, and transmittance depend on the composition of the system. Consequently, a wide variety of experimental techniques for determining the diffusion coefficient of systems have been developed.

Self-Diffusion Measurements by NMR

As an alternative to the tracer techniques, there are several methods that allow the direct observation of the diffusion path, i.e., the mean square displacement of the random walk of the diffusing molecules. Based on Einstein's equation, the coefficient of molecular diffusion can be calculated knowing the mean square displacement of the particles within a given diffusion time. However, the displacements of the molecules must be much larger than the mean length of the elementary steps of diffusion. These displacements can be measured by the Nuclear Magnetic Resonance Pulsed Field Gradient Technique ("PFG NMR") or with variants of the CPMG method with constant gradient.

Pulsed Field Gradient NMR (PFG NMR)

The principle of measuring molecular diffusivity using PFG NMR is that the spatial position of each spin (and hence, each molecule) is marked by its specific Larmor frequency within a spatially inhomogenous magnetic field. PFG NMR spectrometers are equipped with additional coils that create a switchable, well-defined magnetic field. This additional magnetic field is often referred to as the 'magnetic field gradient' because it creates a gradient of the effective magnetic field over the sensed volume when superimposed onto the background magnetic field. Since the Larmor frequency of precessing spins is directly proportional to the magnetic flux density effective at the position of the respective spin, a magnetic field gradient over the sensed volume will result in a variation of the Larmor frequency and tag the position of each magnetic moment with respect to the direction of the magnetic field gradient.

Experimentally, during the radio frequency (RF) pulse sequence used to create a spin echo (like the Hahn, or the stimulated echo sequence), the magnetic field gradient pulses are switched on for a short duration (typically up to a few milliseconds). The sequence of RF- and magnetic field gradient pulses is chosen such that the variation of the Larmor frequency brought about by an individual field gradient pulse is exactly compensated for by a subsequent field gradient pulse if the spins have not changed their positions during the time interval between the two gradient pulses. However, if the

spins have moved, a net variation of the Larmor frequency will remain after all RF- and magnetic field gradient pulses have been applied. Therefore, diffusion of spins will result in a measurable attenuation of the NMR signal. The effect is proportional to the intensity of the magnetic field gradient pulses, *g*, duration, δ, the diffusion time (time between subsequent field gradient pulses), Δ, and the self-diffusion coefficient of the molecules, *D* (Stejskal and Tanner, 1965):

$$\psi = \frac{M}{M_0} = \exp\left(-\gamma^2 g^2 \delta^2 D\left(\Delta - \delta/3\right)\right) \ . \qquad (31)$$

The spin-echo attenuation, ψ, is the ratio of the amplitudes of the spin echoes with and without the application of magnetic field gradient pulses, *M* and M_0, respectively. In this way, additional attenuation of the spin echoes due to relaxation processes during the diffusion time will be cancelled out. During a PFG NMR experiment, the amplitude of spin echoes is measured as a function of the area of the field gradient pulses, $g \times \delta$, at a given diffusion time. The slope of this echo attenuation curve is proportional to the self-diffusion coefficient.

It has been shown (Mitra, 1992; Fleischer, 1994; Cowan, 1997) that the PFG NMR experiment can be interpreted in terms of a generalized scattering experiment. This approach implies the possibility of defining a "generalized wave vector" , $\mathbf{k} = \gamma\,\delta\,\mathbf{g}$, and, therefore, of determining the space scale probed in the experiment. Using the strong field gradients of the stray field of a cryomagnet, the NMR field gradient technique can provide a maximum spatial resolution of about 100 Å. Since the accessible diffusion times can vary between milliseconds up to seconds, a broad range of diffusion coefficients can be determined. Hence, it is possible to apply PFG NMR to determine the diffusivity of gases and liquids, including crude oils.

Self Diffusion of Hydrocarbon Systems

The self-diffusion coefficient of super critical methane correlated as a function of density and temperature is shown in Fig. 22. The data shown here is correlated with data in the range of 273° to 454° K. The temperature dependence is correlated with temperature raised to the inverse 0.7 power.

The exponent was reported to range from 0.6 to 0.9 for data that included saturated vapor along the coexistence curve (Oosting and Trappeniers, 1971; Harris, 1978). The inverse square root temperature dependence is appropriate for a smooth hard sphere fluid in the low-density limit (Reid, Prasunitz, and Poling, 1987, pg. 595-6). The correlation curve in Fig. 22 is fitted to a quadratic function of density.

$$10^6 \frac{\rho D}{T^{0.7}} = 2.64 + 1.26\,\rho - 11\,\rho^2 \qquad (32)$$

where ρ is the density in g/cm^3, D is the diffusion coefficient in cm^2/s, and T is the temperature in K. The Chapman-Enskog theory predicts that the curve should have a zero slope as density approaches zero. A plot of the methane diffusion coefficient as a function of pressure and temperature is shown in Fig. 23 (Kleinberg and Vinegar, 1996).

The self-diffusion coefficients of alkanes, including methane, ethane, propane, and mixtures of methane and higher alkanes, are shown as a function of viscosity/temperature in Fig. 24. The correlation indicates that the Stokes-Einstein relationship is followed. The relaxation time is shown as a function of the self-diffusion coefficient in Fig. 25. While the self-diffusion coefficient and relaxation time are proportional for the higher alkanes, methane, ethane, propane and mixtures of methane with higher alkanes depart from the linear relationship because methane relaxes by the spin-rotation mechanism, even when dissolved in the liquid phase.

Figure 26 shows the distribution of self-diffusion coefficients for a 33º API live crude oil with about 825 Scf/STB dissolved gas. Similar to their relaxation response, crude oils have a broad distribution of diffusivities compared to that of pure alkanes. While the diffusivity of a gas-free system is relatively insensitive to pressure, a clear shift of the diffusion coefficient towards smaller values with increasing pressure can be observed for the live oil. This trend is also illustrated in Fig. 27, which also compares the diffusion coefficients of live oils with those at ambient conditions after the solution gas has been depleted.

Figure 28 shows the diffusivities of various live and dead oils and oil-based mud filtrates as a function of fluid viscosity. The diagram also illustrates the correlation that has been developed from measurements on pure higher alkanes and dead crude oils. Experiments have shown that live oils have a better correlation between self-diffusion coefficient and fluid viscosity than between NMR relaxation time and viscosity. This trend makes sense because both diffusion and viscosity are governed by the same underlying physical principle, i.e., molecular migration.

Self-Diffusion Measurements by CPMG with Constant Magnetic Field Gradients.

Current NMR logging tools are not equipped with switchable magnetic field gradients. However, information about fluid diffusivity can be obtained with the static field gradient of the logging tool and changing the echo spacing. The underlying concept is that the NMR response for fluids confined to the pore space is given by:

$$\frac{1}{T_1} = \frac{1}{T_{1,bulk}} + \frac{1}{T_{1,surface}} = \frac{1}{T_{1,bulk}} + \rho_1 \frac{S}{V} ,$$
$$\frac{1}{T_2} = \frac{1}{T_{2,bulk}} + \frac{1}{T_{2,surface}} + \frac{1}{T_{2,diffusion}} = \frac{1}{T_{2,bulk}} + \rho_2 \frac{S}{V} + \frac{(\gamma g TE)^2 D}{12} . \quad (33)$$

In these equations, the pore fluid has a diffusion coefficient, *D*, and is confined to pores with a surface-to-volume ratio, *S/V*. The surfaces of these pores have a surface relaxivity of ρ which is effective either for the longitudinal or the transverse relaxation process, ρ_1 and ρ_2 respectively. The transverse relaxation time is measured with a CPMG pulse sequence using an inter-echo spacing, *TE*, and a constant magnetic field gradient, *g*. γ is the proton gyromagnetic ratio.

Based on the above equations, it is possible to calculate an averaged diffusion coefficient of the pore fluids. However, several assumptions need to be fulfilled:

One approach is to measure both the T_1 and T_2 of the system and look for the difference. The relaxation times T_1 and T_2 for the bulk fluids must be equal, i.e., the NMR relaxation must be governed by the motional narrowing process. In order to cancel surface relaxation effects, the surface relaxivities for both the T_1 and the T_2 relaxation process also need to be equal. Naturally, there is no contribution from surface relaxation if bulk fluids are measured under laboratory conditions.

Under these assumptions, a clear difference between the measured T_1 and T_2 relaxation times will be observed if the diffusion term dominates the relaxation response. That is generally the case only for fluids with low viscosities (which also satisfy the motional narrowing requirement), measured as a bulk sample or as a non-wetting phase. An additional complication is that the calculated diffusion coefficient is an 'apparent' diffusivity. The difference between T_1 and T_2 does not reveal whether the diffusion has become restricted because the propagation of molecules has been hindered by the geometry of the pore network.

Alternatively, the estimation of the diffusion coefficient of the pore fluids can be based on T_2 measurements only. If the transverse relaxation time is measured with a CPMG technique at various inter-echo spacings, *TE*, the diffusivity of the fluids can be calculated from the observed shift of the relaxation spectra towards shorter relaxation times with increasing *TE*'s. Similar to the T_1/T_2 method mentioned above, this approach will only work if the relaxation response is dominated by the diffusion term. Experimentally, the available range of inter-echo spacings, and, therefore, detectable diffusion coefficients is limited. Finally, it has to be verified that the calculated relaxation time distribution is not shifted because of different sampling interval with the change in echo spacing, even in the absence of any field gradients. The recently introduced, "diffusion editing" sequence (Hurlimann *et al*., 2002, Prammer *et al*., 2002)) partially overcomes this limitation by using variable duration echo spacing only for the first echo and using short echo spacing for the subsequent echos.

Constituent Viscosity Model

Interpretation of NMR well logs is often complicated by the relaxation time distributions of hydrocarbons that overlap the relaxation time distribution of the water. The water has a distribution of relaxation times because of surface relaxation by pore walls. Several methods have been introduced to distinguish between the oil and water [Akkurt (1999), Looyestijn (1996), and Slijkerman *et al*. (1999)]. These methods rely on the magnetic field gradient of the logging tool and the difference in diffusivity (diffusion coefficient) between the oil and water. Freedman *et al*. (2001) introduced the constituent viscosity model (CVM) to distinguish oil and water. "In the CVM, each hydrocarbon molecule in the mixture is assumed to relax and diffuse like it would in the pure-state liquid except the macroscopic pure-state viscosity is replaced by the microscopic constituent viscosity." This implies that the relaxation time distribution and diffusivity distribution are coupled through a common "constituent viscosity." The expressions for the mixture's and the constituent's relaxation time, diffusivity, and viscosity are as follows.

$$
\begin{aligned}
&T_{2,LM} = \frac{aT}{\eta}, \qquad T_{2,k} = \frac{aT}{\eta_k}, \qquad T_{2,LM} = \prod_{k=1}^{N} T_{2,k}^{f_k} \\
&D_{LM} = \frac{bT}{\eta}, \qquad D_k = \frac{bT}{\eta_k}, \qquad D_{LM} = \prod_{k=1}^{N} D_k^{f_k} \\
&\frac{D_{LM}}{T_{2,LM}} = \frac{D_k}{T_{2,k}} = \frac{b}{a} \\
&\eta = \prod_{k=1}^{N} \eta_k^{f_k} = \frac{aT}{T_{2,LM}} = \frac{bT}{D_{LM}} \\
&\sum_{k=1}^{N} f_k = 1
\end{aligned}
\tag{34}
$$

The parameter, f_k, is the proton fraction of the *k*-th molecular constituent. The parameters, a and b, were determined from the measurements of the relaxation time and diffusivity of pure components and the mean value of the mixture. It has been established that for the alkanes the ratio of b/a is equal to 5.28×10^{-6} (cm^2/s^2) while for dead crude oils b/a is approximately 1.26×10^{-5} (cm^2/s^2). This model assumes that relaxation time and diffusivity distributions are coupled with each constituent having a

common proportionality constant, b/a. A correction for the GOR should be made for live oils (Freedman *et al*., 2001).

The relation between the relaxation rate and viscosity of *n*-hexane and *n*-hexadecane mixtures was investigated by Zega *et al*. (1990). They found the mole fraction weight-average relaxation rate to be proportional to the viscosity as in pure fluids. The proton fraction average relaxation rate was not exactly proportional to viscosity. Lo *et al*. (2000) found that the individual-component relaxation times of *n*-hexane and *n*-hexadecane mixtures were quite different but the proton-fraction-weighted geometric mean relaxation time was a good approximation to the relaxation time – viscosity relation for pure alkanes. The diffusivity distribution of *n*-hexane and *n*-hexadecane mixtures overlapped too much to determine if the diffusivity distribution corresponded to the relaxation time distribution. Freedman *et al*. (2001) studied mixtures of *n*-hexane (C_6H_{14}) and squalene ($C_{30}H_{50}$) and demonstrated the relation between the relaxation time and diffusivity distributions for these mixtures.

The relaxation time and diffusivity distributions are shown in Figs. 29 and 30, respectively, and are summarized in Table 2. The values in the tables are the bi-exponential fit results. The light vertical line on each plot is the relaxation time estimated by fitting the CPMG response to a bi-exponential model. H(C6) is the proton fraction of hexane in the mixture. A(C6) is the fraction of the area attributed to hexane. There is good agreement between H(C6) and A(C6). The peaks of the diffusivity distributions are broader than those of the T_2 distributions. This can be explained by the difference in signal/noise for the two measurements. Figure 31 plots constituent and log mean relaxation time and diffusivity as function of composition. There is about an order of magnitude change in the relaxation time and diffusivity of squalene. The change for *n*-hexane is less. Figure 32 is a plot of the ratio of diffusivity and relaxation time for squalene and *n*-hexane. The dashed line is the ratio, b/a, determined for pure and mixtures of alkanes. The average absolute deviation of the ratio, D/T_2, from the independently determined value of b/a is 27%. It is clear that the deviation could be reduced if b/a was determined specifically for the *n*-hexane and squalene mixture. Figure 33 is

the correlation between the pure and constituent diffusivity and relaxation time for the *n*-hexane and squalene systems. The measured points compare well with the correlation that was independently developed from pure alkanes and mixture of alkanes.

Table 2 Relaxation time and diffusivity of *n*-hexane and squalene mixtures

H(C6)	T_2(C6), s	T_2(C30), s	D(C6), cm^2/s	D(C30), cm^2/s
0.00		0.294		1.01E-06
0.38	4.59	0.90	1.27E-05	3.47E-06
0.50	5.75	1.18	1.70E-05	4.94E-06
0.69	7.52	1.69	3.02E-05	9.89E-06
1.00	9.78		4.60E-05	

The measurements of relaxation time and diffusivity for the pure materials and mixtures of *n*-hexane and squalene verify the coupling between the relaxation time and diffusivity of constituents in a mixture. The area fractions in the distributions correspond to the proton fraction of the corresponding constituent.

HYDROGEN INDEX

Definition of Hydrogen Index

The amplitude of the response of the NMR logging tool is calibrated with respect to that of bulk water at standard conditions. Thus the amplitude of the magnetization before attenuation by relaxation processes, M_0, is expressed as:

$$M_0 \propto \phi\left(S_w\ HI_w + S_o\ HI_o + S_g\ HI_g\right) \tag{35}$$

where ϕ. is the porosity, S_p is the saturation of phase p, and HI_p is the hydrogen index of phase p, where p = brine, oil, or gas. The HI is defined as follows,

$$\begin{aligned} HI &\equiv \frac{\text{Amount of hydrogen in sample}}{\text{Amount of hydrogen in pure water at STP}} \\ &= \frac{\text{moles H/cm}^3}{0.111} \\ &= \frac{\rho_m\ N_H\ /\ M}{0.111} \end{aligned} \tag{36}$$

where ρ_m. is the mass density of the fluid in g/cm^3 , N_H is the number of hydrogen in the molecule, and M is the molecular weight. The denominator of the last expression, 0.111, is the moles of hydrogen in one cubic centimeter of water at standard conditions. The numerator is the number of moles of hydrogen in the same volume of the bulk sample at the conditions of the measurement.

The HI of a fluid sample can be measured in the laboratory by measuring the response of the sample of known volume at the conditions of interest:

$$HI = \frac{\left(M_{o,fluid}\ /\ V_{fluid}\right)_{\text{at conditions of interest}}}{\left(M_{o,H_2O}\ /\ V_{H_2O}\right)_{\text{at standard conditions}}} \tag{37}$$

M_0 can be determined either by the extrapolation of a CPMG or FID response to zero time to recover any signal losses that might have occurred during the dead time of the spectrometer. Alternatively, the cumulative distribution of relaxation times after inverting the measured signal decay can be used to determine M_0. However, when using the latter procedure, errors brought about by oscillations in the early echoes might be harder to detect.

M_{0,H_2O} is the respective magnetization of water at standard conditions. When determining the *HI* experimentally, the decreasing sensitivity of the spectrometer with increasing temperature according to Curie- and Boltzmann effects needs to be considered.

HI of Brines

Recall that the *HI* is relative to pure water at ambient conditions. Thus brine that contains a large quantity of salts may have a *HI* that deviates significantly from unity (Fig. 34).

HI of Gas

The *HI* of gas mixtures can be determined by extending the definition of *HI*:

$$\begin{aligned} HI &= \frac{\text{moles H/cm}^3}{0.111} \\ &= \frac{\tilde{\rho}\, N_H}{0.111}, \quad \text{for single component} \\ &= \frac{\sum_i^n \tilde{\rho}_i\, N_{H,i}}{0.111}, \quad \text{for mixture} \\ &= \frac{\bar{\tilde{\rho}} \sum_i^n y_i\, N_{H,i}}{0.111} = \frac{\bar{\tilde{\rho}}\, \bar{N}_H}{0.111} = \frac{\bar{\tilde{\rho}}\left(\text{moles/liter}\right) \bar{N}_H}{111} \end{aligned} \tag{38}$$

where $\tilde{\rho}, \tilde{\rho}_i$ and $\bar{\tilde{\rho}}$, are molar density, partial molar density, and average molar density, respectively. The final expression has the density expressed as moles/liter, the units commonly used in PVT calculations. $y_i, N_{H,i}$, and $\bar{N}_H$ are mole fraction, number of hydrogen per molecule of component *i*, and the average moles of hydrogen per mole of mixture, respectively . Table 3 is an example calculation for the average moles of hydrogen for a typical separator gas.

The *HI* of the gas can be computed by multiplying the molar density from PVT calculations with the average number of hydrogen per molecule, Fig. 35.

Table 3. Example calculation for the average moles of hydrogen in a mole of a typical separator gas mixture		
Component	Mole fraction, y_i	$N_{H,i}$
Carbon dioxide	0.0167	0
Nitrogen	0.0032	0
Methane	0.7102	4
Ethane	0.1574	6
Propane	0.0751	8
i-Butane	0.0089	10
n-Butane	0.0194	10
i-Pentane	0.0034	12
n-Pentane	0.0027	12
Hexanes	0.0027	14
Heptanes plus	0.0003	16
Total or average	1.0000	4.785

Correlations for Hydrogen Index

Gaymard and Poupon (1968) introduced a correlation of *HI* for hydrocarbons as a function of the mass density. Their correlation is based on the assumption that the hydrocarbons can be represented by alkanes.

$$HI = 9\rho_m \left[0.15 + 0.2(0.9 - \rho_m)^2\right] \tag{39}$$

Vinegar *et al*. (1991) and Kleinberg and Vinegar (1996) introduced a correlation based on the measurements of stock tank crude oils at ambient conditions. Their correlation has the *HI* equal to unity for oils lighter than 25º API and decreasing for heavier oils. These two correlations are illustrated in Fig. 36 along with the calculated *HI* for some pure hydrocarbons at ambient conditions and methane at elevated pressures.

Figure 36 shows that the correlation of Gaymard and Poupon is satisfactory for methane at high pressures and for the pure liquid alkanes at ambient conditions. Thus one can expect that the correlation will also be satisfactory for the gas phase or methane dissolved in a liquid phase containing only higher alkanes, such as gas condensate. The correlation of Kleinberg and Vinegar appears to capture the reduction in *HI* that is observed for aromatic or polyaromatic hydrocarbons. However, the correlation is for stock tank oil and thus may not adequately represent live oils with a high GOR.

HI of Heavy Oils

LaTorraca *et al*. (1999, 2000) pointed out that the measured *HI* values of heavy crude oils may be less than actual values because of information lost due to finite echo spacing time. Thus the authors defined an apparent *HI* that depends on the inter-echo spacing and emphasized that the *HI* of heavy oil should be measured at the same echo spacing as the logging tool if the information is to be used to interpret logs. They also claim that the actual *HI*, based on geochemical analysis, should be within 5% of unity. While the apparent *HI* can be used to estimate the viscosity of the heavy oil, measurements of the *HI* of crude oils and pure hydrocarbons have shown that samples with T_2 much greater than the echo spacing had measured *HI* of about 0.9, Fig. 37. Also, 1-methylnaphthlene and toluene, both of which have T_2 greater than 1 second, have measured *HI* less than 0.7. Mirotchnik *et al*. (1999) demonstrated the increase in apparent *HI* with increased temperature for bitumen. Increasing temperature shifted the T_2 distribution towards longer

times, and more of the distribution could be measured for a given echo spacing.

HI for Hydrocarbon Mixtures and Live Oils

The *HI* of live oils, i.e., oils with a certain amount of solution gas, can significantly deviate from unity. Although live oils often occur as undersaturated oils, a significant amount of solution gas can be dissolved in the oil phase especially in high temperature, high pressure reservoirs. As a result, the density of the formation fluid is reduced while thermal expansion coefficients and compressibility are increased compared to stock tank conditions. Therefore, the *HI* of live oils are reduced and more pressure-dependent than those of gas-free oils.

When representative samples of the formation fluids have been preserved, the measurement of their NMR response at reservoir conditions can significantly reduce the uncertainty in the interpretation of wireline NMR data. The correct determination of the *HI* of the hydrocarbon phase directly impacts crucial reservoir parameters such as porosity and hydrocarbon saturation. Indirectly, uncertainties in the estimation of the *HI* are carried forward to the calculation of formation permeability based on NMR logging data since the ratio of bound- and free fluids also depends on the *HI*. Figure 38 illustrates the impact of wrongly determined *HI* on the calculation of porosity and permeability. Since typically only movable hydrocarbons show *HI* smaller than unity, the error is increased for smaller ratios of bound fluids to total porosity. This calculation is based on the assumption that the error in hydrogen index determination affects all movable fluids. This situation represents the NMR measurements acquired in an undrained reservoir well above the transition zone.

Experimentally, the hydrogen index of live oils can be measured by comparing their NMR response to that of water at standard conditions. The experimental setup needs to address the decreased sensitivity of the spectrometer with increasing temperature. Care needs to be taken to ensure that the formation fluid can be transferred from a pressurized storage cylinder to the NMR probe without falling below either the bubble point or the onset

pressure of asphaltene precipitation. The pressurized fluid sample needs to be carefully equalized prior to the NMR measurement to ensure that no changes in the chemical composition have occurred.

Figure 39 illustrates the results of the *HI* measurements on live oils and mixtures of oil-based mud filtrates and methane at various conditions. Gas-free oil-based mud filtrates have *HI* very close to unity. With increasing GOR, the *HI* continuously decreases, related to changes in fluid density. The lowest values of around 0.8 were obtained for undersaturated oils with solution gas-oil ratios of about 2000 Scf/STB. If a 25% porosity formation was saturated to 80% with this oil, and an *HI* of unity was wrongly assumed in the interpretation of NMR log data, the NMR-determined porosity of this formation would be undercalled by about 4 porosity units.

Calculation of the HI of Live Oils

The *HI* of a hydrocarbon mixture can be calculated exactly from the mass density and hydrogen: carbon ratio (H:C), *R*, if contributions to the NMR signal arising from the hydrogenated compounds of heteroatoms, like sulphur compounds (mercaptans or thiols) or oxygen compounds (organic acids in immature crude oils) can be neglected. (Zhang *et al*., 1998)

$$HI = \frac{\rho_m \left[R/\left(12.011 + 1.008R\right) \right]}{0.111} \tag{40}$$

This formula is convenient for pure hydrocarbons or mixtures for which the density and *R* can be determined. However, H:C is generally not known for crude oils and complete geochemical analysis might not always be available. Because there are only three parameters in the above relation, the value of *R* can be determined for a stock tank oil if the *HI* and density are measured at ambient conditions.

$$R_{STO} = \frac{1.333 HI_{STO}}{\rho_{m,STO} - 0.112 HI_{STO}} \tag{41}$$

If one has the usual PVT data, the mass density and *R* can be determined for the live oil. A PVT report expresses the volumetric data and composition such as the oil formation volume factor, *Bo*, and the solution gas:oil ratio, R_s, as a function of pressure at reservoir temperature.

The mass density can be determined as follows,

$$\rho_m = \frac{\rho_{m,STO}}{B_0} + 0.178 \frac{R_s \, \rho_{m,gas}}{B_0} \tag{42}$$

Here R_s has the units of Scf/STB and $\rho_{m,gas}$. is the gas density at standard conditions. The H:C for a live oil can be determined with the following formula.

$$R = \frac{R_{STO} + 0.178 \dfrac{R_{gas} \, R_s \, \rho_{gas} \left(11.9 + R_{STO}\right)}{\rho_{STO} \left(11.9 + R_{gas}\right)}}{1 + 0.178 \dfrac{R_s \, \rho_{gas} \left(11.9 + R_{STO}\right)}{\rho_{STO} \left(11.9 + R_{gas}\right)}} \tag{43}$$

The composition of the separator gas yields its H:C ratio, R_{gas}. As a result, the *HI* of the live oil can be calculated using the mass density and H:C ratio determined from the previous two equations.

The *HI* of two live GOM crude oils were calculated at reservoir conditions. One is a 30º API crude oil with a solution gas/oil ratio of 749 Scf/STB at a bubble point pressure of 4150 psia. The other is a 38º API gravity crude oil with a solution gas/oil ratio of 1720 Scf/STB at a bubble point pressure of 4575 psia. The results are shown in Fig. 40 along with the G&P and K&V correlations.

At stock tank oil condition, the *HI* value of the 30º API crude oil is 0.959, which is close to the default value of unity. However, when pressure increases, more gas (mostly methane) dissolves in the crude oil, causing decreasing density and increasing H:C ratio. When pressure reaches the bubble point pressure, *HI* reduces to the lowest value of 0.857. As pressure continues to increase above bubble point, no more gas dissolves in the crude oil, but instead the oil is compressed. Since the composition does not change, the H:C ratio of the reservoir fluid remains constant. *HI* then linearly

increases with increasing density above the bubble point. The 38º API crude oil has a *HI* of 0.983 at stock tank conditions but the *HI* reduces to about 0.806 at the bubble point pressure of 4575 psi. The higher solution gas/oil ratio of the 38º API crude causes its *HI* to deviate from unity more significantly than for the 30º API crude. Both oils show significant deviation from the G&P and K&V correlations.

ACKNOWLEGMENT

One of the authors (GJH) acknowledges the financial support of NSF, USDOE, and a consortium consisting of Arco, Baker Atlas, Chevron, Exxon-Mobil, Halliburton-NUMAR, Kerr McGee, Marathon, Norsk Hydro, Phillips, PTS, Saga, Schlumberger, and Shell. Also, the contributions of S.-W. Lo, Q. Zhang, Y. Zhang, W.V. House, and R. Kobayashi are recognized.

REFERENCES

Akkurt, R., Vinegar, H.J., Tutunjian, P.N., and Guillory, A.J.: "NMR Logging of Natural Gas Reservoirs," *The Log Analyst* (1996), November-December, 33-42.

Appel, M., Freeman, J.J., Perkins, R.B., and van Dijk, N.P.: "Reservoir Fluid Study by Nuclear Magnetic Resonance," paper HH, SPWLA 41st Annual Logging Symposium, (4-7 June, 2000) Dallas, TX.

Benedek, G.B. and Purcell, E.M.: "Nuclear Magnetic Resonance in Liquids under High Pressure," *J. Chem. Phys*. (1954), **22**.12, 2003-2012.

Bloembergen, N., Purcell, E.M., and Pound, R.V.: "Relaxation Effects in Nuclear Magnetic Resonance Adsorption," *Phys. Rev*. (1948), **73**.7, 679-712.

Bloom, M., Bridges, F., and Hardy, W. N., 1967, Nuclear Spin Relaxation in Gaseous Methane and Its Deuterated Modifications: *Canadian Journal of Physics*, v. 45, p. 3533-3554.

Bouton, J., Prammer, M.G., Masak, P., and Menger, S.: "Assessment of Sample Contamination by Downhole NMR Fluid Analysis," SPE 71714 presented at the 2001 SPE ATCE, New Orleans, LA, 30 September- 3 October.

Cowan, B.: *Nuclear Magnetic Resonance and Relaxation*, Cambridge University Press (1997), New York, NY.

Dawson, R., Khoury, F., and Kobayashi, R.: "Self-Diffusion Measurements in Methane by Pulsed Nuclear Magnetic Resonance," *AIChE J*.(1970), **16**.5, 725-729.

Freedman, R., Lo, S.-W., Flaum, M., Hirasaki, G.J., Matteson, Sezginer, A.: "A New NMR Method of Fluid Characterization in Reservoir Rocks: Experimental Confirmation and Simulation Results," *SPEJ* (December 2001) 452-464.

Freedman, R., Heaton, N., and Flaum, M.: "Field Application of a New Nuclear Magnetic Resonance Fluid Characterization Method" SPE 71713 presented at the 2001 APE ATCE, New Orleans, LA (Sept. 30 – Oct. 3, 2001)

Gerritsma, C.J. and Trappeniers, N.J.: "Proton-Spin-Lattice Relaxation and Self-Diffusion in Methanes I. Spin-Echo Spectrometer and Preparation of the Methane Samples," *Physica* (1971) **51**, 365-380.

Gerritsma, C.J., Oosting, P.H., and Trappeniers, N.J.: "Proton-Spin-Lattice Relaxation and Self-Diffusion in Methanes II. Experimental Results for Proton Spin-Lattice Relaxation Times," *Physica* (1971) **51**, 381-394.

Gordon, R.G.: "Kinetic Theory of Nuclear Spin Relaxation in Gases," *J. Chem. Phys.* (1966) **14**.1, 228-234.

Greiner-Schmid, A., Wappmann, S, Has, M., and Ludemann, H.-D.: "Self-diffusion in the compressed fluid lower alkanes: Methane, ethane, and propane," *J. Chem. Phys*. (1991) **94**.9, 5643-5649.

Harris, K.R.: "The Density Dependence of the Self-Diffusion Coefficient of Methane at –50, 25 and 50 C," *Physica* (1978), **94A**, 448-464.

Hennel, J.W. and Klinowski, J.: *Fundamentals of Nuclear Magnetic Resonance*, Longman Scientific & Technical (1993) Essex, England.

Horkowitz, J.P., Vinegar, H.J., Hartman, D.E., Coates, G.R., and Clerke, E.A.: "Residual Oil Saturation Measurements In Carbonates With Pulsed NMR Logs," paper Q, SPWLA 36th Annual Logging Symposium, (26-29 June, 1995) Paris, France.

Hubbard, P. S., "Theory of Nuclear Magnetic Relaxation by Spin-Rotational Interactions in Liquids", *Phys. Rev.* (1963), **131**, 1155-1165.

Hubbard, P.S.: "Nuclear Magnetic Relaxation by Intermolecular Dipole-Dipole Interactions," *Phys. Rev*. (1963) **131**, 275-282.

Hurlimann, M.D., Venkatarmanan, L., Flaum, C., Speier, P., Karmonik, C., Freedman, R., and Heaton, N.: "Diffusion Editing: New NMR Measurement of Saturation and Pore Geometry," paper FFF presented at the SPWLA 43rd Annual Logging Symposium, Oiso, Japan, (June 2-5, 2002).

Jameson, C. J., Jameson, A. K., and Smith, N. C., 1987a, ^{15}N Spin-Relaxation Studies of N_2 in Buffer Gases. Cross Sections for Molecular Reorientation and Rotational Energy Transfer: *The Journal of Chemical Physics*, v. 86, p. 6833-6838.

Jameson, C. J., Jameson, A. K., Smith, N. C., Hwang, J. K., and Zia, T., 1991, ^{13}C and ^{1}H Spin Relaxation in CH_4 in the Gas Phase: *The Journal of Physical Chemistry*, v. 95, p. 1092-1098.

Jameson, C. J., Jameson, A. K., Smith, N. C., and Jackowski, K., 1987b, Cross Sections for Transfer of Rotational Angular Momentum in CO_2 from ^{13}C Spin Relaxation Studies in the Gas Phase: *The Journal of Chemical Physics*, v. 86, p. 2717-2722.

Johnson, C.S. and Waugh, J.S.: "Nuclear Relaxation in Gases: Mixtures of Methane and Oxygen," *J. Chem. Phys*. (1961), **35**.6, 2020-2024.

Kashaev, S.Kh.G, Le, B., and Zinyatov, M.Z.: "Proton Spin-Lattice Relaxation, Viscosity, and Vibration of Molecules in the Series of n-Paraffins," translated from *Doklady Akademii Nauk SSSR*, **157**.6, 1438-1440 (August, 1964) 846-848.

Kleinberg, R.L. and Vinegar, H.J.: "NMR Properties of Reservoir Fluids," *The Log Analys*t (1996), November-December, 20-32.

Krynicki, K.: "Proton Spin-Lattice Relaxation in Pure Water between 0°C and 100°C," *Physica* (1966), **32**, 167-178.

LaTorraca, G.A., Stonard, S.W., Webber, P.R., Carlson, R.M., and Dunn, K.J.: "Heavy Oil Viscosity Determination using NMR Logs," paper PPP, SPWLA 40th Annual Logging Symposium, (30 May – 3 June, 1999), Oslo, Norway.

LaTorraca, G.A., Dunn, K.J., Webber, P.R., and Carlson, R.M.: "Low-Field NMR Determination of the Properties of Heavy Oils and Water-in Oil Emulsions," *Magnetic Resonance Imaging* (1998) **16**, 5/6, 659-662.

Lo, S.-W., Hirasaki, G.J., House, W.V., Kobayashi, R.: "Mixing Rules and Correlations of NMR Relaxation Time with Viscosity, Diffusivity, and Gas/Oil Ratio of Methane/Hydrocarbon Mixtures," SPE 63217 presented at the 2000 SPE ATCE, (1-4 October, 2000), Dallas, TX.

Lo, S.-W.: *Correlations of NMR Relaxation Time with Viscosity/Temperature, Diffusion Coefficient and Gas/Oil Ratio of Methane-Hydrocarbon Mixtures*, (1999) Ph.D. thesis, Rice University, Houston, TX.

McConnell, J., *The Theory of Nuclear Magnetic Relaxation in Liquids*, Cambridge University Press, New York, 1987.

Mirotchnik, K.D., Allsopp, K., Kantzas, A., Curwen, D., and Badry, R.: "Low Field NMR-Tool for Bitumen Sands Characterization: A New Approach," SPE 56764 presented at the 1999 SPE ATCE, Houston, TX, 3-6 October.

Mitra, P.P., Sen, N.S., Schwartz, L.M., and Le Doussal, P.: "Diffusion Propagator as a Probe of the Structure of Porous Media," Phys. Rev. Lett. (1992), Vol. 68, No. 24, 3555-3558.

Morriss, C.E., Freedman, R., Straley, C., Johnston, M., Vinegar, H.J., and Tutunjian, P.N.: "Hydrocarbon Saturation and Viscosity Estimation from NMR Logging in the Belridge Diatomite," *The Log Analyst* (1997), March-April, 44-59.

Muller, B.H. and Nobel, J.D.: "Proton Spin-Lattice Relaxation in Pure Liquid Ethane and Some of Its Duterated Modifications," (not complete)

Oosting, P.H. and Trappeniers, N.J.: "Proton-Spin-Lattice Relaxation and Self-Diffusion in Methanes III Interpretation of Proton Spin-Lattice Relaxation Experiments," *Physica* (1971) **51**, 395-417.

Prammer, M.G., Akkurt, R., Cherry, R., and Menger, S.: "A New Direction in Wireline and LWD NMR," paper DDD presented at the 43rd SPWLA Annual Logging Symposium, Oiso, Japan (June 2-5, 2002).

Prammer, M.G., Mardon, D., Coates, G.R., and Miller, M.N.: "Lithology-Independent Gas Detection by Gradient-NMR Logging," SPE 30562 presented at the SPE ATCE, (22-25 October, 1995), Dallas, TX.

Prammer, M.G., Bouton, J., and Masak, P.: "The Downhole NMR Fluid Analyzer," paper N, SPWLA 42nd Annual Logging Symposium, (17-20 June, 2001), Houston, TX,.

Rajan, S., Lalita, K, and Babu, S.V.: "Intermolecular Potentials from NMR Data: I. CH_4-N_2 and CH_4-CO_2," *Can. J. Phys*. (1975), **53**, 1624-1634.

Reid, R.C., Prausnitz, J.M., and Poling, B.E.: *The Properties of Gases & Liquids*, (1987), McGraw-Hill, New York, NY, pp. 595-596.

Sandhu, H.S.: "Effect of Paramagnetic Impurities on Proton Spin-Lattice Relaxation Time in Methane," *J. Chem. Phys*. (1966), **44**.6, 2320-2321.

Stejskal, E.O. and Tanner, J.E.: "Spin diffusion measurements: spin echo in the presence of a time-dependent field gradient," *J. Chem. Phys*. (1965) **43**, 288-292.

Vinegar, H.J.: "NMR Fluid Properties," NMR Short Course, SPWLA 36th Annual Symposium, (June 26, 1995), Paris, France.

Zega, J.A., House, W.V., and Kobayashi, R.: "A Corresponding-States Correlation of Spin Relaxation in Normal Alkanes," *Physica A* (1989),**156**, 277-293.

Zhang, Q., Lo, S.-L., Huang, C.C., Hirasaki, G.J., Kobayashi, R., and House, W.V.: "Some Exceptions to Default NMR Rock and Fluid Properties," paper FF, SPWLA 39th Annual Logging Symposium, (May 26-29, 1998), Keystone, CO.

Zhang, Q.: *NMR Formation Evaluation: Hydrogen Index, Wettability and Internal Field Gradients*, Ph.D. thesis, Rice University, (2001).

Zhang, Y.: "NMR Relaxation and Diffusion Characterization of Hydrocarbon Gases and Liquids," Ph.D. Thesis, Rice University (April, 2002).

Zhang, Y., Hirasaki, G.J., House, W.V., and Kobayashi, R.: "Oil and Gas NMR Properties: The Light and Heavy Ends" paper HHH prepared for presentation at the 43rd Annual Logging Symposium, (June 2–5, 2002), Oiso, Japan.

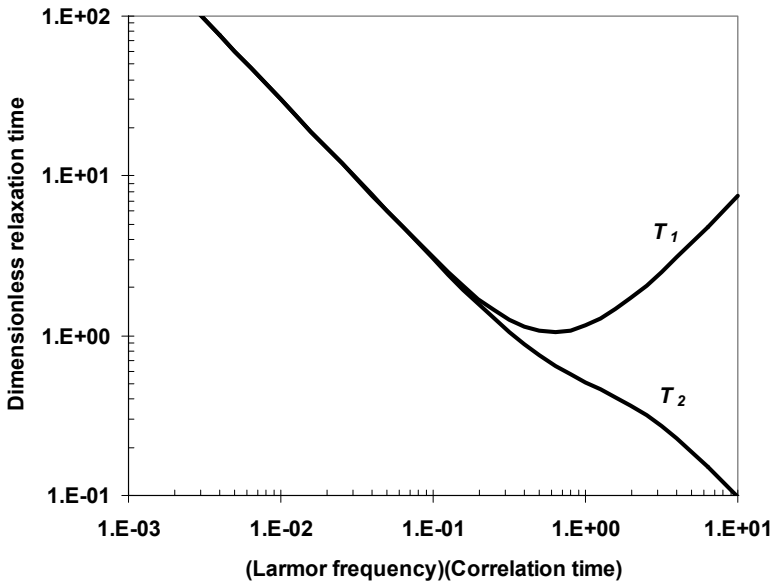

Fig: 1. Dependence of the NMR relaxation times, T_1 and T_2, on the Larmor frequency and rotational correlation times for fluids by intra-molecular dipole-dipole interactions.

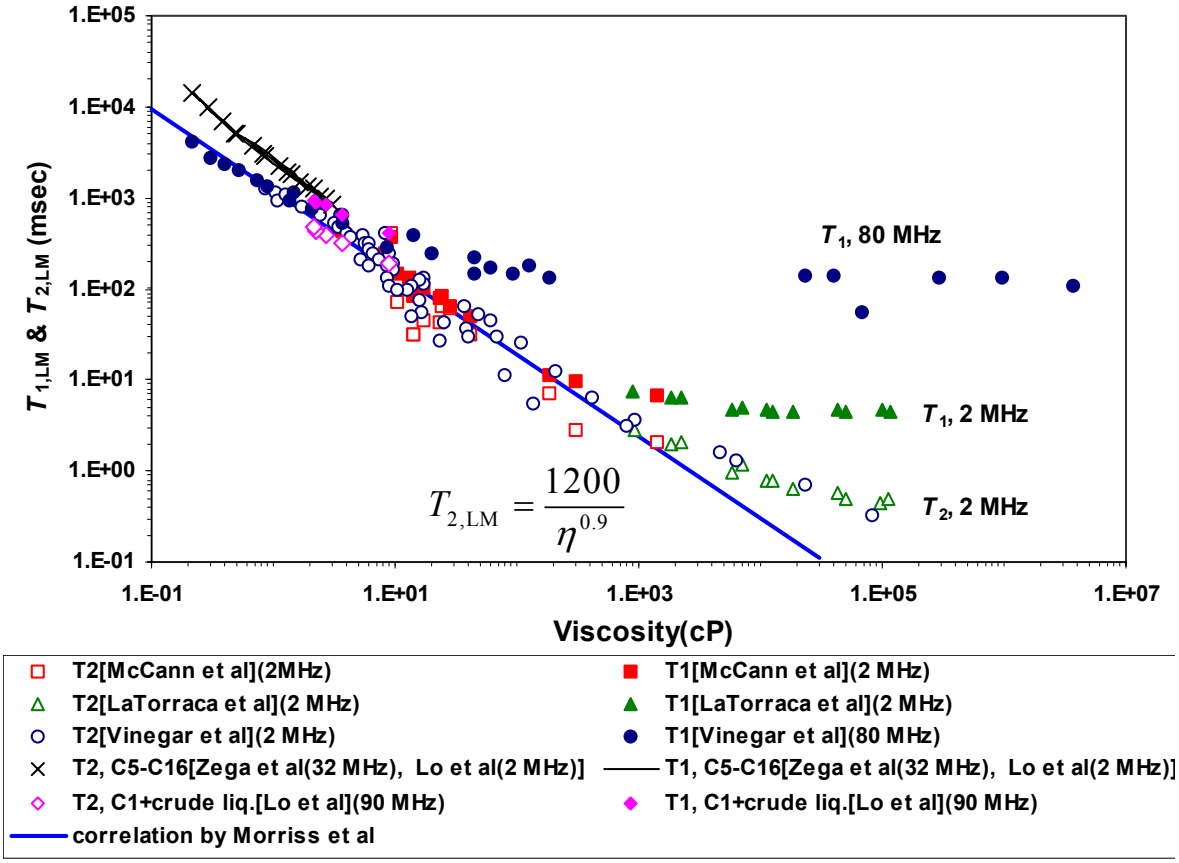

Fig. 2: $T_{1,\mathrm{LM}}$ and $T_{2,\mathrm{LM}}$ relaxation times as a function of viscosity and Larmor frequency at 2 MHz and 80 MHz. (Zhang, 2002)

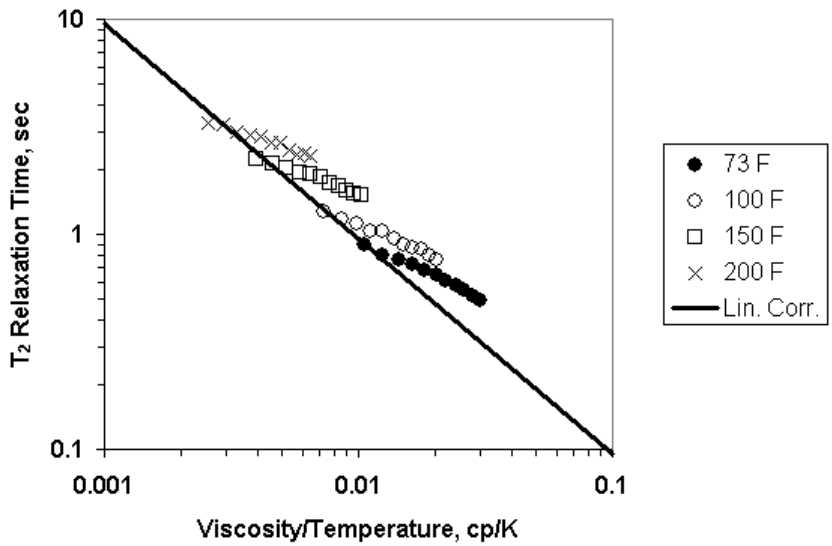

Fig. 3: T_2 relaxation time of OBM base oil as a function of temperature and pressure up to 10,000 psi.

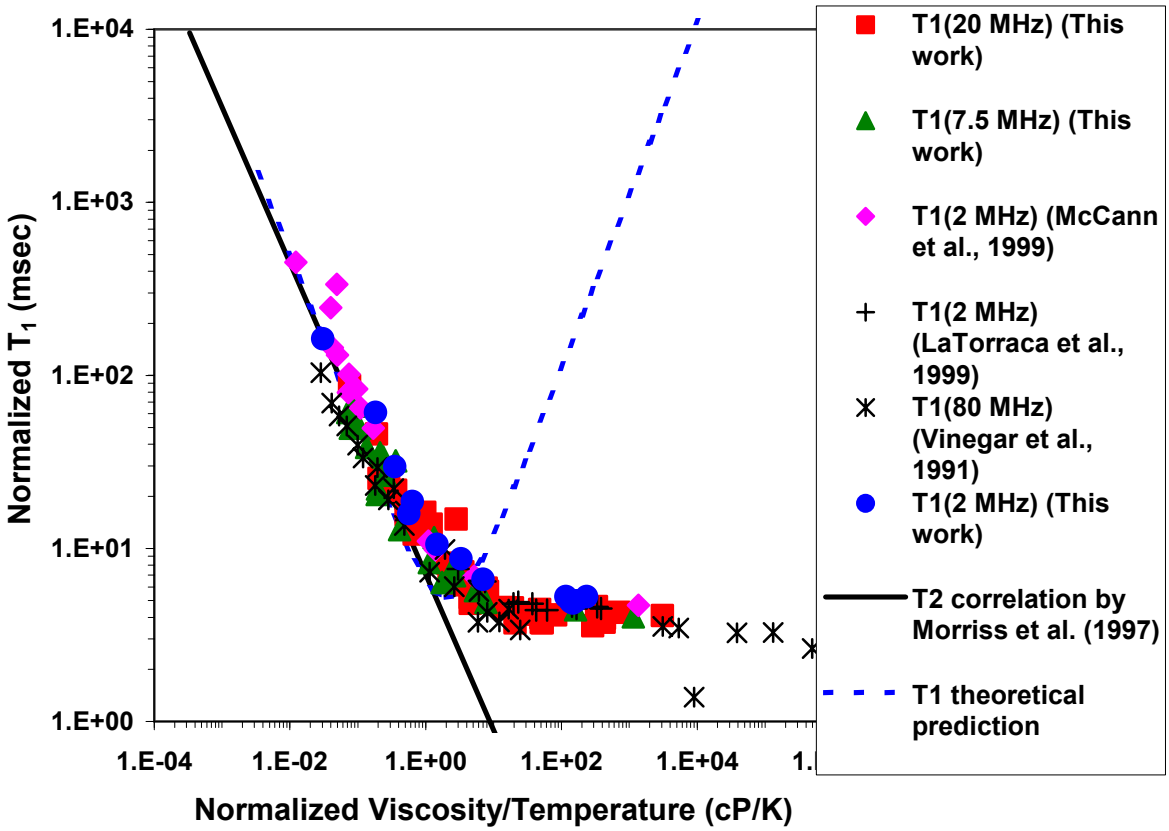

Fig. 4: T_1 of viscous crude oils will correlate on to a single curve if normalized with the Larmor frequency. At higher viscosities, the measured $T_{1,LM}$ data depart from the theoretical prediction calculated for a system with a single correlation time. (Zhang, 2002)

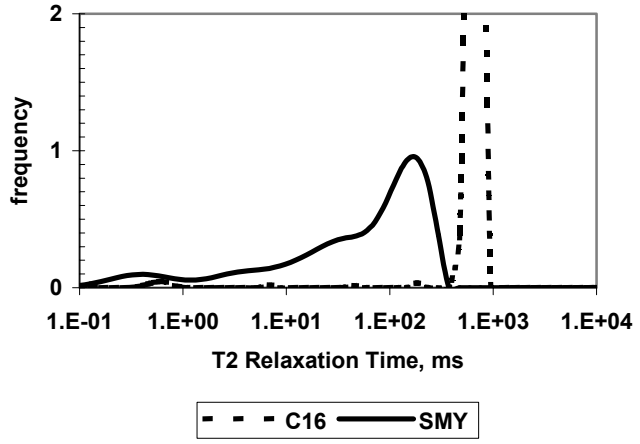

Fig. 5: Comparison of the relaxation time distribution of a 30º API crude oil with that of hexadecane. (Zhang, 2002)

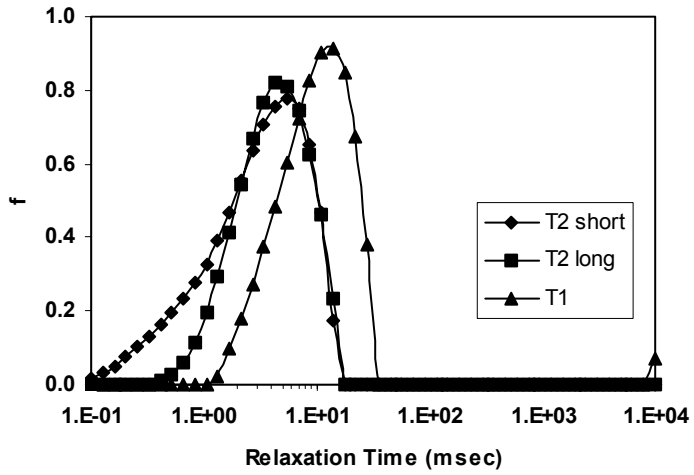

Fig. 6: Relaxation time distributions of a 19°API crude oil at 2 MHz. (Zhang, 2002)

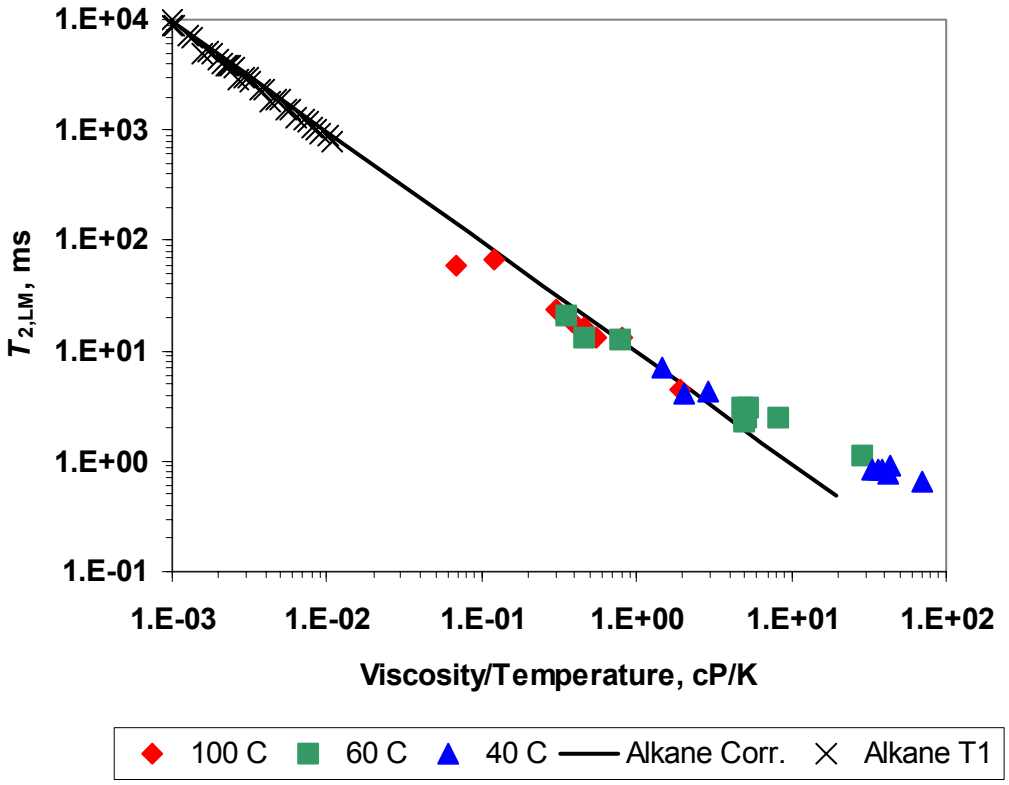

Fig. 7 Temperature dependence of $T_{2,LM}$ for viscous crude oils, Larmor frequency = 20 MHz, TE=0.2 ms (Zhang, 2002).

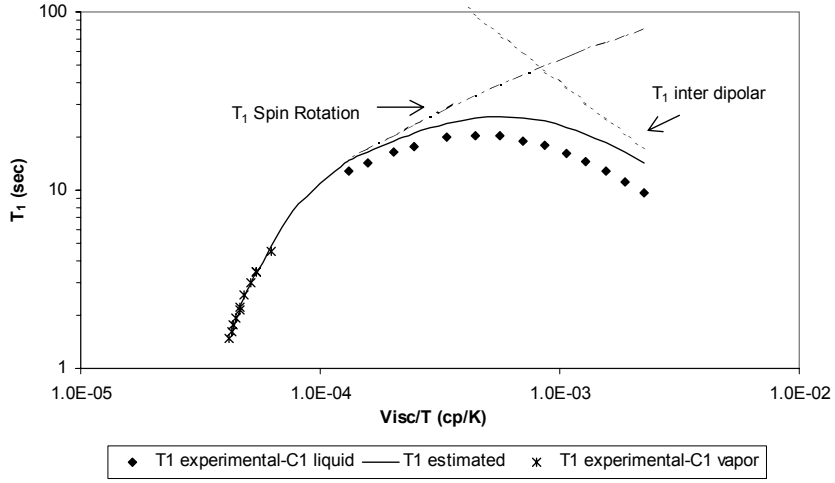

Fig. 8: Contributions to the proton relaxation time of methane. (Lo, 1999)

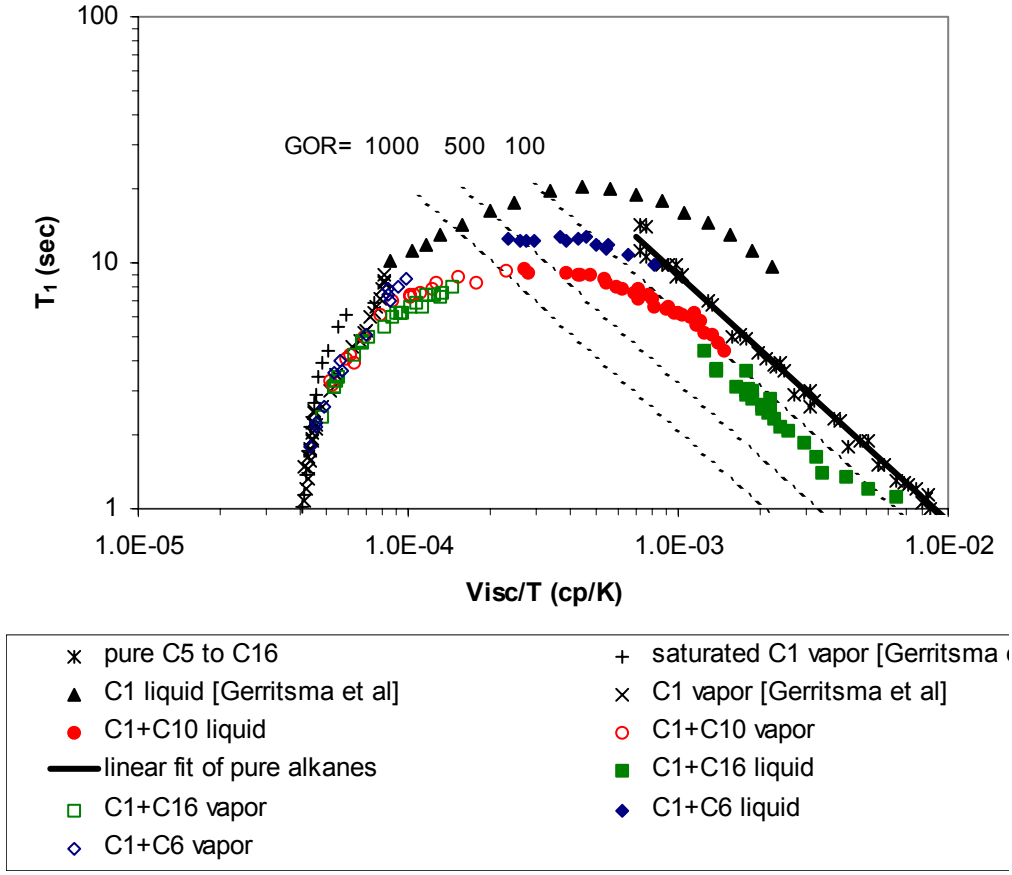

Fig. 9: Correlation of relaxation time as a function of viscosity/temperature and GOR (m^3/m^3) (Lo *et al*., 2002)

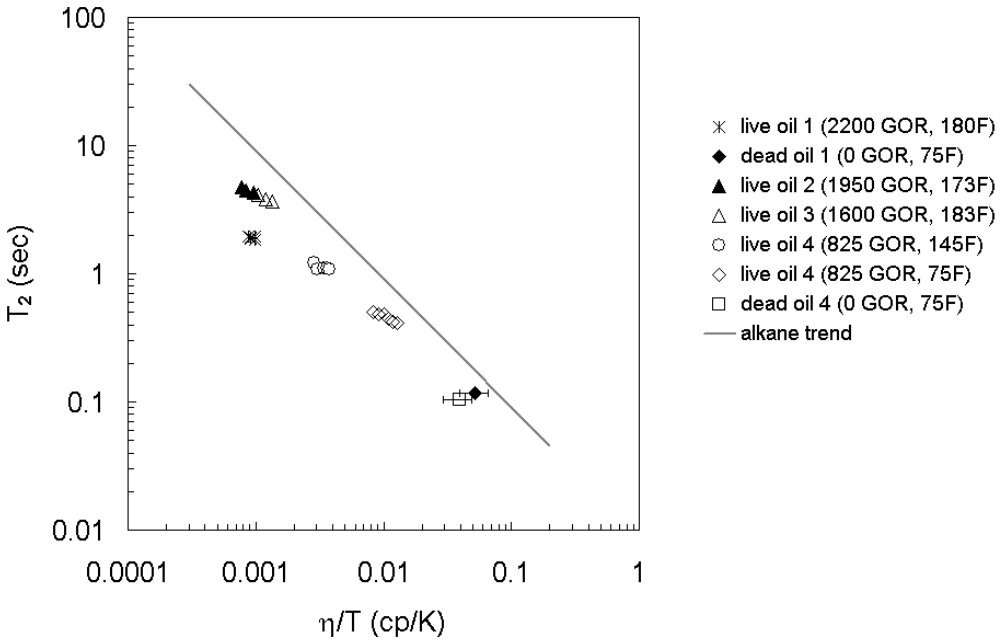

Fig. 10: Transverse relaxation times of live and dead reservoir fluids as a function of viscosity over temperature.

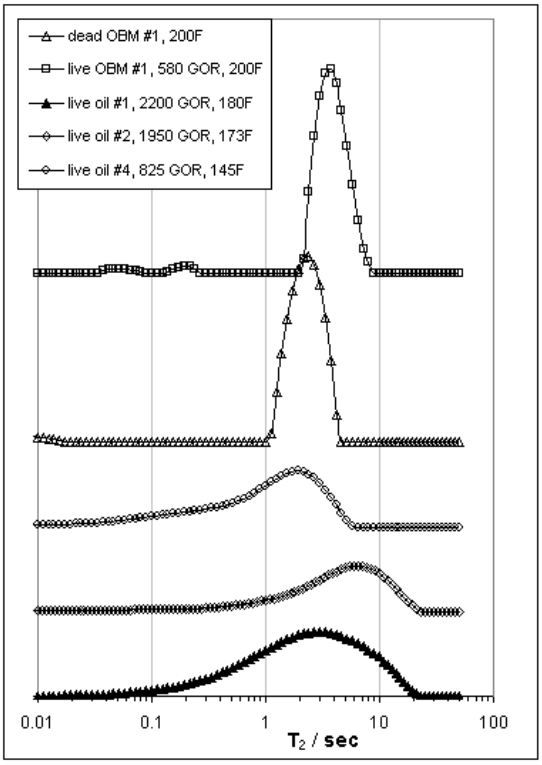

Fig. 11: Spectra of transverse relaxation times of live and dead oils and oil-based mud filtrates. All measurements have been acquired at a pressure of 10,000 psi.

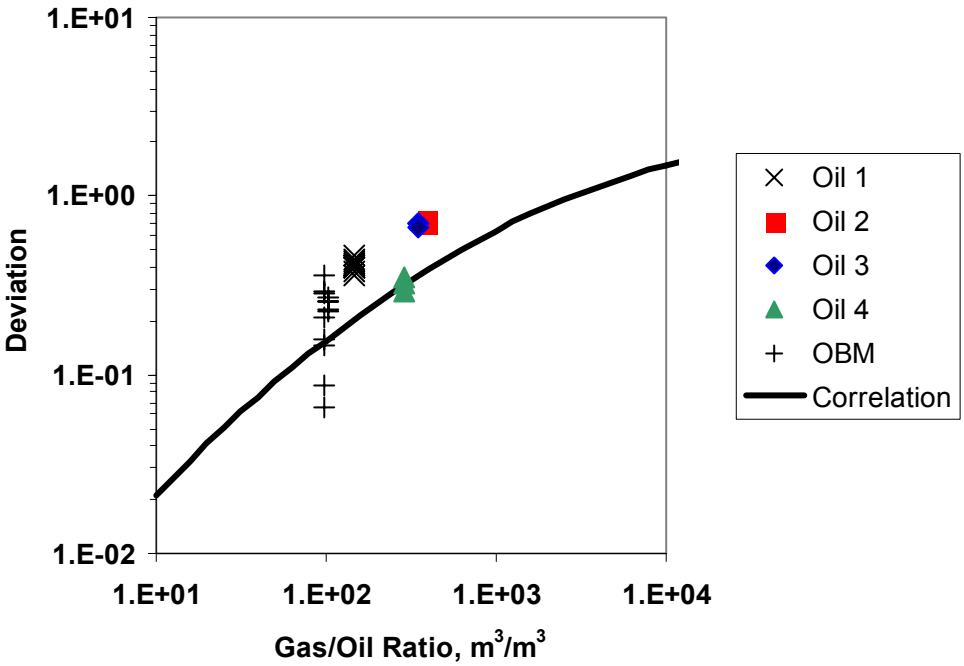

Fig: 12 Comparison of experimental data for live crude oils and OBM with the correlation that was developed for alkanes.

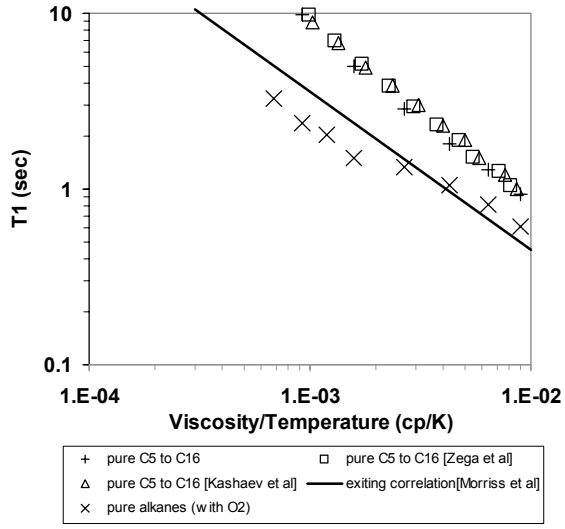

Fig: 13: Effect of dissolved air on the relaxation time of alkanes. (Zhang, 2002)

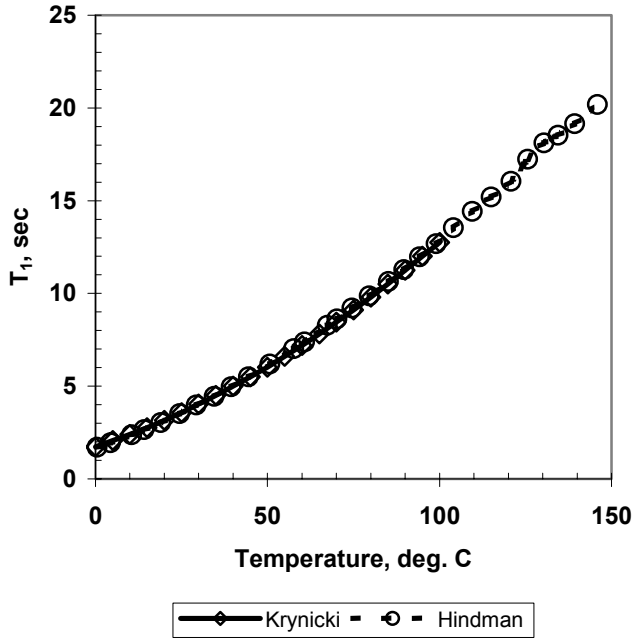

Fig. 14: Temperature dependence of the relaxation time of pure water (Krynicki, 1966, Hindman *et al*., 1973)

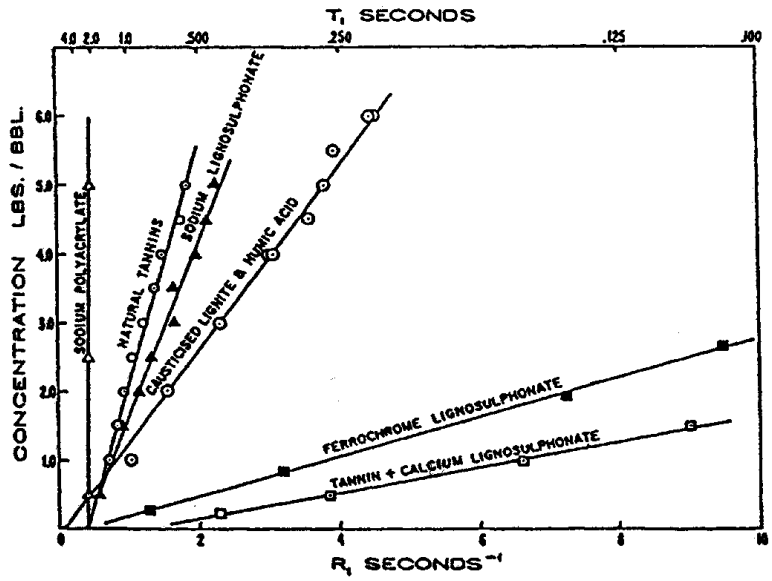

Fig. 15: Enhanced relaxation due to drilling mud additives (reproduced from Coolidge, et al., 1962).

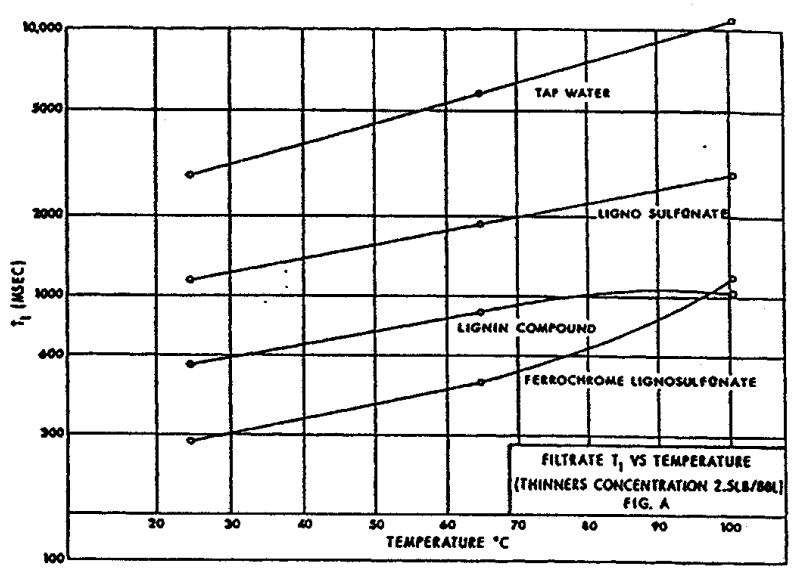

Fig. 16: Effect of additives and temperature on relaxation time (reproduced from Wyman, 1962).

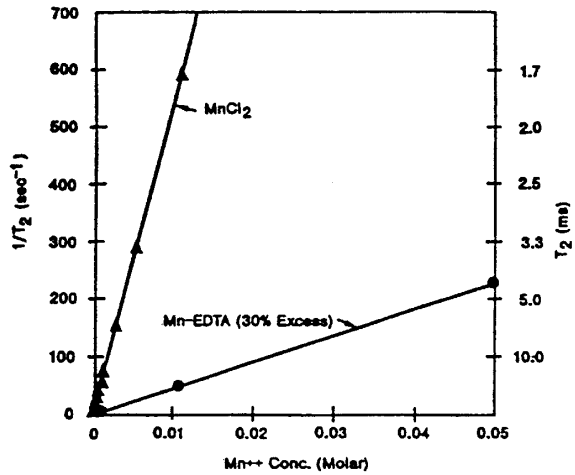

Fig. 17: T_2 of $MnCl_2$ and Mn-EDTA brines (temperature = 80° F, Larmor frequency = 1 MHz)(reproduced from Horkowitz, et al., 1997).

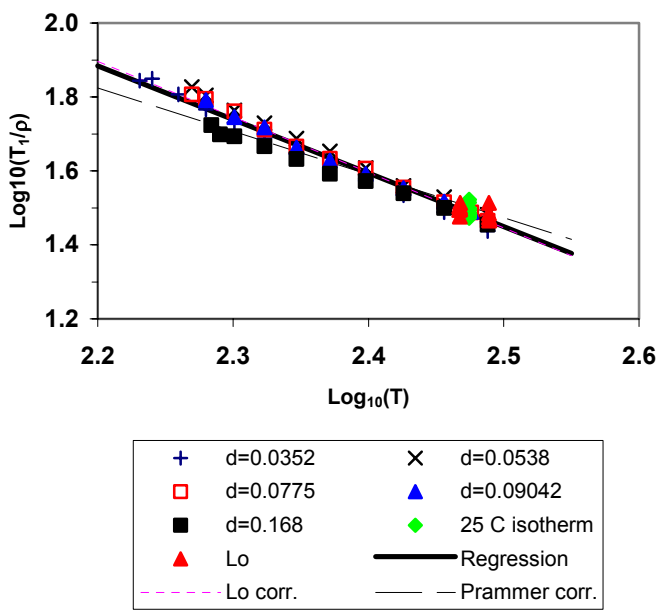

Fig. 18: Relaxation time data for methane Gerritsma, et al., (1970) and Lo (1999). The units of T_1, ρ, and T are s, g/cm^3, and K, respectively.

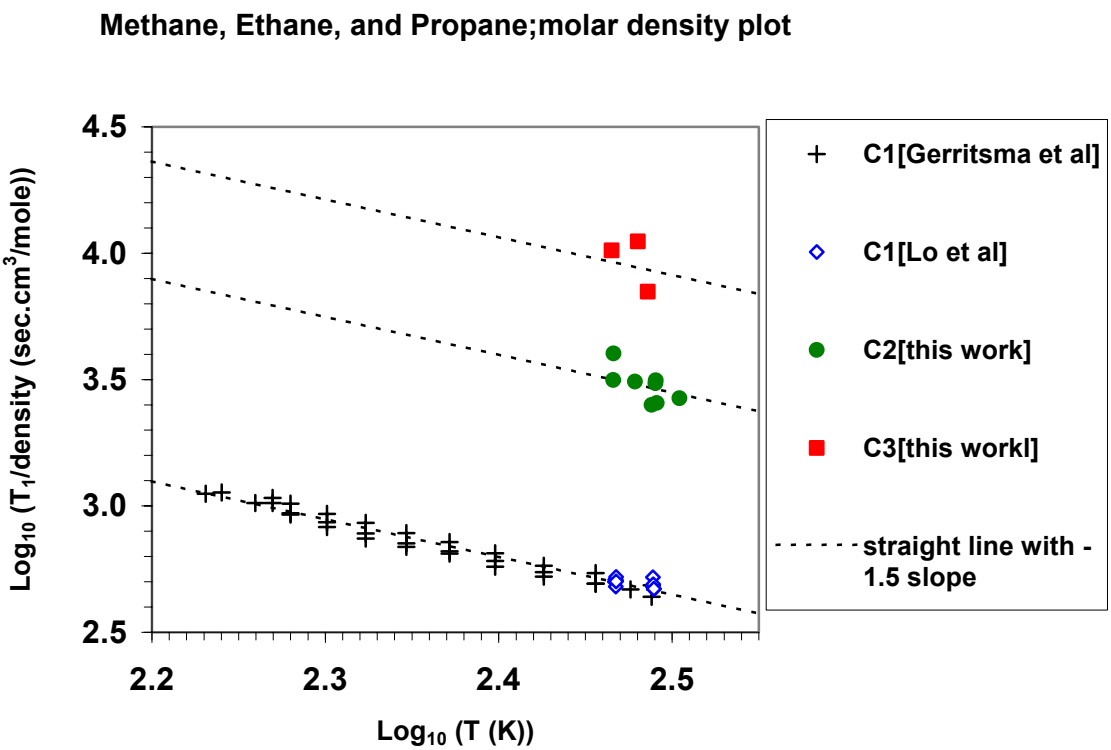

Fig. 19: Relaxation time of propane and ethane compared to methane (Zhang, 2002).

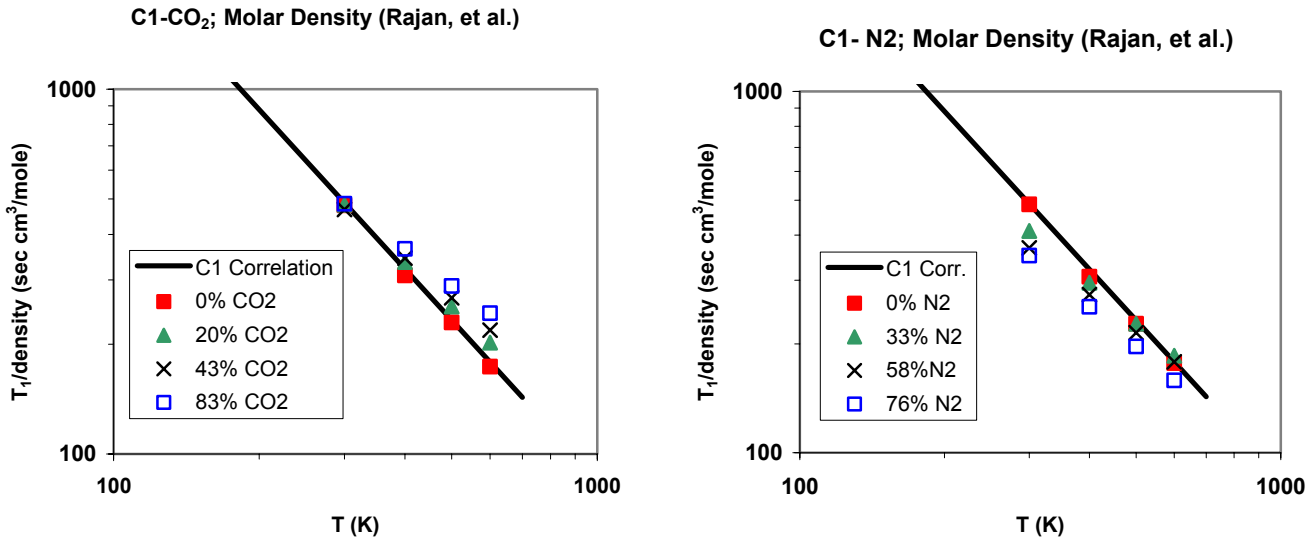

Fig. 20: Relaxation time of methane - CO_2 and methane – N_2 mixtures (Rajan *et al*, 1975).

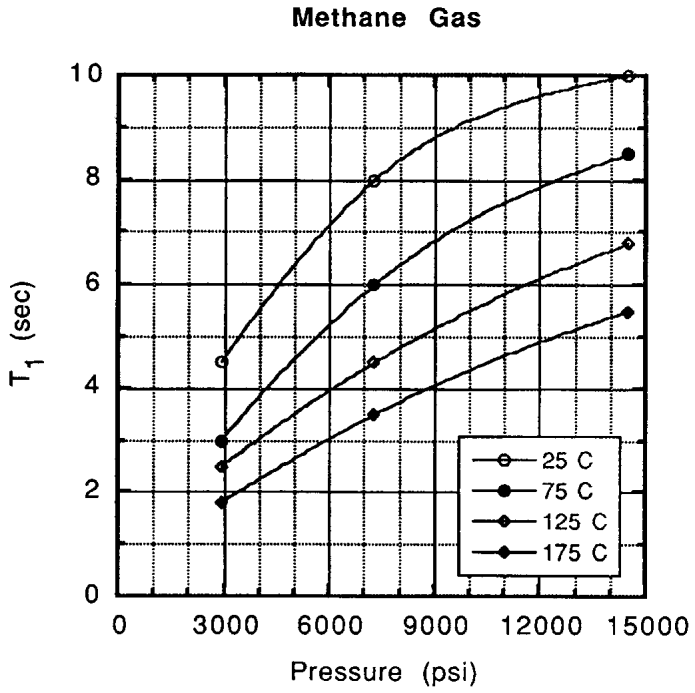

Fig. 21: Relaxation time of methane, (Kleinberg and Vinegar, 1996, Gerritsma *et al*., 1971)

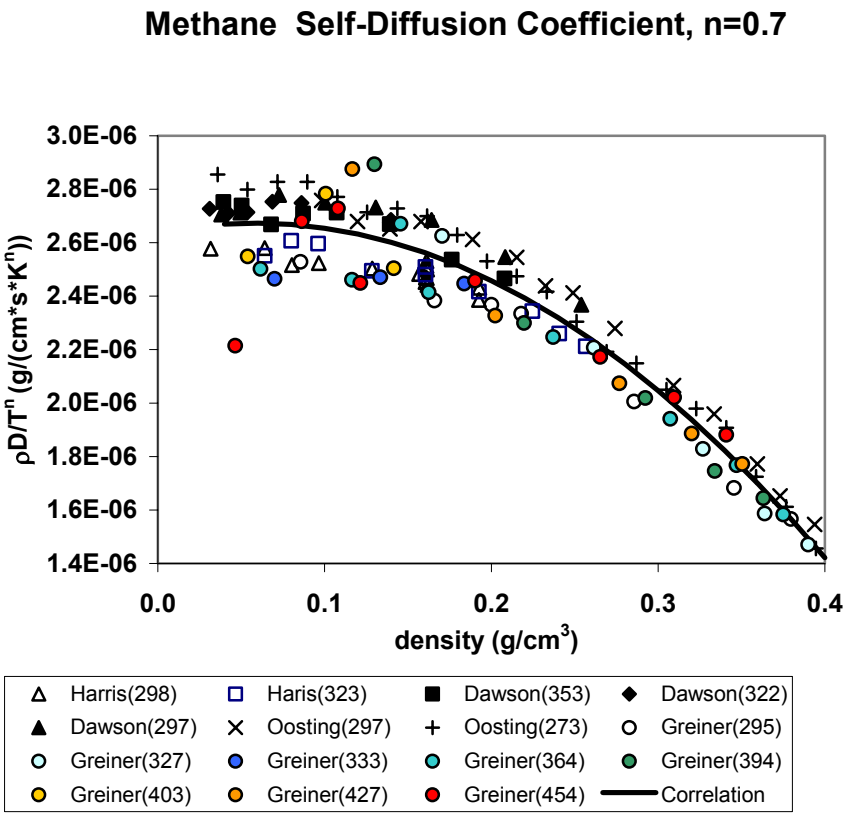

Fig. 21: Correlation for methane diffusion coefficient

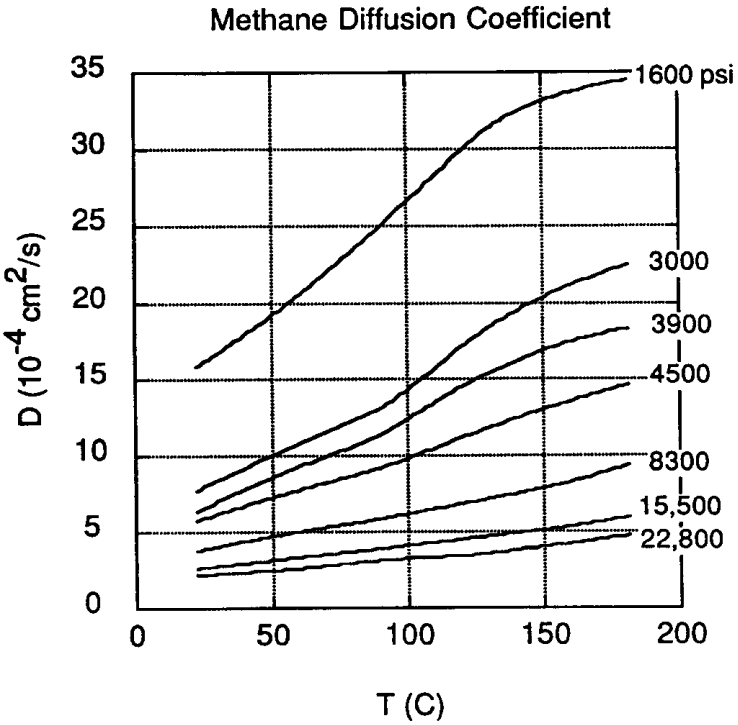

Fig. 23: Methane diffusion coefficient (Kleinberg and Vinegar, 1996)

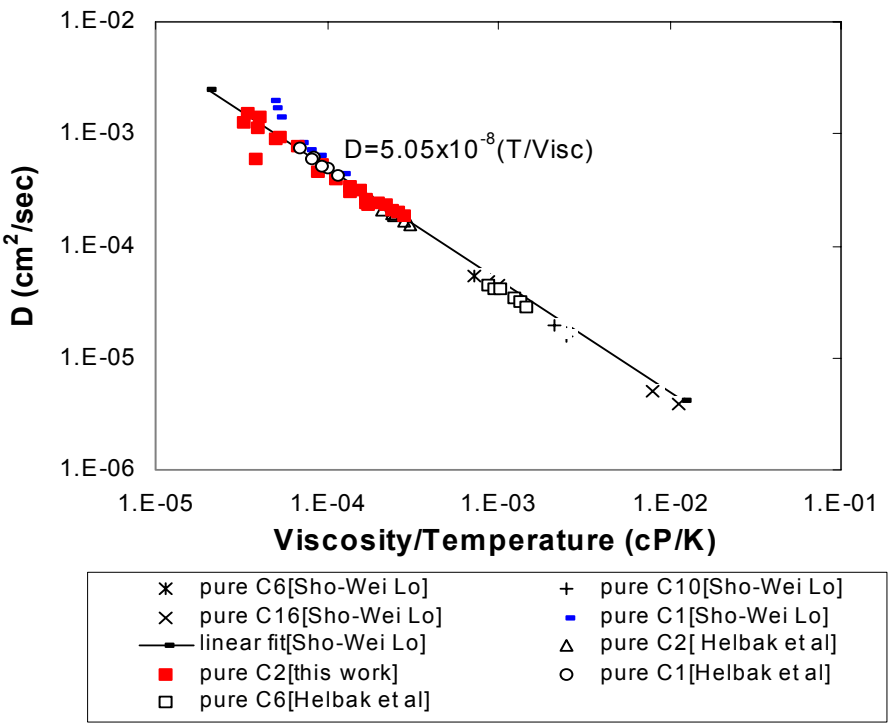

Fig. 24: Diffusion coefficient dependence for alkanes on viscosity/temperature (Y. Zhang, 2001).

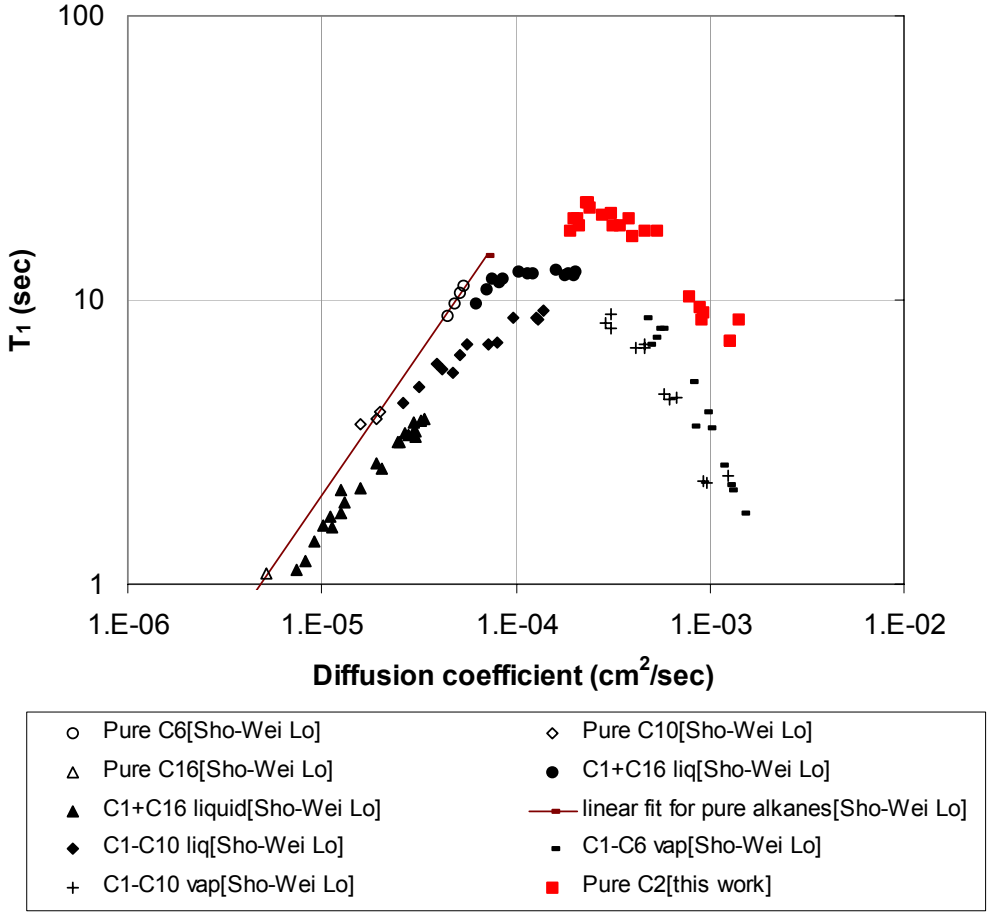

Fig. 25 : T_1 dependence on diffusion coefficient (Y. Zhang, 2001).

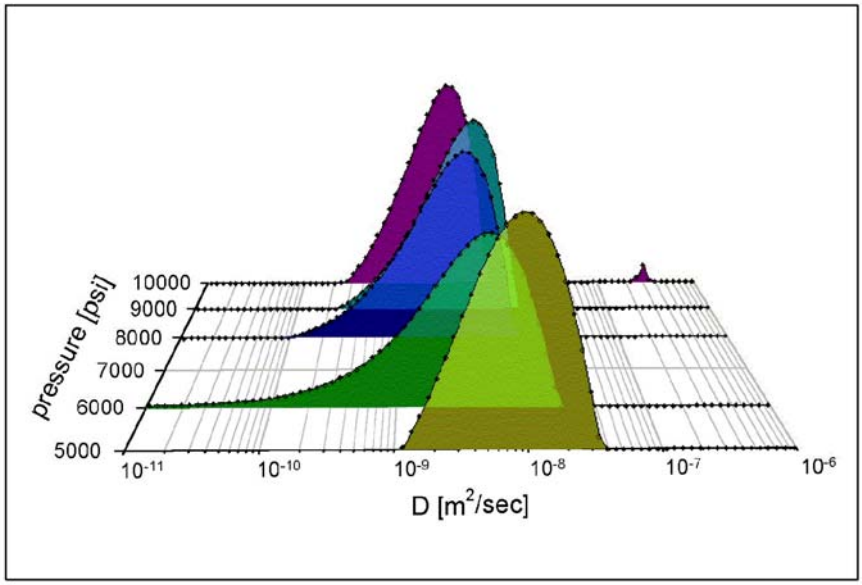

Fig. 26: Distribution of self-diffusion coefficients of a 33º API live crude oil with 825 SCF/STB GOR as function of pressure. The PFG NMR measurements have been made at 75ºF.

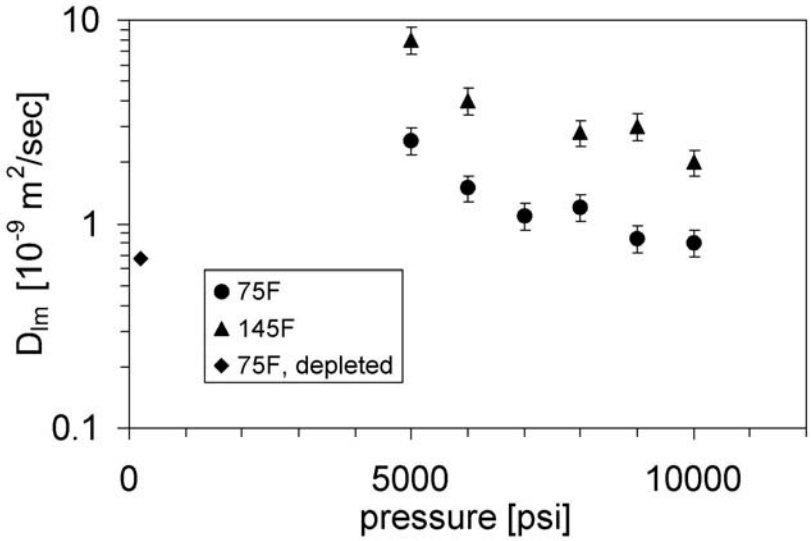

Fig. 27: Diffusivities of a 825 SCF/STB GOR live oil as function of pressure. The measurements were taken at two different temperatures and are compared to the diffusivity of the same oil after the solution gas has been depleted.

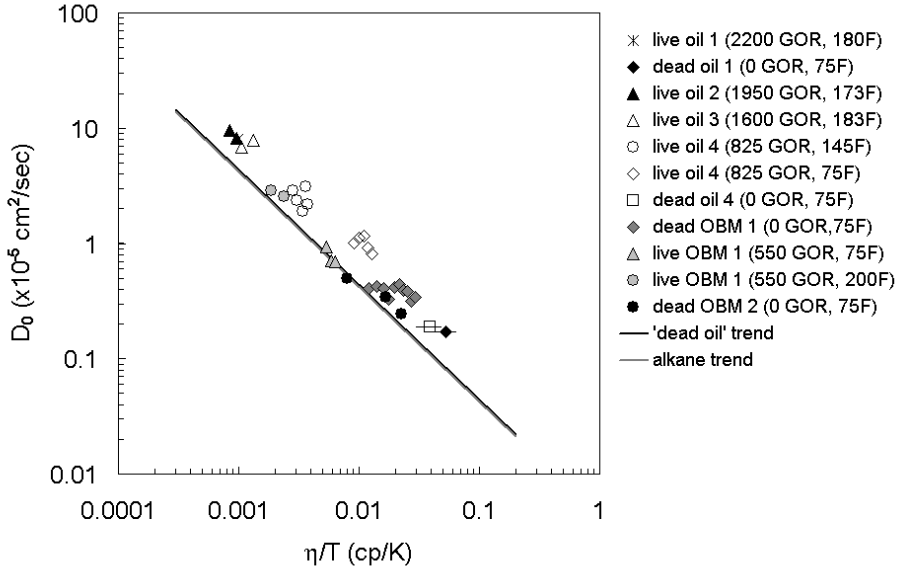

Fig. 28: Diffusivities of various live and dead oils and oil-based mud filtrates as function of fluid viscosities over temperature.

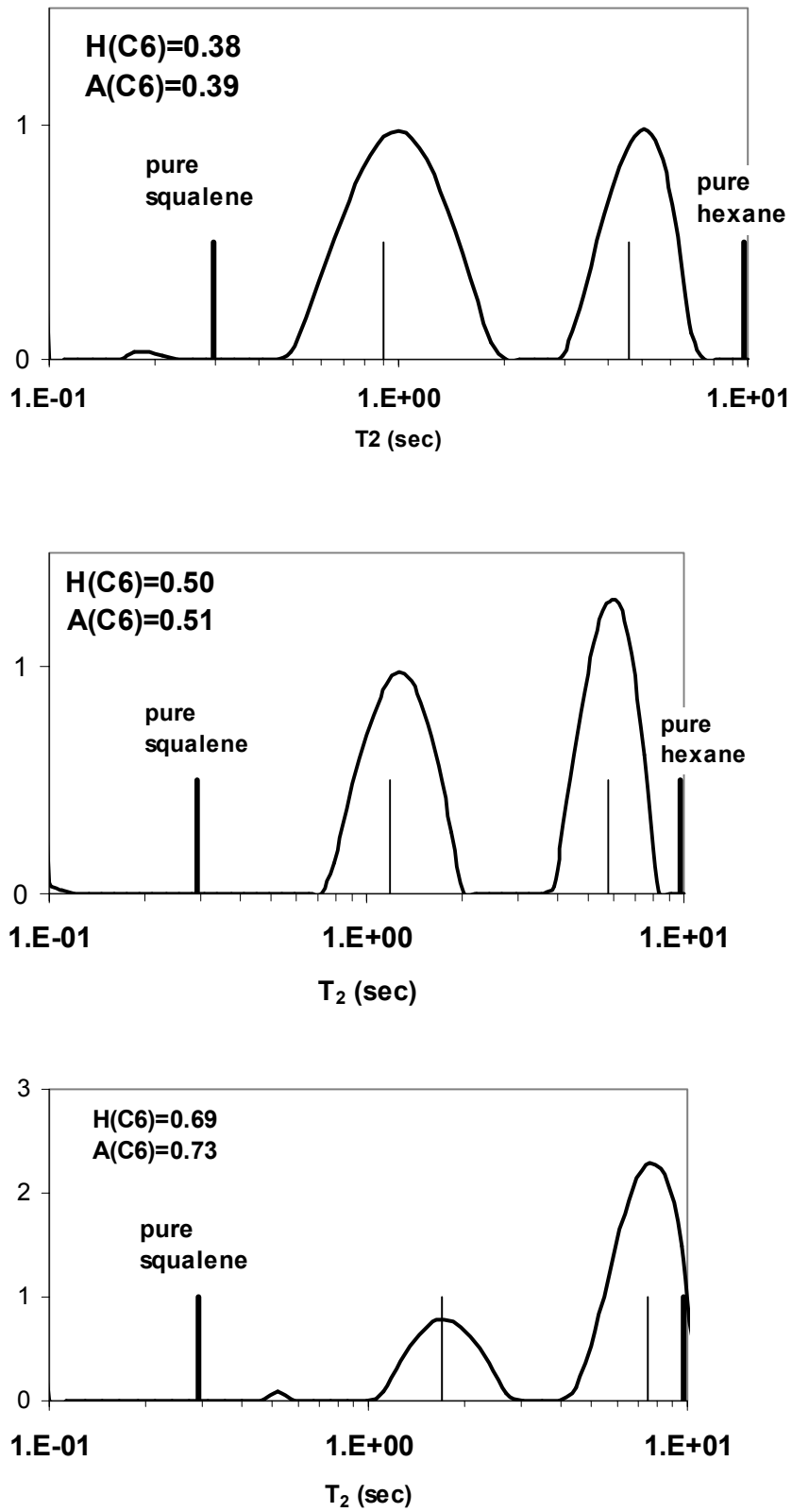

Fig. 29: Relaxation time distributions of *n*-hexane and squalene mixtures. Thin line is estimate from bi-exponential fit. (Freedman *et al*., 2001)

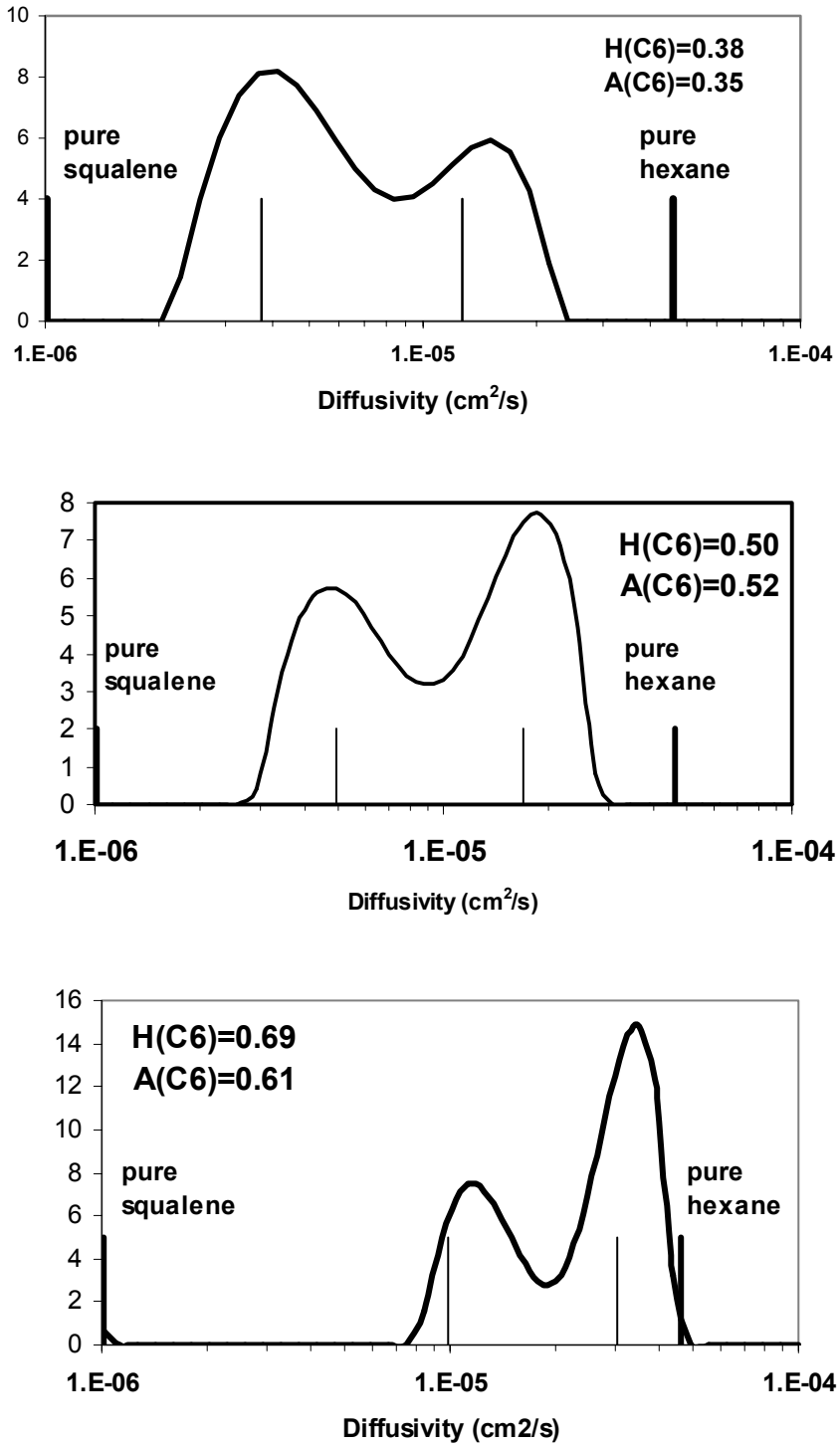

Fig. 30: Diffusivity of *n*-hexane and squalene mixtures. (Freedman et al., 2001)

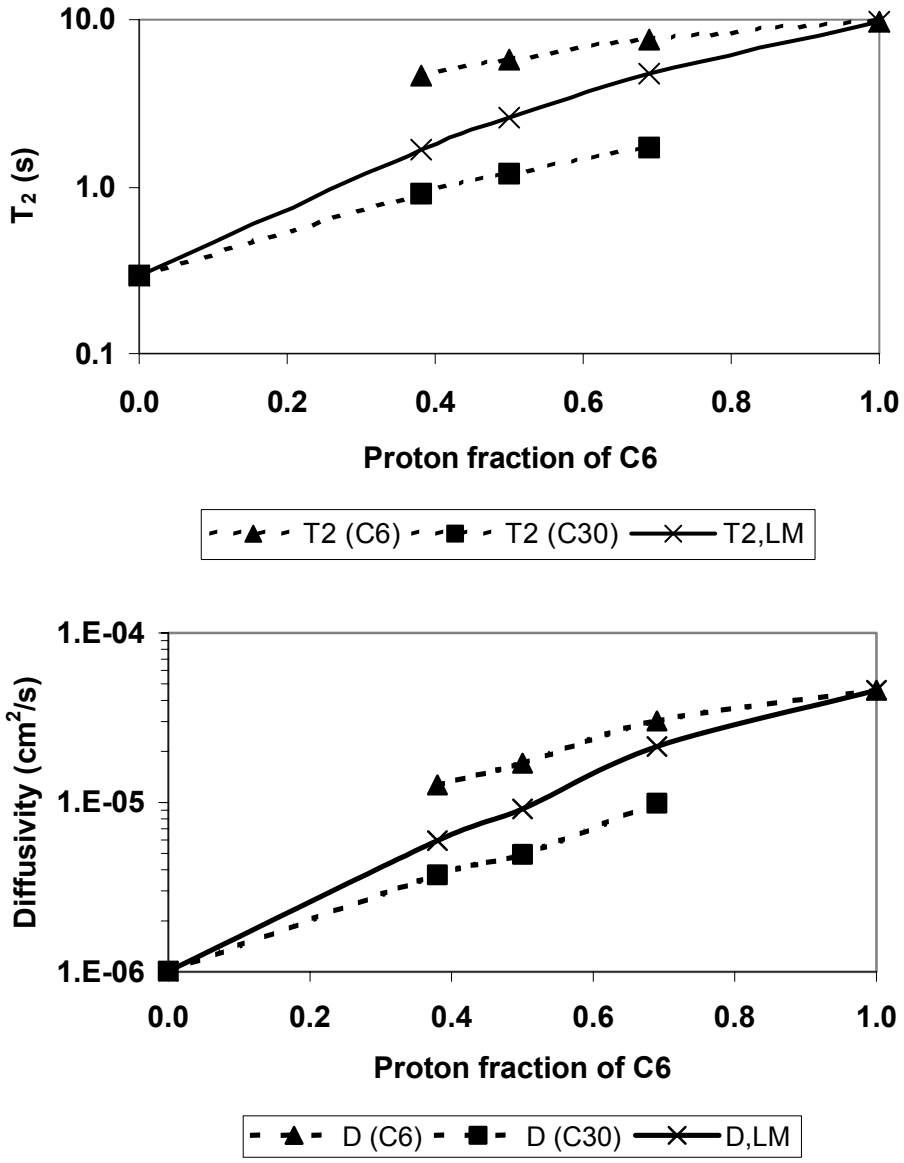

Fig. 31: Constituent relaxation time and diffusivity as a function of concentration.

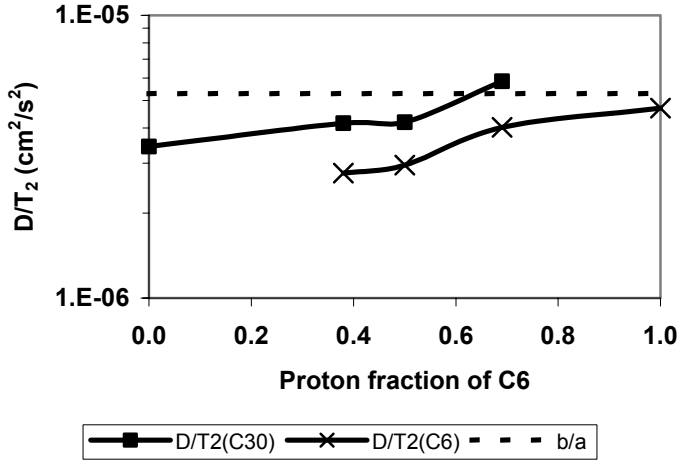

Fig. 32: Ratio of constituent diffusivity and relaxation time compared to that of the correlation.

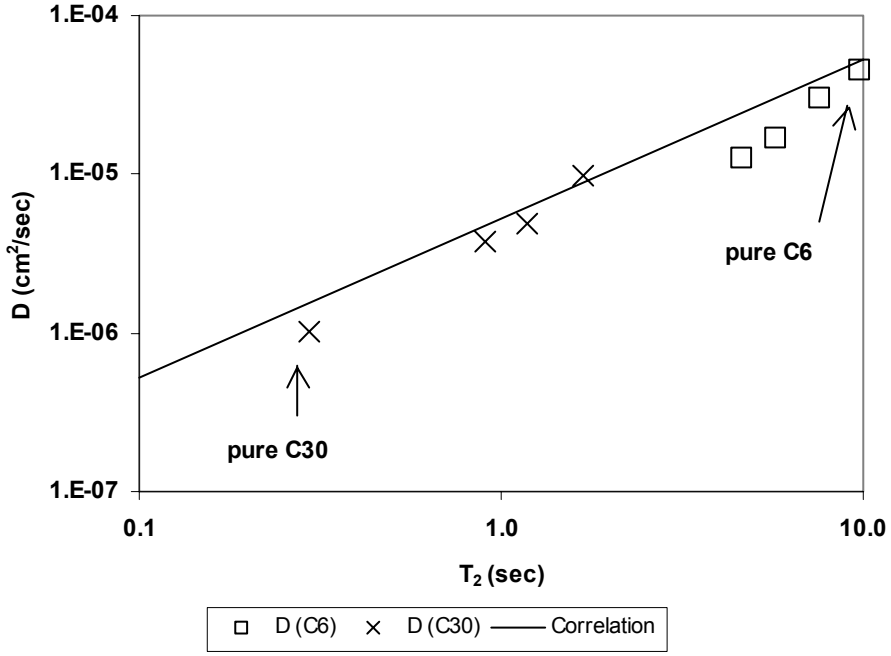

Fig. 33: Correlation between constitutent diffusivity and relaxation time of *n*-hexane and squalene. The line is the correlation predicted by the constitutive viscosity model (Freedman *et al*., 2001).

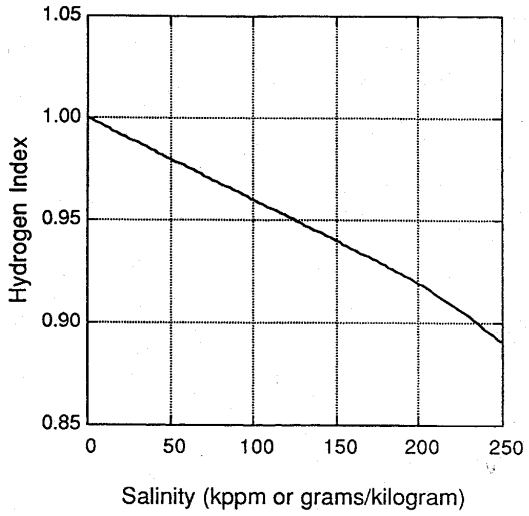

Fig. 34: *HI* as a function of salinity, (Kleinberg and Vinegar, 1996).

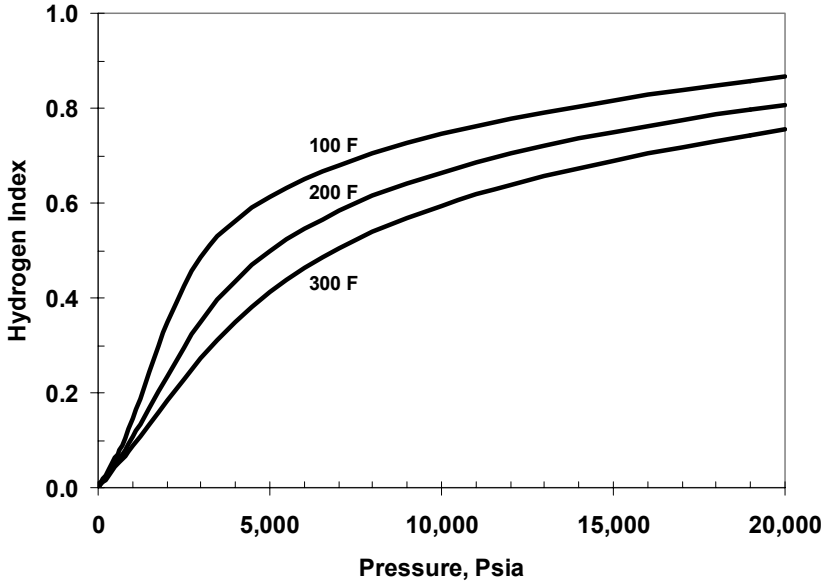

Fig. 35: Hydrogen index of a gas with the composition shown in Table 2.

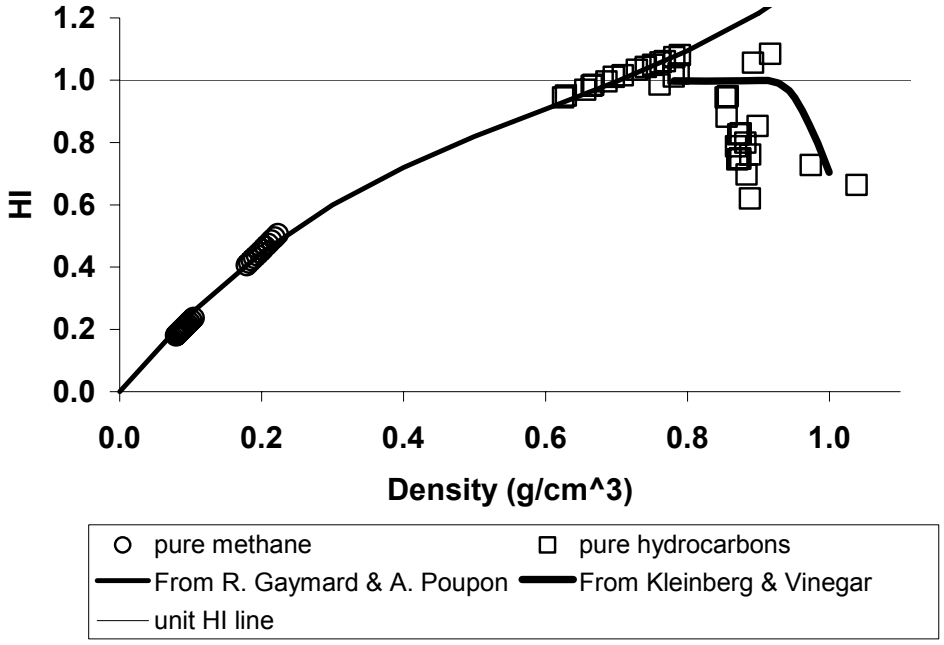

Fig. 36: *HI* from correlations and for pure hydrocarbons (Zhang, *et al*. , 1998).

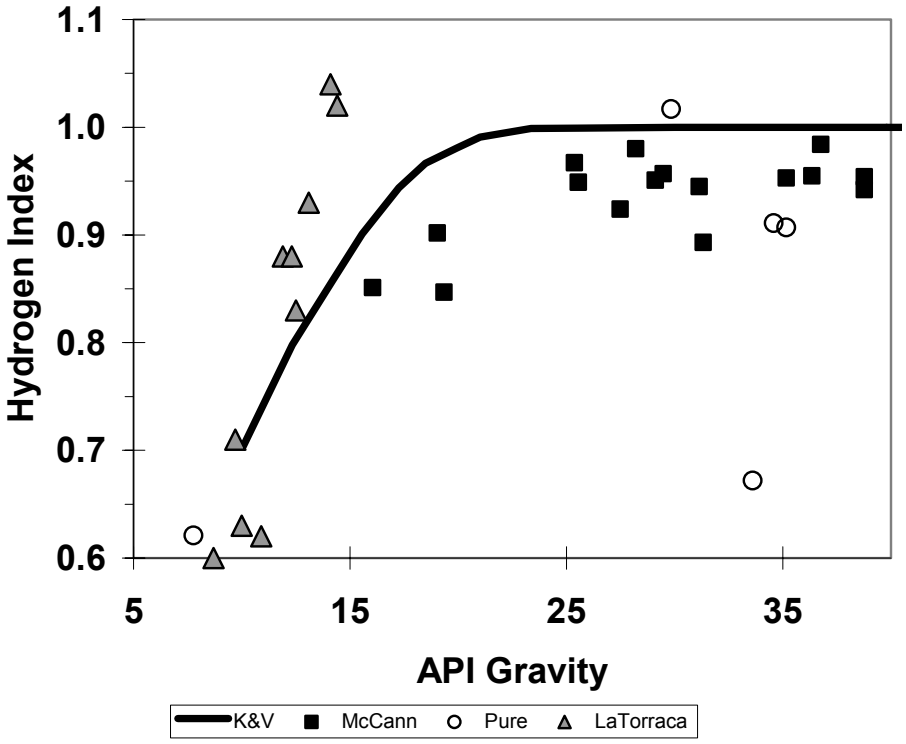

Fig. 37: Comparison of the Kleinberg and Vinegar (1996) correlation with measurements of LaTorraca et al. (1999),*TE*=0.20 ms and McCann (1999), *TE*=0.24 ms.

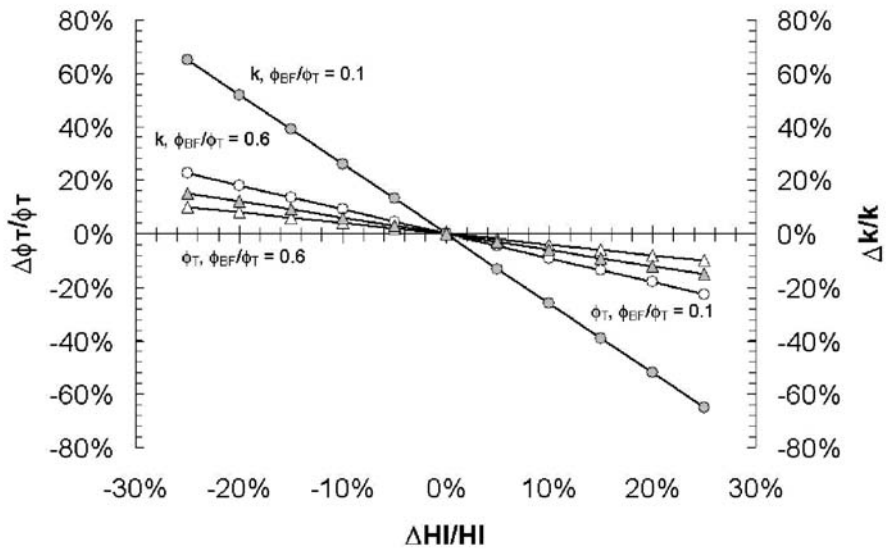

Fig. 38: Impact of the uncertainty in the determination of the hydrogen index on porosity and permeability for 10% and 60% *BVI.*

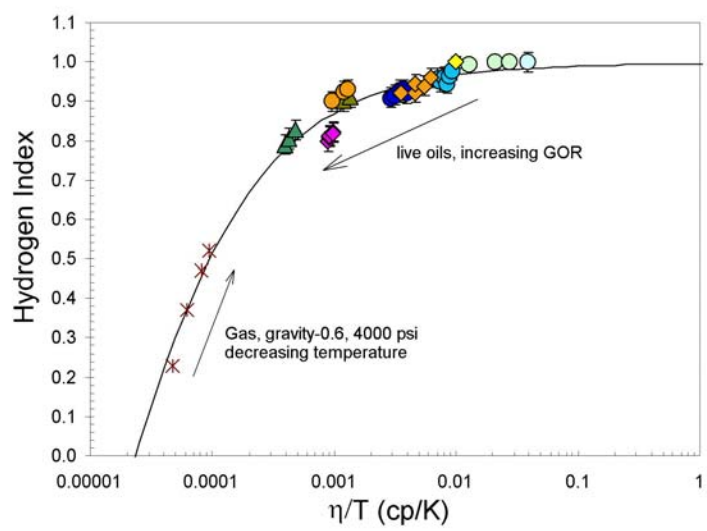

Fig. 39: *HI* measurements on live oils and mixtures of oil-based mud filtrates and methane at various conditions.

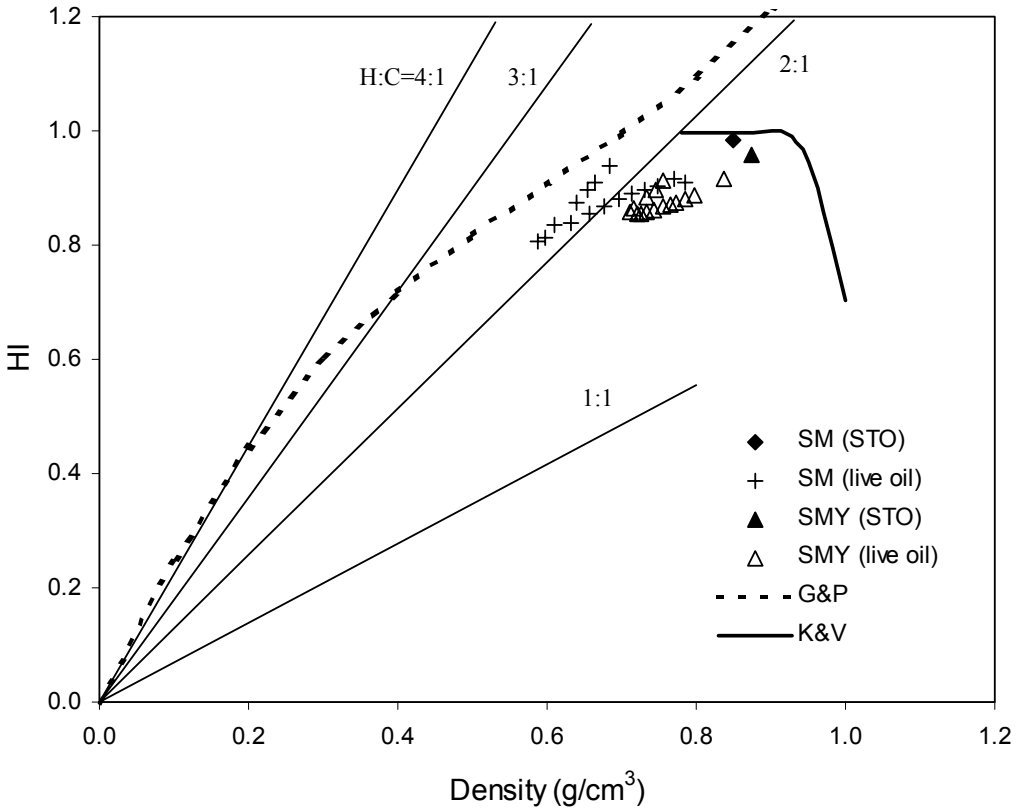

Fig. 40: Calculated *HI* for two live crude oils (Q. Zhang, 2001).

Effect of Drilling-Mud Base-Oil Contamination on Crude Oils T_2 Distributions

Arjun Kurup, Robert Freedman, George J. Hirasaki

Abstract

Oil-based drilling fluids used to aid in drilling oil wells often contaminate crude oils in those wells. This report details NMR T_2 measurements made on mixtures of NovaPlus, an example of a drilling fluid base oil, with three crude oils of viscosities ranging from 13.7 to 207 cp to determine the effect of the contamination. It is found that the T_2 distributions of more viscous crude oils change more drastically for the same level of contamination, and with all crude oils the effects are more pronounced for higher NovaPlus concentrations. The mixtures follow correlations between $T_{2,LM}$, the logarithmic-mean-average T_2, and viscosity developed for dead crude oils. The measured viscosities and $T_{2,LM}$ values for the mixtures independently follow concentration-weighted logarithmic-mean averages of the measured $T_{2,LM}$ values and viscosities of unmixed NovaPlus and crude oil. Using cumulative T_2 distributions, particular relaxation time bins were found to contain more useful data than others. A contamination index is defined as a parameter capable of relating information in the T_2 distribution to the level of contamination.

Introduction

Oil wells are often drilled with the aid of oil-based fluids. The oil phase forms the continuous phase in the drilling fluid, and the oil used in the drilling fluid is called a base oil. During the drilling process, an oil-based mud (OBM) is formed from the mixture of drilling fluid and drill cuttings. Filtrates from these oil-based muds invade oil-bearing formations and mix with crude oils. OBM filtrates change the properties of the crude oils with which they mix. In NMR well logging, a specific concern is whether the measured T_2 relaxation time distribution (or T_2 distribution) changes enough to affect the predicted viscosity, which can be derived from these measurements through existing correlations. Such concerns

are particularly valid because OBM filtrates are similar in molecular structure to the crude oils themselves. This inhibits attempts to separate the OBM filtrate signal from the crude oil signal in NMR measurements.

Previous work regarding the use of NMR for determining contamination is relatively scarce. Bouton, *et al*. (2001) have developed a sharpness parameter to characterize T_1 relaxation times of mixtures of crude oils and base oil. This parameter is at a maximum for the base oil alone and decreases monotonically for higher concentrations of crude oil. Continuing this work, Masak, *et al*. (2002) uses a downhole fluid sampler to characterize contamination by measuring T_1 relaxation times during the pumping process. Here, measurements are made as time progresses, and the change in measured signal amplitudes is used to characterize the contamination.

In this study, NovaPlus is the base oil. NovaPlus is a mixture of 16- to 18-carbon internal olefins. It is a common base oil used in drilling wells. The crude oils used are a North Sea oil (13.7 cp), a Gulf of Mexico oil (21.0 cp), and an offshore China crude oil (207 cp). Henceforth, the crude oils will be called STNS, SMY, and PBB, respectively.

The objective in this study is to relate the contamination level to features in the T_2 distributions and to the viscosities of the samples. Since viscosities have been closely correlated with NMR logging measurements, observing viscosity effects with contamination yields additional insight into the T_2 distributions themselves. Multiple crude oils are used to determine the ease of contamination characterization for different crude oils. In this study, logarithmic-mean T_2 values (log-mean T_2 or $T_{2,LM}$) are first used in the characterization. Then, samples are characterized by amplitudes at different relaxation times in each T_2 distribution. This is done in order to salvage any information that may be lost in the average represented by $T_{2,LM}$.

Experimental

The experimental procedure used is the same for each of three sets of mixtures, each set containing NovaPlus and differing in the crude oil, namely

STNS, SMY, or PBB. For each set, crude oil mixtures with NovaPlus were prepared at volumetric concentrations of 10, 20, 50 and 75% NovaPlus. The crude oil (0% NovaPlus) and NovaPlus (100% NovaPlus) were also included in the measurements.

For all samples, the T_2 relaxation time and the viscosity are measured. The instrument used for T_2 relaxation time measurements is a MARAN instrument with 2 MHz operating frequency, manufactured by Resonance Instruments. The experiment performed uses a Carr-Purcell-Meiboom-Gill (CPMG) pulse sequence. In this measurement, the decay in signal amplitude, or magnetization, is measured as function of time. The decay process is characterized by the following equation:

$$M = \Sigma_j M_{0,j} \exp(- t / T_{2,j}) \qquad [1]$$

In this expression, M is the total magnetization at time t, $M_{0,j}$ is the initial magnetization of component j, and $T_{2,j}$ is the T_2 value corresponding to component j.

The acquired data is then processed, converting the time-domain data to the T_2-domain. Amplitudes in the T_2 domain are placed at predetermined relaxation times, which are spaced apart equally in logarithmic scale. These chosen individual T_2 values, $T_{2,i}$, at which amplitudes are placed are called bins. An amplitude corresponding to these bins are given the symbol, A_i. The index j is used for the time domain and index i is used for the T_2 domain to signify that bins chosen do not match the intrinsic T_2 values for the mixture components in general.

In T_2 experiments done here, the acquisition conditions used are 128 scans, 9216 (9k) echoes or time-domain data points, 320 μs echo spacing or time between echoes in each scan, and a 5 s wait time between neighboring scans. The viscosities are measured using a Brookfield rheometer, Model Number DV-III+. Measurements are made near the maximum shear rate that

does not exceed torque limits or the rotation speed of the instrument. The temperature of both T_2 relaxation time and viscosity measurements is 30 ^{o}C.

Results and Discussion

Fig. 1 shows the conventional T_2 distributions (as opposed to cumulative distributions) for mixtures of STNS and NovaPlus. The plots represent data from 50 T_2 bins. The top panel shows the distribution for NovaPlus, and subsequent panels contain increasing amounts of STNS. For a light crude oil like STNS, the mode, or T_2 value corresponding to the highest amplitude in the distribution, does not differ greatly from the drilling fluid base oil, Nova Plus. As STNS is present in higher quantities in the mixtures, the most noticeable change is the appearance and growth of a shoulder, which is a plateau adjacent to a peak in the distribution, occurring near and below 100 ms. The amplitude in a large range of relaxation times of the distribution shows very little change from one mixture component to the other.

Fig. 2 is the analogous set of distributions for SMY and NovaPlus. Once again, the data is presented with NovaPlus on the top panel and the crude oil, SMY, on the bottom panel. Distributions between these panels contain NovaPlus concentrations indicated in the panel. There is a noticeable, although not large, shift in the mode of the distribution as more crude oil is present in the mixtures. However, the distributions for SMY and the mixture containing 10% NovaPlus are not visually distinguishable. In fact, obvious departure from the crude oil distribution becomes perceptible for the mixture, 50% NovaPlus.

The situation is different for PBB mixtures, Fig. 3. Fig. 3 shows T_2 distributions for mixtures in the same format as for Figs. 1 and 2. In these mixtures, all measured concentrations can be differentiated. Both the mode and the shoulder of the distribution are visibly shifted for all concentrations. These features are seen even at a concentration of 10% NovaPlus. From inspection of the distributions in Figs. 1-3, one would expect more reliable predictions for PBB mixtures than for the other two crude oils. Since PPB mixtures show a large,

progressive shift with changes in concentration, characterizing contamination is likely to be an easier task.

Table 1 shows the log-mean relaxation times ($T_{2,LM}$) for mixtures with all three crude oils. Logarithmic-mean averages are commonly reported for T_2 because mixture viscosities often shift in an exponential fashion between the viscosities of the mixture components. Since this implies that T_2 also shifts exponentially, a logarithmic average is the appropriate representation. One trend from Table 1 is that $T_{2,LM}$ decreases as more crude oil is added. A second trend is that this decrease in $T_{2,LM}$ is more severe with heavier crude oils. One unusual result is that for 10% NovaPlus with SMY. Here, $T_{2,LM}$ actually increases, compared to SMY. A subsequent measurement (data not shown) has suggested that this slight decrease may fall within experimental uncertainty. Hence at 10% NovaPlus concentration, the mixture may be undistinguishable from SMY. Table 2 shows the measured viscosities for the same mixtures in Table 1. As with $T_{2,LM}$, the viscosity changes more drastically for heavier crude oils. However, viscosity increases as more crude oil is present in the mixture.

Fig. 4 shows a cross-plot of the data in Tables 1 and 2. The line is the expected behavior based on an existing correlation between $T_{2,LM}$ and viscosity, η, for dead crude oils. The correlation is known as the Morriss Correlation (Morriss, *et al*. 1997), and its formula is as follows:

$$T_{2,LM} = 1200/\eta^{0.9} \qquad [2]$$

As Fig. 4 shows, the mixtures behave in accordance with this expected behavior.

Fig. 5 characterizes $T_{2,LM}$ for the mixtures of the various crude oils with NovaPlus. The experimental values of $T_{2,LM}$ are compared with a linear interpolation between the measured log-mean T_2 values for the crude oil and for NovaPlus. The interpolations are based on the $T_{2,LM}$ values for NovaPlus and the crude oil in question according to the following equation:

$$T_{2,LM}^{\ mix} = (T_{2,LM}^{\ crude})^{1-f}(T_{2,LM}^{\ NovaPlus})^{f} \qquad [3]$$

In this equation, $T_{2,LM}^{mix}$ is the interpolated log-mean relaxation time of the mixture, and $T_{2,LM}^{crude}$ and $T_{2,LM}^{NovaPlus}$ are the experimental log-mean relaxation times for the crude oil and for NovaPlus, respectively. f is the volume fraction of NovaPlus. Experimental data are shown as points; the interpolated data are represented as lines. Fig. 5 shows that this characterization of $T_{2,LM}$ as a weighted log-mean of the $T_{2,LM}$ values of the two components provides a good description of the trend seen in the experimental data.

Fig. 6 repeats the comparison for viscosities. The equation for the interpolation of mixture viscosities is as follows:

$$\eta^{mix} = (\eta^{crude})^{1-f}(\eta^{NovaPlus})^{f} \qquad [4]$$

Here, η^{mix} is the interpolated viscosity of the mixture, η^{crude} is the experimental crude oil viscosity, and $\eta^{NovaPlus}$ is experimental NovaPlus viscosity. f is the NovaPlus volume fraction. Once again, the interpolated equation (lines in Fig. 6) describes the trend of the experimental data (points in Fig. 6).

Although Figs. 5 and 6 suggest a trend from concentration-weighted logarithmic-mean averages for mixtures of NovaPlus and crude oils, deviations of up to 60% are observed. In order to improve the characterization of contamination from the T_2 distributions, an attempt is then made to utilize not just the log-mean value $T_{2,LM}$, but also other information in the distribution. Using signal amplitudes at various T_2 bins allows more of the collected data to serve in mixture analysis, without being lumped in an average like the logarithmic mean.

Cumulative distributions for the same mixtures as in Figs. 1-3 are shown in Figs. 7-9. The amplitude of a cumulative distribution at a specific bin is a running sum of amplitudes from conventional T_2 distributions, belonging to that bin and to all bins at lower values of T_2. Thus, cumulative distributions continually increase from low to high relaxation times. Cumulative distributions are preferred because they exhibit a more monotonic behavior when the same T_2 bin is compared for different concentrations. The cumulative distributions here are in the T_2 domain, just like conventional distributions, and are normalized such

that the final amplitude (after amplitudes from all relaxation times have been summed) for each sample is equal to 1. In general, Figs. 7-9 show that cumulative T_2 distributions for samples with greater crude oil content rise more quickly than those with a lesser fraction of crude oil.

Figs. 7-9 show normalized cumulative amplitude for 50 bins as a function of relaxation time. In Fig. 10-12, cumulative amplitudes from 11 of these bins—equally spaced in a logarithmic time scale—are shown for STNS, SMY, and PBB mixtures, respectively. Notes that bins placed in the upper part of the legend are the bins with the highest cumulative amplitudes in the plot. Each set of data points represents one bin, with the points within one set coming from different mixtures of NovaPlus and the appropriate crude oil. The lines for linear regression are also shown. Those bins having regression lines of the greatest slope are most responsive to contamination and thus would be more useful in characterizing the relative amounts of NovaPlus and crude oil.

Figs.13-15 plot the linear regression parameters for Figs. 10-12, except that such parameter for all 50 bins are included. The square of the regression coefficient, R^2, and the magnitude of the slope are included in the plot. The importance of slope is mentioned in the previous paragraph. R^2 is important because it indicates the deviation from linearity of the relationship between cumulative amplitude and NovaPlus concentration. If R^2 is very high (~0.98) for particular bins, a strong linear trend exists for the cumulative amplitudes in those bins. Knowing the extent of linear behavior between cumulative amplitude and NovaPlus concentration is helpful information in seeking a quantitative relationship between the variables. In general, Figs. 13-15 show that regions of highest R^2 correspond to maximum slope magnitudes, with R^2 being a less discriminating parameter.

Next, the contamination indices are calculated for all 50 bins as follows:

$$I_{f,i} = (A_i^{\text{sample}} - A_i^{\text{crude}})/(A_i^{\text{NovaPlus}} - A_i^{\text{crude}}) \qquad [5]$$

In this equation, $I_{f,i}$ is the contamination index for NovaPlus volume fraction f and bin i. $A_{f,i}^{\text{sample}}$ refers to the cumulative amplitude for sample with NovaPlus

concentration f for bin i and A_i^{NovaPlus} and A_i^{crude} are the cumulative amplitudes in bin i of NovaPlus and of the appropriate crude oil, respectively. The contamination index is defined such that it runs from 0 (for crude oils) to 1 (for NovaPlus). Figs. 16-18 show plots of contamination index, as it depends on concentration. Different data sets plotted represent different T_2 bins. The data plotted correspond to the subset of bins with slopes between 20% and 80% of the peak slope in Figs. 13-15, with the T_2 values of selected bins not exceeding the T_2 value of the bin with maximum slope. The goal of the characterization is to calculate a contamination index that correlates with the NovaPlus volume fraction f.

Table 3 shows the average contamination indices for each concentration of each of the three mixtures. These values are obtained as arithmetic means of all bins included in Figs. 16-18. The error shown is the standard deviation. Note that standard deviations for NovaPlus and for the crude oil are zero because of the definition of the contamination index. In general, the contamination index for a mixture is numerically greater than the NovaPlus volume fraction. The one notable exception is for the SMY mixture with 10% NovaPlus, which has a contamination index near zero. The deviation of the defined contamination index from the volume fraction for other samples is due to nonlinear effects of cumulative T_2 amplitude with concentration.

Conclusions and Future Work

Mixtures of three crude oils and NovaPlus have been measured, yielding NMR T_2 relaxation times and viscosity values. Conventional T_2 distributions show that more viscous crude oils show a greater effect from contamination with NovaPlus. For all sets of mixtures, effects were more pronounced in samples with more NovaPlus content. With SMY, it is difficult to differentiate between the crude oil and the sample with 10% contamination.

All the mixtures behave according to the Morriss correlation, relating viscosity to $T_{2,LM}$. Furthermore, mixture log-mean relaxation times and viscosities could be interpolated with Equations 3 and 4, respectively.

In order to improve the potential for predicting contamination, a scheme to use the data in T_2 relaxation time bins was used. Starting with cumulative distributions in the T_2 domain, a contamination index is calculated from bins that show a strong dependence on concentration. This method yields strong correlations for contamination when appropriate bins are selected. For these bins, the contamination indices at measured NovaPlus concentrations are consistent, as indicated by the small standard deviations in Table 3.

The approach taken thus far can be extended as follows. The strategy involves fitting the data in Figs. 16-18 to a spline function. This would have the immediate benefit of providing interpolations to relate subsequent T_2 measurements to contamination levels. However, this data would be system-specific; i.e. each fit would refer to a particular combination of crude and base oils.

References

1. Bouton J., Prammer M. G., Masak P., Menger S. "Assessment of Sample Contamination by Downhole NMR Fluid Analysis," paper 71714 presented at 2001 SPE Annual Technical Conference and Exhibition. New Orleans, LA, USA. Sept. 30 – Oct. 3, 2001.
2. Masak P. C., Bouton J., Prammer M. G., Menger S., Drack E., Sun B., Dunn K.-J., Sullivan, M. "Field Test Results and Applications of the Downhole Magnetic Resonance Fluid Analyzer," paper GGG presented at SPWLA 43rd Annual Logging Symposium. Oiso, Japan. June 2-5, 2002
3. Morriss C. E., Freedman R., Straley C., Johnston M., Vinegar H. J., Tutunjian P.N. "Hydrocarbon Saturation and Viscosity Estimation from NMR Logging in the Belridge Diatomite." *The Log Analyst*. March-April, 1997.

Table 1: Log-mean T_2 Values for Mixtures of NovaPlus Base Oil with Crude Oils

	$T_{2,LM}$ (ms)		
NovaPlus (%)	STNS	SMY	PBB
0	114.7	55.1	9.9
10	145.3	50.0	16.4
20	171.7	67.7	27.8
50	288.3	149.6	52.6
75	403.2	283.7	233.5
100	534.6	540.9	512.4

Table 2: Viscosities for Mixtures of NovaPlus Base Oil with Crude Oils

	Viscosities (cp)		
NovaPlus (%)	STNS	SMY	PBB
0	13.7	21.0	206.7
10	11.1	20.1	103.0
20	9.2	15.1	57.0
50	5.8	6.6	26.8
75	4.3	4.7	6.3
100	3.3	3.2	3.3

Table 3: Contamination Indices for Mixtures of NovaPlus Base Oil with Crude Oils

	Contamination Indices		
Nova Plus (%)	STNS	SMY	PBB
0	0.00 ± 0.00	0.00 ± 0.00	0.00 ± 0.00
10	0.20 ± 0.05	0.00 ± 0.03	0.27 ± 0.03
20	0.36 ± 0.02	0.21 ± 0.01	0.49 ± 0.04
50	0.70 ± 0.02	0.62 ± 0.03	0.68 ± 0.04
75	0.88 ± 0.03	0.83 ± 0.01	0.94 ± 0.02
100	1.00 ± 0.00	1.00 ± 0.00	1.00 ± 0.00

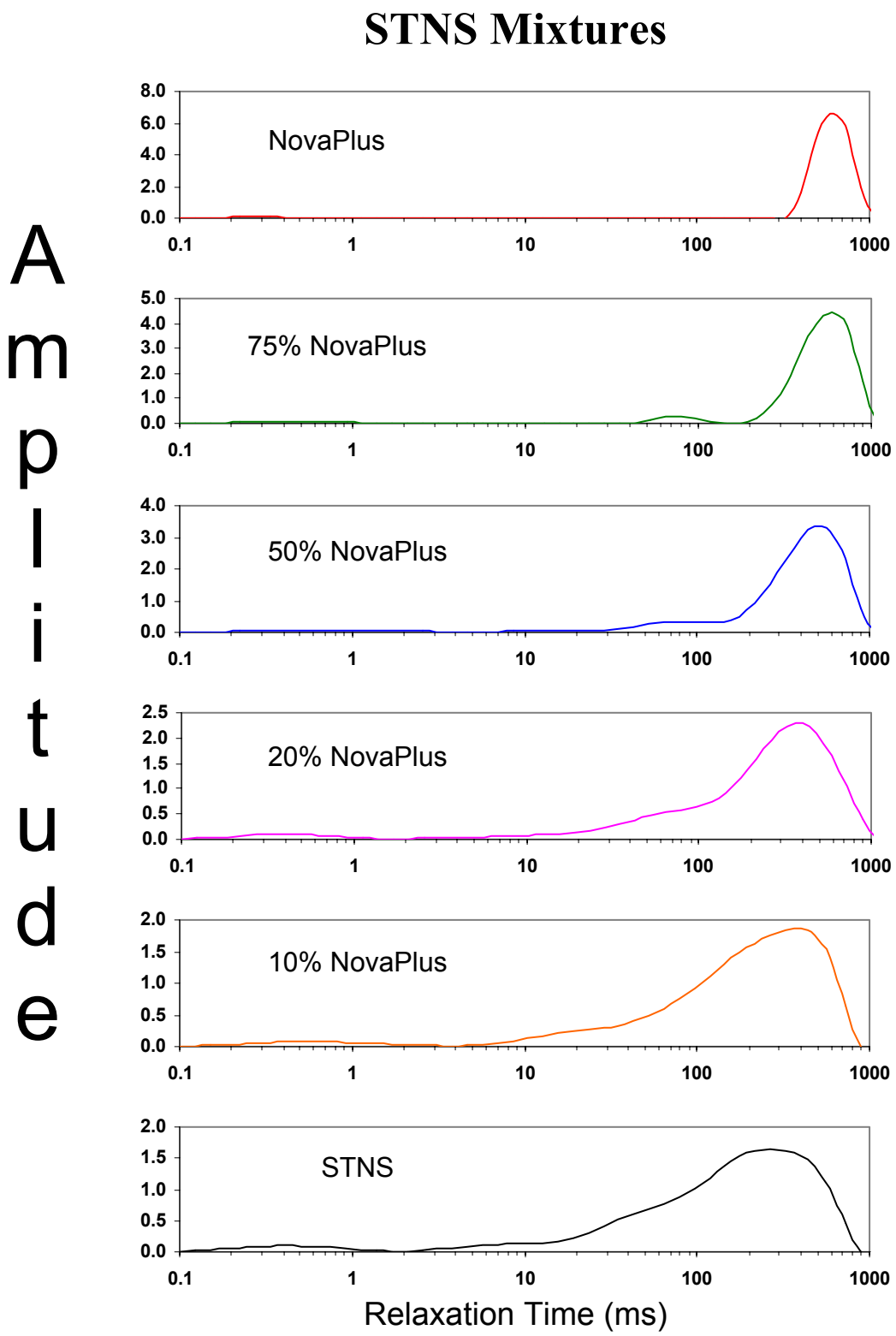

Figure 1: Stacked plots showing the progressive change in T_2 relaxation time distributions for mixtures of STNS crude oil and NovaPlus base oil. Note that the amplitude axis is not to scale for all curves in the stack.

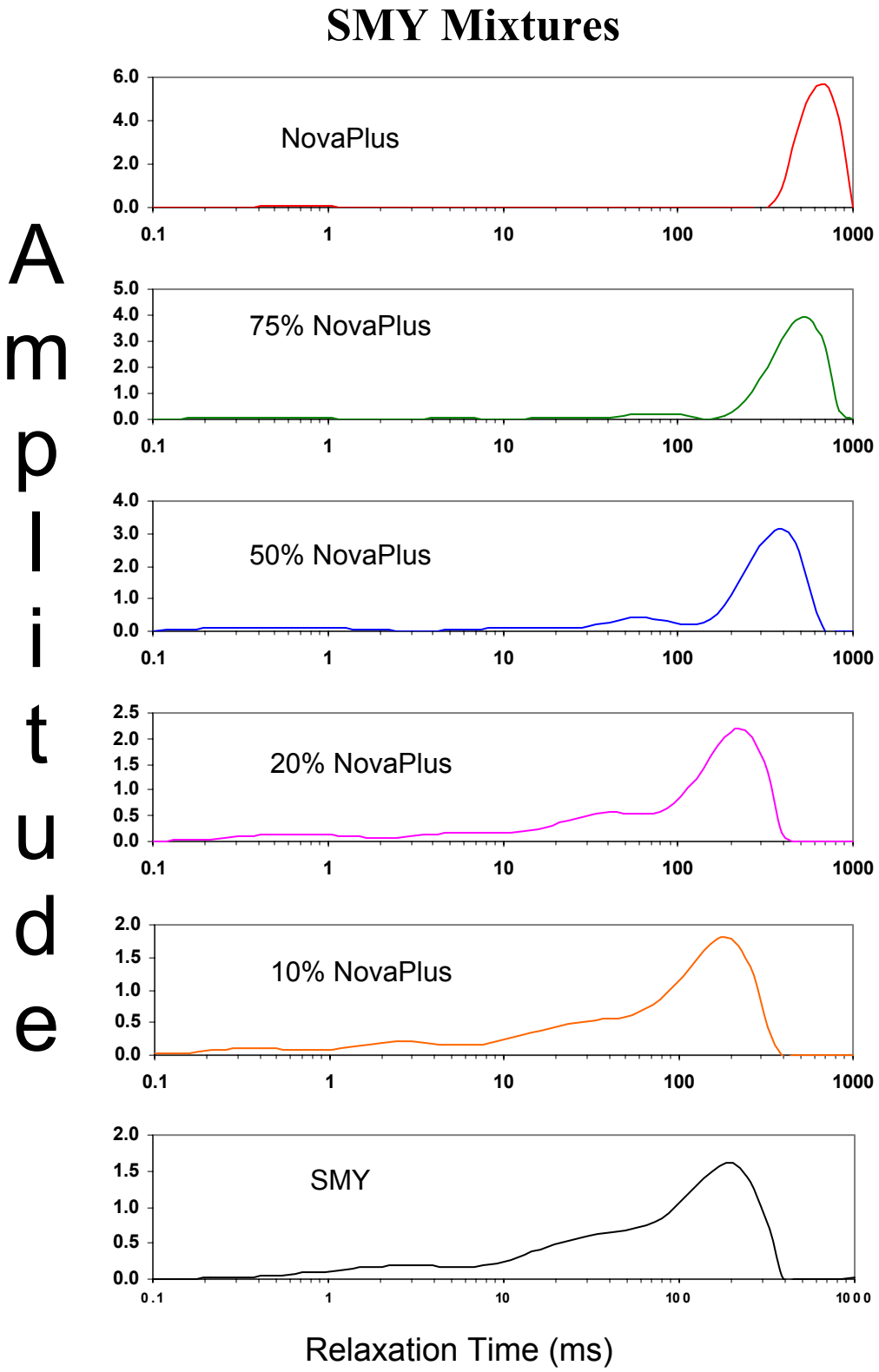

Figure 2: Stacked plots showing the progressive change in T_2 relaxation time distributions for mixtures of SMY crude oil and NovaPlus base oil. Note that the amplitude axis is not to scale for all curves in the stack.

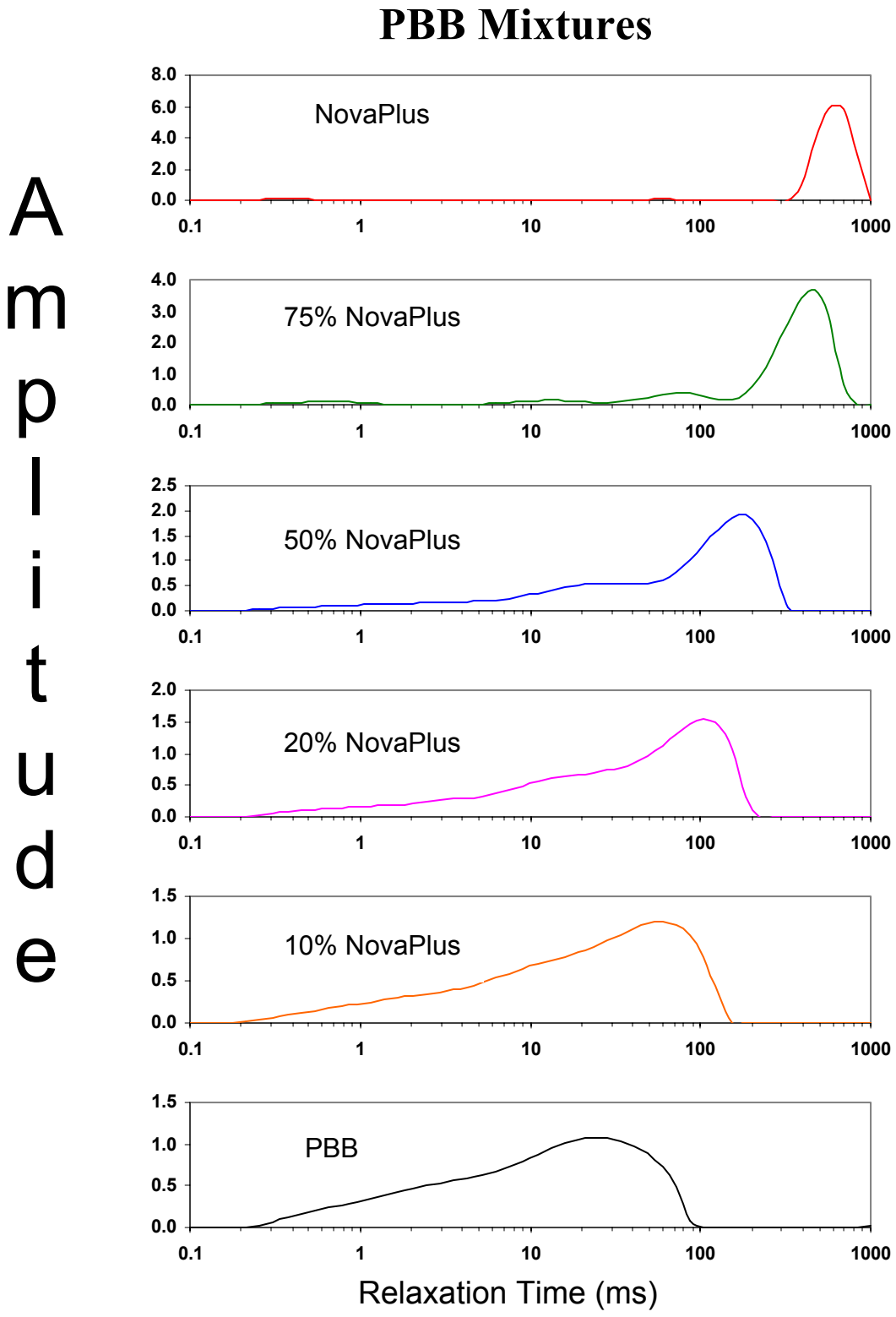

Figure 3: Stacked plots showing the progressive change in T_2 relaxation time distributions for mixtures of PBB crude oil and NovaPlus base oil. Note that the amplitude axis is not to scale for all curves in the stack.

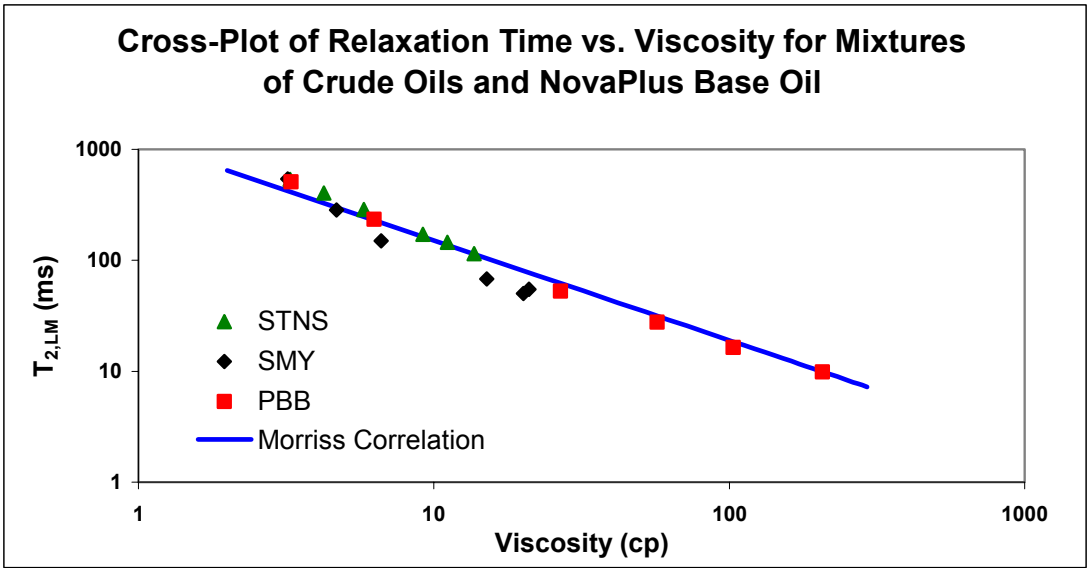

Figure 4: Relationship between viscosity and $T_{2,LM}$: Comparison of measurements to Morrriss Correlation.

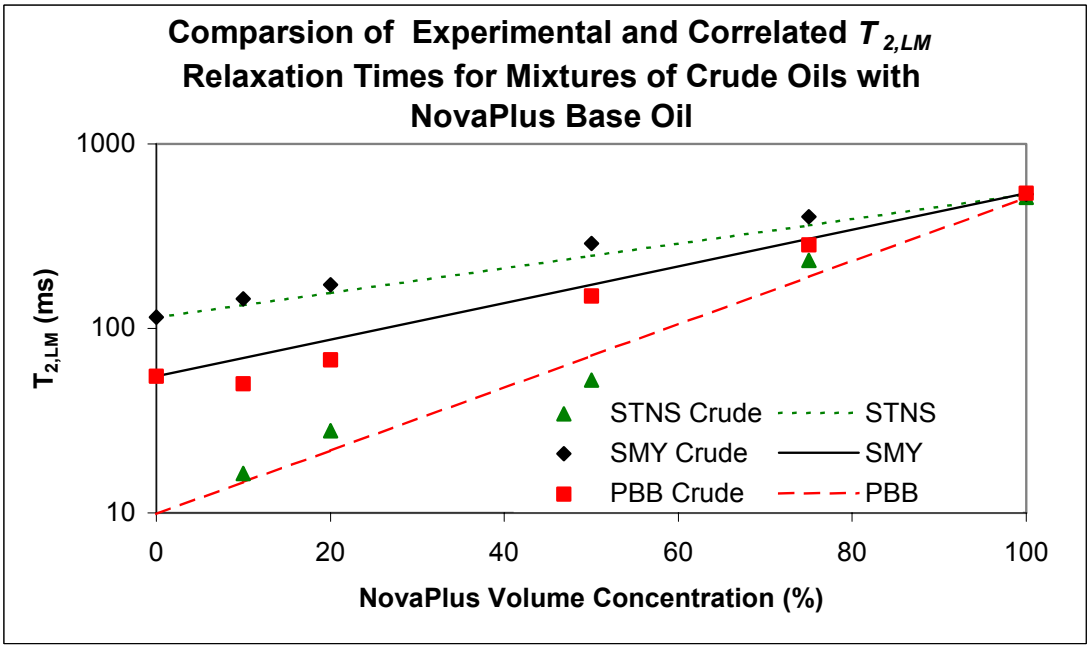

Figure 5: Comparison of experimental $T_{2,LM}$ values with interpolations for mixtures of crude oil and NovaPlus based on concentration-weighted logarithmic-mean averages of measured $T_{2,LM}$ values for unmixed NovaPlus and crude oil.

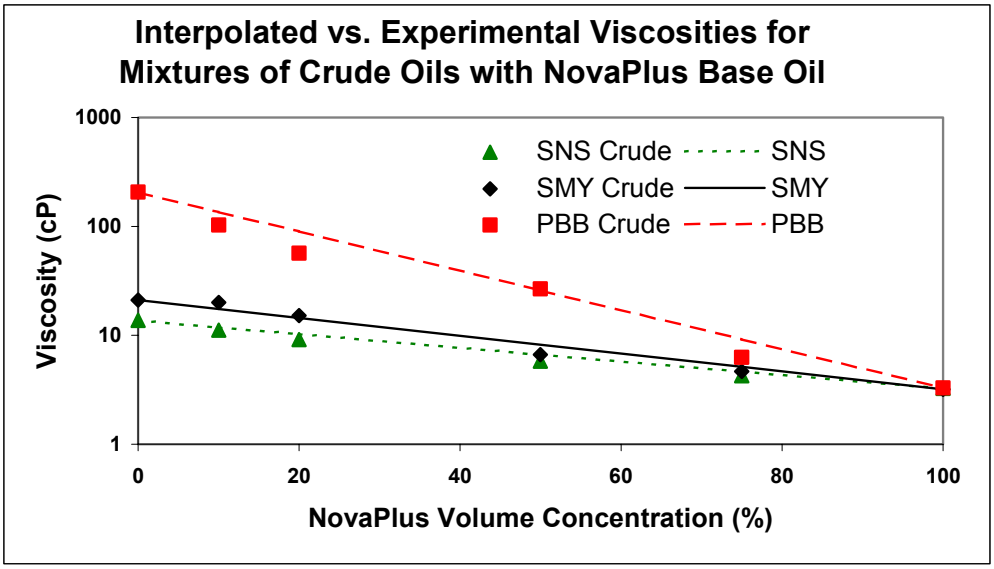

Figure 6: Comparison of experimental viscosities with interpolations for mixtures of crude oils and NovaPlus based on concentration-weighted logarithmic-mean averages of measured viscosities for unmixed NovaPlus and crude oil

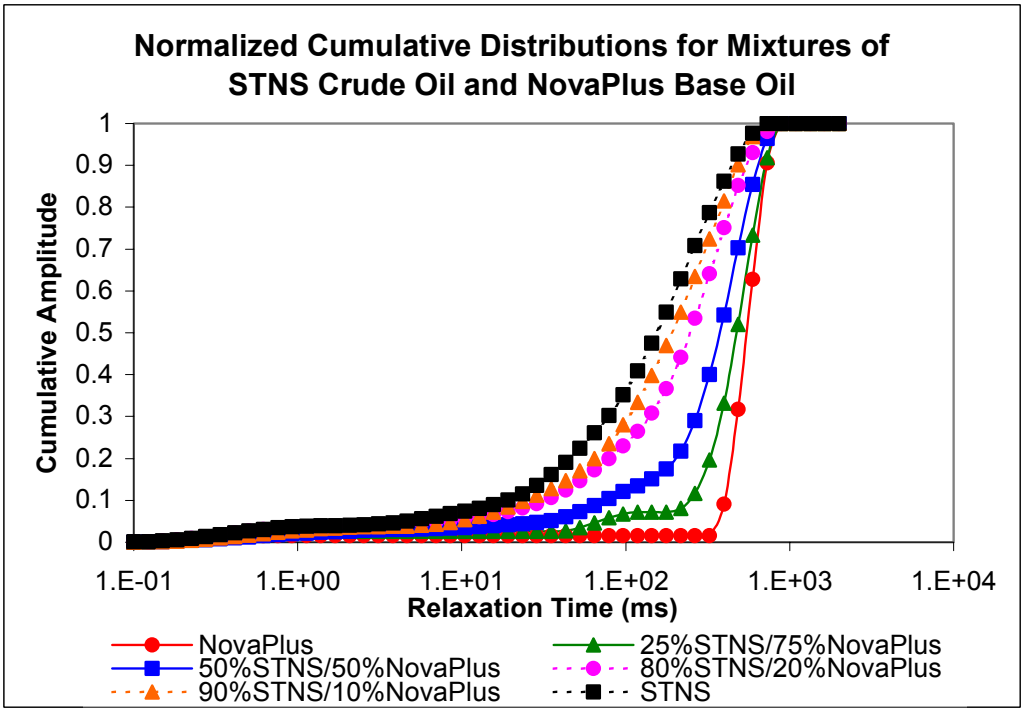

Figure 7: Normalized, cumulative T_2 distributions for mixtures of STNS crude oil and NovaPlus base oil

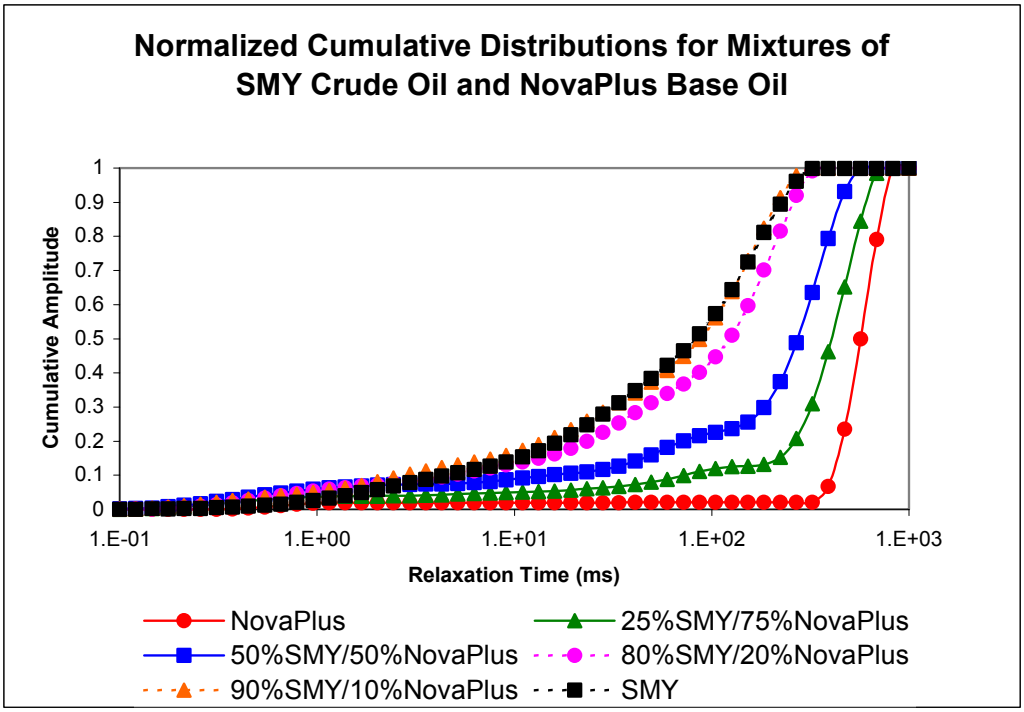

Figure 8: Normalized, cumulative T_2 distributions for mixtures of SMY crude oil and NovaPlus base oil

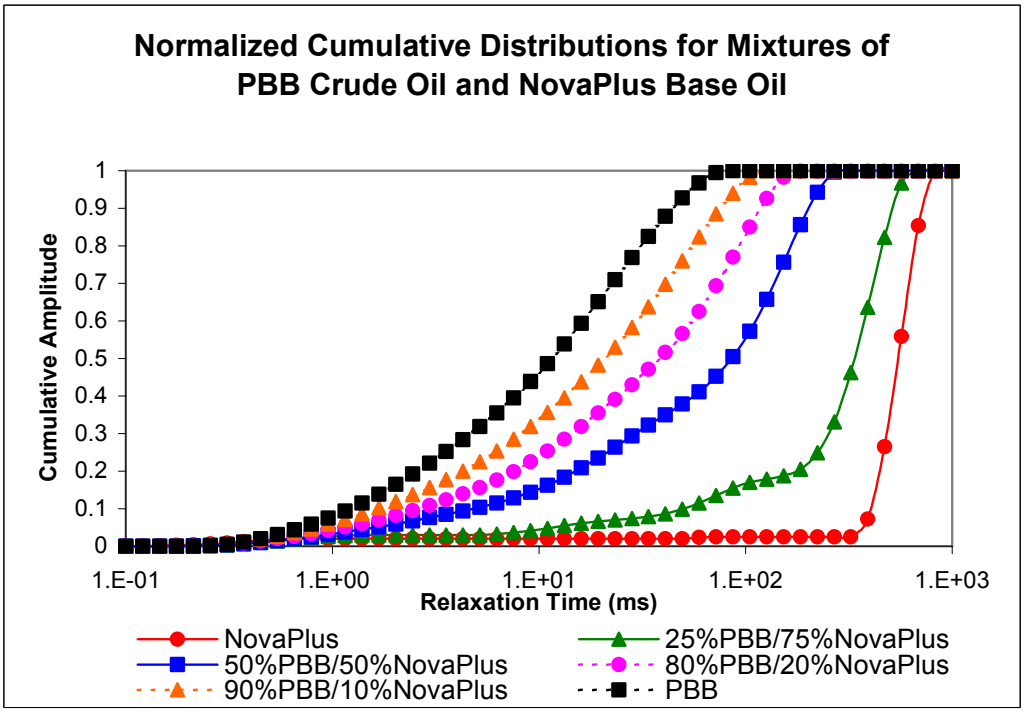

Figure 9: Normalized, cumulative T_2 distributions for mixtures of PBB crude oil and NovaPlus base oil

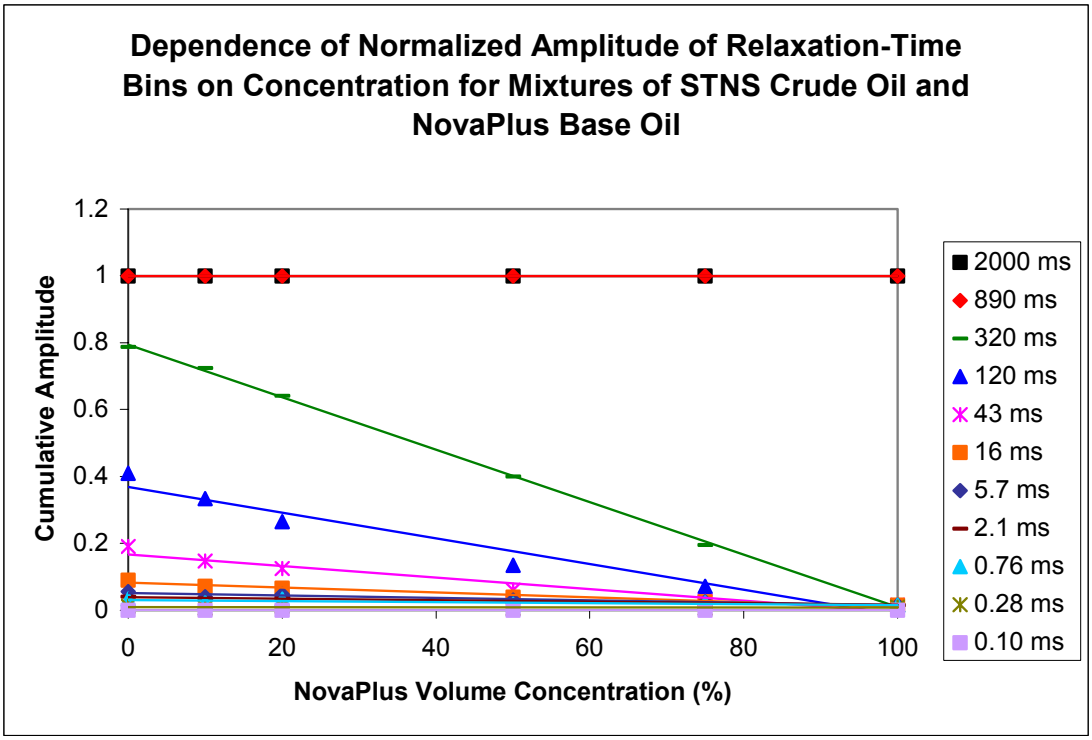

Figure 10: Behavior of signal amplitude in selected T_2 bins as a function of NovaPlus concentration in mixtures of STNS crude oil and NovaPlus base oil

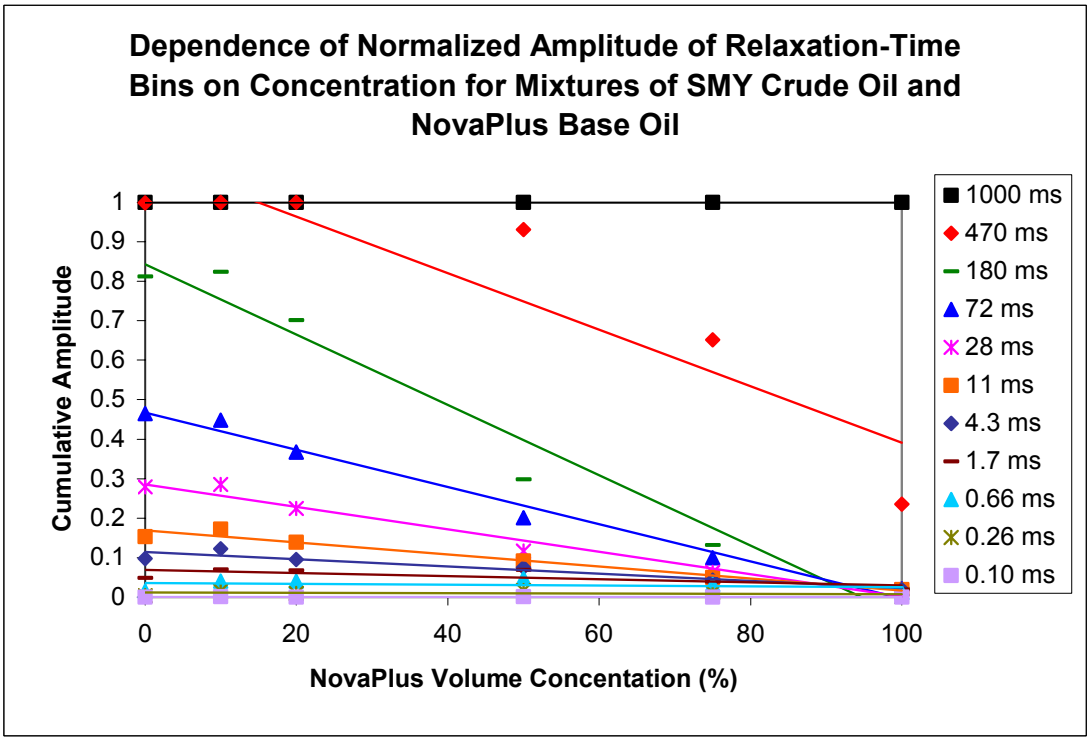

Figure 11: Behavior of signal amplitude in selected T_2 bins as a function of NovaPlus concentration in mixtures of SMY crude oil and NovaPlus base oil

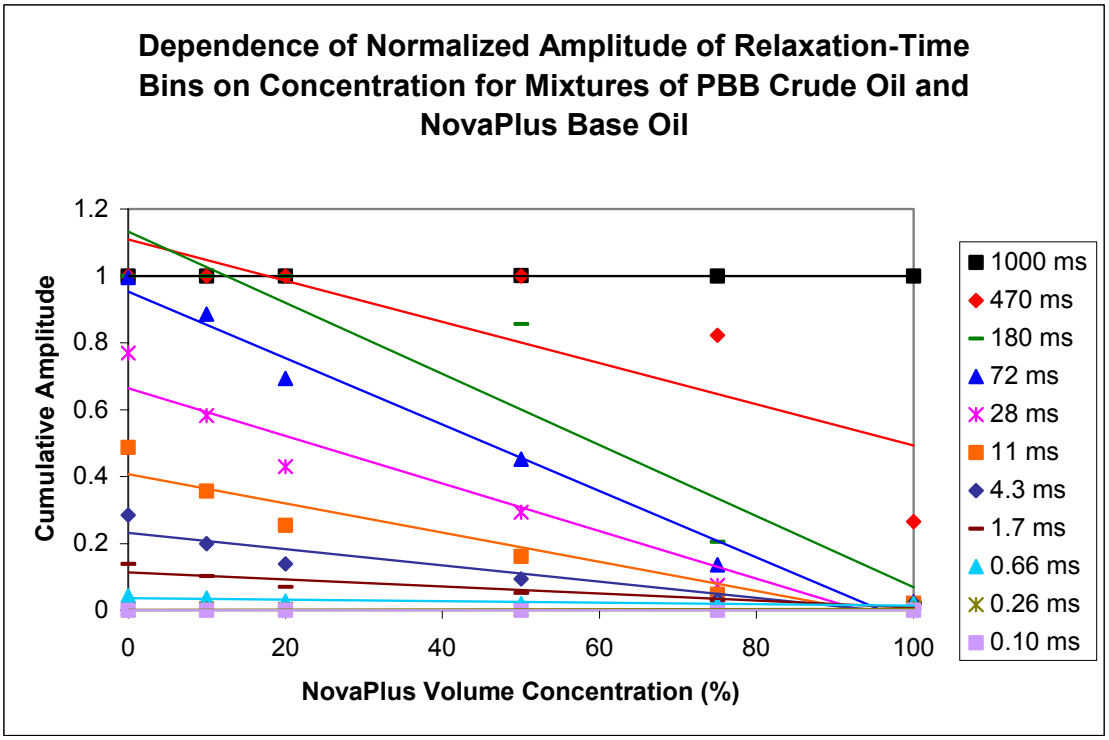

Figure 12: Behavior of signal amplitude in selected T_2 bins as a function of NovaPlus concentration in mixtures of PBB crude oil and NovaPlus base oil

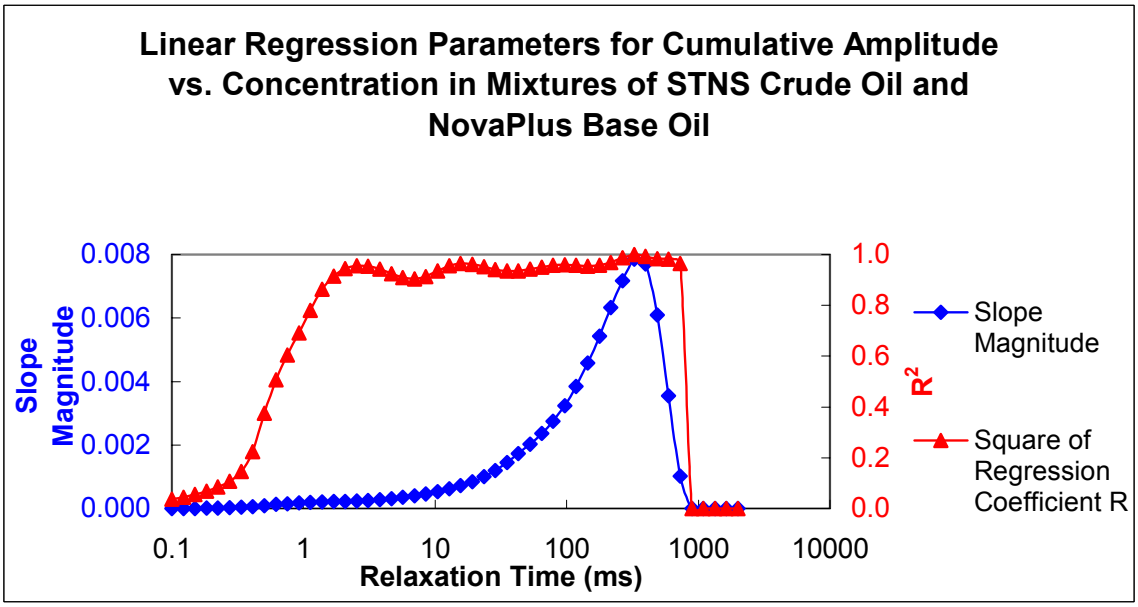

Figure 13: Linear regression parameters of T_2 cumulative amplitude against concentration for all bins in mixtures of STNS crude oil and NovaPlus base oil

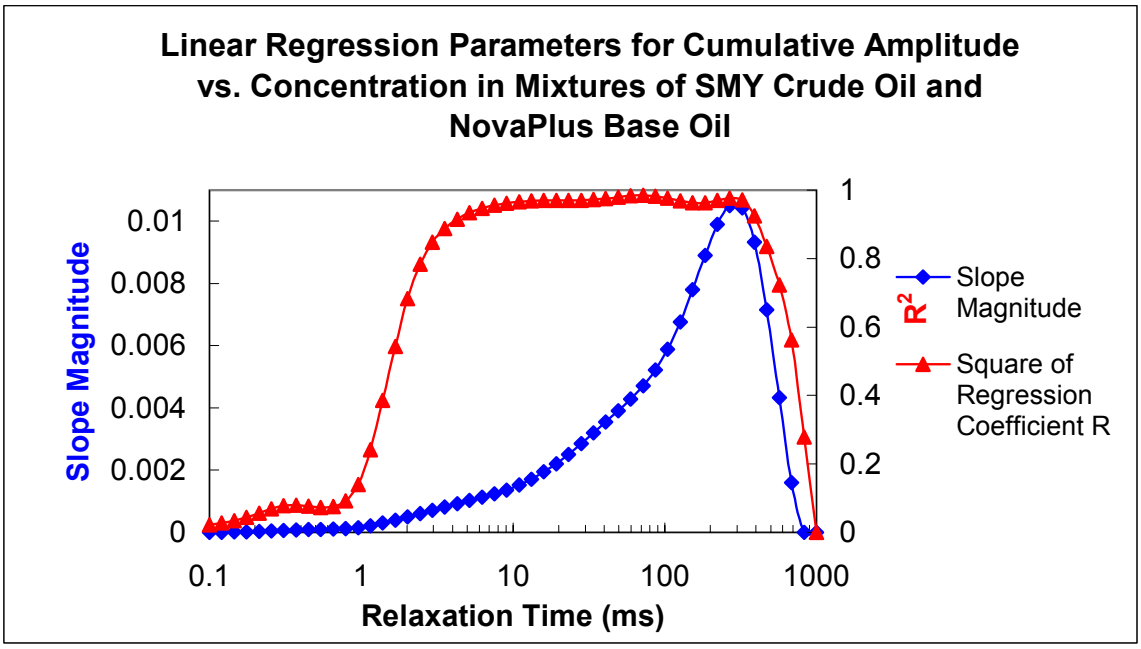

Figure 14: Linear regression parameters of T_2 cumulative amplitude against concentration for all bins in mixtures of SMY crude oil and NovaPlus base oil

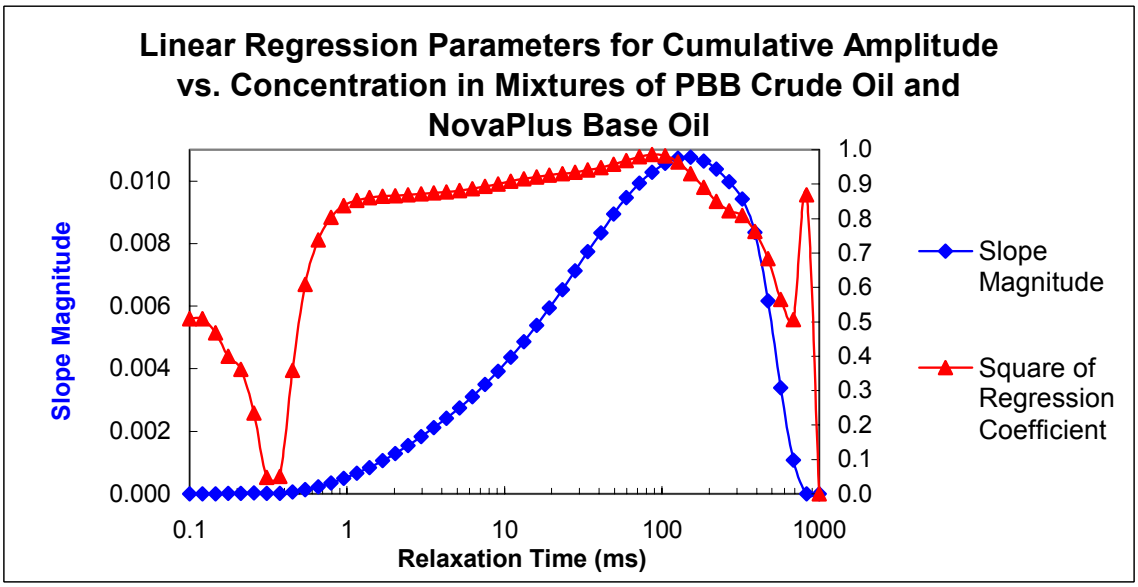

Figure 15: Linear regression parameters of T_2 cumulative amplitude against concentration for all bins in mixtures of PBB crude oil and NovaPlus base oil

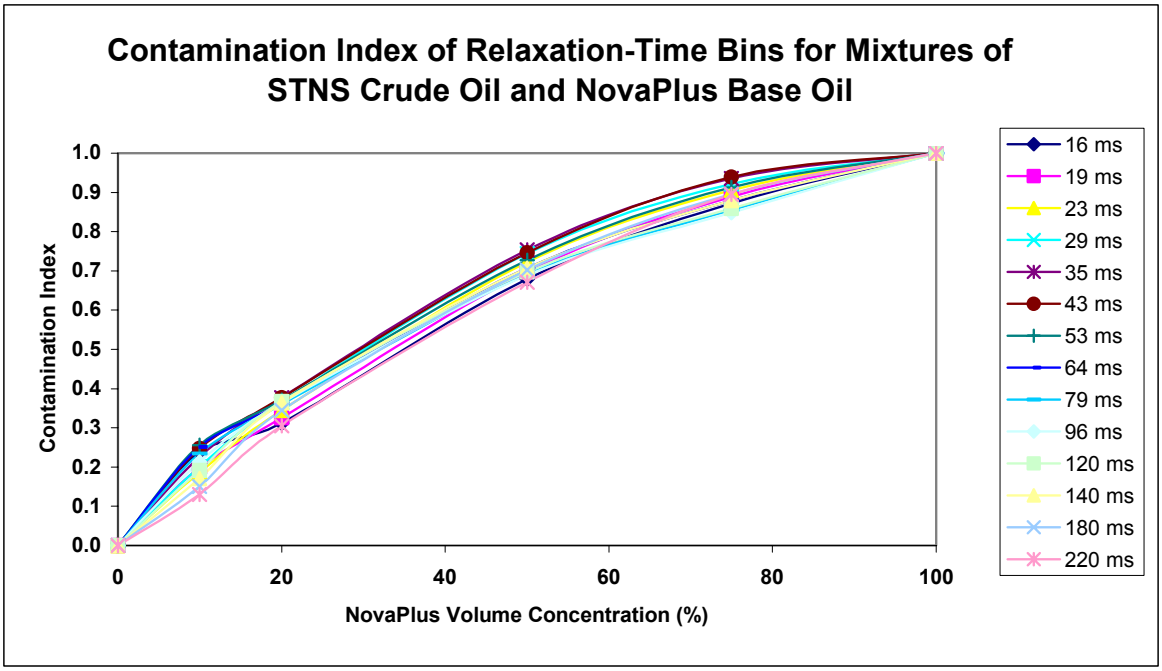

Figure 16: Contamination index for selected bins in mixtures of STNS crude oil and NovaPlus base oil

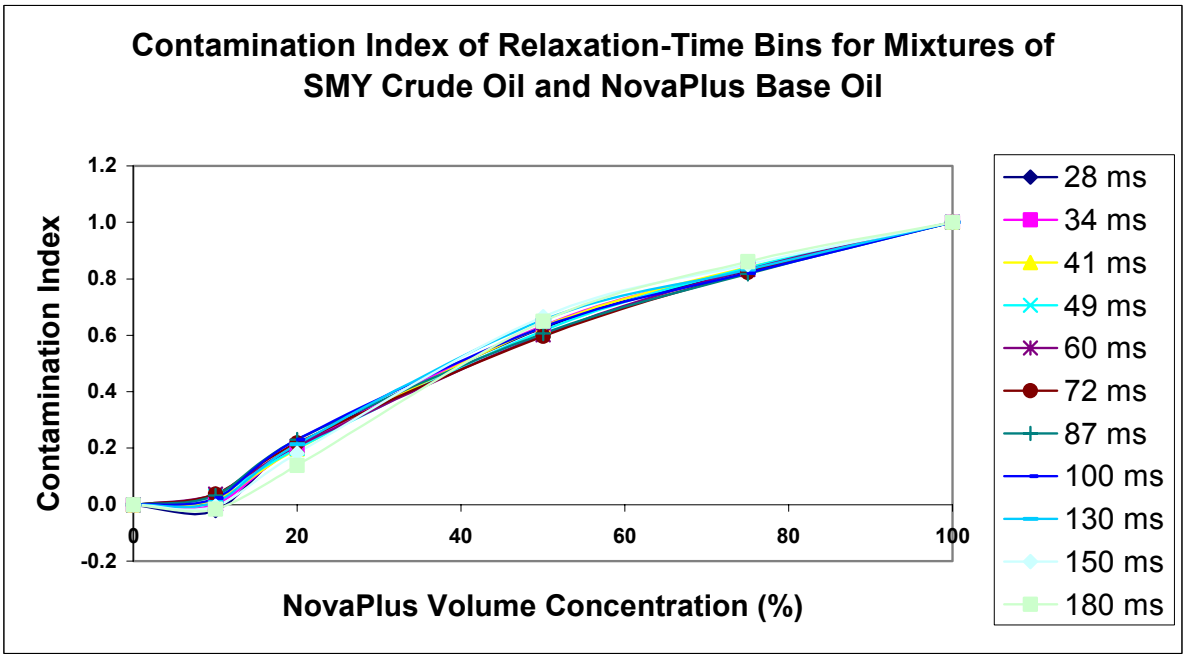

Figure 17: Contamination index for selected bins in mixtures of SMY crude oil and NovaPlus base oil

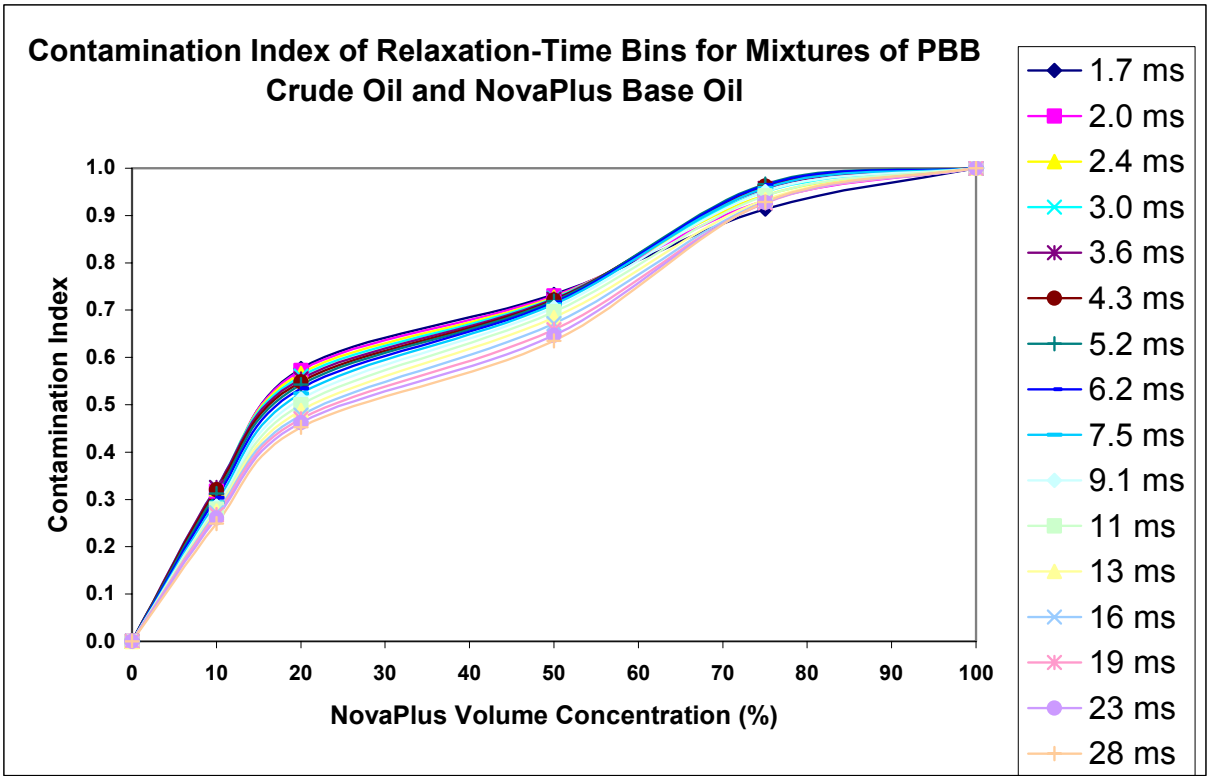

Figure 18: Contamination index for selected bins in mixtures of PBB crude oil and NovaPlus base oil

Correlating Viscosity and NMR Relaxation Times for Drilling Fluid Base Oils and Cyclic Crude Oil Components

Arjun Kurup, George J. Hirasaki

Abstract

In NMR well logging, correlations are used to determine viscosity from relaxation time measurements. Correlations have been developed for dead crude oils, for oils containing methane, and for linear alkanes. The leaves out a pair of important classes of materials, base oils for drilling fluids and cyclic molecules. Data is presented for T_1 and T_2 relaxation times for some drilling fluid base oils and for some bicyclic compounds. Furthermore, T_1 data in the literature is shown for monocyclic compounds. Viscosity data for base oils and cyclic compounds allows comparison of the relationship of relaxation time to viscosity for these materials to that of linear alkanes. Monocyclic molecules show a strong deviation from the linear correlation, whereas all materials measured in this work fall on or near the correlation line. For the cyclic compounds measured in this work, lack of deoxygenation may be an issue. Future work aims to study more cyclic molecules and base oils to provide an explanation for any deviations seen from the correlation for linear alkanes.

Introduction

NMR well logging is used in the characterization of rock formations and of the fluids present in these formations. Of the latter application, characterizing crude oils by their viscosities is an important, widely used technique (Kleinberg and Vinegar 1996). This relationship between NMR well logging and viscosity is possible because of correlations developed between NMR relaxation times, T_1 and T_2, and crude oil viscosity (Brown 1961, Morriss *et al*. 1997). Unlike pure or relatively pure fluids, which have characteristic T_1 or T_2 values, relaxation times in crude oils are characterized logarithmic mean averages denoted by $T_{1,LM}$ or $T_{2,LM}$ because a distribution of relaxation times occurs. Thus, correlations developed for crude oils involve logarithmic mean relaxation times. The

correlations themselves have theoretical basis in dipole-dipole interactions that predominate in liquids. Both types of dipole-dipole interactions, intermolecular (i.e. between hydrogen atoms on different molecules) and intramolecular (i.e. between hydrogen atoms on the same molecule), predict that relaxation time is inversely proportional to the ratio of viscosity to temperature (η/T).

However, there are limitations in the strategy conventionally employed. First, correlations are developed for dead crude oils, after the native crude oils have been removed from down hole conditions. The elevated temperature and pressure in the formation cause crude oils to have different compositions under native conditions, especially in the content of gas present.

Gases are particularly important because the primary gas in crude oil mixtures is methane. Methane relaxes by a different mechanism than liquid crude oil components. The methane mechanism, namely spin-rotation, exhibits the opposite dependence on η/T as compared to dipole-dipole interactions. Relaxation times for methane are proportional to η/T. To address the concern of dissolved gases present, Lo *et al*. (2000) developed a correlation to account for the effect of dissolved methane gas on the relationship between viscosity and relaxation time. In addition, Lo *et al*. (2000) developed a correlation for relaxation time based on diffusivity. These modified correlations are based on the deviations between relaxation times for the correlation of dead crude oils and the oils containing dissolved methane. The parameter to account for this deviation is the gas-oil ratio (GOR), which is indicative of the ratio of the amount of methane to the amount of liquid in the crude oil.

A further limitation of correlating NMR relaxation time to viscosity for dead crude oils is the observation that some crude oils do not follow the correlation developed (Morriss *et al*. 1997). This is probably because crude oils are a mixture of many compounds, with many functional groups represented in the mixture. Differences in the compositions of crude oils could cause different behavior in the relaxation at the same viscosity-to-temperature ratio. This would

be true if the crude oil constituents differed in the relative importance of various mechanisms in determining the relaxation times.

In order to better understand the behavior of crude oils as a whole, different components can be studied separately. Lo, *et al*. (2000) have developed a correlation for linear alkanes. This correlation is show in Fig. 1. Later plots include this correlation, to which other data is compared.

This report details two other cases whose study would help improve the NMR characterization of crude oils. This work follows in the philosophy of remedying the second limitation of NMR correlations developed for dead crude oils: By studying components in the mixture separately, the mixture itself—the crude oil—may be better known. The first case involves base oils for drilling fluids. These fluids potentially contribute to the observed oil relaxation time distributions. This is because base oils from drilling fluids often contaminate native oils in the drilling process. Each base oil contains molecules with particular functional groups, with olefins and ester base oils in common use. The other class of molecules is cyclic in nature, either aliphatic or aromatic. The more constrained structure of these compounds subjects their protons to different interactions than for linear molecules, perhaps affecting the relaxation time.

Experimental and Conditions for Literature Data

Experiments are done for four drilling-fluid base oils and three cyclic molecules. The drilling fluid base oils are SF Base, Escaid 110, NovaPlus, and Petrofree/LE Base. These are single base oils except Petrofree/LE Base, which is a mixture of 90% LE Base and 10% Petrofree. SF Base and NovaPlus are 16- to 18-carbon internal olefin mixtures. Escaid 110 consists of light, hydrotreated petroleum distillates. In Petrofree/LE, Petrofree is a fatty acid ester and LE Base is a natural gas derivative.

Relaxation times, T_1 and T_2, were measured at 30 ^{0}C using a MARAN instrument manufactured by Resonance Instruments and operating at 2 MHz resonant frequency. Table 1 shows the experimental conditions for T_1 measurements, and Table 2 shows the conditions for T_2 measurements.

Viscosities of the base oils were obtained using a Cannon-Fenske capillary viscometer for SF Base and Escaid 110. For NovaPlus and Petrofree/LE Base, data is obtained from K. Y. Song (private communication). The temperature for all obtained viscosities is 30 ^{0}C.

The cyclic molecules measured in this work are α-methylnaphthalene, tetralin, and decalin. α-methylnaphthalene consists of two fused benzyl rings and a pendant methyl group. Tetralin is also bicyclic, with one aromatic ring and one aliphatic ring. Decalin is similar to tetralin, with the distinguishing feature that the fused rings are both aliphatic. The relaxation times, T_1 and T_2, are measured at 30 ^{0}C with the same MARAN instrument as for base oil measurements.

The experimental conditions for the T_1 measurements are shown in Table 3, and T_2 experimental conditions are in Table 4. In addition to the measured compounds, T_1 data are obtained from the literature for four monocyclic compounds: benzene toluene, cyclohexane and cyclopentane. Table 5 shows the conditions used along with the sources for the data.

Viscosities for both monocyclic and bicyclic molecules are all obtained from the literature. For benzene, cyclopentane, cyclohexane, and decalin, empirical correlations from Viswanath and Natarajan, eds. (1989) were used. For toluene, data is taken from F.D. Rossini, *et al*., eds. (1953). The exception to these statements is that viscosity data provided in Pendred, *et al*. (1966) is used for benzene and toluene measurements from that source. The other sources of relaxation time data do not provide information on viscosity. Viscosity for tetralin is obtained from Byers and Williams (1987). Finally, SUPERTRAPP (NIST 1999) is used for the viscosity of α-methylnaphthalene. The quality of these results was checked with data from Byers and Williams (1987), which reports viscosity for α-methylnaphthalene at a slightly different temperature. All viscosities mentioned here are obtained at temperatures matching the temperatures of the corresponding relaxation time measurement, namely either 30 ^{0}C or the appropriate temperature in Table 5.

Results and Discussion

Table 6 shows the results of T_1 and T_2 measurements for the drilling fluid base oils studied. The viscosities obtained are also shown. As the data show, there is no significant difference between T_1 and T_2, except for Escaid 110. This was the only sample deoxygenated, and it appears that the deoxygenation was more successful for the T_2 measurement than for T_1. This leads to a T_2 value that is greater than the apparent T_1. Since this is almost certainly caused by the ineffective deoxygenation for T_1, the value obtained for T_2 is used in place of the T_1 value. Hence although the correlation plot between relaxation time and η/T, Fig. 2, is only shown for T_1 relaxation time, the data for Escaid 110 is T_2 data. For the base oils here, the behavior seen matches that of linear alkanes. This information is useful because it allows one to look for base oils in a relaxation time distribution as if it were a component of the crude oil obeying the linear relationship between T_1 (or T_2) and the η/T on a logarithmic scale. That said, some base oils (data not shown), particularly some containing esters, appear not to follow the correlation (J. Chen, private communication). The difference between such base oils and those measured here could elucidate structural features that affect NMR relaxation time correlations.

Table 7 shows the T_1 and T_2 values, along with the viscosities of bicyclic compounds. Even more than with drilling-fluid base oils, the difference between T_1 and T_2 is negligible. The slightly greater value for T_2 as compared to T_1 in two of the measurements is an indication of the level of error, because T_1 should not be less than T_2. Table 8 shows T_1 data for the monocyclic compounds. Unlike both the drilling fluid base oil data and bicyclic compound data measured in this work, these values are not logarithmic means. However, since the distributions are sharp for all samples measured, the different definitions of T_1 would give only slightly different values. For the data from the literature, several values are reported, the scatter of which is mostly an indication of the different conditions of measurement.

Fig. 3 shows all the data for cyclic molecules together. In this plot, α-methylnaphthalene is called 1-methylnaphthalene. The data for monocyclic compounds show a clear deviation from the correlation line for alkanes. However, the bicyclic compounds fall on the correlation line for the linear alkanes. This may indicate that deviations are present only for lower-molecular weight cyclic molecules. A more probable cause for why bicyclic compound do not deviate is that they were not deoxygenated prior to measurements. This step was omitted because of irreproducible relaxation time obtained after employing the freeze-pump-thaw deoxygenation procedure for hexane.

Conclusions and Future Work

In this preliminary study, it has been found that the studied base oils follow the linear alkane correlation in general, but monocyclic molecules do not. Bicyclic molecules appear to follow the correlation for linear alkanes. The aim of continuing this work is to observe these and other classes of molecules that could potentially contribute to the observed NMR signal. Building a database consisting of various molecules of a particular type would provide a set of data with which to observe trends, and ultimately the goal is to convert these trends into correlations based on structural features of the molecules in question.

In order to obtain reliable data, deoxygenation procedure needs to be robust. Work is currently in progress to repair the freeze-pump-thaw process for deoxygenation.

References

1. Brown R.J.S. "Proton Relaxation in Crude Oils." *Nature*. p. 387. February 4, 1961

2. Byers C.H., Williams D.F. "Viscosities of Pure Polyaromatic Hydrocarbons." *Journal of Chemical Engineering Data*. **32**, 344, 1987.

3. Homer J., Dudley A. R.,. McWhinnie W.R. "Removal of Oxygen from Samples used in Nuclear Magnetic Resonance Studies of Spin-Lattice

Relaxation Times." *Journal of the Chemical Society: Chemical Communications*. p. 893. December, 1973.

4. Kashaev S.Kh.G, Le B., Zinyatov M.Z. "Proton Spin-Lattice Relaxation, Viscosity, and Vibration of Molecules in the Series of n-Parrafins," translated from Russian. *Doklady Akademii Nauk SSSR*, **157.6**, 846, 1964.

5. Kleinberg R.L., Vinegar H.J. "NMR Properties of Reservoir Fluids." *The Log Analyst.* p. 20, November-December, 1996

6. Lo S.-W. Hirasaki G. J, House W.V., Kobayashi, R. "Mixing Rules and Correlations of NMR Relaxation Time with Viscosity, Diffusivity, and Gas/Oil Ratio of Methane/Hydrocarbon Mixtures," paper 63217 presented at 2000 SPE Annual Technical Conference and Exhibition. Dallas, TX, USA. Oct. 1 – 4, 2000.

7. Lo S.-W. *Correlations of NMR Relaxation Time with Viscosity/Temperature, Diffusion Coefficient, and Gas/Oil Ratio of Methane-Hydrocarbon Mixtures*. Ph.D. Thesis, Rice University. Houston, TX, 1999.

8. Moniz W.B., Steele W.A., Dixon J.A. "Nuclear Spin Relaxation in Liquids. Spheroidal Molecules." *Journal of Chemical Physics* **38**, 2418,1963.

9. Morriss C. E., Freedman R., Straley C., Johnston M., Vinegar H. J., Tutunjian P.N. "Hydrocarbon Saturation and Viscosity Estimation from NMR Logging in the Belridge Diatomite." *The Log Analyst*. March-April, 1997.

10. NIST. *NIST Thermophysical Properties of Hydrocarbon Mixtures Database (SUPERTRAPP)*. National Institute of Standards and Technology (1999).

11. Nederbragt G.W., Reilly C.A. "Nuclear Spin-Lattice Relaxation Time of Aromatic and Aliphatic Protons." *Journal of Chemical Physics*. **24**, 1110,1956.

12. Pendred T.L., Pritchard A.M., Richards R.E. "Spin-Lattice Relaxation Times of Protons in Some Orgainc Compounds." *Journal of the Chemical Society A*. p. 1009,1966.

13. Rossini F.D., *et al*., eds. *Selected Values of Physical and Thermodynamic Properties of Hydrocarbons and Related Compounds*. Carnegie Press, Pittsburgh. 1953.

14. Viswanath D.S., Natarajan G. *Data Book on the Viscosity of Liquids.* Hemisphere Publishing Corporation. 1989.

15. Zega J.A. *Spin-Lattice Relaxation in Pure and Mixed Alkanes and their Correlation with Thermodynamic and Macroscopic Transport Properties*. MS Thesis, Rice University. Houston, TX, 1987.

Table 1: Acquisition Parameters for T_1 Measurements of Drilling Fluids Base Oils

Drilling Fluid Base Oil	Number of Data Points	Interval Spanned by Data Points (s)	Wait Time (s)	Number of Scans	Signal Acquisition Interval (μs)
SF Base	20	0.1 – 3.0	4.0	16	8.0
Escaid 110	30	0.5 – 6.0	7.5	16	8.0
NovaPlus	20	0.1 – 3 .0	6.0	16	8.0
Petrofree/LE Base	20	0.1 – 4.0	3.6	16	8.0

Table 2: Acquisition Parameters for T_2 Measurements of Drilling Fluids Base Oils

Drilling Fluid Base Oil	Echo Spacing (ms)	Number of Echoes	Wait Time (s)	Number of Scans
SF Base	0.50	5120	4.0	16
Escaid 110	0.40	8192	7.5	16
NovaPlus	0.40	6144	3.0	16
Petrofree/LE Base	0.40	7168	3.6	16

Table 3: Acquisition Parameters for T_1 Measurements of Bicyclic Molecules in this Work

Compound	Number of Data Points	Interval Spanned by Data Points (s)	Wait Time (s)	Number of Scans	Signal Acquisition Interval (μs)
α-methylnaphthalene	20	0.1 – 5.0	7.5	16	8.0
Tetralin	20	0.1 – 7.0	7.0	16	8.0
Decalin	20	0.1 – 6.0	6.0	16	8.0

Table 4: Acquisition Parameters for T_2 Measurements of Bicyclic Molecules

Compound	Echo Spacing (ms)	Number of Echoes	Wait Time (s)	Number of Scans
α-methylnaphthalene	0.40	7168	7.5	32
Tetralin	0.32	13312	7.0	64
Decalin	0.32	11264	6.0	64

Table 5: Some Experimental Details for Monocyclic Compounds

Source	Larmor Frequency (MHz)	Temperature (^{0}C)	Experimental Method	Compounds Measured
Pendred, *et al*.	30	25	Adiabatic rapid passage (a.r.p.)	benzene toluene cyclohexane cyclopentane
Moniz, *et al*.	Not stated	25 (toluene) 27 (cyclopentane) 20 (cyclohexane)	Not stated	toluene cyclohexane cyclopentane
Nederbragdt and Reilly	40	25	Saturation recovery; a.r.p.	benzene toluene
Homer, *et al*.	Not stated	36	a.r.p.	benzene toluene

Table 6: Relaxation Times and Viscosities for Drilling Fluid Base Oils

Drilling Fluid Base Oil	T_1 (ms)	T_2 (ms)	Viscosity (cp)
SF Base	670	642	2.75
Escaid 110	993	1400	1.49
NovaPlus	670	653	2.80
Petrofree/LE Base	784	764	2.04

Table 7: Relaxation Times and Viscosities for Bicyclic Compounds

Compound	T_1 (s)	T_2 (s)	Viscosity (cp)
□-methylnaphthalene	1.43	1.44	2.6
Tetralin	1.47	1.41	1.9
Decalin	1.13	1.16	2.2

Table 8: T_1 Relaxation Times and Viscosities for Monocyclic Compounds

Compound	T_1 (s)	Viscosity (cp)	T_1 Source
Benzene	19	0.606	Nederbragt & Reilly
Benzene	24	0.519	Homer, *et al*.
Benzene	22	0.600	Pendred, *et al*.
Toluene—Ring	16	0.552	Nederbragt & Reilly
Toluene—Ring	22	0.486	Homer, *et al*.
Toluene—Ring	16	0.556	Pendred, *et al*.
Toluene—Ring	16	0.552	Moniz, *et al*.
Toluene—Methyl	9	0.552	Nederbragt & Reilly
Toluene—Methyl	12	0.486	Homer, *et al*.
Toluene—Methyl	10	0.556	Pendred, *et al*.
Toluene—Methyl	10	0.552	Moniz, *et al*.
Cyclohexane	7	0.867	Moniz, *et al*.
Cyclopentane	14	0.437	Moniz, *et al*.

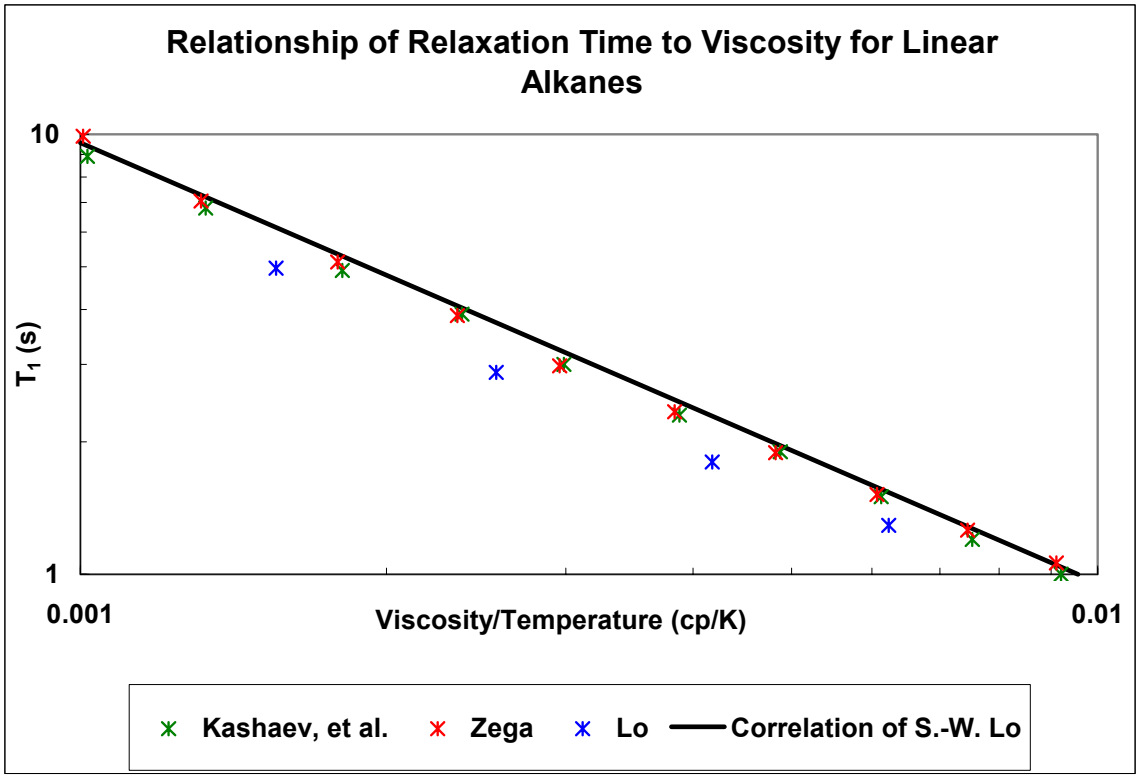

Figure 1: Correlation for T_1 relaxation time with η/T shown along with the basis data.

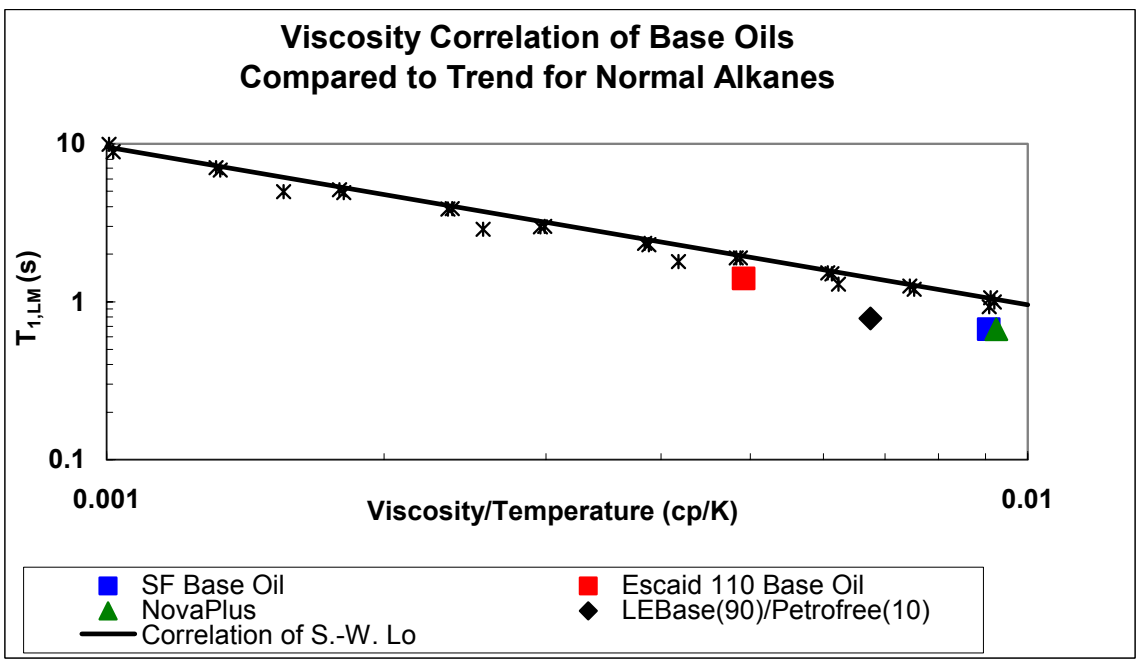

Figure 2: Plot of relaxation time against η/T for drilling fluid base oils, compared to correlation for linear alkanes

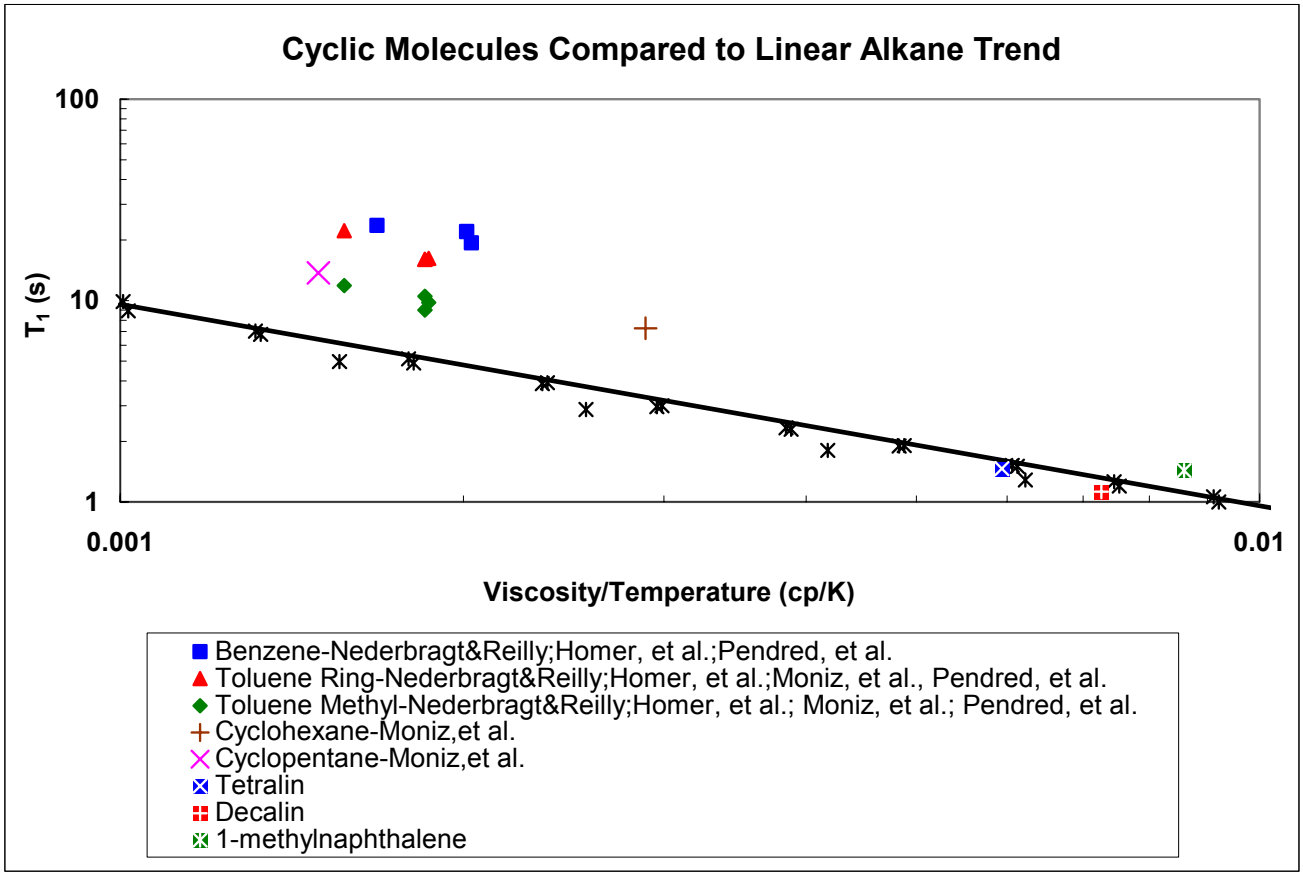

Figure 3: Plot of relaxation time against η/T for cyclic molecules, compared to correlation for linear alkanes

Task 2.0 Fluid-Rock Interactions

Subtask 2.1 Wettability Alterations

The following articles appeared in a publication and will not be repeated here.

G. Q. Zhang, C.-C. Huang, G. J. Hirasaki, "Interpretation of Wettability in Sandstones with NMR Analysis," *Petrophysics*, (2000), **41**, No. 3, 223-233.

Wettability alteration by surfactants and its effects on NMR surface relaxation

Jiansheng Chen, Dr. George J. Hirasaki

Abstract

The effect of oil based drilling fluid filtrate on the NMR response was investigated by studying the effect of surfactants on the water and oil relaxation in silica sand. T_2 relaxation time distributions for 100% water saturated, 100% oil saturated, and water/oil partially saturated silica flour were measured. The wettability of the silica flour surface was changed by surface adsorption of cationic surfactant dodecylamine or commercial emulsifier (BPAFA). The wettability alteration was quantitatively determined by the contact angle measurements of glass/water/oil system. It shows that for water/oil partially saturated silica flour, surface relaxivity ρ_2 increases for oil and decreases for water when dodecylamine or BPAFA is present in the oil phase. The anionic surfactant, stearic acid, does not alter the wettability of silica flour surface, leaving the surface relaxivity unchanged.

Introduction

Wettability is defined as “the tendency of one fluid to spread on or adhere to a solid surface in the presence of other immiscible fluids” (Craig, 1971). In porous media with mixed-wettability (Salathiel, 1977), The smaller pores are filled with brine and thus remain water-wet. The larger pores, which were filled with

oil, are oil-wet during imbibition. Wettability controls the location, flow and distribution of fluids in a reservoir. Therefore, it affects capillary pressure, relative permeability, waterflood behavior, irreducible water saturation, residual oil saturation (Anderson, 1986).

Wettability of various materials was investigated using NMR techniques (Brown and Fatt, 1956, Devereux, 1967, Saraf, 1970, Williams, 1982, Borgia, 1991, Hsu, 1992, Doughty, 1993, Øren, 1994, Rueslåtten, 1994, Howard, 1994, 1998, Zhang, 2000, Daughney, 2000, Bryar, 2001). Brown and Fatt (1956) started the pioneering work using uncoated sand packs as water-wet porous media and Dri-film treated sand packs as oil-wet porous media. They found that water relaxed faster in the water-wet system than in the oil-wet system. Moreover, for mixtures of oil-wet and water-wet sand the relaxation time varied linearly with the percentage of oil-wet sand. Later work by Saraf et al. (1970) for water-wet glass bead and oil-wet polymer bead systems showed similar results.

The link between wettability and NMR relaxation was also explored when both water and oil were present, which is more representative of oil reservoirs. Øren et al. (1994) studied T_1 relaxation time of water-wet Berea sandstone at various saturations during low rate water imbibition displacements. They found that oil relaxed at its bulk value when a continuous water film spread over the pore surfaces. Moreover, the intensity of the oil phase relaxation time component was in quantitative agreement with the measured oil saturation. Straley et al. (1995) obtained similar results for kerosene/water partially saturated sandstone, in which kerosene relaxed with its bulk value, rather than the shorter T_1 when kerosene fully saturated the dry sandstone. Studies for intermediate-wet sandstone (Rueslåtten, 1994, Borgia, 1991) also showed that information about wettability and oil-water configurations could be determined from NMR relaxation time.

Similar studies were done for carbonate samples. Hsu (1992) measured T_1 of water in carbonate cores with different wetting characteristics. They found that the proton T_1 relaxation rates for oil-wet cores were about 50% less than

those for water-wet cores. Howard (1994, 1998) studied NMR T_1 and T_2 relaxation time of water-wet and oil-wet chalks at different water saturations. He showed that for these fine-grained chalk samples, the water saturation could be easily determined by the bimodal relaxation time distribution, and the estimated water saturation correlated well with the core analysis value.

Instead of using synthetic wettability-altering chemicals, several researchers used actual crude oil components to change the rock wettability and studied its effects on NMR relaxation time (Devereux, 1967, Zhang, 2000). Devereux (1967) showed that the adsorption of surface-active components and asphaltene from the crude oil could change the water surface relaxation. Zhang (2000) showed that Benteim and Berea sandstone were water-wet with refined oil, but became mixed-wet with crude oil after aging.

NMR relaxation time is sensitive to the surface wettability, but the quantitative mechanisms of wettability effects on surface relaxation are still not very clear. On one hand, because of the basic intermolecular forces between fluid molecules and solid surface the molecular translational and rotational motion will be different near surfaces with different wettability. On the other hand, the materials adsorbed on the surface to make it oil-wet serve as a physical shielding between the fluid molecules and the paramagnetic sites on the surface (Brown and Fatt, 1956, Daughney et al., 2000). Daughney et al. (2000) studied the effects of adsorbed crude oil on the NMR T_1 relaxation time of water-saturated silica gel. They found that in the absence of paramagnetic iron impurities, T_1 remained constant with different amounts of adsorbed hydrocarbons. But T_1 increased with increasing surface hydrocarbon concentration when the silica surface was coated with iron oxyhydroxide.

The objective of this study is to quantitatively investigate the degree of wettability alteration by surfactant and its effect on NMR surface relaxation. Well-calibrated model system silica flour was used. T_2 relaxation time distributions for 100% water saturated, 100% oil saturated, and water/oil partially saturated silica flour were measured. The wettability of the silica flour surface was changed by

surface adsorption of cationic surfactant dodecylamine or commercial emulsifier BPAFA. The wettability alteration was determined by contact angle measurements of glass/water/oil system.

Experimental Procedures

Materials

Table 1. Characterization of silica flour samples

Sample	Sf # 1	Sf # 2
Mean diameter (μm)	1.69	1.28
BET surface area (m^2/g)	1.987	2.236
Grain density (g/cm^3)	2.65	2.65
Fe_2O_3 (ppm)	200	200

The silica flour samples (from U.S. Silica Company) are listed in Table 1. The mean diameter was determined by a N4 plus Coulter Counter (Coulter scientific instrument). Two light base oil escaid (from Baker Atlas) and SF Base (from Baroid) were used. Escaid is a light hydro-treated petroleum distillate (density: 0.80g/ml, viscosity: 1.78cp). SF Base is a mixture of internal olefins with C_{16} to C_{18} (density: 0.78g/ml, viscosity: 2.75cp). The surfactants are dodecylamine (*DDA*), stearic acid (*SA*) and emulsifier BPAFA.

Sample Preparation for NMR

The procedures of preparing the 100% water or 100% oil saturated silica flour were as follows: Silica flour was slowly added into water or oil in a beaker and stirred with a magnet bar. The silica flour slurry was then removed into a centrifuge tube (diameter 3 cm) and centrifuged at 500 g for 6 minutes. The supernatant liquid layer was removed. The procedures of preparing the water/oil partially saturated silica flour were as follows: Firstly, water-saturated silica flour slurry was prepared by the procedures described above. Then it was removed into a large, flat Petri dish to be heated on a Thermolyne heater. The silica flour was stirred during the heating process to make the sample homogeneous. After part of the water evaporated from the system, the silica flour particles stuck strongly with each other. A sharp spatula was used to cut the stuck particles

before they were added to an excess amount of oil in the centrifuge tube. Ultra-sonication was then used to further separate the stuck particles. Finally, the sample was centrifuged as before and the supernatant liquid layer removed. The silica flour samples were weighted in each step to determine the water saturation.

NMR T_2 Relaxation Measurements

NMR T_2 measurements were made at room temperature with a Maran-2 spectrometer (Resonance, Inc.) using a CPMG pulse sequence. Short echo spacing (0.3 ms) was used to prevent relaxation due to diffusion. A non-negative non-linear least square inversion method developed in our laboratory was used to estimate the multi-exponential T_2 relaxation time distribution (Chuah, 1996).

Contact Angle Measurements

The captive drop method (Yang, 2000) was used to measure the contact angles of glass/water/oil systems. Glass slides cleaned with methanol and toluene were used to simulate the silica flour surface. Both receding and advancing contact angles were measured. A microburet was filled with oil and placed about 2 mm above the glass slide surface, which was equilibrated with water in a glass cell. For the receding contact angle, an oil drop was slowly formed and pressed against the glass slide surface, and then the receding contact angle was measured with the goniometer after equilibrium. For the advancing contact angle, the oil drop was slowly withdrawn from the glass slide surface, and similarly the advancing contact angle was measured after equilibrium.

Results and discussion

As shown in Fig. 1 (*a*), the T_2 relaxation time distribution for water or oil totally saturated silica flour is a sharp single peak. For water/oil partially saturated silica flour, the T_2 relaxation time distribution is bi-model, the shorter little peak corresponds to water and the longer big peak corresponds to oil. The Log Mean T_2 was calculated as follows,

$$T_{2,LM} = \exp(\sum_i f_i \cdot \ln(T_{2,i})) \quad (1)$$

Where $T_{2,i}$ and f_i are the relaxation times and intensities in the multi-exponential relaxation time distribution, respectively.

For water or oil totally saturated silica flour, surface relaxivity ρ_2 was calculated as follows,

$$\rho_2 = \frac{\phi}{1-\phi} \cdot \frac{1/T_2 - 1/T_{2,B}}{S_{BET} \cdot \rho_g} \quad (2)$$

Where ϕ is porosity, T_2 is the Log Mean value calculated by (1), $T_{2,B}$ corresponds to bulk fluid, S_{BET} and ρ_g are the specific surface area and grain density of the silica flour as listed in Table 1, respectively.

Similarly, for water/oil partially saturated silica flour,

$$\rho_{2W,eff} = \frac{\phi}{1-\phi} \cdot S_W \cdot \frac{1/T_2 - 1/T_{2,B}}{S_{BET} \cdot \rho_g} \quad (3)$$

$$\rho_{2O,eff} = \frac{\phi}{1-\phi} \cdot (1 - S_W) \cdot \frac{1/T_2 - 1/T_{2,B}}{S_{BET} \cdot \rho_g} \quad (4)$$

Where the surface relaxivity is an effective surface relaxivity, indexes W and O correspond to water and oil, respectively. S_W is water saturation.

Fig. 1, 2 and 3 show that for silica flour partially saturated with water and pure base oil, the surface relaxivity ρ_2 of water is about the same as that for 100% water saturated silica flour, on the other hand, the surface relaxivity ρ_2 of oil is much less than that for 100% oil saturated silica flour. However, when cationic surfactant, dodecylamine or emulsifier BPAFA is added in the oil phase, the surface relaxivity decreases for water and increases for oil. This surface relaxivity change is due to the wettability change and correspondingly the fluid distribution change. Originally, the silica flour surface is water-wet. Therefore,

almost all the surface of the silica flour particles is covered by a water film, which shields the contact of oil with the surface (The reason for a finite value of surface relaxivity of oil is not clear now, but it could be due to some finite contact of oil with several spot of the surface or due to surface relaxation for oil at the oil-water interface (Peña, 2002)). When dodecylamine or emulsifier BPAFA is added in the oil phase, the wettability of the silica flour surface is changed to be partially or locally oil-wet due to the surfactant adsorption by electrostatic attraction or hydrogen bonding forces. Therefore, oil contacts part of the surface and relaxes faster and water loses part of its surface contact and relaxes slower. This effect is stronger when the surfactant concentration in the oil phase is larger (Fig. 3).

As a comparison, Fig. 4 shows that for water/oil partially saturated silica flour, T_2 relaxation time and surface relaxivity ρ_2 remain almost unchanged when anionic surfactant stearic acid is added in the oil phase. Since the anionic head group of stearic acid has the same charge as silica, it does not adsorb onto silica surfaces. Therefore, the wettability of the surface as well as the fluid distribution will not be changed, resulting in almost unchanged T_2 relaxation time and surface relaxivity.

The contact angle measurements (Fig. 5 and 6) support the above illustration about wettability change. Fig. 5 shows that the glass surface is preferentially water-wet when the oil phase is pure escaid or escaid plus 0.5% stearic acid (no surfactant adsorption). But the glass surface becomes oil-wet when the oil phase is escaid plus 0.74% dodecylamine (with surfactant adsorption). Fig. 6 shows that the glass surface is water-wet in both receding and advancing directions when the oil phase is pure SF Base. When the oil phase is SF Base plus emulsifier BPAFA, the glass surface is intermediate water-wet in receding direction since the receding contact angles are close to and less than 90 degrees but oil-wet in advancing direction since the advancing contact angles are close to 180 degrees.

Conclusions

1. Oil in contact with dry silica has a surface relaxivity that is ¼ to ½ of that of water. In the absence of surfactant, the surface relaxivity of oil in the presence of water is greatly reduced to about 1/8 of that of water. This is apparently due to a wetting film of water shielding most of the oil from the silica.

2. Cationic surfactant Dodecylamine or emulsifier BPAFA present in the oil phase of water/oil partially saturated silica flour alters the wettability of the silica flour surface. Therefore, water relaxes slower and oil relaxes faster. This is apparently due to oil partially shielding water from the silica surface and increasing the contact of oil with the silica. This effect is stronger when the surfactant concentration in the oil phase is larger.

3. Anionic surfactant stearic acid does not alter the wettability of silica flour surface, leaving surface relaxivity unchanged.

4. Contact angle measurements for water/oil/glass systems prove that wettability alteration (water-wet to oil-wet) occurs when cationic surfactant is present in the oil phase but not when the anionic surfactant, stearic acid is present.

Reference

Anderson, W. G.: "Wettability Literature Survey-Part 1: Rock/Oil/Brine Interactions and the Effects of Core Handling on Wettability," *Journal of Petroleum Technology* (1986), October.

Borgia, G. C., Fantazzini, P., and Mesini, E.: "Wettability Effects on Oil-Water Configurations in Porous Media: A Nuclear Magnetic Resonance Relaxation Study," *J. Appl. Phys*. (1991), **70** (12).

Brown R. J., and Fatt I.: "Measurement of Fractional Wettability of Oilfield Rocks by the Nuclear Magnetic Relaxation Method," *Thans. AIME* (1956), **207**, 262-264.

Bryar, T. R., Caputi, M., Daughney, C., and Knight, R.: "Influence of Adsorbed Crude Oil on NMR Relaxation of Water in Saturated Silica Sand," Magnetic Resonance Imaging (2001), 19.

Chuah, T. L.: *Estimation of relaxation time distribution for NMR CPMG measurements* (1996). Master thesis, Rice University, Houston, TX.

Craig, F. F.: "The Reservoir Engineering Aspects of Waterflooding," *monograph series* (1970), SPE, Richardson, TX.

Daughney, C. J., Bryar, T. R., and Knight, R. J.: "Detecting Sorbed Hydrocarbon in a Porous Medium Using Proton Nuclear Magnetic Resonance," *Environ. Sci. Technol* (2000), 34, 332-337.

Devereux, O. F.: "Effect of Crude Oil on the Nuclear Magnetic Relaxation of Water Protons in sandstones," *nature* (1967), 215.

Hirasaki, G. J.: "Wettability: Fundamentals and Surface Forces, *SPE Formation Evaluation*, June 1991.

Howard, J. J.: "Wettability and Fluid Saturations Determined from NMR T_1 Distributions," *Magnetic Resonance Image* (1994), 12 (2), 197-200.

Howard, J. J.: "Quantitative Estimates of Porous Media Wettability from Proton NMR Measurement," *Magn. Reson. Imaging* (1998) **16**, 529-533.

Hsu, W. F., Li, X., and Flumerfelt, R. W.: "Wettability of Porous Media by NMR Relaxation Methods," paper 24761: Society of Petroleum Engineers, presented at 67th Annual Technical Conference and Exhibition.

Øren, P. E., Rueslåtten, H. G., Skjetne, T., and buller, A. T.: "Some Advance in NMR Characterization of Reservoir sandstones," North Sea Oil and Gas Reservoirs *III,* Kluwer academic publisher group, 1994.

Peña, A. A., and Hirasaki, G. J.: "Combined NMR PGSE-CPMG Technique to Characterize Water-In-Oil Emulsions," Presented at the AICHE 2002 spring national meeting (10-14, March, 2002), New Orleans, LA.

Rueslåtten, R., Øren, P. E., Robin, M., Rosenberg, E., and Cuiec, L.: "Fluid Distribution in Rocks Interred from NMR Spectroscopy and Cryo-SEM," presented at the SPE/DOE 9th symposium on improved oil recovery. 1994.

Salathiel, R. A., *Journal of petroleum Technology*, 25(2), 1216-1224.

Saraf, D. N., Kumar, J., and Fatt I.: "Determination of Wettability of Porous Materials by the Nuclear Magnetic Resonance Technique," *Indian J. of Technology* (1970), **8**, 125-130.

Straley, C., Morriss C. E., Kenyon W. E., and Howard J. J.: "NMR in Partially Saturated Sandstones: Laboratory Insights into Free Fluid Index, and Comparison with Borehole Logs," *The Log Analyst* (1995), **36**(1), 40-56.

Williams, C. E., and Fung, B. M.: "The Determination of Wettability by Hydrocarbons of Small Particles by Deuteron $T_{1\rho}$ Measurement," *J. Magn. Reson*. (1982), **50**, 71-80.

Yang, S.Y.: *Mechanisms of Wettability for Crude oil/Brine/Mica System* (2000). Ph.D. thesis, Rice University, Houston, TX.

Zhang, G. Q., Huang, C. C., and Hirasaki, G. J.: "Interpretation of Wettability in sandstones with NMR Analysis, *Petrophysics* (2000), **41**(3), 223-233.

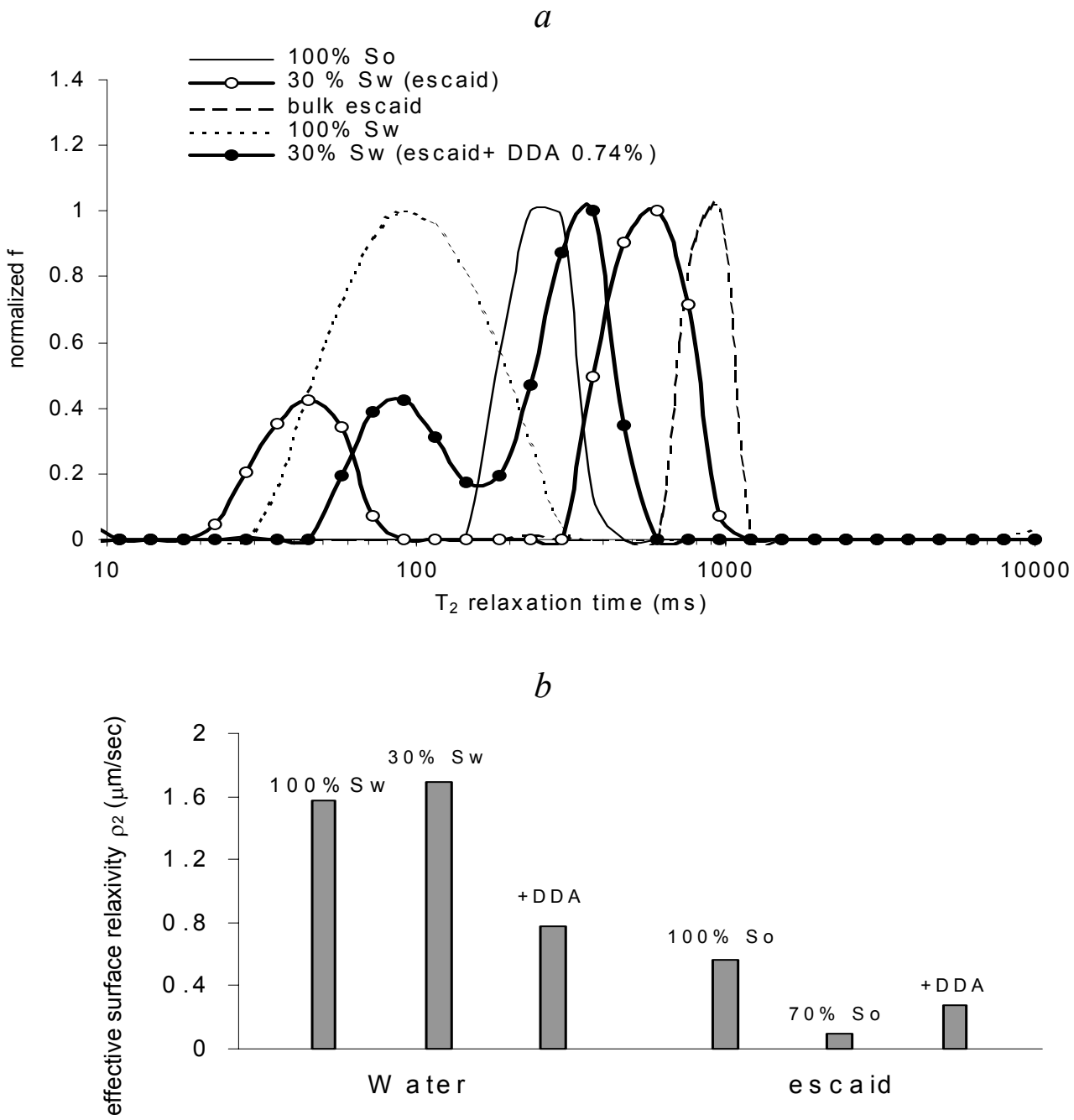

Fig. 1 T_2 relaxation time distribution (*a*) and surface relaxivity ρ_2 (*b*) for silica flour saturated with 100% S_w, 100% *So*, 30% S_w with pure escaid, and 30% S_w with escaid plus 0.74% dodecylamine (*DDA*).

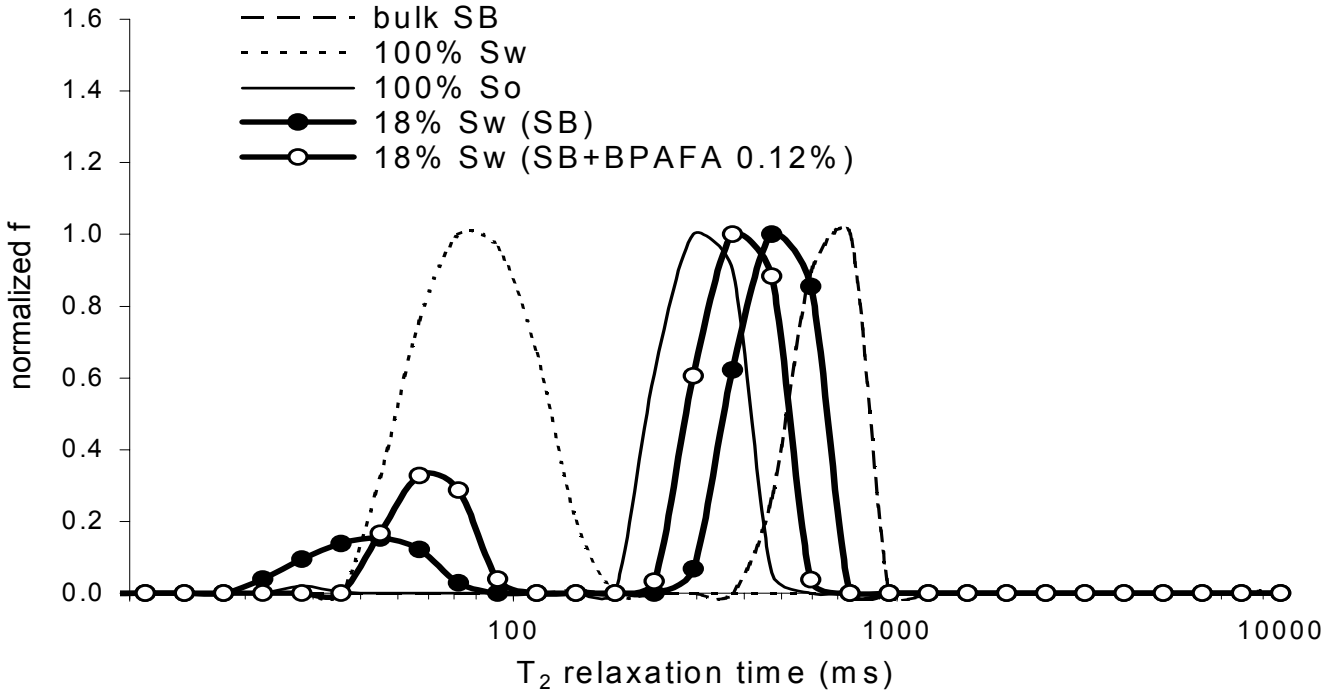

Fig. 2 T_2 relaxation time distributions for silica flour saturated with 100% S_w, 100% S_o, 18% S_w with SF Base (*SB*), and 18% S_w with SF base plus 0.12% emulsifier BPAFA.

a

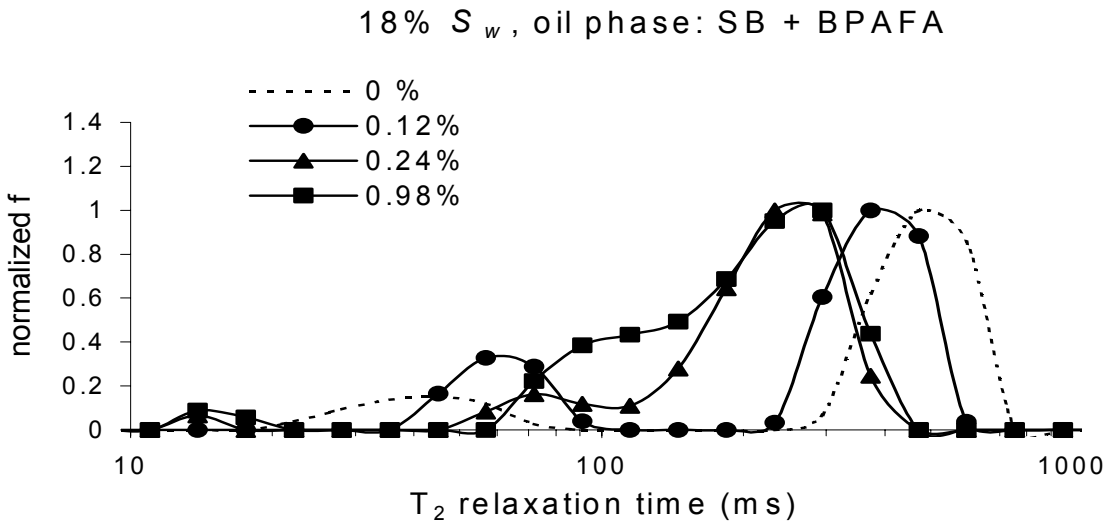

b

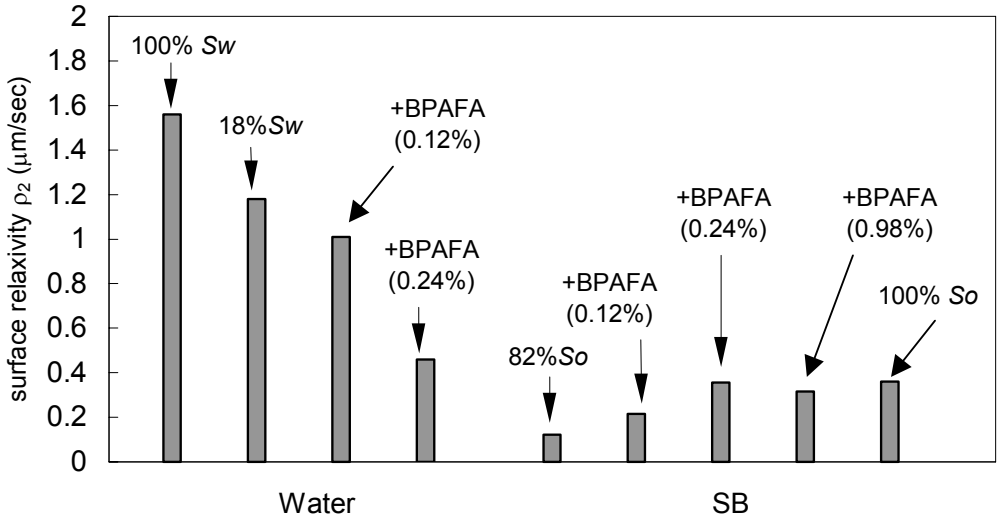

Fig. 3 Comparison of T_2 relaxation time distributions (*a*) and surface relaxivity ρ_2 (*b*) for 18% S_w saturated silica flour among cases with different concentration of emulsifier BPAFA in the SF Base (*SB*) oil phase.

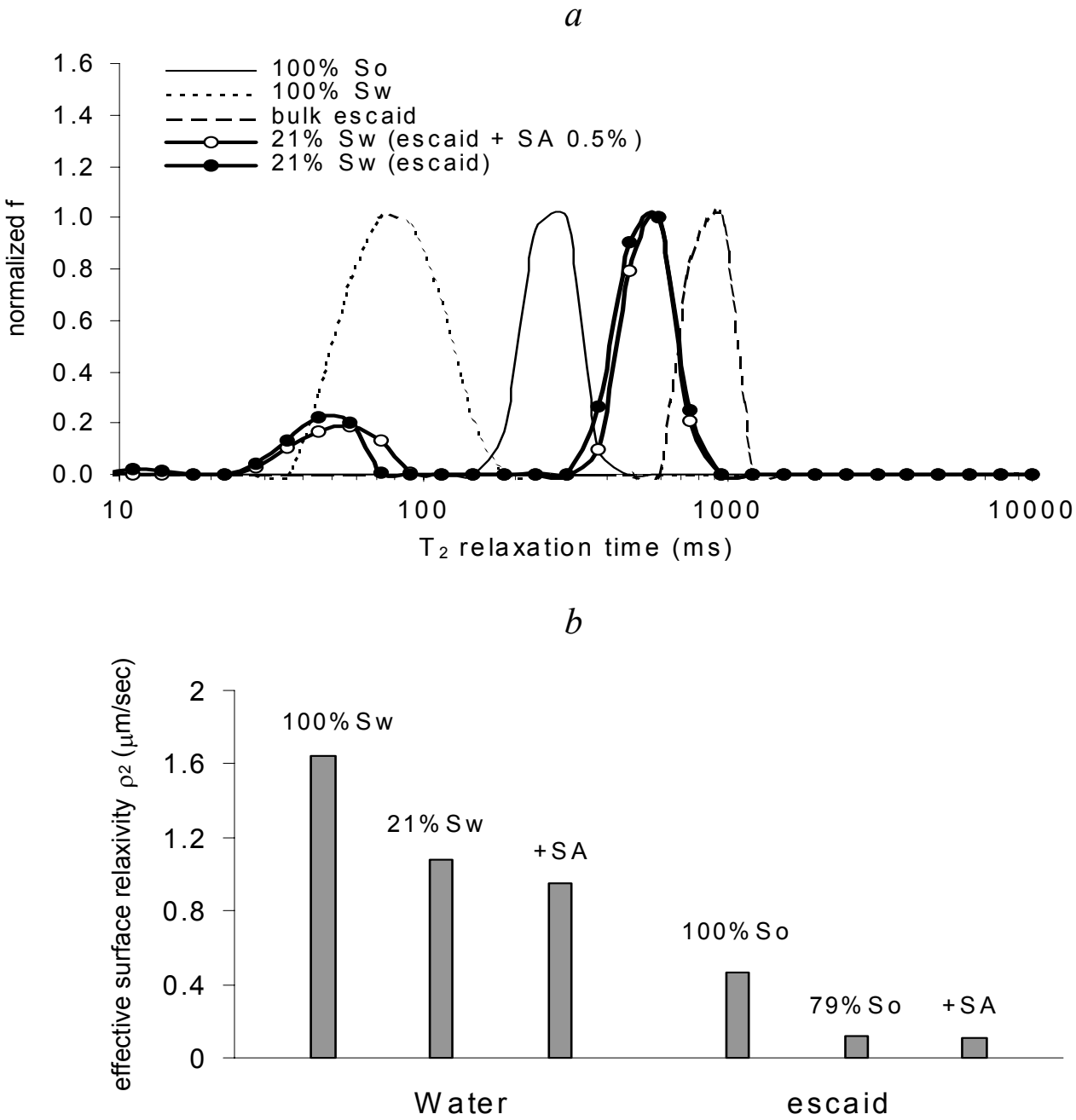

Fig. 4 T_2 relaxation time distribution (*a*) and surface relaxivity ρ_2 (*b*) for silica flour saturated with 100% S_w, 100% S_o, 21% S_w with pure escaid, and 21% S_w with escaid plus 0.5% stearic acid (*SA*).

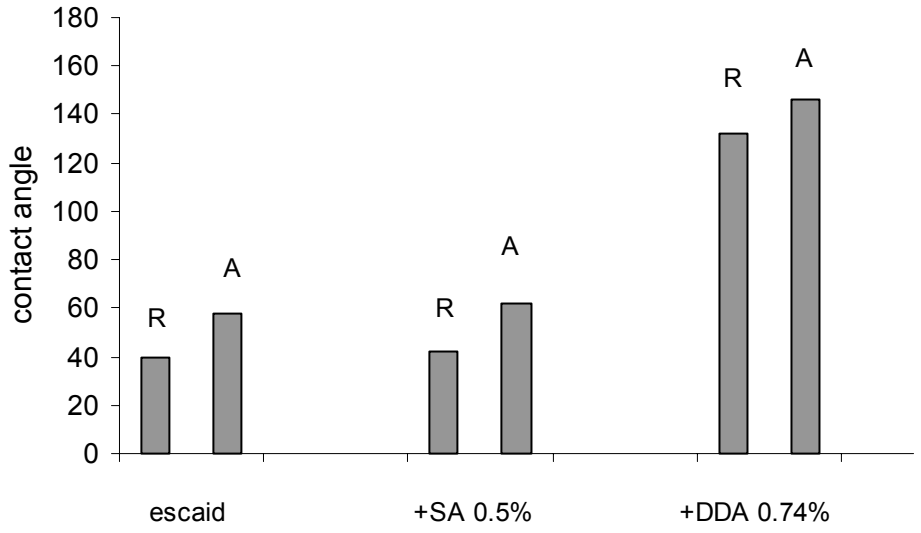

Fig. 5 Contact angles for water/oil/glass systems. The glass surface is water-wet when the oil phase is pure escaid or escaid plus 0.5% stearic acid (*SA*). But the glass surface becomes oil-wet when the oil phase is escaid plus 0.74% dodecylamine (*DDA*).

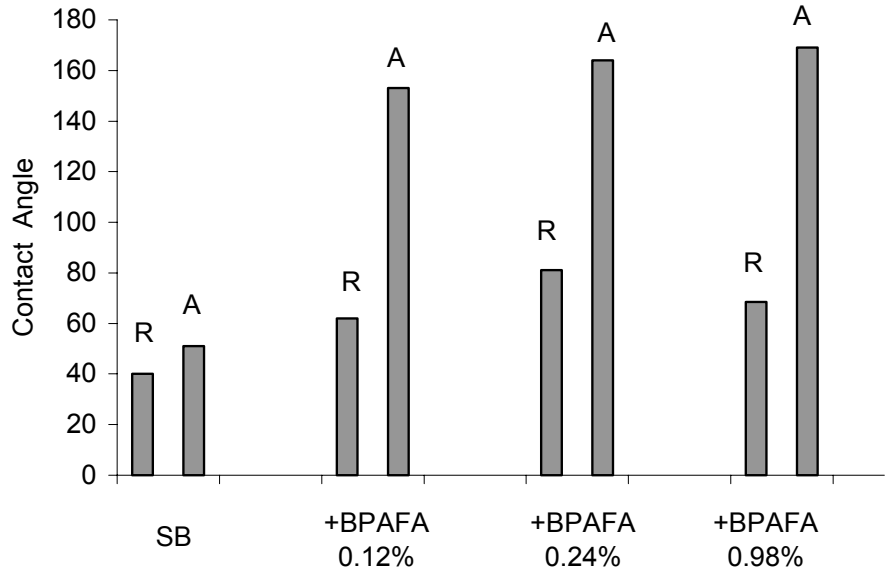

Fig. 6 Contact angles for water/oil/glass systems. The glass surface is water-wet in both receding (*R*) and advancing (*A*) directions when the oil phase is pure SF Base (*SB*). When the oil phase is SF Base plus emulsifier BPAFA, the glass surface is intermediate-wet in receding direction but oil-wet in advancing direction.

Subtask 2.2 Diffusion in Internal Gradients

Subtask 2.4 Restricted Diffusion

The following two articles appeared in a publication and will not be repeated here:

G. Q. Zhang, G. J. Hirasaki, and W. V. House, "Effect of Internal Field Gradients on NMR Measurements," *Petrophysics*, **42**, No. 1 (Jan.-Feb. 2001), 37-47.

"Internal Field Gradients in Porous Media," poster presentation by Q. Zhang at the SPWLA 41st Annual Logging Symposium, Dallas, TX, June 4-7, 2000.

Fluid and Rock Characterization Using New NMR Diffusion-Editing Pulse Sequences and Two Dimensional Diffusivity-T_2 Maps

Mark Flaum and George Hirasaki

Rice University

Introduction

New down-hole nuclear magnetic resonance (NMR) measurement and interpretation techniques have substantially improved fluid and reservoir characterization. These techniques take advantage of the magnetic field gradient of the logging tools to make diffusion sensitive NMR measurements. In our work, new NMR pulse sequences called "diffusion-editing" (DE) are used to measure diffusivity and relaxation times for water, crude oil, refined oil, and a series of partially saturated core samples. We use a new inversion technique to obtain two-dimensional maps of diffusivity and relaxation times.

It is well known that T_2 relaxation time distributions for water-saturated samples provide useful information about the pore-size distribution of the samples. A number of correlations relate aspects of these distributions to permeability. However, when a sample is partially saturated with oil and water, it

is difficult to separate the oil and water relaxation time distributions from each other. Crude oil relaxation time distributions correlate with viscosity, so that oil distributions can also be used to estimate the viscosity of the oil provided that one can obtain separate water and oil distributions. Recent papers by Freedman[1, 2] et al use a suite of gradient CPMG measurements to exploit the diffusivity contrast between the water component of the signal and the crude oil component, providing accurate saturations and separated relaxation distributions for both fluids. The data suite consists of CPMGs that include measurements with very long echo spacings that are required in order to robustly differentiate oil from water. For the sequences with very long echo spacings only a relatively few echoes have appreciable signal because the signal decays very rapidly. This limits the long time information that is obtained using a suite of CPMGs and in some cases compromises the robustness of the estimated relaxation time distributions.

The new pulse sequence discussed in this report overcomes this limitation by changing the echo spacing not for the duration of each CPMG, but only for the first two spin echoes. Subsequent echoes are collected at the minimum echo spacing, providing precise relaxation information about the sample. Papers by Freedman[3] *et al.* and Hurlimann[4, 5] *et al.* discuss fluid and rock characterization using the DE sequence. We use the same two-dimensional inversion for D-T_2 maps described by Hurlimann *et al*., but this work presents the first laboratory measurements employing both diffusion-editing and the two-dimensional inversion applied to reservoir and quarry rocks saturated with crude oil. The rocks selected for this study include Berea, Bentheim, and North Burbank sandstones as well as carbonates from the Yates formation that contain pore size distributions over several orders of magnitude.

The D- T_2 maps provide a wealth of information not previously available from simple relaxation time distributions. For example, the diffusion distribution of a water-saturated sample can give evidence of restricted diffusion, which could then be used to provide pore-size distribution information independent of that provided by T_2 distributions. Oil relaxation times that do not correlate with

viscosity may indicate the oil is wetting the rock surface, which would also be indicated by shifts in the relaxation time distribution. Water diffusivities above that of bulk water can indicate the presence of internal gradients. The D-T_2 maps can be summed or selected to provide bulk distributions or other very specialized information. This work will demonstrate that the D-T_2 map is a valuable new tool for the interpretation of NMR data, and that the DE measurements provide information not available through other means.

Theory

Most down-hole NMR measurements are based on the well-known Carr-Purcell-Meiboom-Gill (CPMG) sequence. This sequence provides T_2 relaxation information with sensitivity to pore surface-to-volume ratio and fluid diffusion. By combining multiple CPMG measurements on partially saturated rocks, it is possible to approach fluid saturation by taking advantage of the diffusivity contrast between oil and water[1]. The measurements described in this report use a form of the CPMG sequence that has been modified to improve the robustness of the petrophysical data obtained through NMR measurements. This sequence is referred to as "diffusion editing" to describe the use of modified pulse timing to "edit" the amplitude of the echo data and provide diffusion information.

The sequence is displayed in Fig. 1. Like other CPMG-based techniques for obtaining saturation data, this technique consists of a suite of similar NMR measurements. In this case, the independent variable that provides diffusion information is the echo spacing of the first two echoes of the sequence (called TEL). An increase in the spacing of these two echoes decreases the amplitude of subsequent echoes due to diffusion effects. The remaining echoes are at a fixed shorter echo spacing (TES) selected to prevent the further diffusion effects. The progressive amplitude loss over the first two echoes for a series of TEL values provides information about the diffusivity of fluids in the sample, while the multi-exponential decay of subsequent data points provides T_2 relaxation distributions, as would an unmodified CPMG. Models that relate T_2 and diffusivity distributions, such as the constituent viscosity model[1], allow the

separation of T_2 relaxation distributions for multiple fluids present in a sample. The technique used in this report, however, uses a method developed by Schlumberger to obtain a model-independent simultaneous inversion for both relaxation and diffusion[5]. This inversion provides the D-T_2 maps, which allow clear and straightforward interpretation of multiple fluid systems. Sample D-T_2 maps can be seen in the Results section.

There are some details involving D-T_2 maps that require extra care in interpretation. The list of TELs used for the measurement suite may need to be carefully tailored for some samples. If the list does not include long enough TEL values to ensure that enough diffusion is measured to fully characterize the diffusivity of the system, the inversion will treat lingering low-diffusivity signal as a non-diffusing fluid presence. This non-diffused signal will manifest as a peak that is narrow in relaxation space at approximately the correct value, but very broad in diffusion space and centered around the minimum end point of the inversion diffusivity range. For this reason, any diffusion contributions occurring at or near the inversion diffusivity minimum cannot be treated with confidence.

On the other hand, the inversion does not take into account any relaxation information from data points shorter than the third echo of the longest TEL. That means if TEL must be long for correct diffusion characterization, short T_2 information will be lost. It is necessary to trade off low-diffusivity information for short relaxation information, or vice versa. At this point, further investigation is necessary to achieve an ideal balance between short-time relaxation information and long-time diffusion results. The limitation is in the inversion stage, so it may be necessary to develop a different inversion method, or to invert one data set multiple times. It should be possible to invert the complete data set to obtain adequate diffusion information, and then invert it a second time dropping the longest TELs, to obtain short T_2 information.

Another issue is with the acquisition of high diffusivity data. To better characterize diffusivities above that of bulk water, it is necessary to collect data at values of TEL that are relatively short (still longer than TES). This data is not

useful when no high-diffusing fluids are present, but is vital if internal gradients or gas are present. If short TEL data is not collected, high diffusivity data will appear smeared and difficult to interpret.

Experimental

Rock Samples

For these measurements, three distinctly different sandstone samples were measured. All were in the form of 1-inch long, 1-inch diameter cylinders. The first sandstone was a highly permeable and nearly clay-free Bentheim sample (BEN3). The second was a Berea sandstone (BER2 and BER3), known to contain kaolinite, illite, and some localized siderite crystals. Two samples of this type were measured. The final sandstone sample was a North Burbank (NBUR3), unusual due to the presence of chlorite flakes, which provide large magnetic susceptibility contrast and therefore large internal gradients. This last sample was only used in the second suite of experiments. All of these samples were included in the study by Zhang[7]. The carbonates used in this study were both dolomites from the Yates field in west Texas (Y1312, Y1573). These samples have a complex dual-porosity pore structure, vugs on the order of 100 microns, and exhibit mixed wettability. Rock properties for these samples are summarized in Table 1.

Bulk fluid experiments

The first suite of partially saturated core experiments was carried out using a North Sea crude oil (SCNS) with an API gravity of 33.2. This oil has no measurable asphaltenes (0.0 %) but a modest fraction of resins (7.9%). The bulk crude oil experiments employed a Gulf of Mexico crude (SMY), with and API gravity of 30.3. This oil has significantly more asphaltenes (5.5%) and more resins as well (12.5%). More details about these crude oils can be found in Table 2. The refined oil used in this study was a drilling fluid base oil referred to as Nova Plus, manufactured by Halliburton. The bulk water sample was tap water, and the hexane sample was not de-oxygenated. The NMR measurements for the water, hexane, Nova Plus, and SMY experiments were carried out in a

Resonance Instruments MARAN Ultra spectrometer at 2.06 MHz with a static gradient of 13.2 G/cm. For the SCNS crude oil, the measurements were carried out in a fringe field apparatus at 1.76 MHz with a static field gradient of 13.2 G/cm. The TEL list for the bulk fluid collection suites was 1.6, 5.6, 8.0, 10.4, 12.8, 17.6, 24.0, 32.0, 48, and 60 ms for the water, hexane, SMY, and Nova Plus. For the North Sea sample, the suite was 1.2, 2.4, 4.4, 8.4, 12.4, 16.4, 20.4, 24.4, 28.4, 32.4, and 36.4 ms. The TES was 0.4 ms for both suites.

Partially-saturated core experiments

The suite of partially-saturated core experiments include only the samples BEN3, BER2, Y1312, and Y1573. The samples were wrapped in heat shrinkable Teflon, water-saturated by vacuum, and then pressurized to remove any air. A set of diffusion editing NMR measurements was performed on these samples at 100% water saturation. The samples were then centrifuged submerged in SCNS crude at 3400 RPM for 11 hours for primary drainage. The samples were then inverted, and centrifuged for an additional hour. A second set of diffusion-editing measurements was performed. At this point, all the samples were submerged in water. For the sandstone samples, spontaneous imbibition was observed and no forced imbibition was performed. For the carbonates, no spontaneous imbibition was observed, so forced imbibition was performed by centrifuging the samples submerged in water at 3400 RPM for one hour. A final set of diffusion-editing experiments was carried out at this stage. The NMR measurements for this suite were carried out in a fringe field apparatus at 1.76 MHz with a static field gradient of 13.2 G/cm. For these measurements, the list of TELs used was 1.2, 2.4, 4.4, 8.4, 12.4, 16.4, 20.4, 24.4, 28.4, 32.4, and 36.4 ms, with a TES of 0.4 ms.

High internal gradient experiments

These experiments were carried out on the North Burbank (NBUR3) sample. The sample was wrapped in heat-shrinkable Teflon, water saturated by vacuum, and then pressurized to remove air. It was then spun at 5000 rpm in SMY crude oil for one hour, aged at 80° C for seven days, submerged in water and centrifuged at 5000 rpm for one hour. Measurements were taken at each

stage of this process. Unfortunately the NMR equipment malfunctioned, and was only possible to obtain usable DE data for the final stage of saturation, where the rock showed approximately 95% water saturation. The NMR measurements for these data sets were carried out in a Resonance Instruments MARAN Ultra spectrometer at 2.06 MHz with a static gradient of 13.2 G/cm. The list for this suite was 0.8, 1.6, 2.4, 4.0, 5.6, 6.4, 8.0, 10.4, 12.8, and 17.6 ms, with a TES of 0.4 ms.

Air de-saturation experiments

These experiments were performed on the BER3 sample. This sample was water saturated by vacuum, and a suite of DE measurements was collected. The sample was the centrifuged at 9500 RPM (100 PSI) for 17 hours, and a second suite of DE measurements was collected. The final S_w achieved was 0.43. The NMR measurements for these data sets were carried out in a Resonance Instruments MARAN Ultra spectrometer at 2.06 MHz with a static gradient of 13.2 G/cm. The TEL list for this suite was 1.6, 5.6, 8.0, 10.4, 12.8, 17.6, 24.0, 32.0, 48, and 60 ms with a TES of 0.4 ms.

Results

The *D-T2* Maps

The D-T_2 maps presented here are contour plots showing two-dimensional distributions of diffusion and relaxation for each sample. The maps are logarithmic for both axes. There are two lines shown on each of the diffusion maps – a horizontal line indicating the diffusion constant of bulk water at the conditions of the experiment, and a diagonal line indicating the correlation between diffusivity and T_2 for hydrocarbon mixtures according to Lo *et al*[9]. A projection of the entire map to the x-axis would provide the more familiar T_2 distribution, while a projection to the y-axis would provide a distribution of the real or apparent diffusivities of the system.

Fig. 2 shows the D-T_2 map for bulk water at 27°C. The log mean values of the diffusivity and relaxation time correspond to known values for bulk tap water.

The log mean T_2 value for that sample is 2.95 seconds, and the log mean diffusivity of the sample is 2.49e-5 cm^2/s, very close to the literature value of 2.50e-5 cm^2/s[6]. Fig. 3 shows the T_2 distribution developed by summing the map bins across all diffusivities, plotted alongside the distribution obtained from the standard Rice T_2 relaxation time inversion[11], applied to the first data set of the DE suite, where TEL = TES. The agreement is very good.

Fig. 4 shows the map for a hexane sample. The diffusivity is higher than that of water, while the relaxation time appears slightly shorter. The T_2 values agree very will with published results by Y. Zhang[10] for non-deoxygenated hexane. Data from Y. Zhang also suggest that if the sample was de-oxygenated, it is expected that the T_2 would increase till the distribution lay on the correlation line. The T_2 distribution, shown in Fig. 5, again agrees very well with the result obtained by a standard inversion.

The distribution for the refined oil mixture, Nova Plus, is shown in Fig. 6. The peak is narrow, and centered exactly on the line indicating the correlation between relaxation and diffusion. Fig. 7 shows the T_2 distribution comparison, and the agreement is very good.

Fig. 8 shows the D-T_2 map of the SMY crude oil. The distribution appears above the correlation by Lo[12]. Examining the T_2 distributions in Fig. 9 shows truncation of short relaxation time data, as discussed in the Theory section. All data before the second echo of the longest TEL sequence is dropped from the D-T_2 map, so a great deal of data is lost for this sample.

Fig. 10 shows the D-T_2 map of the North Sea crude oil sample. This is the oil sample that will be used to partially saturate the core samples. The distributions for both diffusivity and relaxation time are quite broad. The distribution itself is centered on the correlation line, indicating that this oil follows the correlation described by Lo *et al*[9]. No truncation appears to have occurred with this sample, and agreement between the T_2 distributions in Fig. 11 is very good.

BEN3

Fig. 12 shows the D- T_2 map of sample BEN3 fully saturated with water. There is a single peak visible in the plot, with a diffusivity distribution centered at 2.00e-5 cm^2/s and a T_2 range between 200 milliseconds and 1.2 seconds. The diffusivity value indicated suggests that all of the water in the sample diffuses similar to bulk, with little restricted diffusion occurring. The relaxation time distribution agrees well with the same distribution obtained from a single CPMG measurement, as shown in Fig. 13. The BEN3 sample is highly permeable, highly porous, and known to have very low clay content, all of which would agree with the results obtained from the D- T_2 map. Note there is one peak in the standard inversion that is truncated in the map-generated version.

Fig. 14 shows the same BEN3 sample, now at very high oil saturation (approximately 95%). The position of the only strong peak corresponds well to the bulk North Sea oil shown in Fig. 10. The conclusion that can be drawn is that the oil in this rock sample does not wet the surface, as it relaxes and diffuses as the bulk fluid.

Fig. 15 is again the BEN3 sample, this time with an oil saturation of approximately 57%. Here, one peak corresponding to the water content is clearly visible, as well as another representing the oil. The oil peak is very much the same as it appeared at higher saturations, again behaving as bulk oil. The water peak still diffuses as it did in the fully water-saturated measurement, but the T_2 distribution has lost all amplitude above 1 second. This indicates that the largest pores, formerly occupied by water, have been filled with oil instead, and the water is now contained in smaller, faster relaxing pores. The water still lines the walls of the larger pores (otherwise the oil T_2 distribution would be affected by oil wetting) but the reduced volume of water present increases the surface/volume ratio, and thus decreases relaxation time.

BER2

Fig. 16 shows the D-T_2 map for the water BER2 sample. The T_2 distribution covers shorter times than the BEN2, indicating stronger surface

relaxation, probably due to smaller pores and the presence of clays. The diffusion distribution remains close to that of bulk water. In the relaxation distribution comparison, shown in Fig. 17, the agreement between the map distribution is close at the longer times, but the map distribution is clearly missing amplitude below 40 milliseconds. This occurs because the inversion does not use any echo data shorter than twice the longest TEL value, for this sample 78.8 milliseconds.

The BER2 sample at high oil saturation is shown in Fig. 18. The oil does not appear to undergo any surface relaxation, suggesting the surface remains water-wet. The oil portion compares very well to Fig. 10 at lower diffusivities, but at high diffusivities the oil peak seems to merge with the water distribution, suggesting some restricted diffusion may be occurring in the water-filled pores relaxing at a T_2 close to the bulk oil. This would occur when a pore is nearly completely filled with oil, and the water present undergoes restriction between the pore walls and the oil interface. The water relaxation distribution for this sample appears to separate into to distinct peaks, suggesting that diffusive coupling has been broken off between the larger pores and the microporosity

At lower oil saturation, the BER2 sample provides a more complicated picture, shown in Fig. 19. To begin with, the water potion relaxing faster than 200 milliseconds manifests both higher and lower diffusivity values. Our interpretation for this wide range of diffusivity values is that the elimination of diffusive coupling increases the contribution of internal gradients and restricted diffusion. In small pores where internal gradients are large, spins that are not coupled to larger pores spend more time in regions of high gradient, appearing to diffuse faster than they would if coupled. In small pores without large internal gradients, the spins are instead heavily restricted. The diffusivities measured in those pores are lower than that of free-diffusing water. This situation is possible in the BER2 sample, as this sample is known to contain illite, siderite, and kaolinite clays[8]. The siderite clays are not likely to occur near the pore surface, but may serve as an iron source for the illites. The illite clays have been shown to have internal gradients in some circumstances, in particular when iron is

present at the surface of the clay. So iron-bearing illites could account for the portion of the small pores that experience internal gradients. The kaolinites, though, do not create internal gradients, and so water bound to kaolinite clays would only experience restricted diffusion. The diffusivity of clay-bound water can be so low that it appears near the correlation line for hydrocarbons. The signal below 10e-6 cm^2/s, and relaxing faster than 100 milliseconds must be water, as none of the oil shown in Fig. 10 would be found in that region. The peak position and broadness seen in the map may also been an artifact, as discussed in the Theory section. Due to the low diffusivities indicated here, it is not clear that adequate diffusion information took place to correctly characterize the slow-diffusing components of this system. The data set was inverted for a diffusion range of 1e-4 to 1e-7 cm^2/s, and information this close to the minimum of the inversion range is not reliable.

Carbonate results

The fully water-saturated Y1312 sample, shown in Fig. 20, diffuses as bulk, and relaxes as might be typical of vuggy carbonates with broad pore-size distributions, ranging from 200 milliseconds to 1.5 seconds. There is some slight skewing towards lower values in the diffusivity distribution, indicating the possibility of restricted diffusion. The agreement between map-generated and standard inversion-generated T_2 distributions is very good, shown in Fig. 21.

At high oil saturations, there is overlap developing between the oil distribution and severely restricted water diffusion. The D-T_2 map is shown in Fig. 22. Around half of the water distribution lies beneath the line indicating the diffusivity of water, and at short relaxation times, the diffusivity starts to drop off even further. This indicates that all the water present experiences severe restriction, either in small pores or between the pore wall and the oil in the pore body, but the smallest pores experience the greatest restriction. The severely restricted water appears near the hydrocarbon correlation line, as observed with the BER2 sample shown in Fig 19. Again, the peak position and broadness seen in the map may also been an artifact, as discussed in the Theory section.

When this carbonate sample undergoes forced imbibition, little new information is revealed. The D- T_2 map is shown in Fig. 23. The water again behaves largely as bulk, with short components alone indicating restricted diffusion. The water in the larger pores relaxes at higher values than in the fully water-saturated sample in Fig. 20, indicating that the effective surface area for water in large pores has been decreased. This would occur either if some of the water exists as droplets in the oil phase, or if some of the large pore surface is oil-wet.

The Y1573 sample shows several features hinted at by the previous sample, but much clearer in this example. Firstly, in the fully water-saturated case shown in Fig. 24, restricted diffusion is clearly visible at shorter T_2s. In the T_2 distribution, shown in Fig. 25, the agreement between the map-produced version and the standard inversion is good until short times. These distributions also make it clear that there are more small pores in this sample than in the Y1312.

After primary drainage, much of the water present in the Y1573 sample experiences severe restriction. The map is shown in Fig. 26. All signal relaxing faster than 100 milliseconds appears below the diffusivity of bulk water. As in the cases of BER2 (Fig, 19) and Y1312 (Fig. 22), a diffusivity peak appears that may be an artifact.

After forced imbibition, the restricted water remains restricted, and most of the oil signal disappears. The D-T_2 map is shown in Fig. 27. The center of the oil distribution has slightly shifted to lower T_2 values, and the amplitude of water above the maximum T_2 of the fully water-saturated sample is higher. This again presents evidence of some mixed wettability in this sample.

NBUR 3

The diffusion time list for this sample was different from the other samples to provide greater information about the higher diffusivity information in the sample. Though the true diffusivity of water does not change regardless of the sample, the measured or effective diffusivity depends upon the static gradient

present. In the presence of an internal gradient, the static gradient experienced will differ from the applied gradient. It has been shown[7] that in a clay-lined rock, there is not a single internal gradient present but in fact a distribution of gradients depending on pore geometry and the nature of the clay present. A diffusion-editing measurement in an internal gradient should provide a diffusivity distribution that corresponds to the distribution of gradients, with some coupling of the peaks to account for spins moving through areas with different static gradients. In any case, this result should be extremely useful in developing a better understanding of how internal gradients exist inside a rock sample.

Fig. 28 shows the D-T_2 map for the NBUR3 sample, fully water-saturated. Most of the signal occurs above the line indicating the diffusivity of water, indicating that the internal gradients are indeed very strong. The lower, higher amplitude peak shows that the gradients increase as the pore size decreases. This is to be expected, as the smaller pores might occur between or around the clay flakes that provide the internal gradients. There is some unexpected data at very high gradients, however, an order of magnitude above that of the larger peak. It is not clear how this peak should be interpreted, but one possibility is proposed considering results obtained by Zhang[8]. This peak might correspond to the spins near the corner of the clay flakes, where the internal field gradients reach very high values in a small area. More measurements would be necessary to better understand this phenomenon, including some measurements where the larger pores would be filled with crude or refined oil, eliminating communication between small and large pores.

Fig. 29 shows the relaxation distribution comparisons for the fully water-saturated NBUR3 sample. For this sample, a large portion of the amplitude falls below the truncation point of 35 ms. This fast-relaxing contribution is not unexpected in a high internal gradient, where the clay particles that contribute to internal gradients also increase the paramagnetic ions concentration at the surface of the pore, and thus increase surface relaxation.

BER3

The D-T_2 map for the fully water-saturated BER3 sample is shown in Fig. 30. Restricted diffusion is evident at short relaxation times, and there is some evidence of internal gradients as well. The D-T_2 for the air de-saturated sample is shown in Fig. 31. In this case, prominent internal gradients and strong restricted diffusion are visible for short relaxation times. The interpretation here is as for the previous Berea sandstone, but without interference from the presence of oil. Restricted diffusion is probably occurring in the kaolinite clay-filled pores, while internal gradients dominate illite clay-filled pores. The effect for both is increased due to the absence of diffusive coupling with larger pores, as those pores no longer contain water. In the air de-saturated system, the non-wetting fluid does not have any NMR signal, so all the measured signal is clearly due to water. This provides confirmation for the interpretation of BER2 above.

The air de-saturated BER3 sample is also useful for examining some of the artifacts that can arise from the DE inversion. The full echo train for this data set is shown in Fig. 32. If the last five data sets from the DE suite for this sample are removed before processing, the resulting D-T_2 map is shown in Fig. 33. The diffusivity distribution has stretched to very low values. Contrast this to the case with the BEN3 sample fully water-saturated, where no such stretching artifact is observed, using a similar maximum TEL. The echo train for the BEN3 sample is shown in Fig. 34, with the D-T_2 map with six data sets removed shown in Fig. 35. The reason for this is that the BEN3 sample contains no slow-diffusing components, and thus enough attenuation occurs, even with a maximum TEL of only 12.4 seconds, to fully characterize the diffusivites of all components of the system. With the BER3 air de-saturated sample, there are more slow-diffusing components, and when the data suite is reduced, not enough diffusion information is available to characterize the slow-diffusing components. The result of this missing data is the broadening of the diffusion distributions seen in Fig. 33. This same effect may explain low-diffusivity peaks present in Fig. 19, Fig. 22, Fig. 24, Fig. 26, and Fig. 27.

Conclusions

The data sets presented in this report present some of the first experiments involving the DE sequence and core samples saturated with real crude oils. In water-saturated samples as well as bulk fluids, the T_2 information obtained from the D-T_2 map agrees well with standard T_2 inversions, while the diffusion information was previously unavailable in any form. The agreement between DE-based and standard inversion relaxation distributions breaks down at short relaxation times, where the DE inversion truncates data below that happens before the second echo of the longest TEL. It is therefore desirable to minimize the TEL. If the longest TEL is too short, however, and not enough sensitivity to low diffusion components is available, artifacts are developed. A balance must be established between fast relaxing components and slow diffusing components to allow artifact-free development of clear D-T_2 maps.

The benefit of clear, easily interpreted D-T_2 maps for partially saturated rocks should be obvious – saturation, oil viscosity, and wettability changes can all be successfully evaluated. In single fluid-saturated sample, there are other petrophysical details that can be interpreted – restricted diffusion and internal gradient effects. As consistent interpretation for the D-T_2 continues to develop, a new, more comprehensive interpretation for NMR well logging data will become available.

Future Work

There is work left to be done determining a method of balancing the diffusion sensitivity with the acquisition of short T_2 information. A weighting function should be developed to combine multiple data sets or inversion of the same data set to balance the maximum possible region of accurate data. More importantly, a method for indicating where the limitations of the inversion are affecting interpretation must be developed. In particular, the effects of regularization artifacts ans signal/noise requirements for a robust inversion need to be recognized.

References

1. Freedman, R. *et al.*: "A New Method of Fluid Characterization in Reservoir Rocks: Experimental Confirmation and Simulation Results" *SPE Journal* (December 2001)
2. Freedman, R., Heaton, N., and Flaum, M.: "Field Applications of a New Nuclear Magnetic Resonance Fluid Characterization Method" SPE paper 71713, presented at 2001 SPE Annual Technical Conference and Exhibition.
3 Freedman, R. *et al.*: "Wettability, Saturation, and Viscosity Using the Magnetic Resonance Fluid Characterization Method and New Diffusion-Editing Pulse Sequences" SPE paper 77397, submitted to 2002 SPE Annual Technical Conference and Exhibition.
4. Hürlimann M. D. *et al.*: "Diffusion-Editing: New NMR Measurement of Saturation and Pore Geometry," paper presented at the 2002 Annual Meeting of the Society of Professional Well Log Analysts, Oiso, Japan, June 2-5 2002.
5. Hurlimann, M. D., and Venkataramanan, L.: "Quantitative Measurement of two dimensional Distribution Functions of Diffusion and Relaxation in grossly Inhomogeneous Fields," submitted to *Journal of Magnetic Resonance*
6. Mills, R.: "Self-diffusion in Normal and Heavy Water in the Range 1-45°," *Journal of Physical Chemistry*, Vol 77, No. 5, 1973
7 Zhang, Q., Huang, C. C., Hirasaki, G. J.: "Interpretation of Wettability in Sandstones," *Petrophysics*, Vol. 41 No 3 (May-June 2000)
8. Zhang, Q., Hirasaki, G.J., House, W. V.: "Effect of Internal Field Gradients on Porous Media," *Petrophysics*, 42, No. 1 (Jan-Feb 2001)
9. Lo, S.-W. et al: "Mixing Rules and Correlations of NMR Relaxation Time with Viscosity, Diffusivity, and Gas/Oil Ratio of Methane/Hydrocarbon Mixtures," *SPE Journal* (March 2002)
10. Zhang, Y.: "NMR Relaxation and Diffusion Characterization of Hydrocarbon Gases and Liquids," PhD dissertation, Rice University, Houston (2002)
11. Chuah, T-L.: "Estimation of Relaxation Time Distributions for NMR CPMG Measurements" Masters dissertation, Rice University, Houston (1996)

Table 1: Rock Properties

Sample	Porosity	Permeability (md)
BEN3	23.4	2960
BER2	19.6	205
BER3	19.4	205
NBUR3	24.6	290
Y1312	20.8	137
Y1572	14.2	57

Table 2: Oil Properties

Oil	API Grav	Density	% asph	% resin	% arom	% sat	Visc.
North Sea	33.2	.856	0.0	7.9	24.9	67.1	9.4
SMY	30.3	.892	5.5	12.5	51.5	30.6	20.9
Nova Plus	-		-	-	-	-	3.20
Hexane	-	0.66	-	-	-	-	0.31

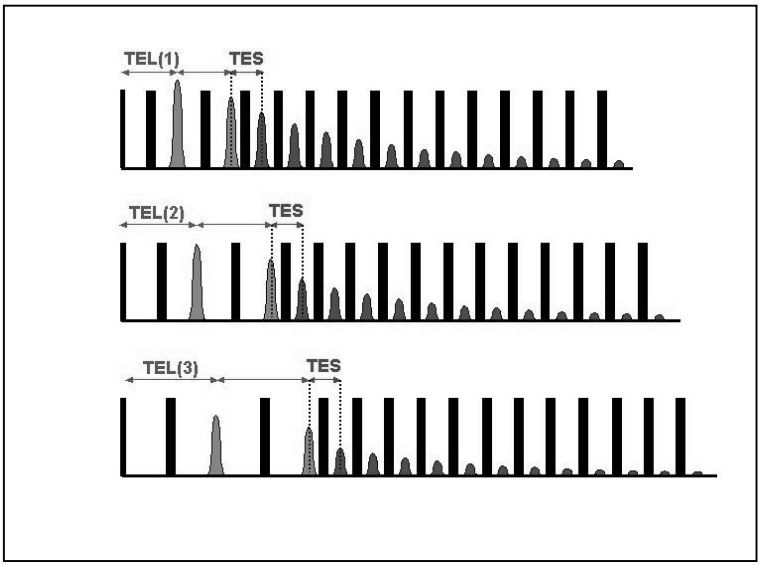

Figure 1: Diagram of DE Pulse Sequence. TEL represents the long echo spacing varied to obtained diffusion information. TES represents the short echo spacing minimizes the gradient effects on T2.

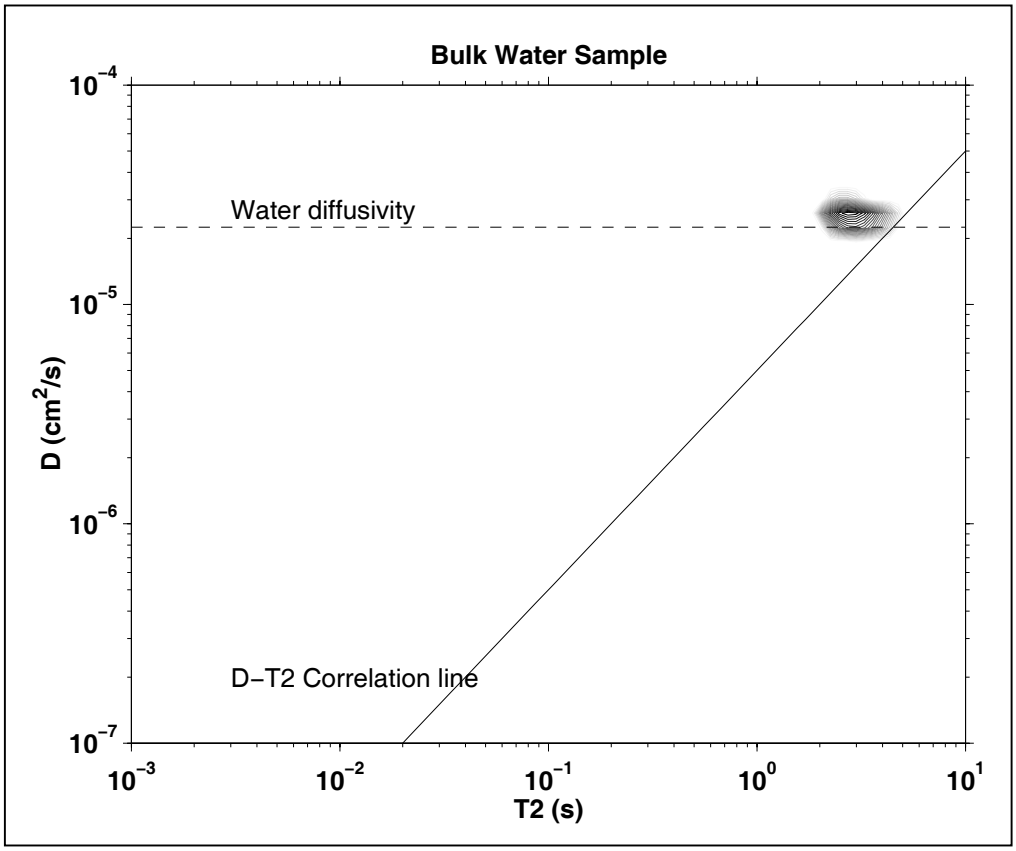

Figure 2: *D- T_2* map of bulk water sample. Relaxation data is truncated below 120 ms.

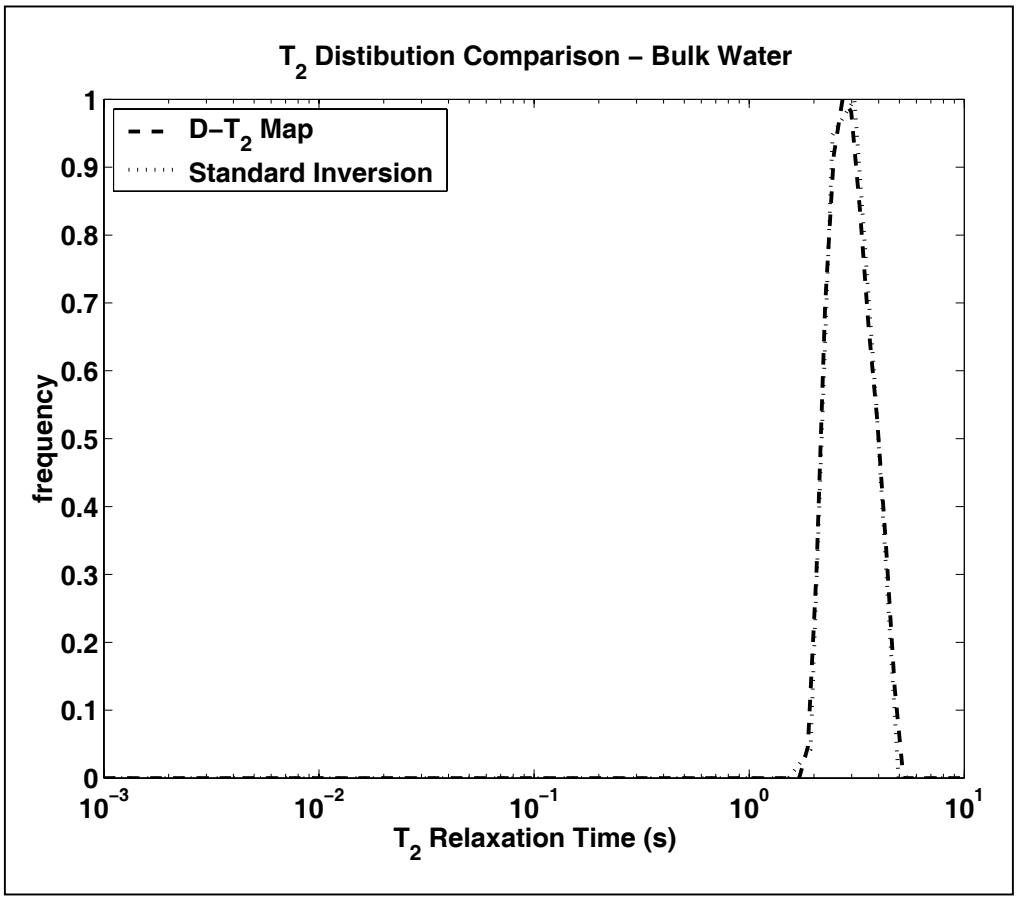

Figure 3: *T_2* distributions of bulk water sample. Relaxation from map data is truncated below 120 ms.

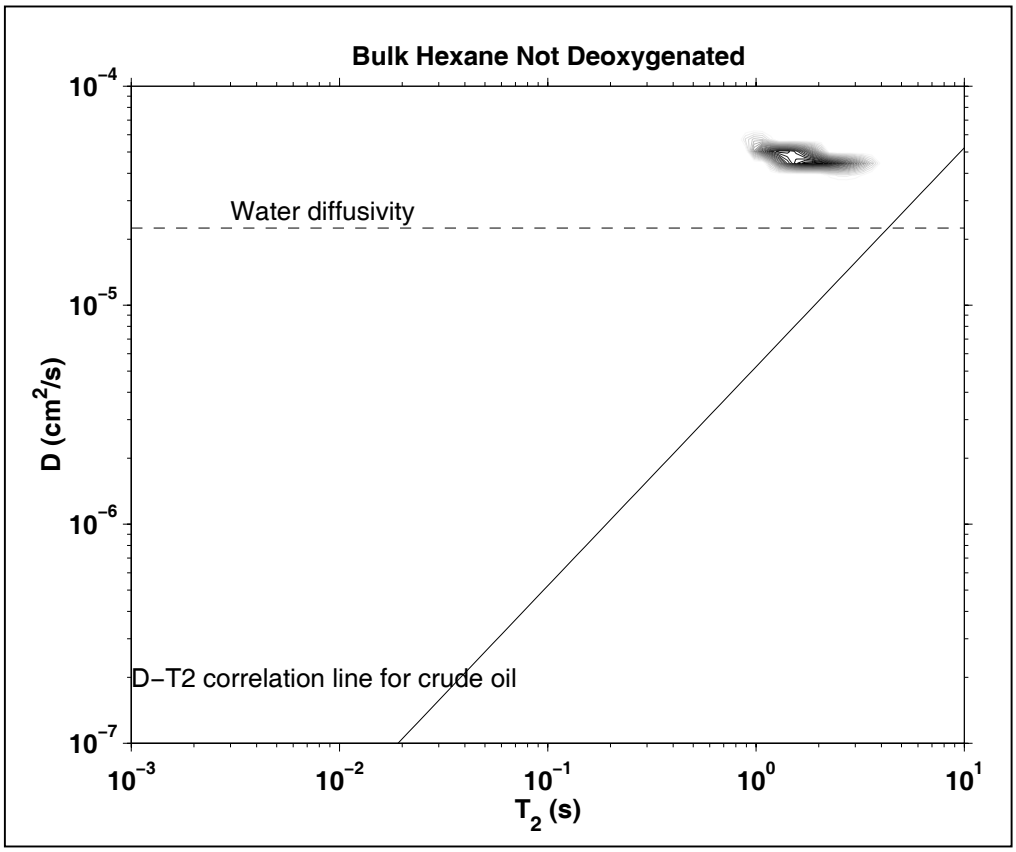

Figure 4: *D- T_2* map of bulk hexane. Relaxation data is truncated below 120 ms.

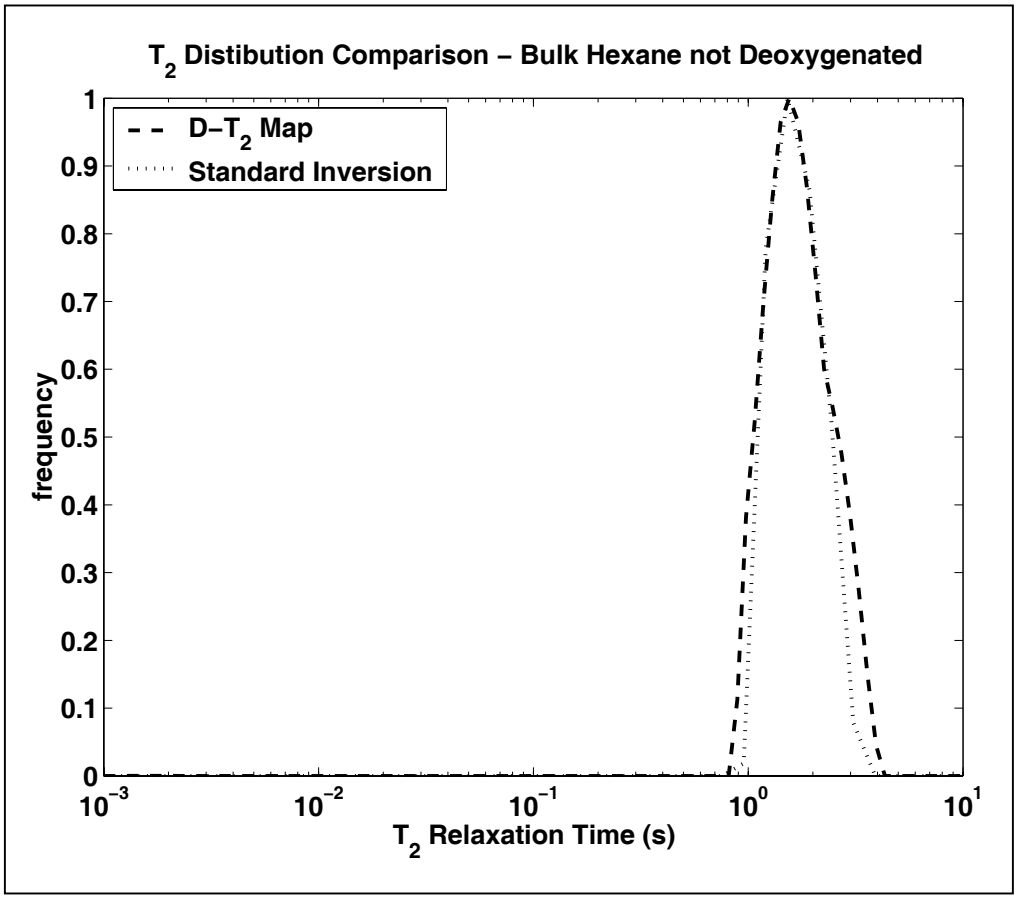

Figure 5: T_2 distributions of bulk hexane sample. Relaxation from map data is truncated below 120 ms.

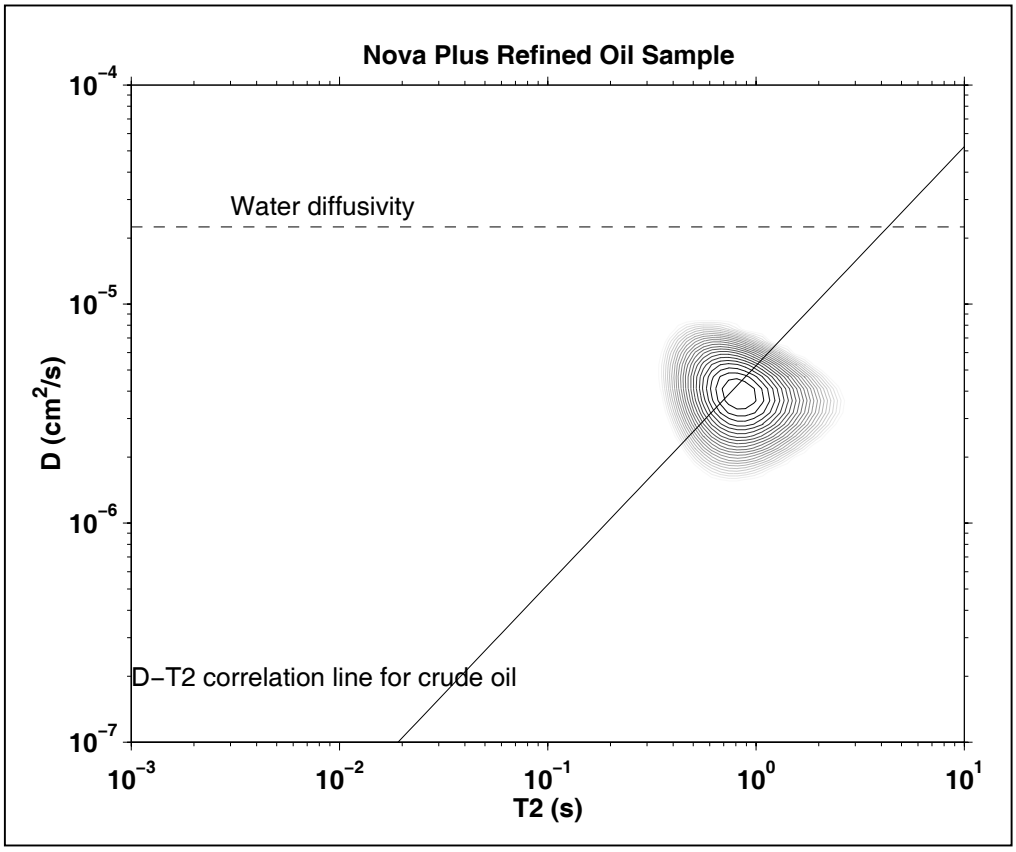

Figure 6: *D- T_2* map of bulk Nova Plus refined oil sample. Relaxation data is truncated below 120 ms.

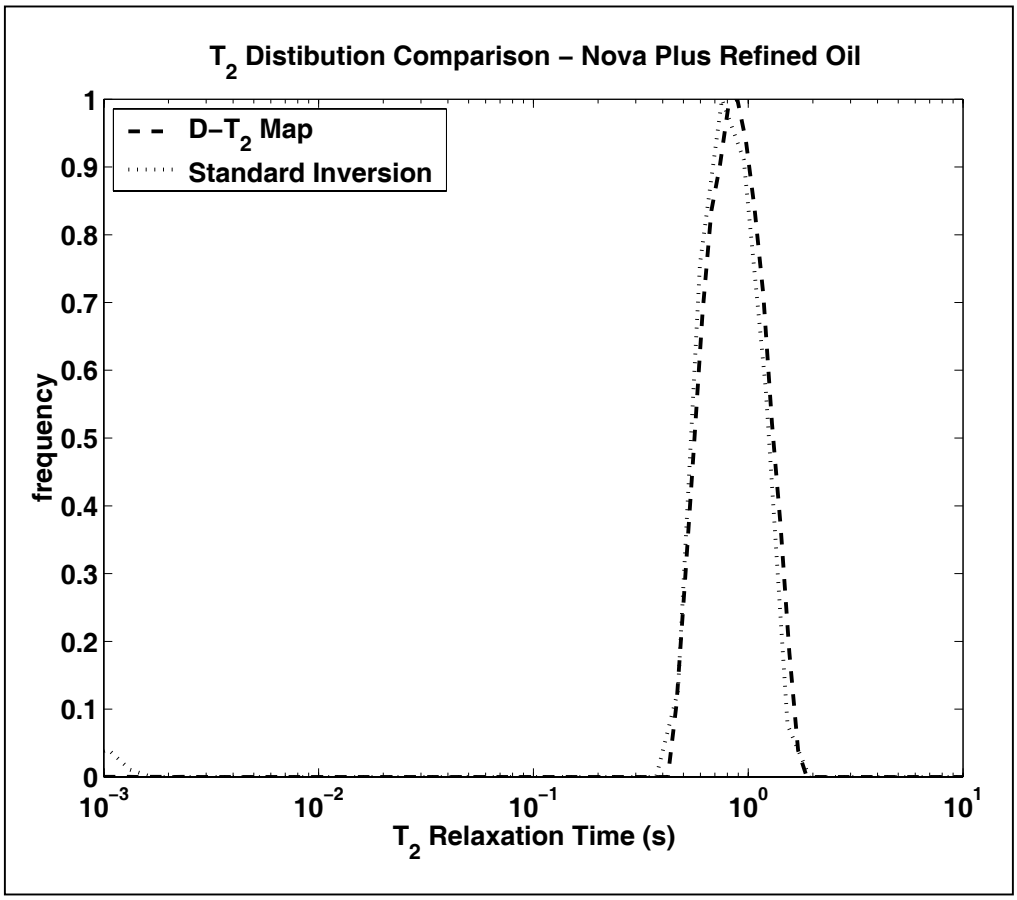

Figure 7: T_2 distributions of bulk Nova Plus refined oil sample. Relaxation from map data is truncated below 120 ms.

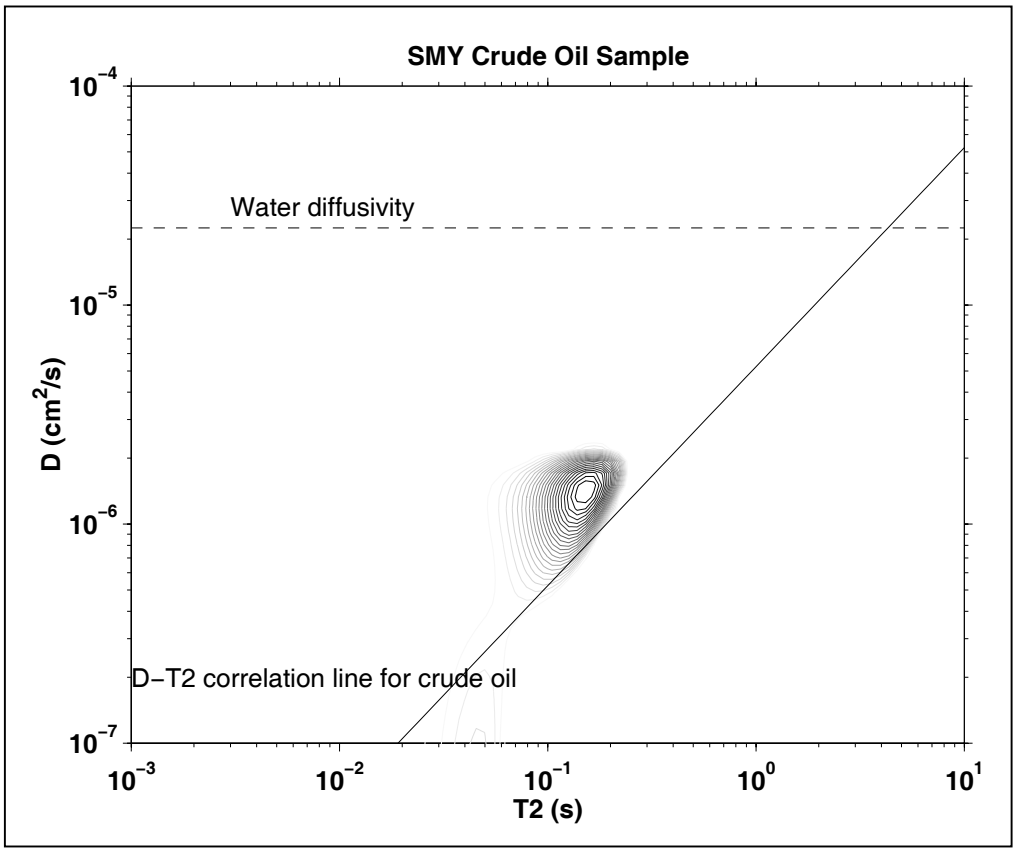

Figure 8: *D- T_2* map of bulk SMY crude oil sample. Relaxation data is truncated below 120 ms.

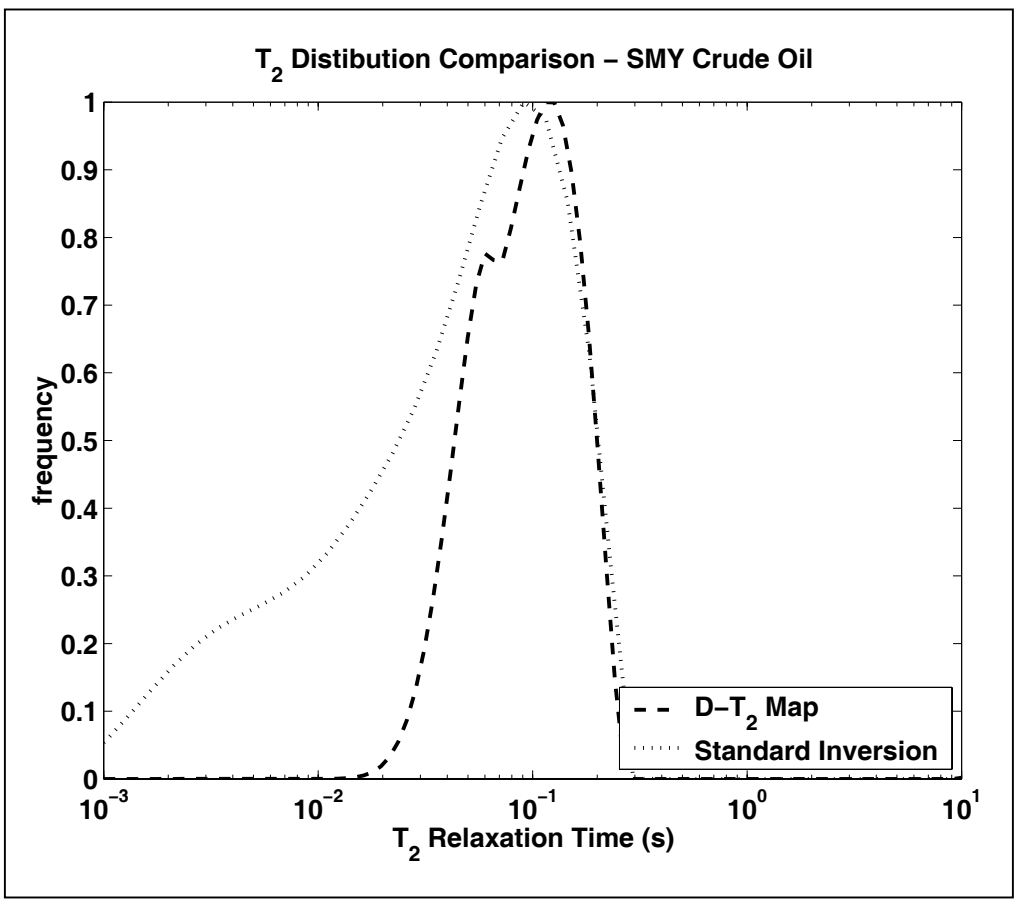

Figure 9: T_2 distributions of bulk SMY crude oil sample. Relaxation from map data is truncated below 120 ms.

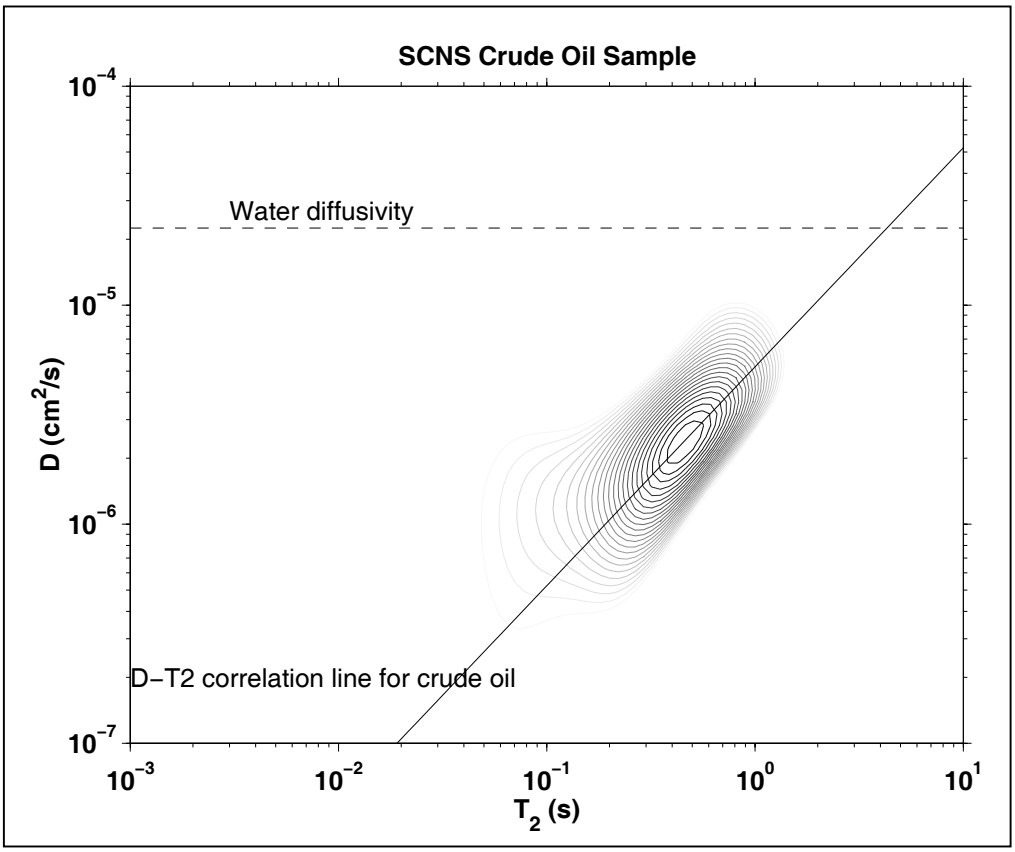

Figure 10: *D*- T_2 map of bulk SCNS crude oil sample. Relaxation data is truncated below 78.8 ms.

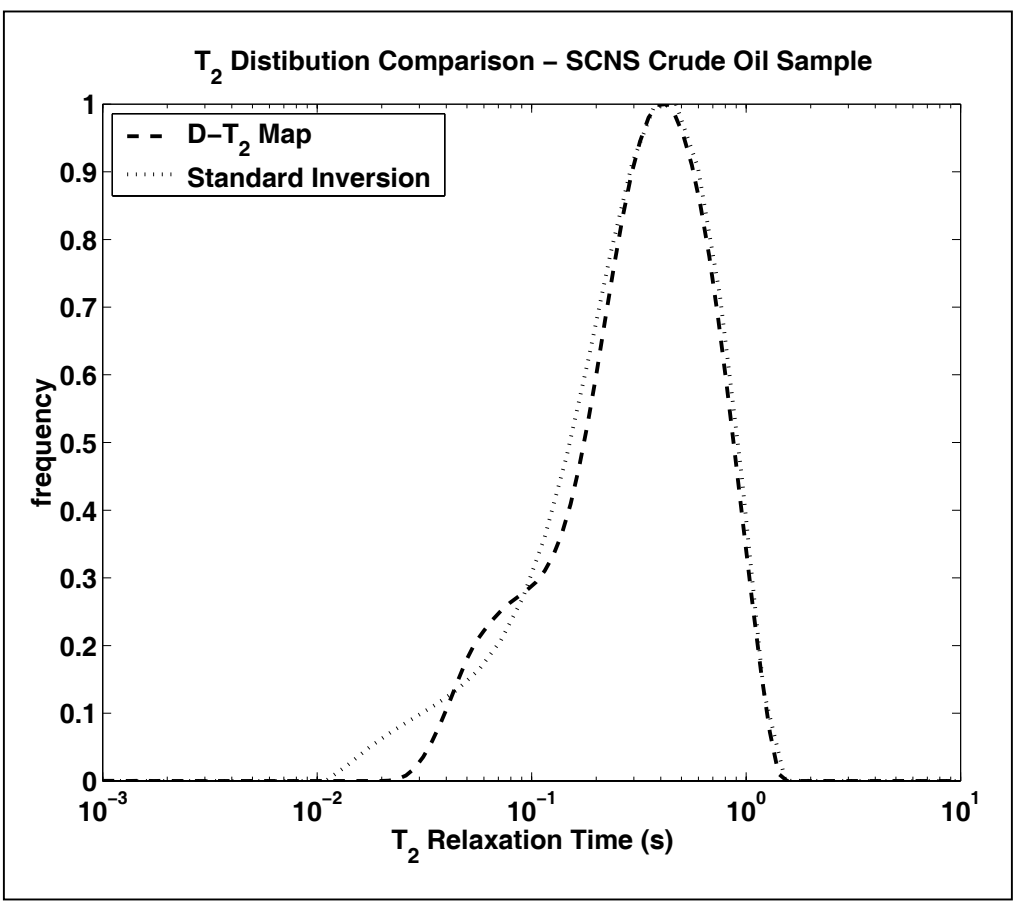

Figure 11: T_2 distributions of bulk SCNS crude oil sample. Relaxation from map data is truncated below 78.8 ms.

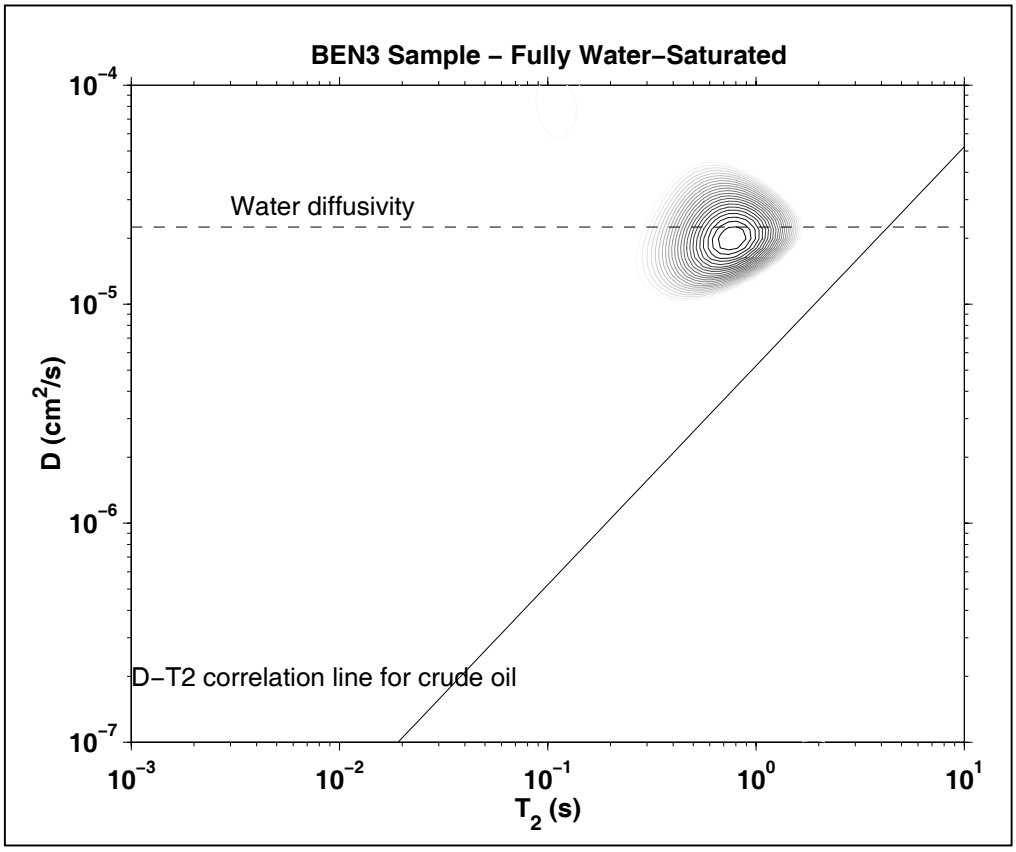

Figure 12: *D- T_2* map of BEN 3 sample, fully water-saturated. Relaxation data is truncated below 78.8 ms.

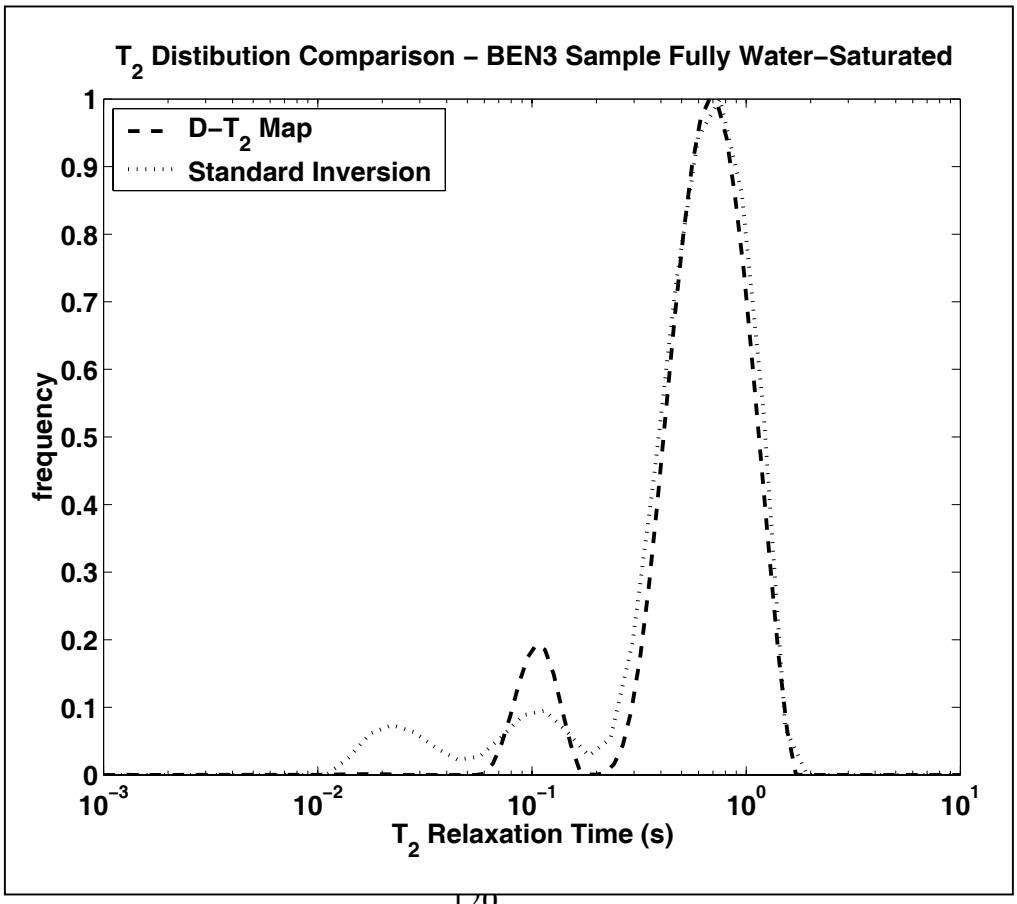

Figure 13: T_2 distributions of BEN 3 sample, fully water-saturated. Relaxation from map data is truncated below 78.8 ms.

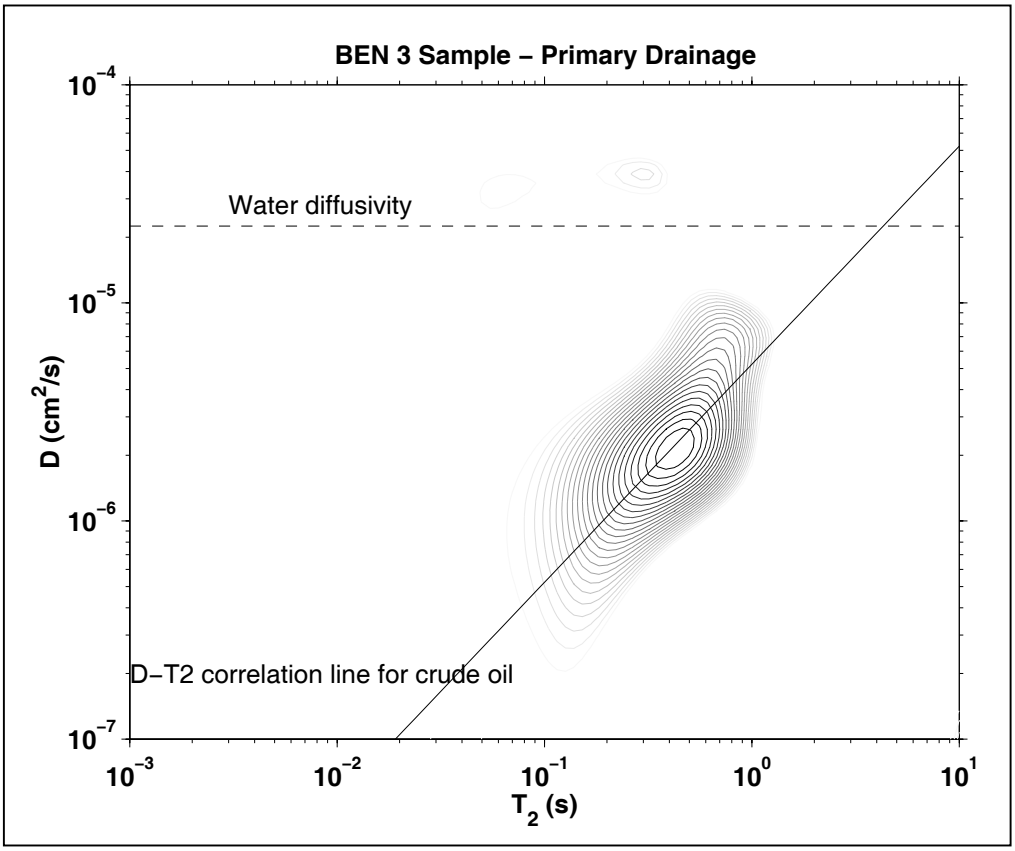

Figure 14: *D*- T_2 map of BEN 3 sample, after primary drainage. S_o is approximately 0.95. Relaxation data is truncated below 78.8 ms.

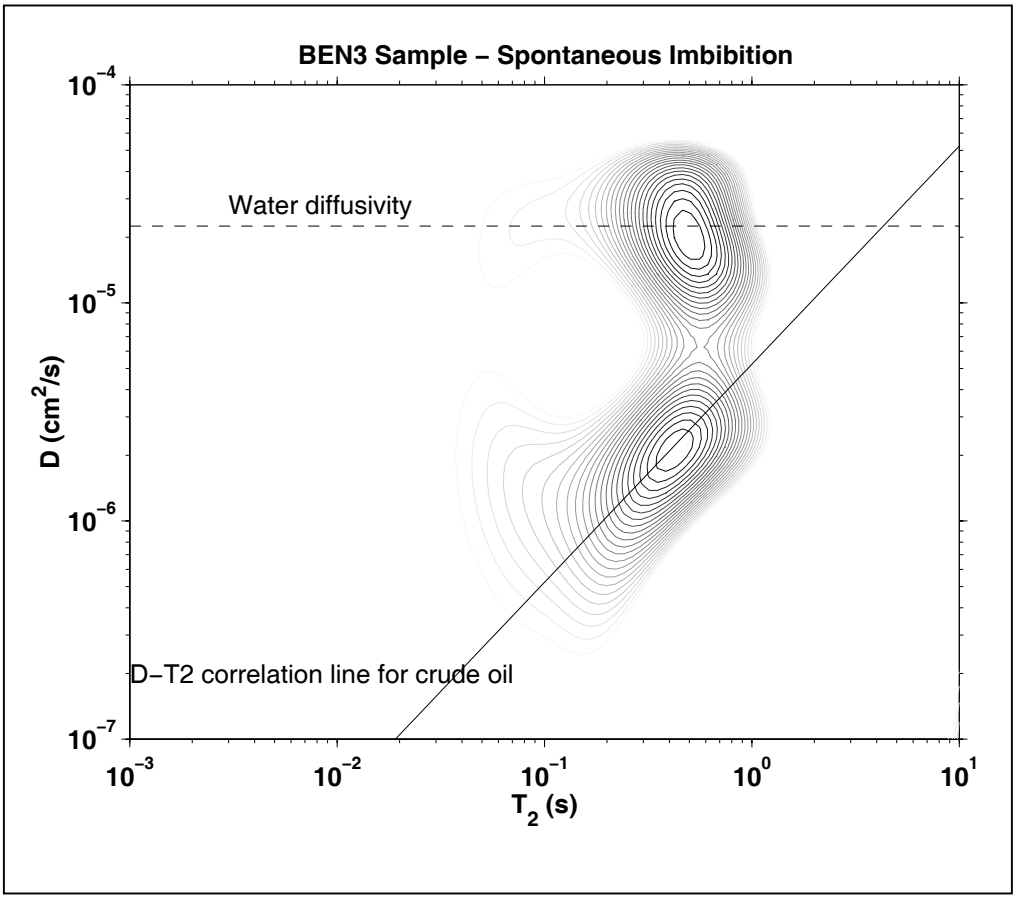

Figure 15: *D*- T_2 map of BEN 3 sample, after spontaneous imbibition. S_o is approximately 0.57. Relaxation data is truncated below 78.8 ms.

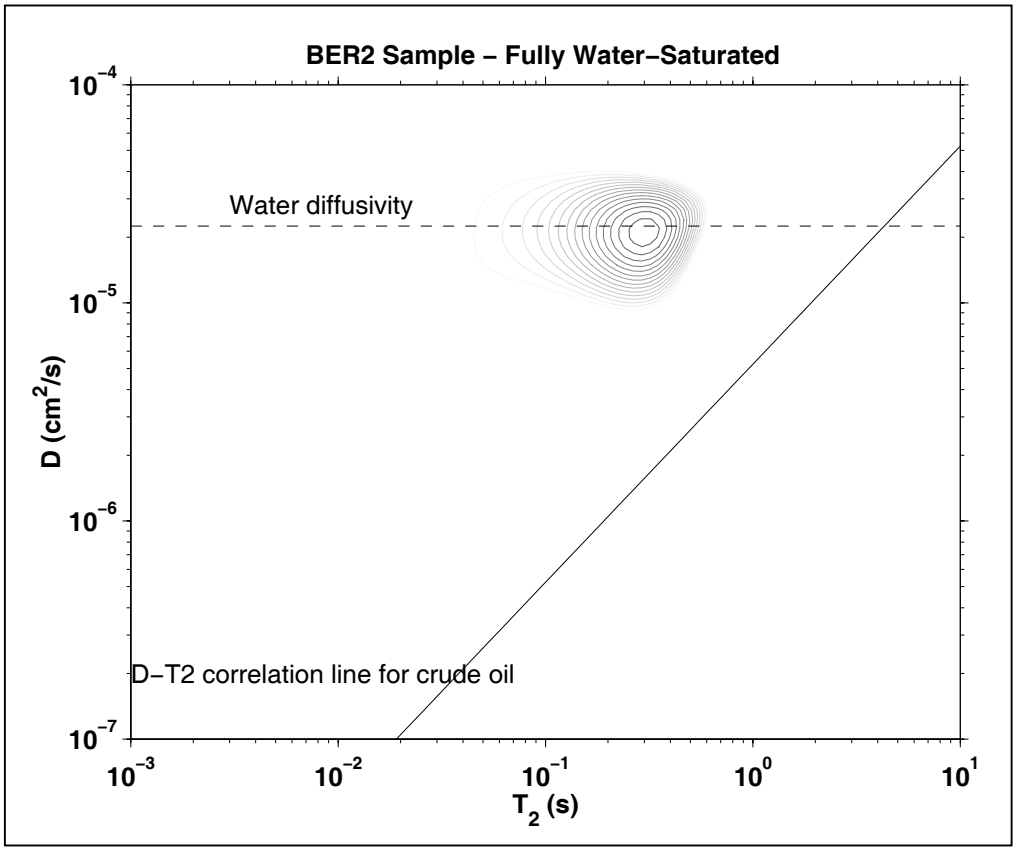

Figure 16: *D- T_2* map of BER 2 sample, fully water-saturated. Relaxation data is truncated below 78.8 ms.

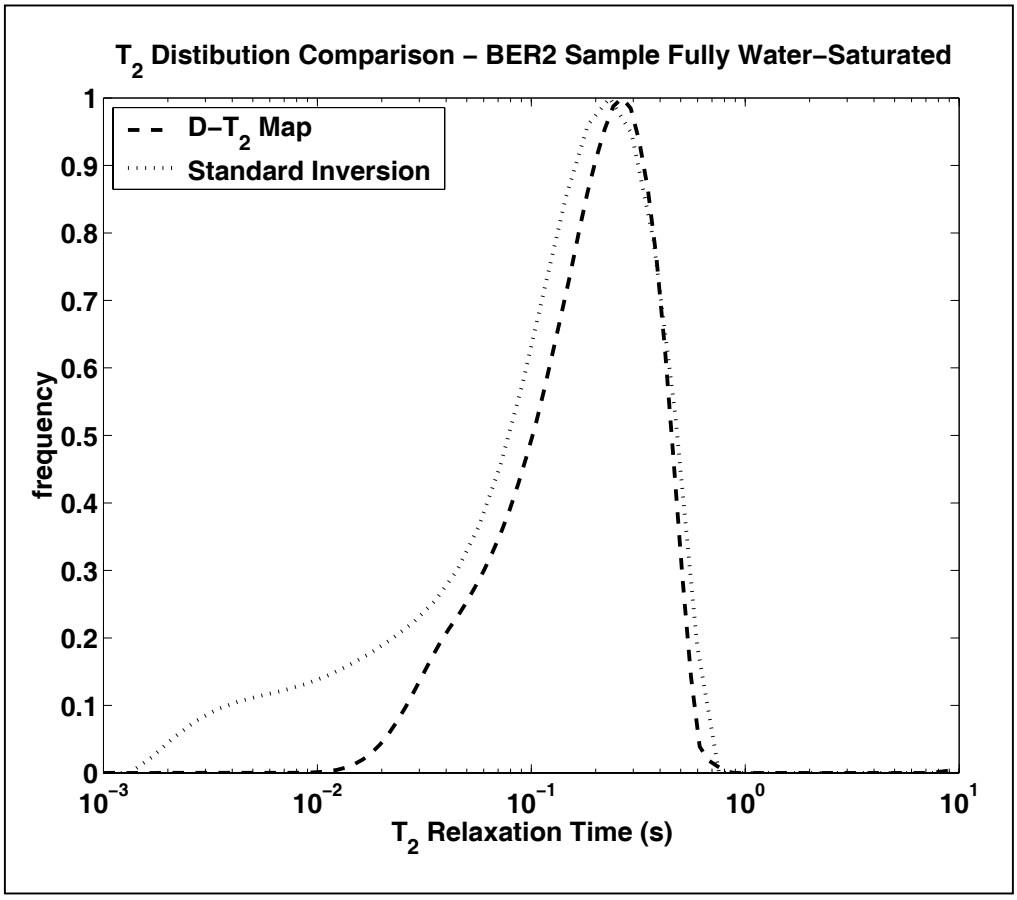

Figure 17: T_2 distributions of BER 2 sample, fully water-saturated. Relaxation from map data is truncated below 78.8 ms.

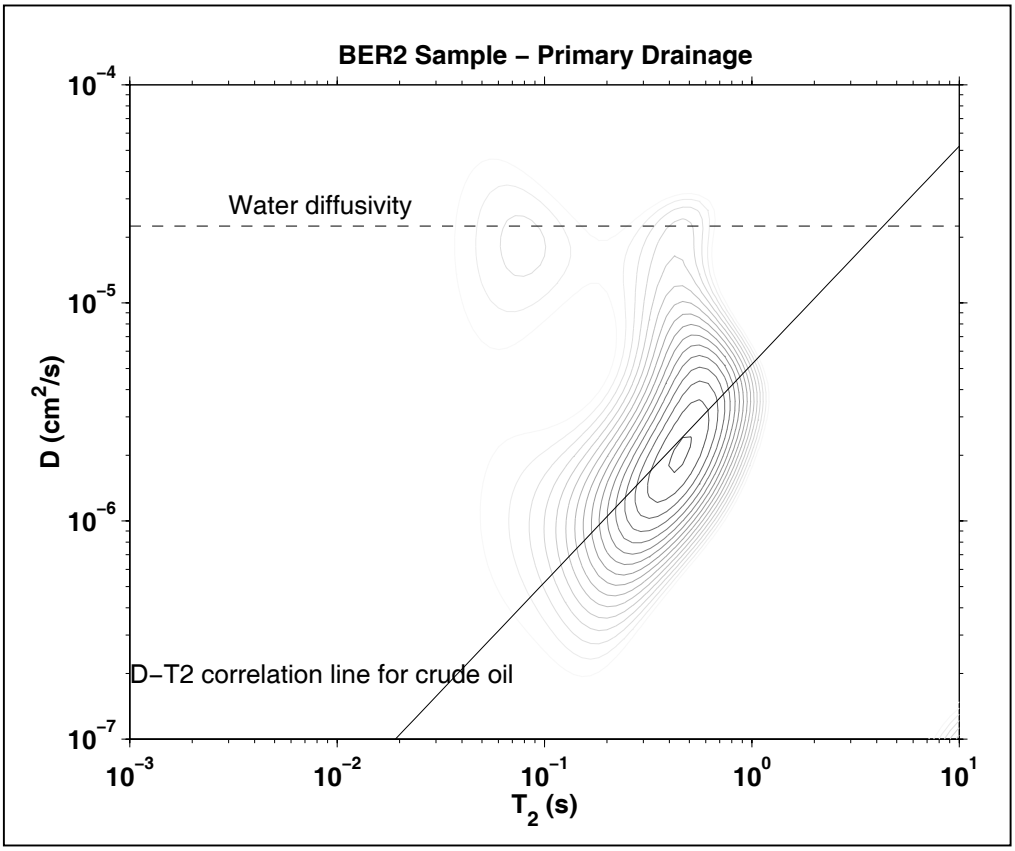

Figure 18: *D- T_2* map of BER 2 sample, after primary drainage. S_o is approximately 0.79. Relaxation data is truncated below 78.8 ms.

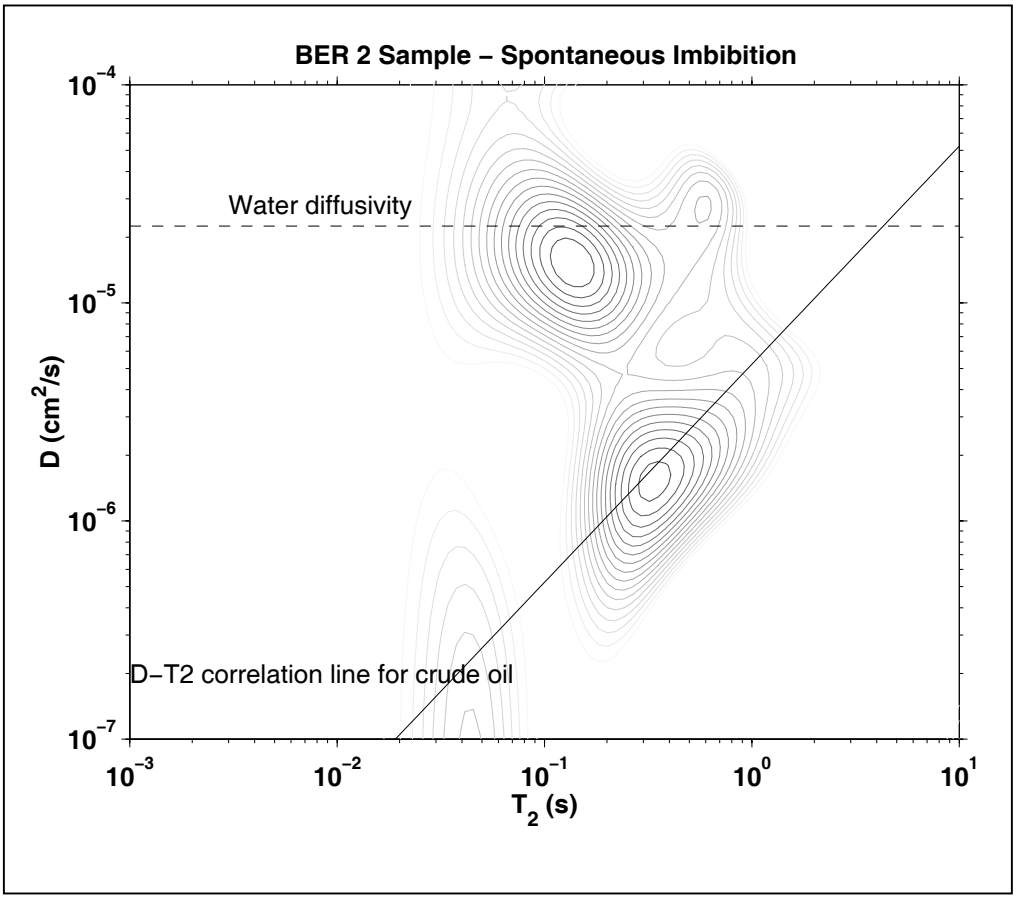

Figure 19: *D- T_2* map of BER 2 sample, after spontaneous imbibition. S_o is approximately 0.46. Relaxation data is truncated below 78.8 ms.

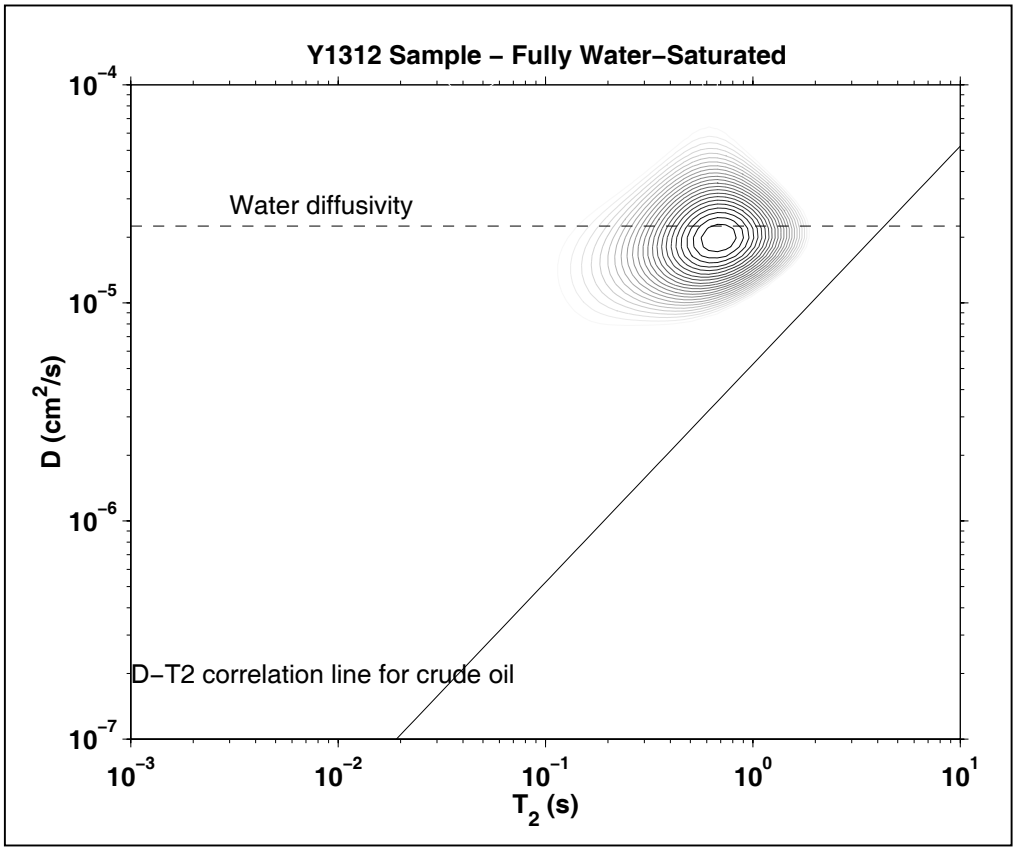

Figure 20: *D- T_2* map of Y1312 sample, fully water-saturated. Relaxation data is truncated below 78.8 ms.

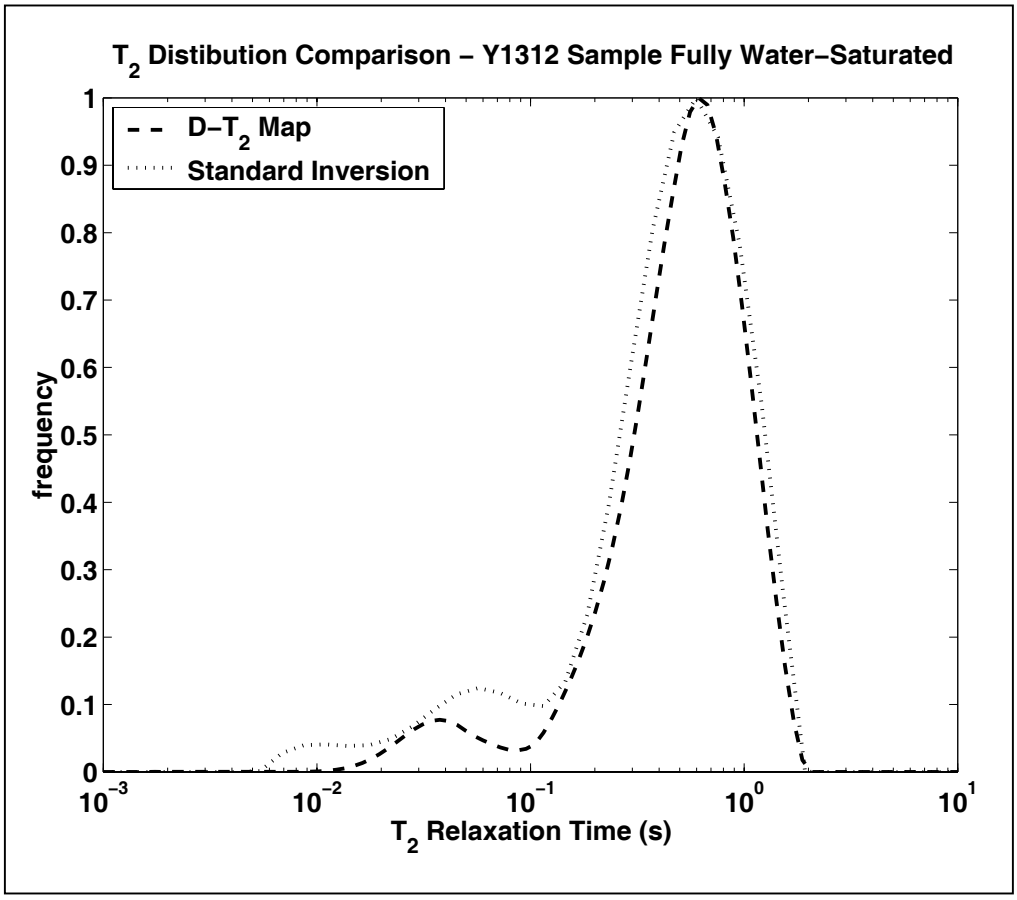

Figure 21: T_2 distributions of Y1312 sample, fully water-saturated. Relaxation from map data is truncated below 78.8 ms.

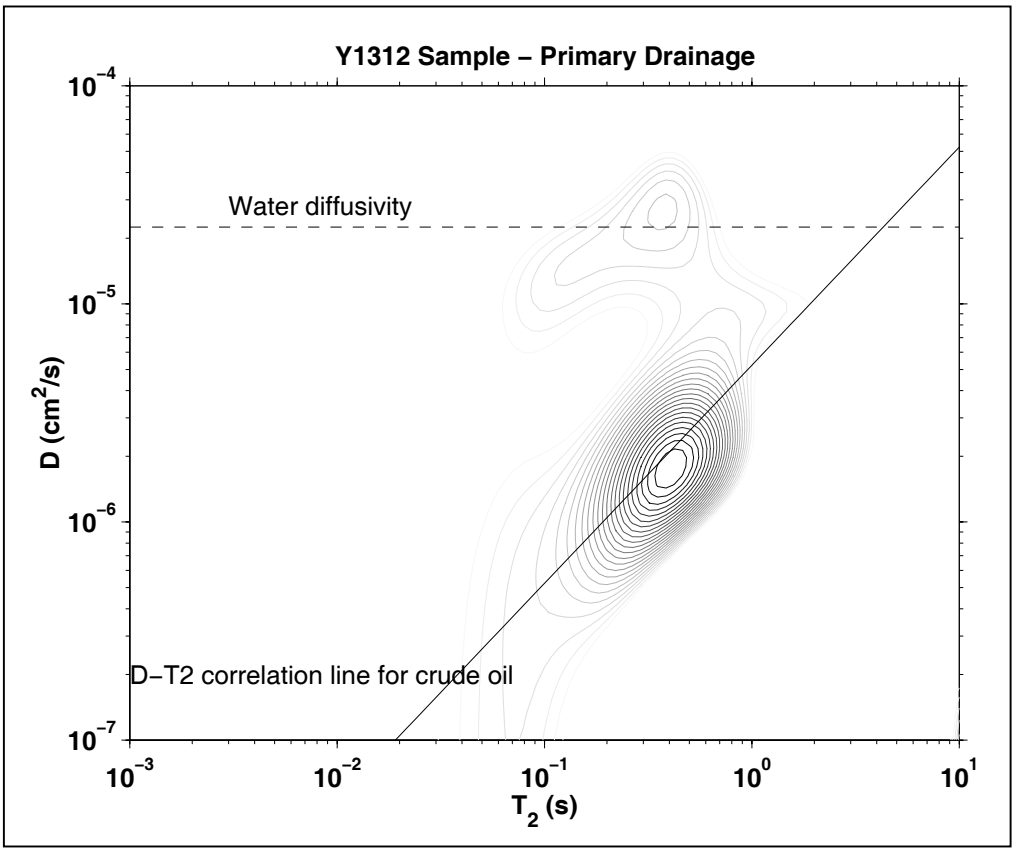

Figure 22: *D*- T_2 map of Y1312 sample, after primary drainage. S_o is approximately 0.86. Relaxation data is truncated below 78.8 ms.

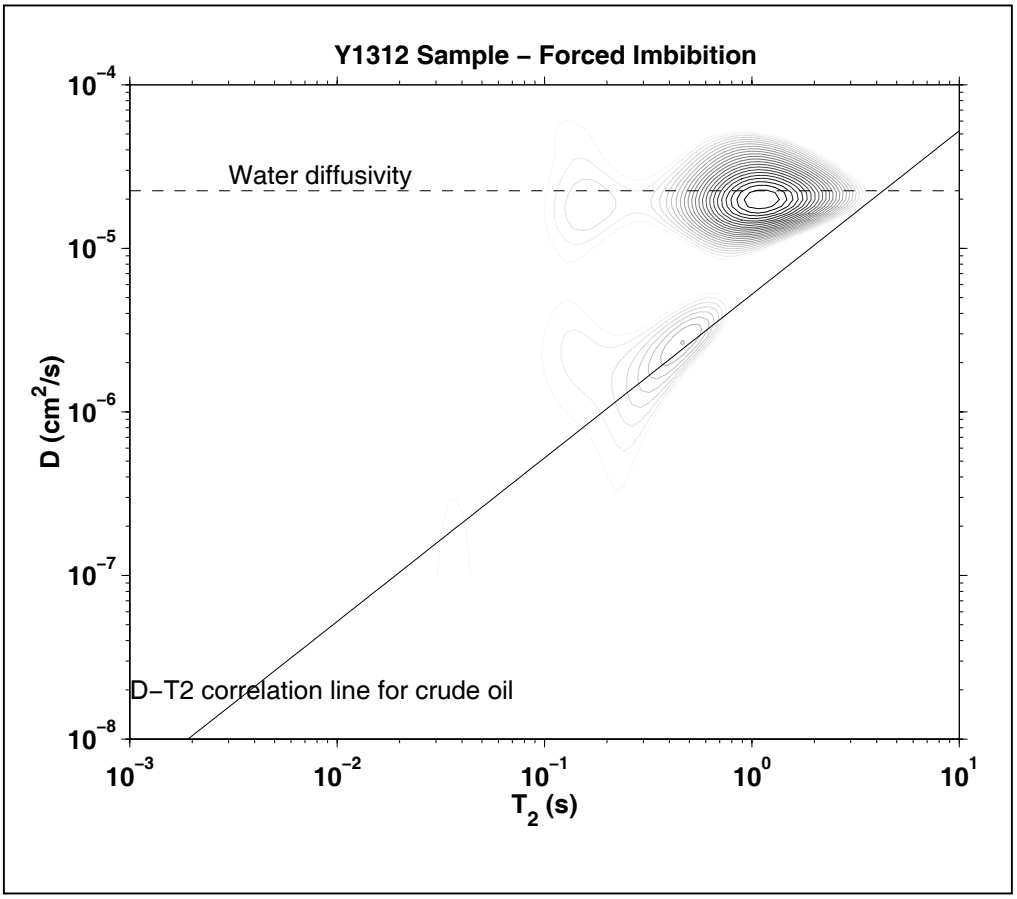

Figure 23: *D*- T_2 map of Y1312 sample, after forced imbibition. S_o is approximately 0.37. Relaxation data is truncated below 78.8 ms.

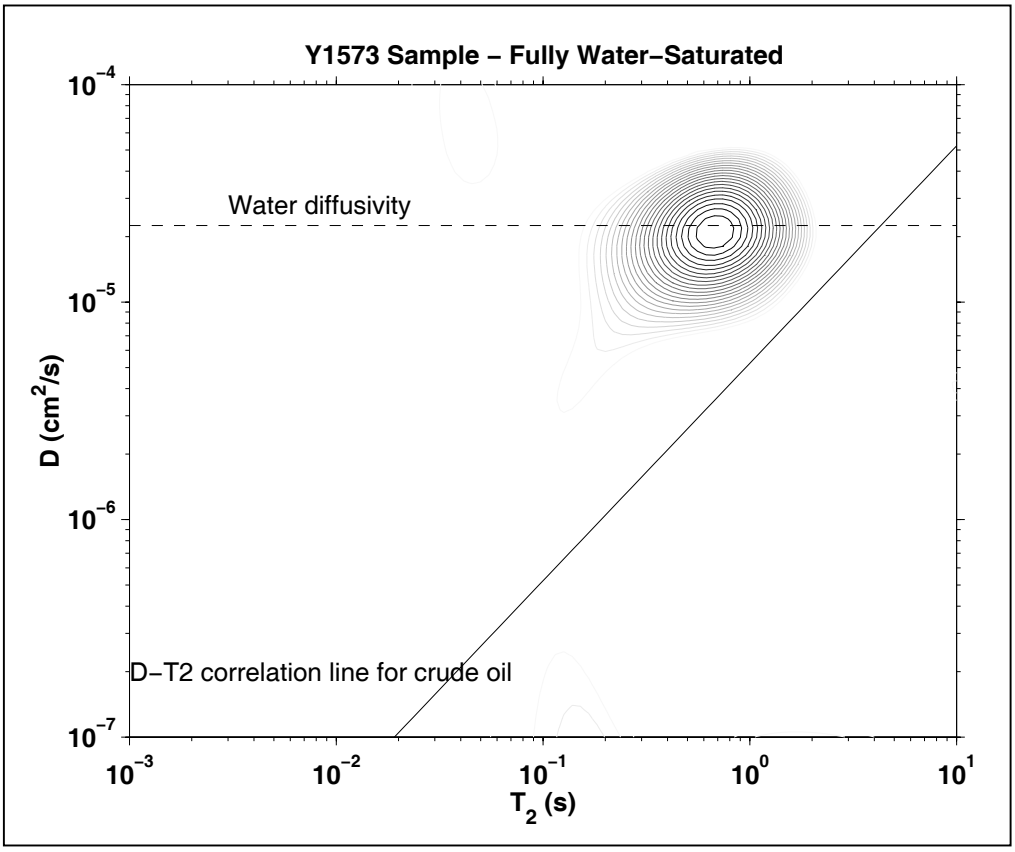

Figure 24: *D- T_2* map of Y1573 sample, fully water-saturated. Relaxation data is truncated below 78.8 ms.

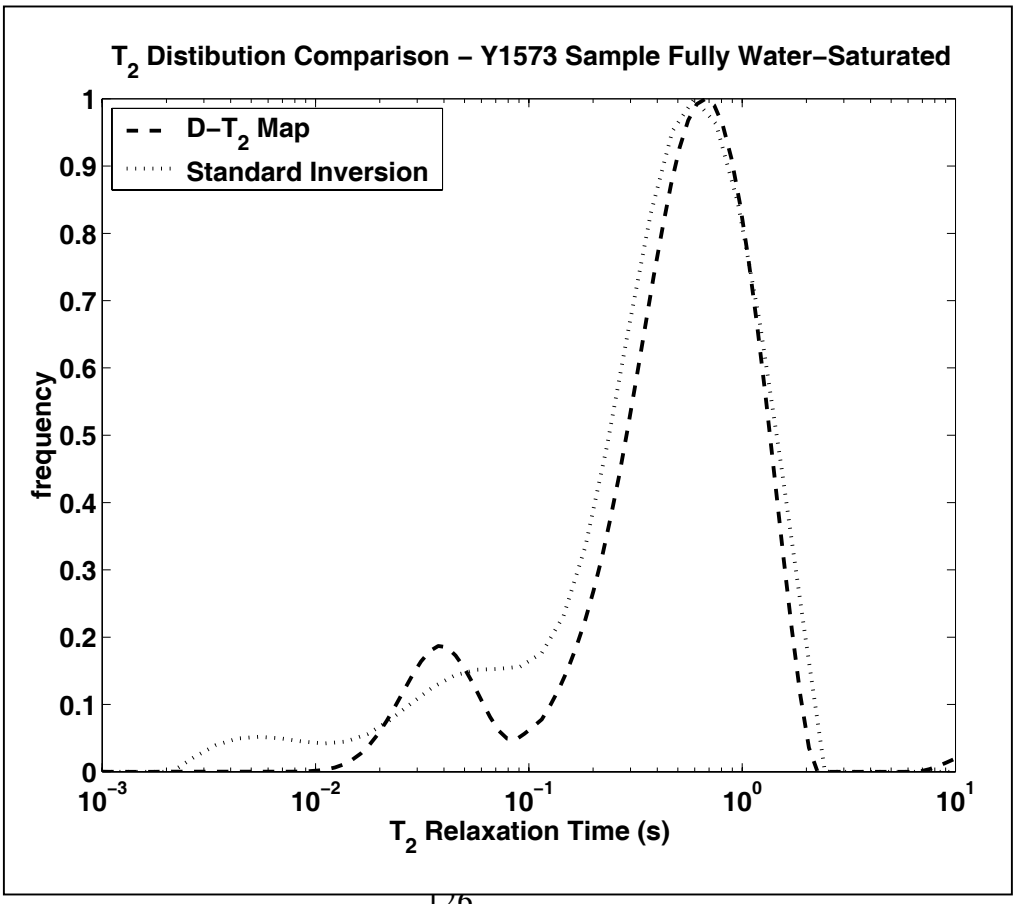

Figure 25: T_2 distributions of Y1573 sample, fully water-saturated. Relaxation data is truncated below 78.8 ms.

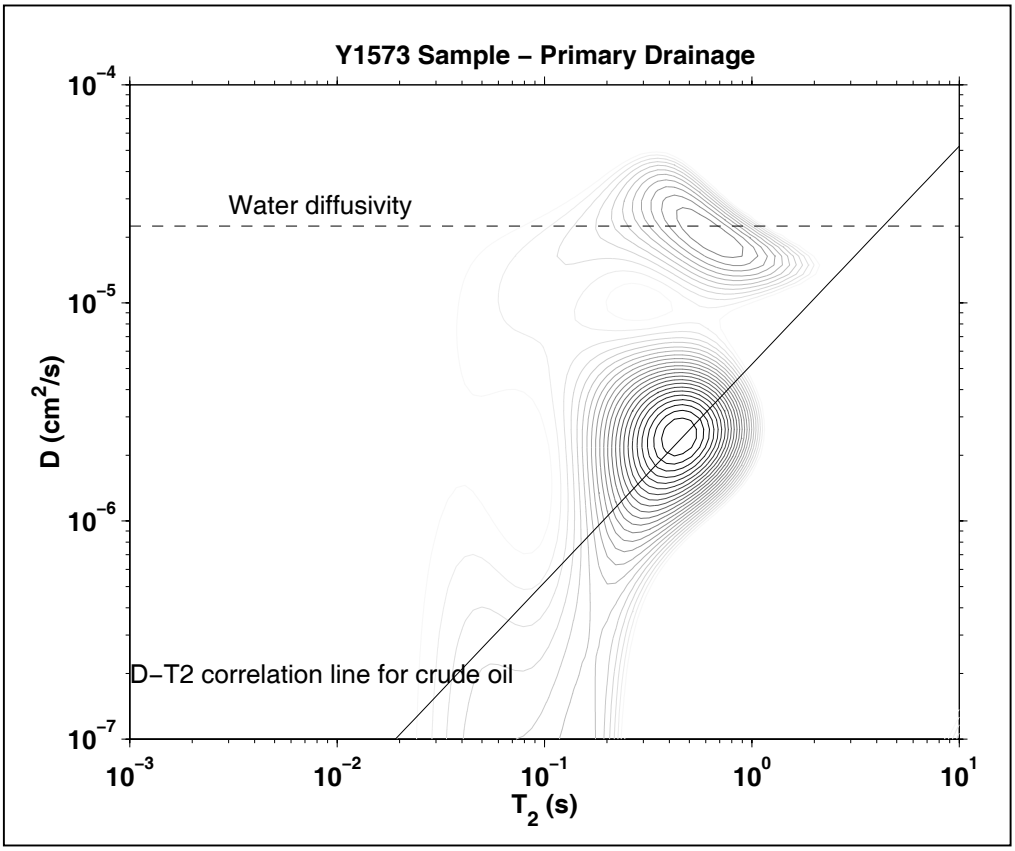

Figure 26: *D- T_2* map of Y1573 sample, after primary drainage. S_o is approximately 0.81. Relaxation data is truncated below 78.8 ms.

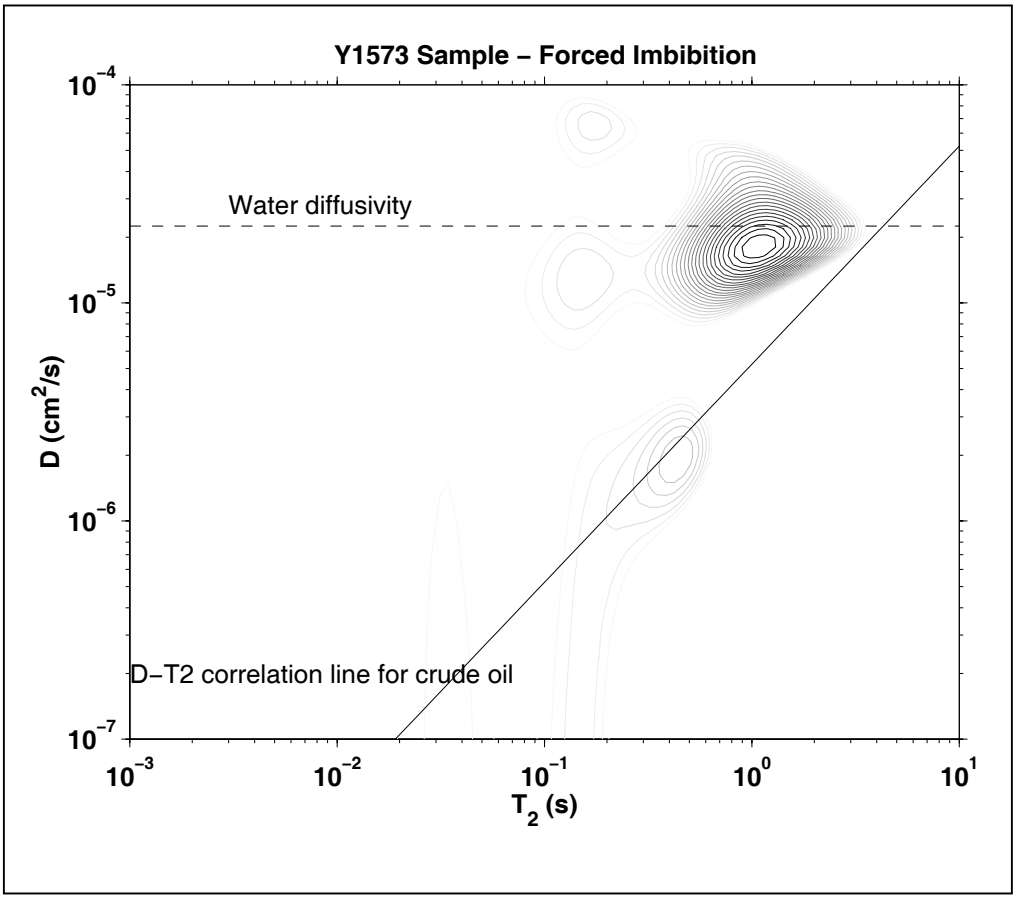

Figure 27: *D- T_2* map of Y1573 sample, after forced imbibition. S_o is approximately 0.33. Relaxation data is truncated below 78.8 ms.

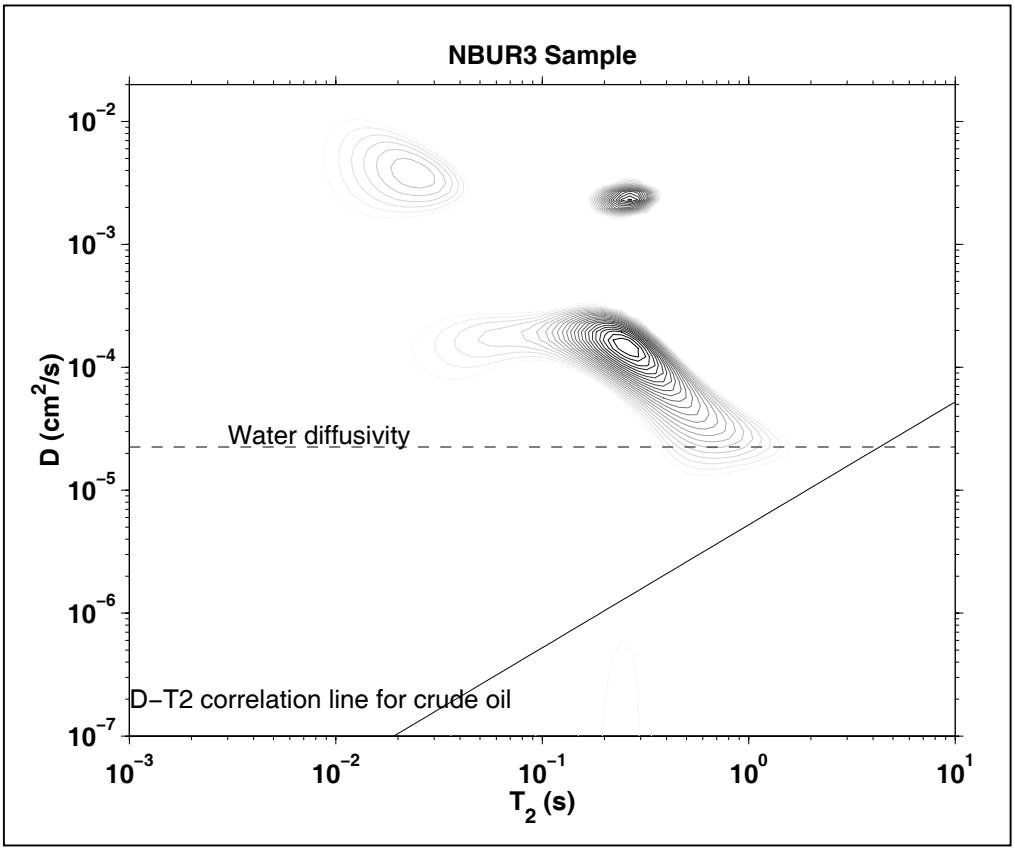

Figure 28: *D- T_2* map of NBUR3 sample. Relaxation data is truncated below 35.2 ms.

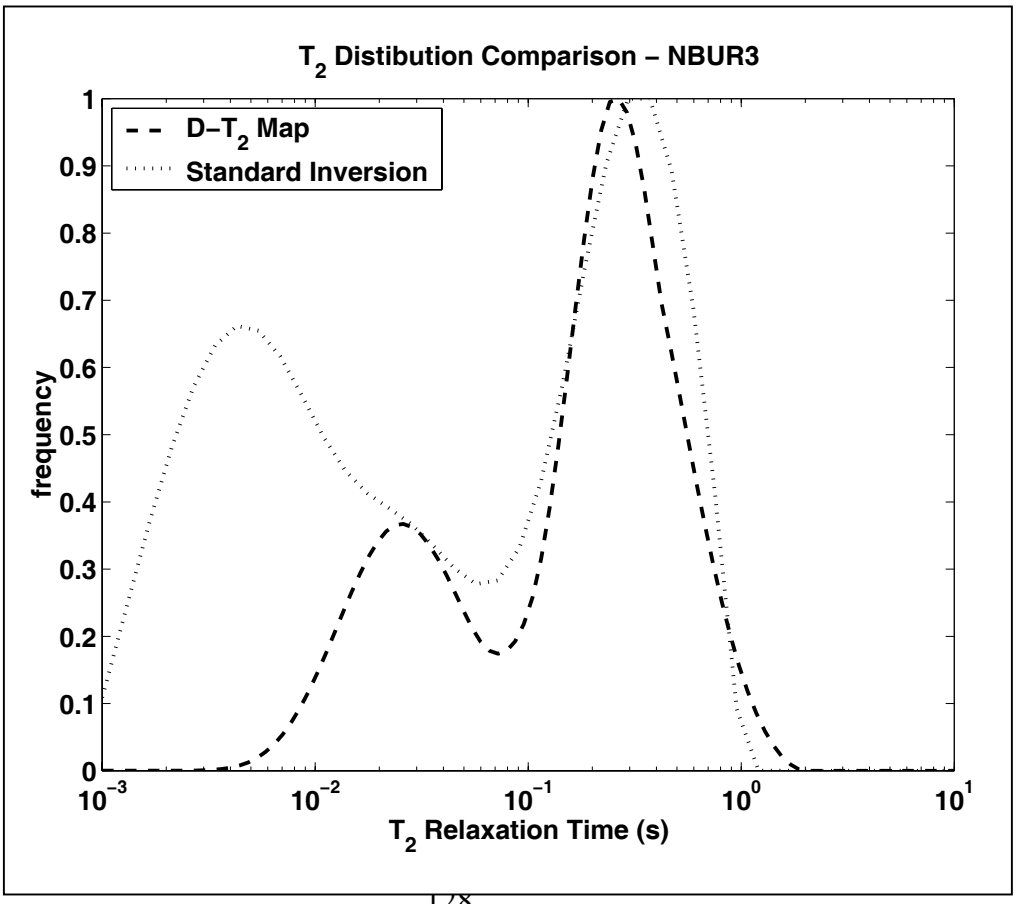

Figure 29: T_2 distributions of NBUR3 sample. Relaxation from map data is truncated below 35.2 ms.

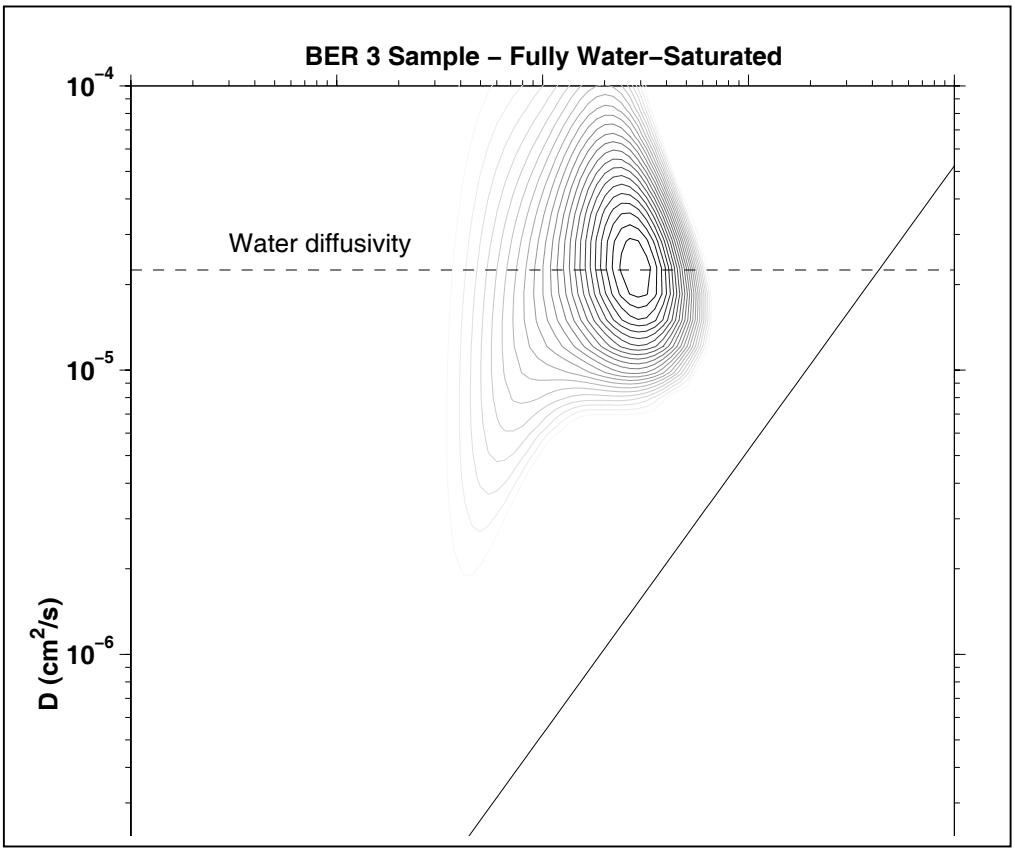

Figure 30: *D*- T_2 map of BER3 sample. Relaxation data is truncated below 120 ms.

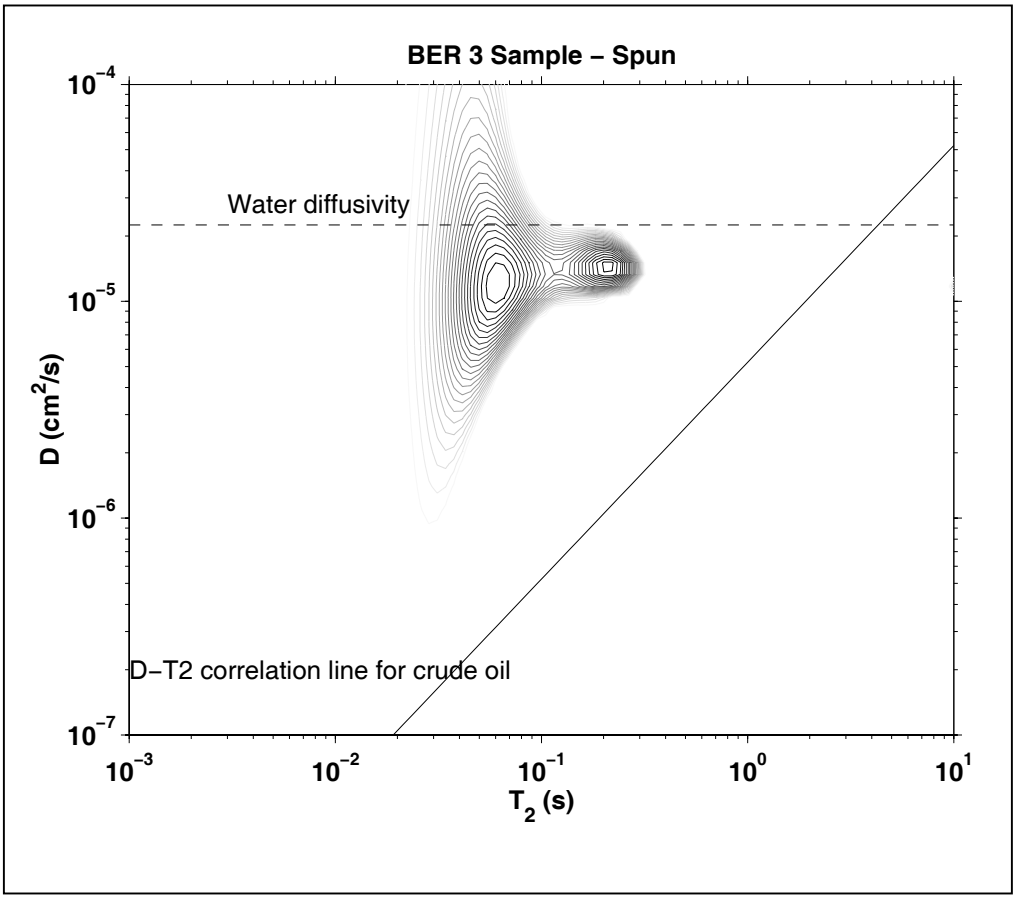

Figure 31: *D*- T_2 map of BER3 sample, after air de-saturation. S_w is approximately 0.43. Relaxation data is truncated below 120 ms.

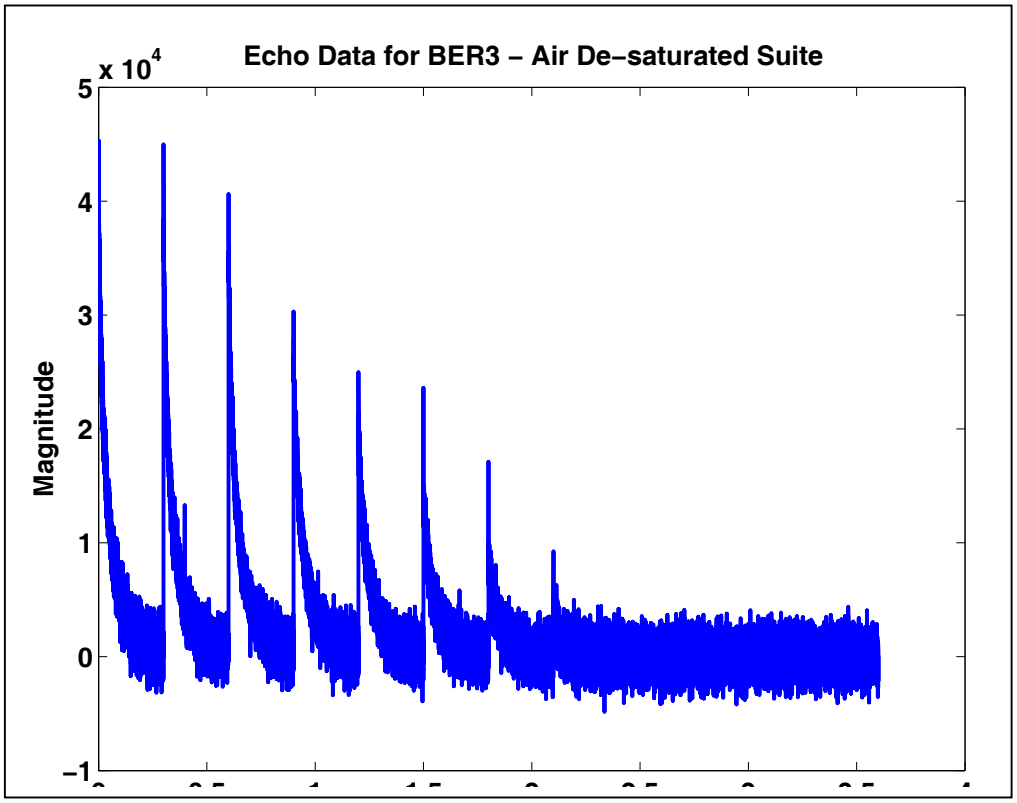

Figure 32: Echo data map of BER3 sample suite after air de-saturatation. The list of TELs used was 1.2, 2.4, 4.4, 8.4, 12.4, 16.4, 20.4, 24.4, 28.4, 32.4, and 36.4 ms, with a TES of 0.4 ms. There are 3000 echoes per set.

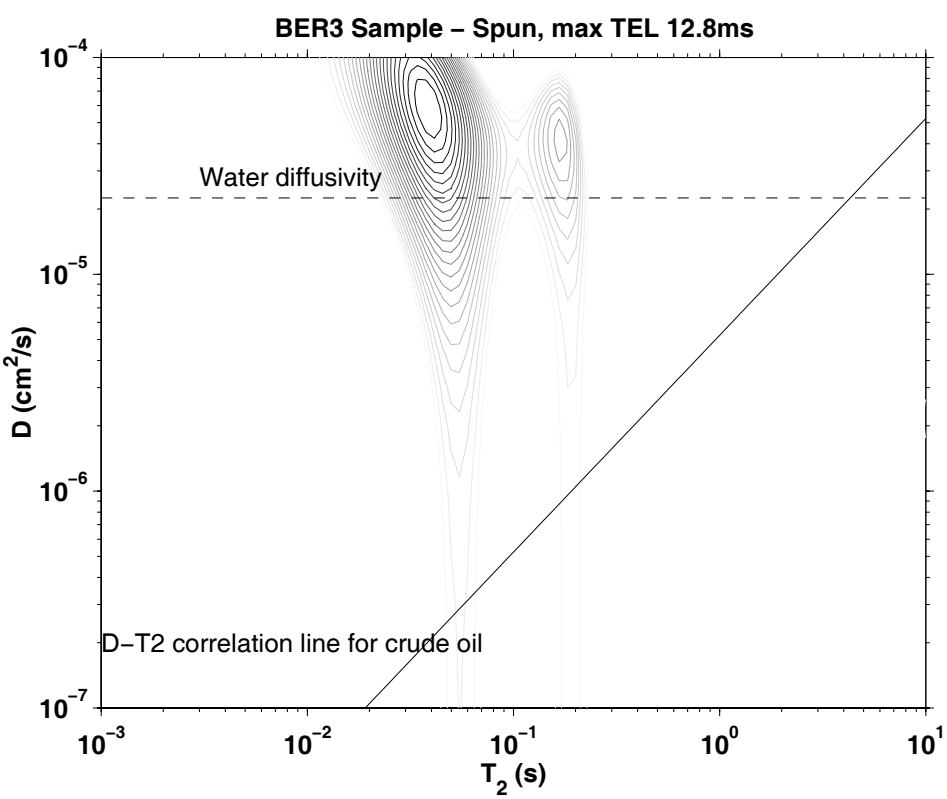

Figure 33: *D*- T_2 map of BER3 sample, after air de-saturation. S_w is approximately 0.43. Relaxation data is truncated below 25.60 ms.

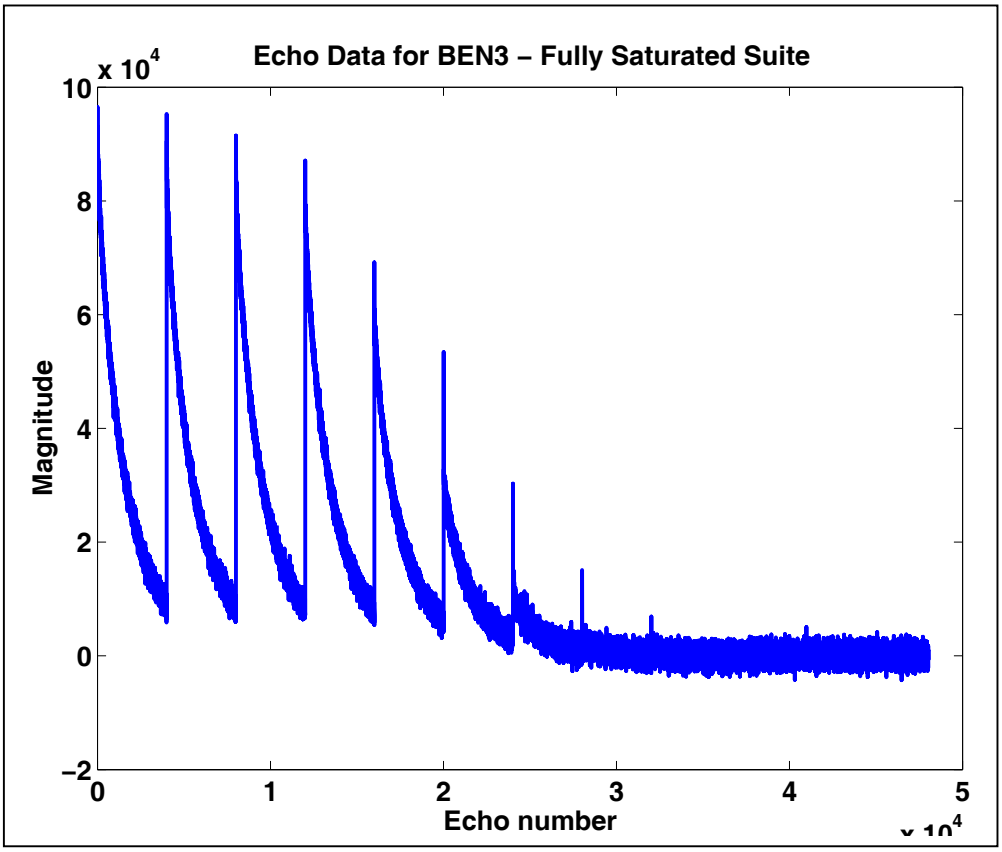

Figure 34: Echo data map of BEN3 sample suite. The list of TELs used was 1.2, 2.4, 4.4, 8.4, 12.4, 16.4, 20.4, 24.4, 28.4, 32.4, and 36.4 ms, with a TES of 0.4 ms. There are 4002 echoes per set.

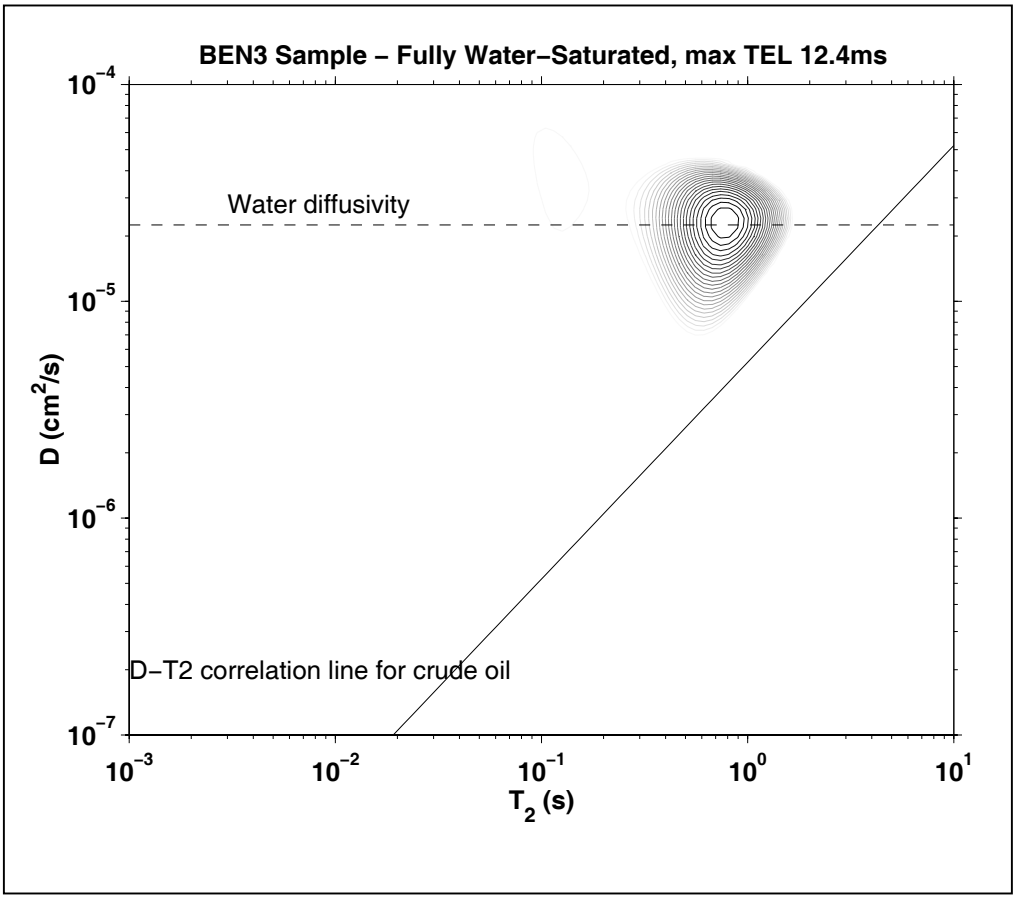

Figure 35: *D*- T_2 map of BEN3 sample, fully water-saturated. Relaxation data is truncated below 24.8 ms.

Task 3.0 Pore Morphology/Rock Characterization

Study of Vuggy Carbonates using NMR and X-Ray CT Scanning

I. Hidajat & K. K. Mohanty

Chemical Engineering Dept.

University of Houston

M. Flaum & G. J. Hirasaki

Chemical Engineering Dept.

Rice University

Abstract

Most existing permeability correlations for carbonates assume that vugs do not contribute to permeability. This may not always be the case, since vugs may be connected in some formations and contribute to the permeability. The objectives of this work are to identify vug connectivity by using X-ray CT scan and thin-section images of carbonates and to improve the NMR correlation for carbonates system. Six carbonate samples from West Texas field were studied. Porosity and permeability of each sample were measured. The pore size distribution of these rocks is characterized by mercury porosimetry and NMR T_2 measurements. Thin sections in the horizontal and vertical directions were prepared from the end pieces of the samples and were analyzed by using optical microscope and SEM. CT scanning of the core materials shows that porosity varies significantly along the core length. Some samples also show very distinct preferentially flow path, which affected the oil recovery. As revealed by the thin section analysis, the permeability of the samples studied is controlled either by the intergranular porosity or by the small channel that connects different vugs. The results of capillary pressure and NMR T_2 measurement shows multimodal pore throat and pore body size distributions. It is observed that the tortuosity can be a good indicator whether the vugs are contributing to the flow or not. A modified Chang model, which includes the tortuosity factor, is proposed and proved to yield a better permeability prediction for the West Texas samples used in this study. It is also shown that for the samples studied the tortuosity can be estimated from NMR T_2 distribution; hence allowing permeability prediction from NMR T_2 distribution alone. The permeability estimation by using effective medium approximation is also presented. All parameters used in effective medium approximation are also derived from NMR T_2 distribution by fitting with trimodal Weibull distribution.

1. Introduction

More than 50% of the world's hydrocarbon reserves are in carbonate formations.[1] However, estimating petrophysical properties from NMR measurements in carbonate rocks have always been a bigger challenge than in sandstone formations. Carbonates are characterized by different type of porosity and complex pore size distribution. Due to the reactive nature, carbonates undergo a more complicated post-depositional diagenesis compared to siliciclastic sandstones. The diagenesis process includes cementation, dissolution, dolomitization, recrystallization and evaporite mineralization.[2] Dolomitization is a process of magnesium ion inclusion into the limestone. Carbonates are also sensitive to the microorganism activity in their depositional environment. Depending on whether it is grain or mud supported, carbonates can be classified into grainstone (no mud), packstone, wackstone and mudstone (mud dominated).[2,3]

Carbonates porosity can be characterized by three different types of porosity: intragranular porosity, intergranular porosity and vugs.[2] Intragranular porosity is the porosity inside the grain and intergranular porosity is the porosity between the grains. Vug is defined as the pore space that is within grains or crystals or that is significantly larger than grains or crystals.[2] In more popular term, vug is a pore that is large enough to be visible with naked eye. Vuggy pore space is subdivided into separate vugs and touching vugs based on vugs interconnection.[2,4]

A permeability correlation from NMR T_2 measurement is given by Chang *et al*.[5]

$$k = 4.75\ (\phi_{750})^4\ (T_{2lm,750})^2\ , \qquad (1)$$

where ϕ_{750} is the porosity and $T_{2lm,750}$ is the logarithmic mean of T_2 of the pore space consisting pores with T_2 less than 750ms. The correlation assumes that vugs do not contribute to the flow and hence the contribution of the vugs in the T_2

above 750 ms is not used. This may not always be the case; in some instances vugs may be connected and contribute to the permeability.

In this work, we study six carbonate samples from West Texas field using X-ray CT scanner, NMR and other routine core analysis such as porosity, air permeability, mercury capillary pressure, thin section and formation factor. This report is organized into four main sections: core characterization procedure, discussion of core properties from experimental results, discussion of permeability correlation from capillary pressure and NMR, and finally the conclusions.

2. Core Characterization Procedure

2.1. Sample Selection

Six vuggy carbonate rocks samples from West Texas field were selected. Before the samples were plugged and cleaned, the samples were scanned by using x-ray CT scanner to identify regions of interest. The samples were cleaned by using toluene, chloroform/methanol azeotrope and methanol in Dean Stark extraction apparatus. The diameters of the plugs were 1”-1.5”. The porosity and the air permeability for the cleaned plugs were measured.

2.2. Mercury Capillary Pressure

End pieces of the samples were dried at approximately 100^0C. They were evacuated to less than 50 microns vacuum and mercury was injected over 117 pressure steps ranging from 1.64 to 60,000 psia.

2.3. Thin Section

The thin section was viewed by using an optical microscope. The picture was captured by using a CCD camera and the video output signal was sent to a PC computer by using a frame grabber PCI card. The picture was then segmented into pore space and solid by using Crabtree’s algorithm.[6] Several contiguous images were taken for the same sample and then they are composed together to form a larger image of about 1-2 cm coverage. The resolution of each pixel is 10 μm. The endpieces or the stubs of the thin sections were also studied by using

SEM (Scanning Electron Microscope) in the BSE (Back Scattered Electron) mode.

2.4. NMR T_2 Measurement

The NMR T_2 measurement was done by using Maran Ultra low field NMR spectrometer. The samples were saturated with 1% NaCl brine.

2.5. 3D Porosity Distribution from CT Scanner

The dry and brine-saturated samples were CT scanned at 2-mm interval in the z-direction. Then the porosity distribution was calculated from the CT number difference between brine and dry saturated core. The CT scanner used was Technicare Deltascan 2060 and the scanner was vertically mounted. The pixel resolution is 254x254 μm in the xy plane and 2mm in the z-direction. The parameters used were 8s scanning time, 120KV, 75mA, and 12.5cm scan diameter.

2.6. Tracer Experiment

12% NaI in 1% NaCl brine was injected from the bottom into the brine-saturated core. CT scans were taken during brine displacement. The NaI outlet concentration was measured by using online microconductivity meter.

2.7. S_{wr} Experiment

15% iodo-decane in decane was injected from the top into the brine-saturated core. CT scans were done only at the end of the experiment. The brine and oil saturation inside the core was calculated from mass balance.

2.8. S_{or} Experiment

Brine was injected from the bottom into the core at S_{wr} condition. CT scans were taken only at the end of the experiment. The final brine and oil saturations inside the core were calculated from mass balance.

2.9. Formation Factor

The formation factor was measured by measuring the resistivity of the brine-saturated samples.

3. Core Analysis

3.1. Porosity and Permeability

The core samples can be divided into two groups: low permeability and high permeability group. The porosity range for low permeability samples is 6% to 7.4%, and the permeability is less than 0.1mD. The porosity range for high permeability samples is 15.2% to 21.8% with permeability in the range of 56mD to more than 2,000mD. Sample no.2A and sample no. 2B are from the same well, so do sample no. 4A and sample no. 4B. **Table 1** gives the measured porosity, porosity from CT scan, permeability, rock descriptions and binarized thin section images. **Fig. 1** shows the 3D cross section of porosity distribution from CT scanner. The porosity calculated from CT scan is lower for sample no. 3 and 4B, some pores were not invaded by the brine. The porosity was calculated by averaging all the pixels for the whole cross sections. **Fig. 2** shows the porosity variation along each core length. Each point was calculated by averaging all the pixels porosity for that cross section. There is significant porosity variation along the core length for each sample compared to Berea sample (**Fig. 2**). Hicks *et al*. also observed similar porosity variation for different carbonate rocks [7].

The spatial dependence of the porosity is measured by using semi-variogram which is determined by

$$SV(h) = \frac{1}{2N(h)} \sum \left(\phi_i - \phi_{i+h}\right)^2, \tag{2}$$

where *SV* is the semi-variogram, *h* is the lag, *N(h)* is the number of pairs of observed data points separated by a lag of *h* and ϕ is the porosity. The semivariograms were calculated from the *x-z* plane (the middle slice in the flow direction) of the CT images and are plotted in **Fig. 3**. Then the semivariogram was fitted by an exponential model given as

$$SV(h) = c\left(1 - \exp\left(-\frac{3h}{a}\right)\right), \tag{3}$$

where *c* is the sill and *a* is the range where semivariogram reaches 95% of the sill[8]. The fitting parameters *c* and *a* are given in **Table 2**. Samples no. 3 and 4B have the highest sill or variance. The heterogeneity of these West Texas samples is found to be in the order of 0.5 to 1.5 cm.

Sample	k (mD)	ϕ ϕ_{CT}	Description	Thin Section
1	0.023	7.4 6.2	Fine peloidal wackstone-packstone dolomite. Anhydrite filled. Small vugs.	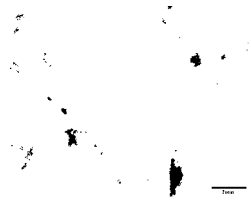
2A	0.022	6.6 6.9	Large crystal, almost no intercrytalline porosity. Large vugs.	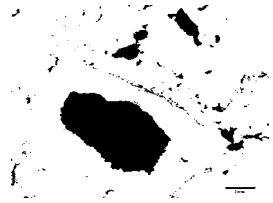
2B	0.08	5.9 4.4	Large crystal, almost no intercrytalline porosity. Large vugs.	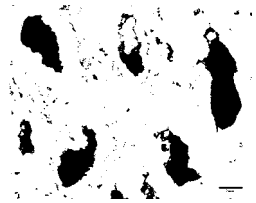
3	56	15.2 7.9	Peloid-fusulinid packstone-wackstone dolomite. Little intergranular porosity. Small fracture. Anhydrite filled. Large vugs.	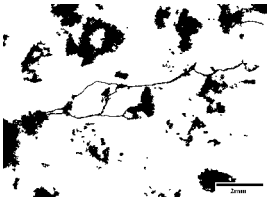
4A	140	15.7 14.1	Interclump appearance. Large vugs.	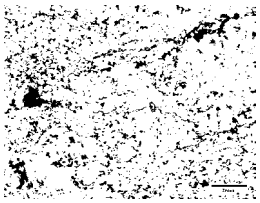
4B	2,321	21.8 16.7	Interclump appearance. Large vugs.	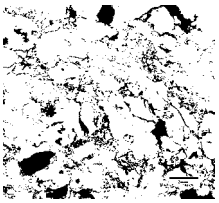

Table 1. Air permeability, porosity, porosity from CT scan, rock description and thin section images.

Sample	x- direction		z- direction	
	c	a (mm)	c	a (mm)
1	7.39	4.70	8.24	5.43
2A	13.40	7.40	13.89	6.61
2B	14.55	5.11	17.17	8.66
3	87.62	5.11	87.81	8.97
4A	16.54	11.65	15.32	14.38
4B	77.81	10.45	76.22	10.62

Table 2. Semivariogram fitting parameters

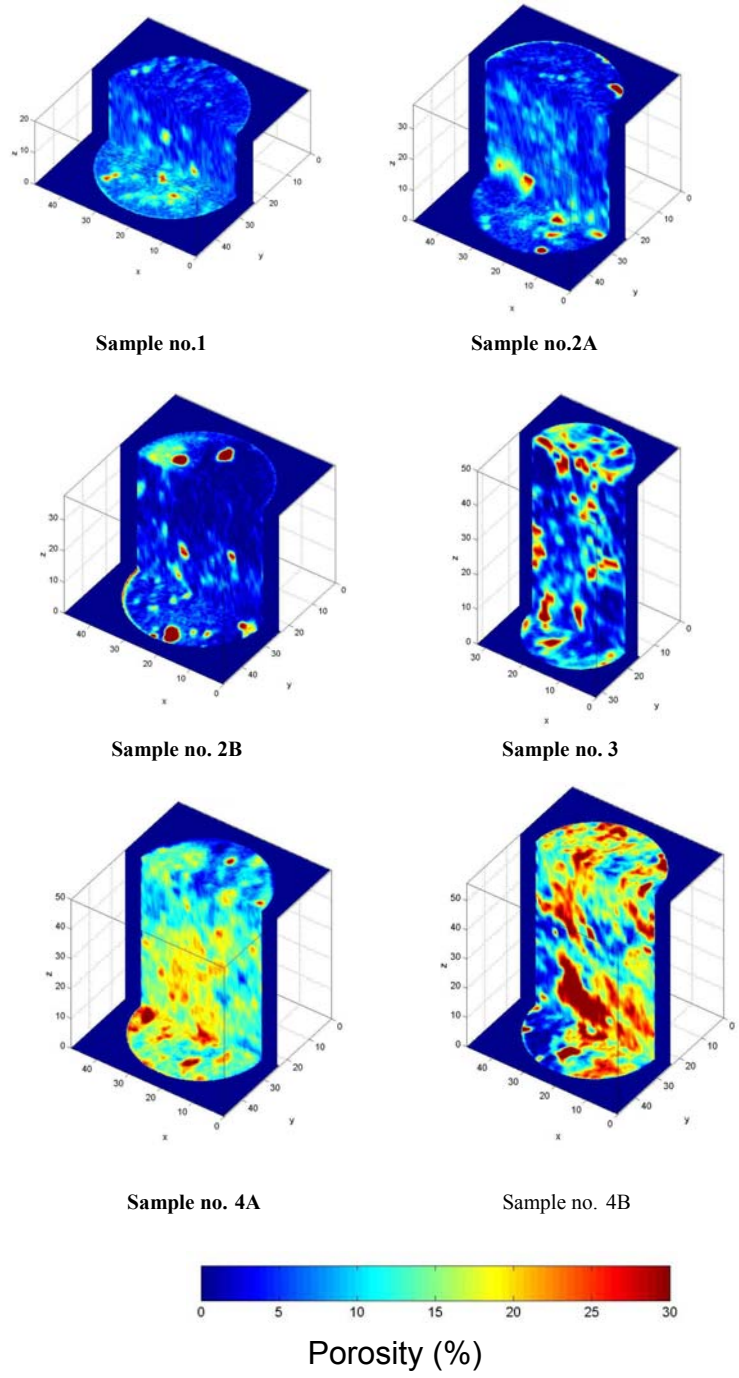

Figure 1. Cross-sectional porosity distribution from CT Scan.

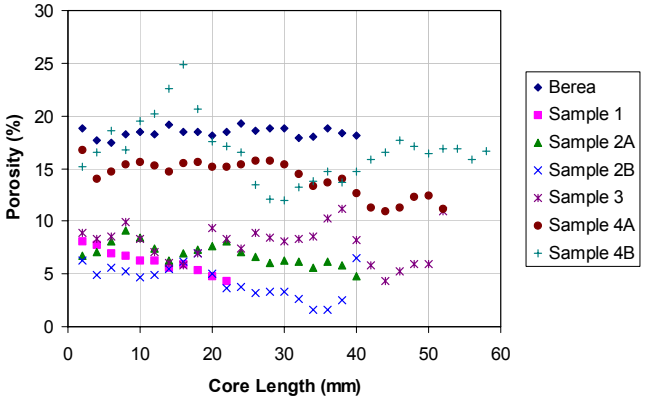

Figure 2. Porosity variation along core length.

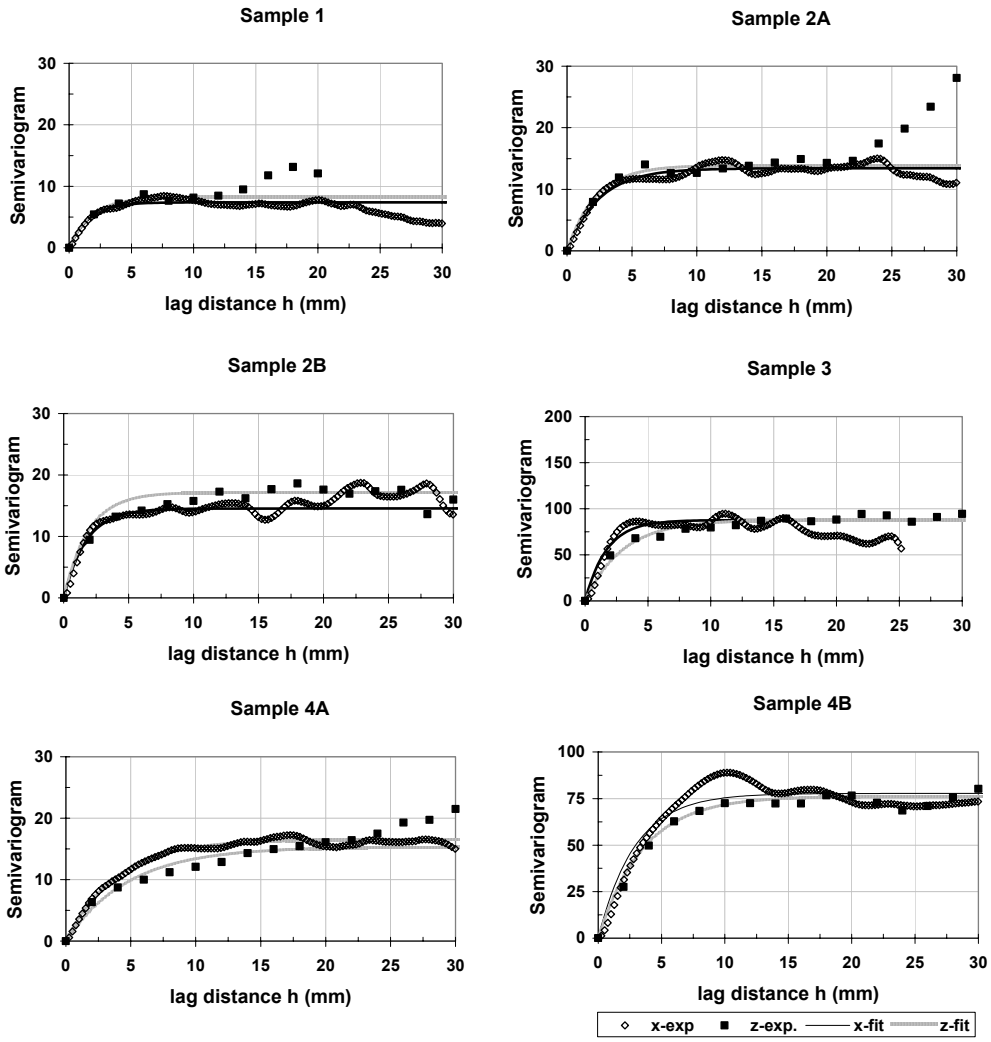

Figure 3. Semivariograms for West Texas samples.

3.2. Rock Descriptions from Thin Section

Sample no. 1 is a fine peloidal wackstone-packstone dolomite. The matrix is filled with anhydride, which reduces the permeability. From SEM image (**Fig. 4**), the matrix has fine and rather uniform crystals with pore opening between the crystals. The vugs are small and mostly less than 0.5mm. A few vugs have size about 1mm. Vugs occur only in some layers, and the others layers are almost free of vugs.

Samples no. 2A and 2B have very large crystals. The crystals are so large that they grow very tight leaving almost no intercrystalline porosity. The SEM image (**Fig. 4**) shows that in between the large crystals, there are sucrosic or sugar-like crystals, which have siginificant pore openings. Both samples are very vuggy and vugs of the size about 1mm up to 5mm are present in these two samples. Vugs are interconnected through the matrix samples. Thus, the microporosity in the matrix controls the permeability for samples no. 1, 2A and 2B.

Sample no. 3 is a peloid-fusulinid packstone-wackstone dolomite. The matrix has very little intergranular porosity. The matrix is also quite heterogenous. As seen from the SEM image (**Fig. 4**), the matrix also has very large crystals with sucrosic crystals in between. Also as seen in **Fig. 1**, there are patches of lower porosity region in the matrix system. Some touching vugs and fractures are observed from the thin section. Some vugs are connected by micro-fractures. Anhydride occurs in the matrix and in the fractures. This sample has a lot of moldic vugs; the vug sizes are about 1mm to 3mm. The Vugs are distributed more or less uniformly throughout the sample.

Samples no. 4A and 4B are very clumpy in appearance. The depositional texture cannot be seen. They look like breccia or agglomerate of different rocks. They may be formed from cave debris that recrystallized. From SEM (**Fig. 4**), it is found that the matrix of sample 4A is surprisingly tight. But both samples have a lot of intergranular porosity that forms an interconnecting flow network as observed from the thin section images that made the permeability high. The integranular pore space is controlling the flow path in these two samples. Both

samples are also quite vuggy, with vug sizes about 1mm to 5mm. Sample no. 4B seems to be more heterogenous than 4A. In **Fig. 1**, sample no. 4B has both patches of high porosity and low porosity.

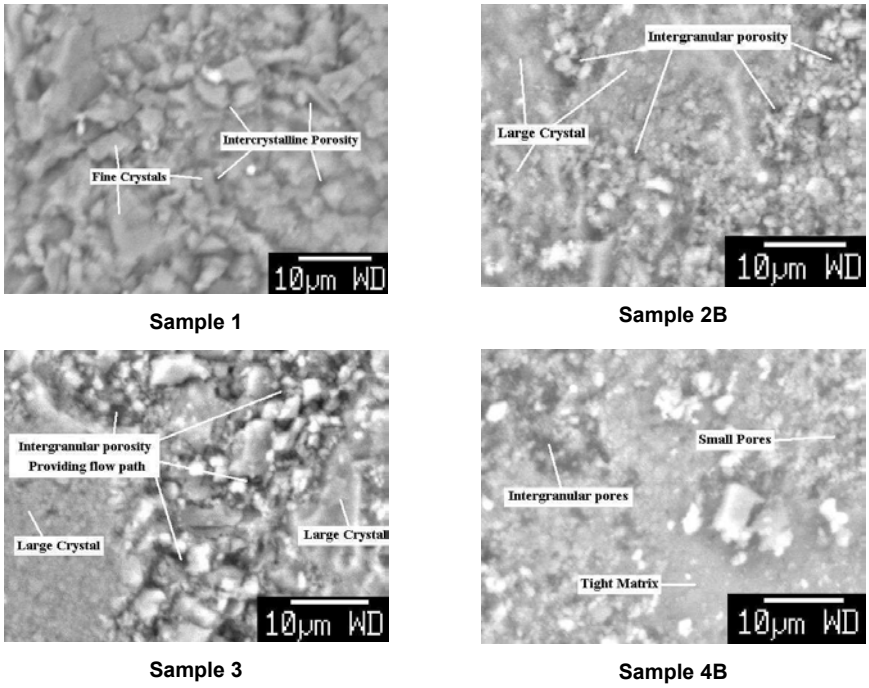

Figure 4. SEM image of the matrix

3.3. Mercury Capillary Pressure

Fig. 5 shows the mercury capillary pressure curves for all samples. With the exception of sample no. 1, all samples contain vugular pores ranging from very small ones in sample no. 4A up to very large ones in sample no. 4B, some of them can be seen on the surface Assuming the capillary bundle model, the pore throat size can be related to capillary pressure injection by

$$P_c = \frac{2\sigma \cos\theta}{r_t}, \tag{4}$$

where P_c is the capillary pressure, σ is the surface tension (480 dyne/cm), θ is the contact angle (40°) and r_t is the pore throat radius. The pore throat size distributions calculated from Eq. 4 are given in **Fig. 6**.

Sample no. 4B has the lowest capillary pressure and sample no. 1 has the highest capillary pressure, which correspond to the highest and the lowest permeability samples, respectively (**Fig. 5**). The capillary pressure curves for those two samples are also similar to monomodal porosity type rock. **Fig. 6** shows that sample no. 1 actually has a monomodal pore throat size distribution and the throat sizes are very small in the range of 0.01-1 μm. Sample no. 4B has a bimodal pore throat size distribution and the two modes almost overlap with each other (**Fig. 6**). The pore throats in sample no. 4B are large, in the range of 1-100 μm.

The capillary pressure curves for sample no. 2A and 2B show the existence of vugs that are connected to the surface (corresponds to low capillary pressure) and then the curves steeply increase to high capillary pressure region, which correspond to small throat size in the matrix (**Fig. 5**). Both samples have very low permeability, hence the vugs in these two samples do not contribute to the flow conductance. There are two distinct modes in the pore throat size distribution, the smaller is in the order of 0.1 μm and the larger is in the order of 100 μm (**Fig. 6**).

The capillary pressure curve for sample no. 3 is similar to those of samples 2A and 2B. 50% of the pore volume is accessed through large or surface pore throats (**Fig. 6**).

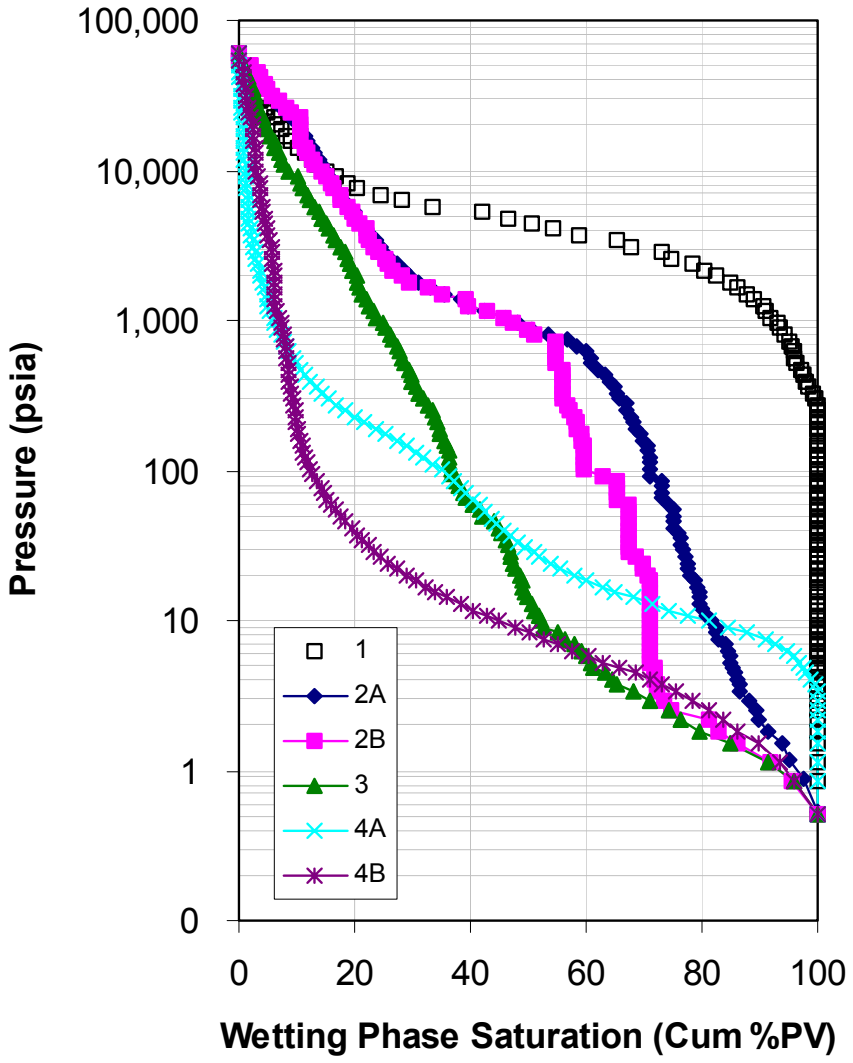

Figure 5. Mercury capillary pressure curves

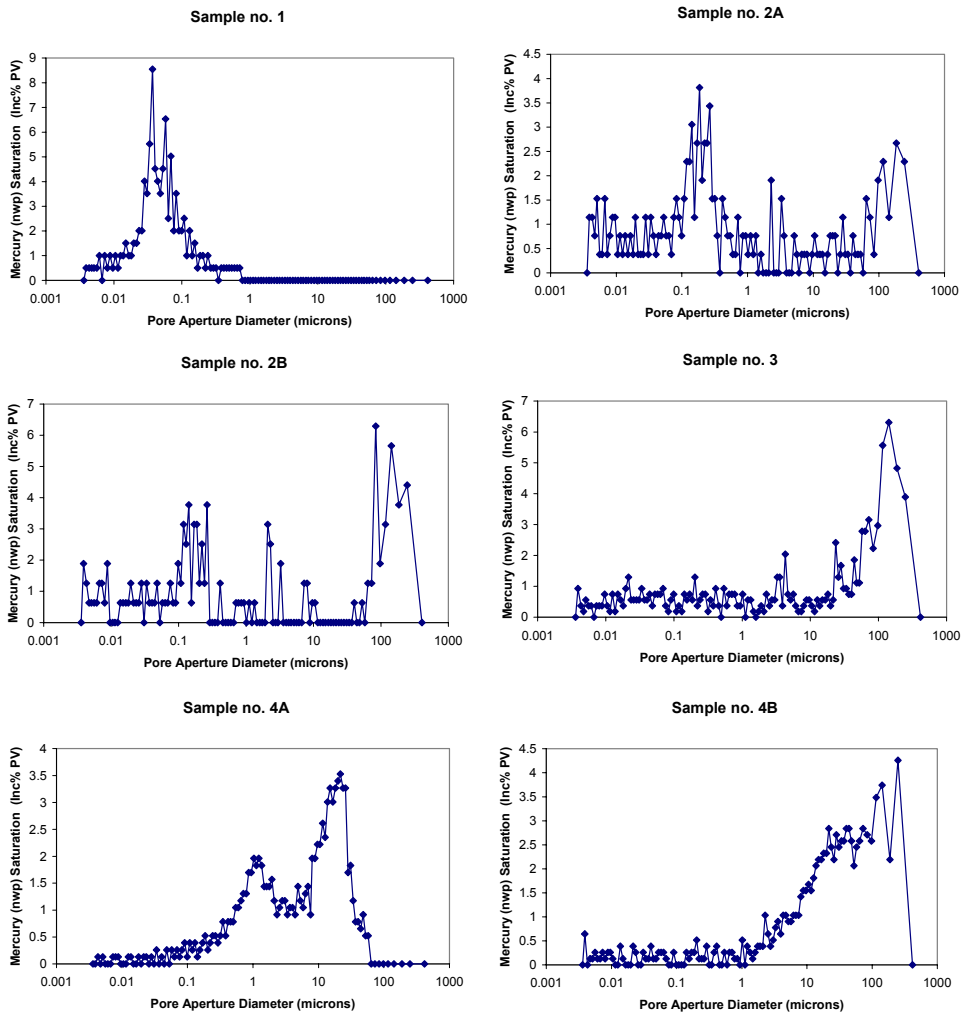

Figure 6. Pore throat size distribution from capillary pressure.

3.4. NMR T_2 Response

NMR T_2 response provides pore body size distribution of a brine-saturated sample (**Fig. 7**). Assuming the fast diffusion limit region and cylindrical pore shape, the T_2 response is related to the pore body size by[9]

$$\frac{1}{T_2} = \frac{1}{T_{2B}} + \rho \frac{2}{r_b}, \tag{5}$$

where T_{2B} is the brine bulk T_2, ρ is the surface relaxivity and r_b is the pore body radius.

The surface relaxivity is computed by matching the median of cumulative distribution of r_t computed from P_c and r_b computed from NMR T_2. The value is the average value of sample no. 4A and 4B since they have the best pore throat-body correlation (**Table 3**). The calculated surface relaxivity is 6.75 μm/s.

All the samples exhibit multimodal T_2 reponse and bulk brine response, meaning that all of the samples have large vugs (**Fig. 7**). By comparing pore body size distribution in with pore throat size distribution (**Fig. 8**), it is observed that in higher permeability samples (samples no. 3, 4A and 4B) the body and the throat are better correlated rather than in lower permeability samples (samples no. 1, 2A and 2B).

Sample	ρ (μm/s)
1	0.35
2A	0.11
2B	0.025
3	1.8
4A	3.5
4B	10

Table 3. Estimated surface relaxivity of West Texas samples

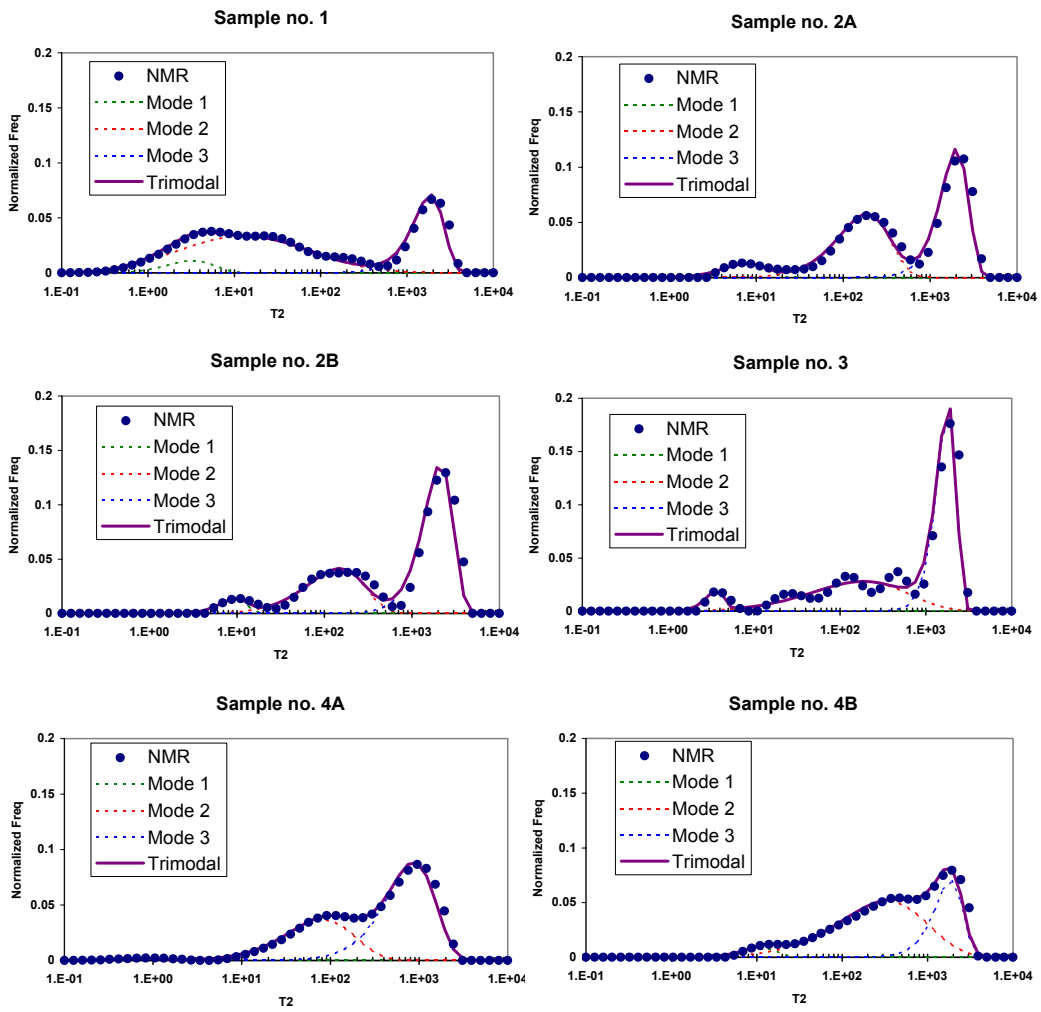

Figure 7. NMR T_2 distribution and trimodal Weibull distribution fit. The dots are NMR experimental data. The solid line is trimodal Weibull distribution. The green dashed line is the first mode, the red dashed line is the second mode and the blue line is the third mode of the trimodal Weibull distribution.

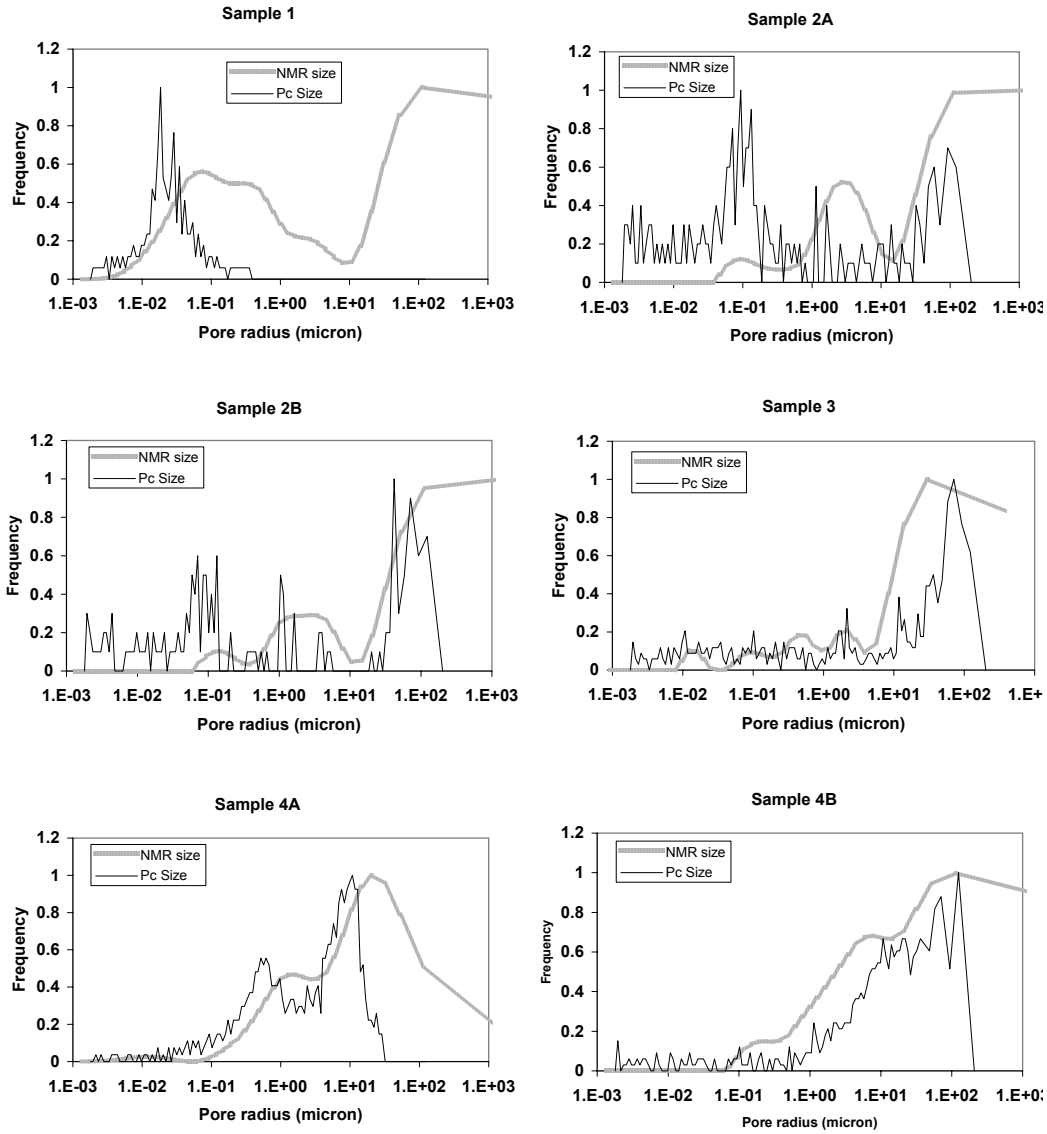

Figure 8. Pore body and pore throat size from NMR (assuming ρ = 6.75 μm/s) and capillary pressure measurement

3.5. Tracer Experiment

Fig. 9 shows the tracer concentration profile for some of the samples after 1PV tracer injection. Sample no. 2A has a preferentially flow path at 45° to the horizontal in the vertical plane. Sample no. 3 has a very distinct preferentially flow path; the tracer transport into the other areas is more of a diffusive transport. Sample no. 4A has a more uniform profile at the bottom part of the core, then the flow tends to go to through the center at the top part of the core. Sample 4B also has an unswept area at the bottom left corner and top right corner. All these confirm the heterogeneity of the carbonate rocks, we studied, at the centimeter scale.

The tracer effluent concentration profiles for the high permebility samples are plotted in **Fig. 10**. The very early breakthrough followed by a long tail is the characteristic of heterogeneous carbonate system. This behavior seems also to indicate the existence of a sample spanning high permeability streak in a tight matrix[10]. This also explains the early water breakthrough with high oil saturation remains in large unswept area that is usually observed in many of the carbonate system.[10-13]

The Coats and Smith dead end pore model[14] was used in order to account for early breakthrough and long tail on experimentally observed effluent concentration profiles. The model divides the pore space of the porous medium into a flowing and a nonflowing or stagnant fraction. The model is described as

$$f_d \frac{\partial C}{\partial t} + (1 - f_d) \frac{\partial C^*}{\partial t} = K_l \frac{\partial^2 C}{\partial x^2} - u \frac{\partial C}{\partial x} \quad , \tag{6}$$

$$(1 - f_d) \frac{\partial C^*}{\partial t} = K' \left(C - C^* \right), \tag{7}$$

where where f_d is the flowing fraction, C is the tracer concentration in the flowing part, C^* is the tracer concentration in the stagnant part, K_l is the longitudinal dispersivity, u is the Darcy velocity and K' is the mass transfer coefficient. The analytical solution is given by Brigham[15] in integral form. The experiment result is

fitted by three parameters f_d, K_l and K' and the effect of those three parameters on the effluent concentration is given in Mohanty and Salter[16]. The fitting parameters are given in **Table 4**.

Sample no. 3 has the largest stagnant fraction, which is consistent with the CT images shown in **Fig. 9**. Sample no. 4B has the largest longitudinal dispersivity coefficient, which also means that this sample has the longest mixing zone due to its heterogeneity. The small mass transfer coefficient for sample no. 3 seems to indicate that this sample has long and narrow dead end pores system.

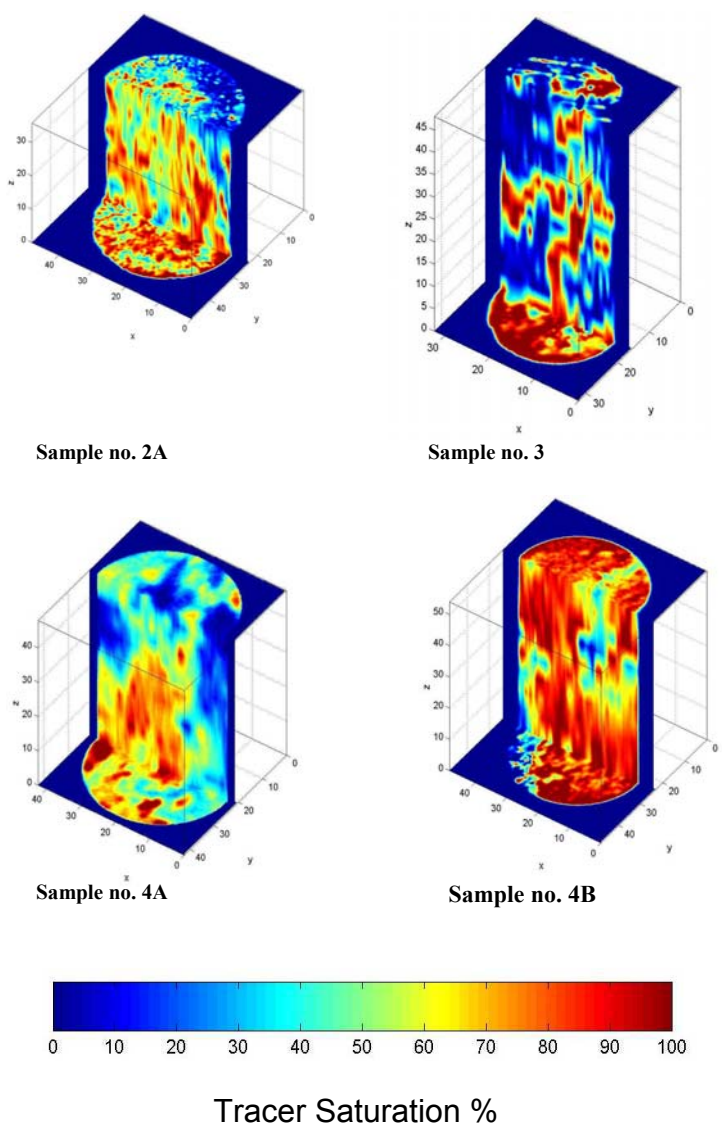

Figure 9. Tracer concentration profile after 1PV injection

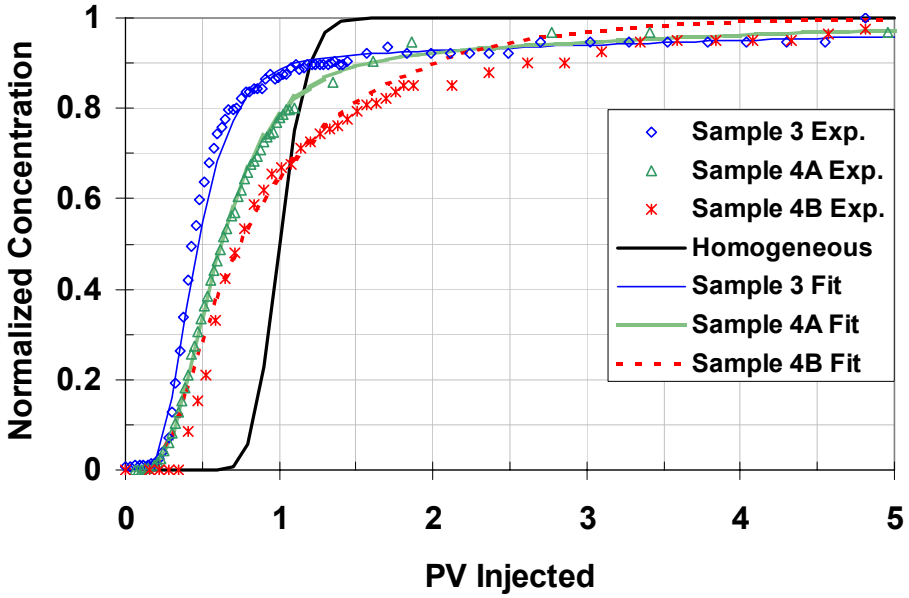

Figure 10. Experimental and model fit of tracer effluent concentration

Sample	f_d	K_l (cm^2/s)	K' (1/s)
3	0.5	1.89E-4	6.99E-6
4A	0.67	3.97E4	1.28E-5
4B	0.7	7.03E-4	5.73D-5

Table 4. Coats and Smith fitting parameters

3.6. S_{wr} and S_{or}

Fig. 11A shows the oil saturation (S_{oi}) at Swr after drainage process and **Fig. 11B** shows the residual oil saturation (S_{or}) after imbibition experiment for some of the samples. **Table 5** gives the S_{oi}, S_{or} and the percentage of oil recovered. For samples no. 2A, 4A and 4B oil fills the area outside preferential flow paths seen in **Fig. 9** at S_{oi} because the oil injection is from the top. In brine injection, oil is recovered mostly from the preferentially flow path. For sample no. 3, oil fills mostly the preferentially flow path area at S_{oi}. Sample no. 4B shows low oil recovery although it has the highest porosity and permeability. Both mass balance and oil saturation calculation from CT number give around 20% oil recovery consistently. We suspect that this sample is more oil wet than the other sample.

Sample	Soi	Sor	%Oil Recovery
1	22.8	20.7	9.4
2A	44.2	26.5	40.0
2B	26.8	14.4	46.3
3	33.7	23	31.5
4A	45.2	26.9	40.5
4B	51.7	41.7	19.5

Table 5. Initial oil saturation, residual oil saturation and percentage of oil recovery

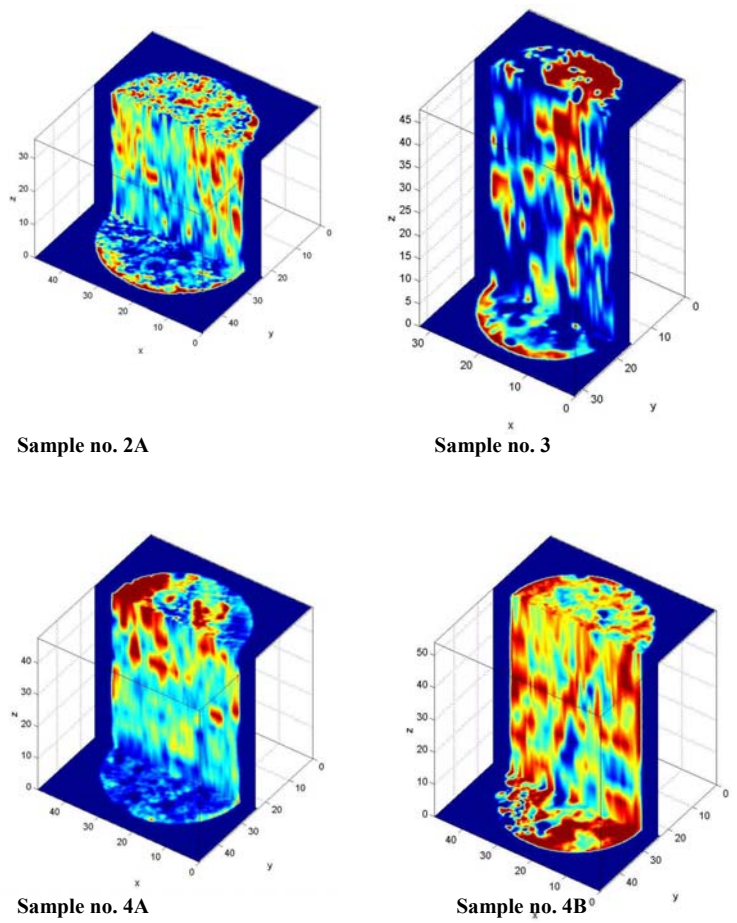

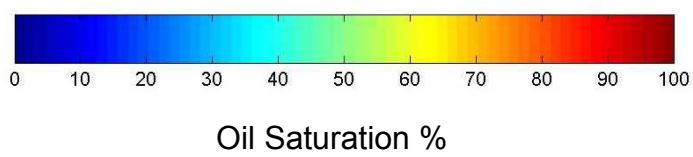

Figure 11A. Initial oil saturation at S_{wr}.

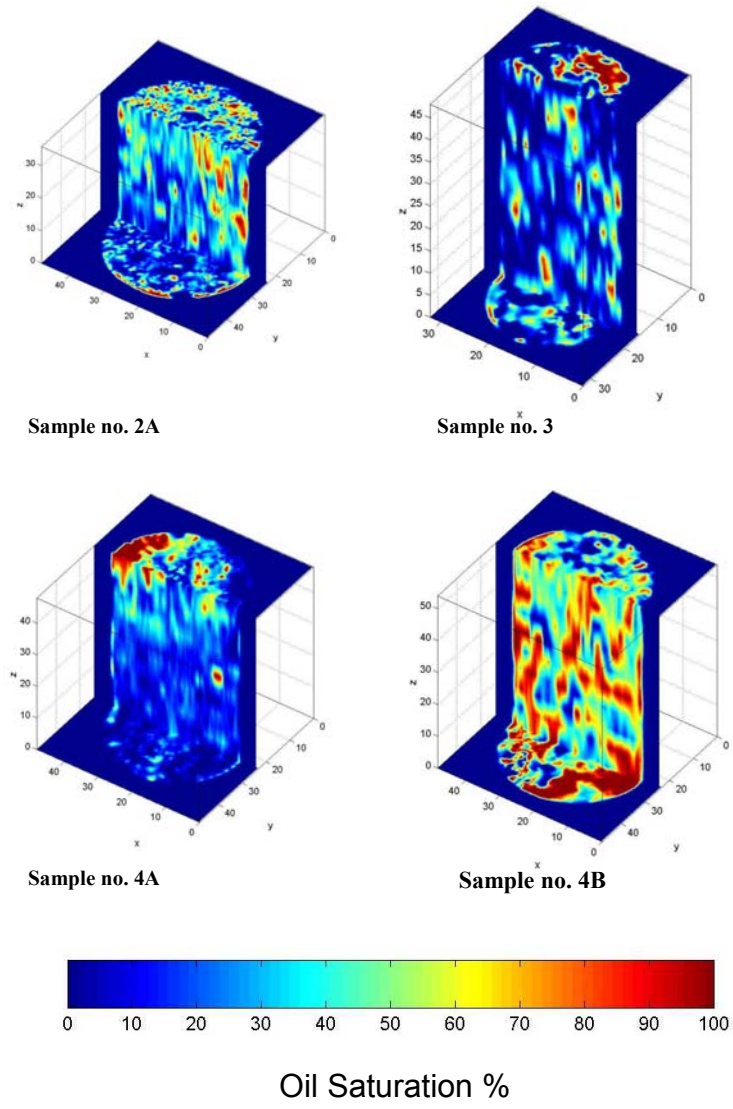

Figure 11B. Residual oil saturation profile

3.6. Formation Factor

The formation factor is obtained by measuring the resistivity of a brine saturated rock and compared it with the resistivity of the brine itself. Assuming a bundle tube model, the tortuosity also can be estimated from formation factor as follow

$$F = \frac{R_{rock+brine}}{R_{brine}} = \frac{1}{\phi^m} = \frac{\tau}{\phi}, \tag{8}$$

where R is the resistivity, ϕ is the porosity, m is the Archie's cementation factor and τ is the tortuosity.

Table 6 shows the measured formation factor, Archie's-m cementation factor and the calculated tortuosity. The cementation factors are larger than 2, which is the expected value for carbonates. It is also observed that the formation factor and the tortuosity correlate well with the permeability. The intergranular and the vuggy porosity can be estimated by using Myer's PCM (Pore Combination Model)[17], which is given as

$$F = \left(\frac{1}{\phi_{\text{int}}}\right)^{1.91} \left(\frac{\phi_{\text{int}}}{\phi}\right)^{1.11}, \tag{9}$$

where ϕ_{int} is the intergranular porosity and $\phi=\phi_{int}+\phi_{vug}$. The calculated results are tabulated in **Table 7**. The results agree very well with the estimated vuggy porosity calculated by using 750 ms vugular cutoff value in the NMR T_2 distribution. Hence, it also means that the formation factor of the West Texas samples can be calculated from the NMR T_2 distribution. **Fig. 12** shows the relationship between the cementation factor and the ratio of vuggy porosity to the total porosity. The cementation factor m increases with increasing vuggy porosity. The relationship obtained from the linear regression is

$$m = 0.51\left(\frac{\phi_{vug}}{\phi}\right) + 1.91. \tag{10}$$

Sample	F	m	τ
1	191	2.02	14.1
2A	304	2.10	20.1
2B	501	2.20	29.8
3	69	2.25	10.5
4B	27	216	5.9

Table 6. Formation factor measurement results

Sample	ϕ_{vuggy} from F (%)	ϕ_{vuggy} NMR 750 ms (%)	ϕ_{vuggy} NMR Weibull (%)
1	2.2	2.3	2.4
2A	3.2	3.1	3.2
2B	3.8	3.5	3.6
3	8.4	8.9	8.5
4B	8.3	8.2	6.5

Table 7. Vuggy porosity computed from formation factor, NMR vT_2 750 ms cutoff and NMR trimodal Weibull distribution

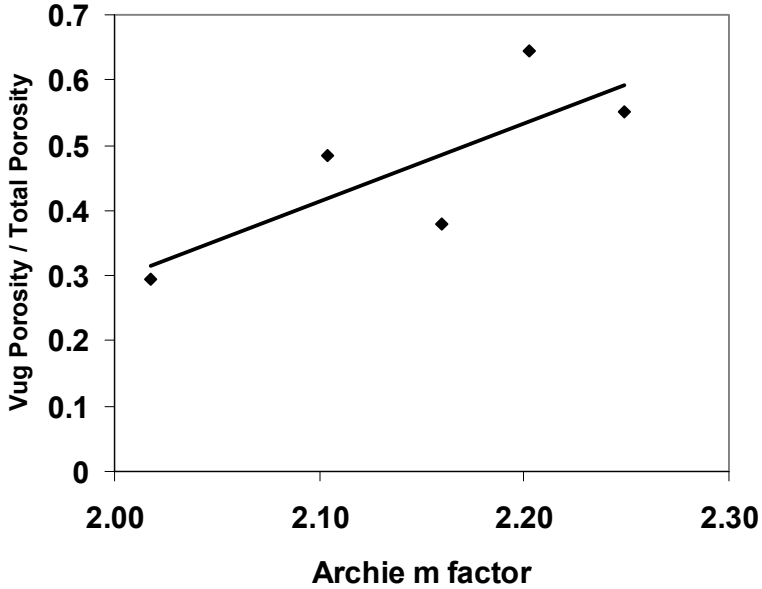

Figure 12. Relationship between Archie's m factor and the vuggy porosity and total porosity ratio

4. Permeability Correlation from Capillary Pressure

The existing correlations from Winland-Pittman[18], Swanson[19] and Katz-Thompson[20] are tested to predict the West Texas samples permeability. The basic concept of the permeability model from capillary pressure is to use a characteristic throat size that governs the flow at the percolation threshold of the porous medium and each model uses a different method to estimate that characteristic throat size. Winland developed a power law models that relates permeability with porosity and pore throat radius and later published by Kolodzie[18]:

$$k = 17.6\phi^{1.470} r_{35}^{\ 1.701}, \tag{11}$$

where r_{35} is the pore radius corresponding to 35% mercury saturation. Swanson proposed a simple correlation between the permeability and mercury capillary pressure as follow[19]

$$k = 399\left(\frac{S_b}{P_c}\right)_{\max}^{1.691}, \tag{12}$$

where S_b is the mercury saturation in percent bulk volume and P_c is the mercury capillary pressure. Starting from percolation concept, Katz and Thompson have related the permeability of a porous medium to a length scale l_c, i.e.,

$$k = \frac{1}{226}\frac{l_c^2}{F}, \tag{13}$$

where l_c is the size of the smallest throat invaded by a non-wetting phase at the percolation threshold. l_c can be estimated from the inflection point of the mercury injection curve.

The predicted permeabilities from Equation 11-13 are tabulated in **Table 8**. The Winland-Pittman model gives the best prediction within a factor of 9 in average. The Katz-Thompson model always underpredicts the permeability. The Swanson model does not work for the West Texas samples because it is not developed for rock that has multimodal porosity.

The Katz-Thompson model is modified by changing its constant value from 1/226 to 32.336. The new constant is obtained by plotting the measured permeability and l_c/F. The prediction is improved (**Table 9**), but it is still not as good as the Windland-Pittman model. The Winland-Pittman model is modified as follow

$$k = 102.36\frac{{r_{35}}^2}{F}. \tag{14}$$

However, in average the original Winland-Pittman model gives a slightly better prediction than the modified one.

Sample	$k_{measured}$ (mD)	$k_{Winland}$ (mD)	k_{Katz} (mD)	$k_{Swanson}$ (mD)
1	0.023	0.0011	0.00004	0.001
2A	0.022	0.031	0.0012	57
2B	0.08	0.38	0.0003	91
3	56	291	1.4	763
4A	140	29	38	84
4B	2,321	343	315	645
Ratio*		9.1	158.5	624.9

* Ratio is the ratio of the predicted value to the measured value or vice versa.

Table 8. Predicted permeability from capillary pressure correlation

Sample	$k_{measured}$ (mD)	$k_{Winland\ modified}$ (mD)	$k_{Katz\ modified}$ (mD)
1	0.023	0.0005	0.0003
2A	0.022	0.021	0.009
2B	0.08	0.3	0.0022
3	56	1,038	10
4A	140	83	274
4B	2,321	1,738	2,305
Ratio*		11.7	21.9

* Ratio is the ratio of the predicted value to the measured value or vice versa.

Table 9. Predicted permeability from the modified capillary pressure correlation

5. Permeability Correlation from NMR

5.1. Trimodal Weibull Distribution Fit

Most of the T_2 response of our samples exhibits trimodal behavior. In order to better estimate the contribution of each mode, the T_2 response was fitted with trimodal Weibull distribution. Weibull distribution was selected because it is a versatile distribution that can take on the characteristics of other types of distributions based on the value of the shape parameter. The trimodal Weibull cumulative distribution is given as[21]

$$P(x) = \sum_{i=1}^{3} \alpha_i \left(1 - \exp\left(-\left(\frac{x}{m_i} \right)^{\beta_i} \right) \right), \tag{15}$$

where α is the fraction of each mode, β is the shape parameter, m is the scale parameter and x is

$$x = \ln \frac{T_2}{T_{2,0}}, \tag{16}$$

where $T_{2,0}$ is the smallest T_2 used in the T_2 distribution (0.1 ms in this case). There are nine parameters to fit and this becomes a constrained non-linear least square problem. The sum of α_i must equal to one; m_i and β_i must be greater than zero.

The trimodal Weibull distribution can fit the T_2 response very well as shown in **Fig. 7**. The fitting parameters are given in **Table 10**. We describe mode 1 as the peak at the smallest T_2, mode 2 at the intermediate T_2 and mode 3 at the largest T_2. The fitting provides a better picture of each mode contribution and where they overlap, especially for samples no. 4A and 4B. The vuggy porosity is estimated

from the mode 3 fraction and agrees well with the calculated value from PCM model and from the vugular 750 ms cutoff (see **Table 7**). The vuggy porosity estimation from vugular 750 ms cutoff is slightly better than the estimation from Weibull distribution.

Sample	α_i	β_i	m_i
1	0.075	6.15	3.60
	0.60	3.32	5.46
	0.325	24.81	9.86
2A	0.07	8.22	4.40
	0.44	11.58	7.59
	0.49	27.55	9.92
2B	0.05	13.37	4.59
	0.34	10.21	7.36
	0.61	26.29	9.98
3	0.05	15.54	3.60
	0.39	6.36	7.74
	0.56	39.19	9.81
4A	0.01	4.24	2.15
	0.36	8.00	6.84
	0.63	14.84	9.12
4B	0.037	11.72	4.86
	0.66	7.34	8.29
	0.30	26.66	9.85

Table 10. Fitting parameters for trimodal Weibull distribution.

5.2. NMR Model

First, the existing NMR models are tested against the measured air permeability. The models tested are the model from SDR, Chang and Coates. The standard SDR model is given by

$$k = 4\phi^4 T_{2lm}{}^2, \tag{17}$$

where T_{2lm} is the logarithmic mean of T_2 distribution. The whole T_2 is used to calculate the permeability. The estimated permeability using SDR correlation is given in **Table 11**. The correlation works well for high permeability samples and does not work for low permeability samples.

Chang's correlation (Eq.1) assumes that the intergranular porosity controls the permeability and its pore volume may be approximated by excluding components with T_2 values above a certain cutoff value.[5] Both porosity and logarithmic mean of T_2 are calculated from the T_2 fraction below the cutoff value.[5] The 750ms cutoff value was selected based the minimum standard deviation provided by correlating over 24 samples[5]. The estimated permeability using this correlation for our samples are given in **Table 11**. The correlation works well for low permeability samples. For higher permeability samples, the correlation gives too low results. Hence, the assumption that vugs do not contribute to permeability is not always true. Most of the samples used by Chang et al.[5] have low permeability.

Another approach to estimate permeability is using bulk volume of irreducible water (*BVI*) in a formation. Without centrifuge data, a value of 92ms is used to estimate the T_2 cutoff for carbonate formation. The pore volume below T_2 cutoff is assumed as the BVI. The Coates model to estimate the permeability from BVI is given as[22]

$$k = 10^4 \phi^4 \left(\frac{FFI}{BVI}\right)^2, \tag{18}$$

where ϕ is the porosity, *BVI* is the bound volume irreducible and *FFI* is the free fluid volume (*FFI* = ϕ-*BVI*). **Table 11** shows that the permeability predicition using Coates's correlation works better for the high permeability samples and overpredicts the low permeability sample by two order of magnitude.

It is observed from the above exercise that for the Chang's model is more suitable for low permeability samples and on the other hand the SDR model is more suitable for high permeability samples. Since the tortuosity is a good indication to differentiate between the low and high permeability samples, we propose to include the tortuosity information into the NMR correlation as follow

$$k = 4.75\left(\left(\frac{\phi}{\phi_{750}}\right)^{a}\phi_{750}\right)^{4}\left(\left(\frac{T_{2lm}}{T_{2lm,750}}\right)^{a}T_{2lm,750}\right)^{2}, \qquad (19)$$

where ϕ is the total porosity, ϕ_{750} is the porosity below 750 ms, T_{2lm} is the logarithmic mean of the whole T_2 distribution, $T_{2lm,750}$ is the logarithmic mean of T_2 distribution by excluding the T_2 values above 750 ms and *a* is defined as

$$a = 1 - \frac{\tau}{\tau_{\max}},\ 0 \le a \le 1\ , \qquad (20)$$

where τ is the tortuosity and τ_{max} is the adjustable parameter.

For the West Texas samples studied, τ_{max} equals to 30. The calculated permeability from this modified Chang's model is given in **Table 12**. The tortuosity is obtained from the resistivity measurement. In average, the modified Chang's model predicts the permeability within a factor of 5.6. As shown in the earlier section, the formation factor can be estimated from the NMR T_2 by using Myer's PCM model; hence the tortuosity also can be calculated from NMR T_2. **Table 12** shows the predicted permeability form the modified Chang's model with tortuosity calculated from NMR T_2. The vuggy porosity is estimated by using the vugular 750 ms cutoff and the intergranular porosity is calculated by substracting the total porosity with the vuggy porosity. Now, the model in average predicts the permeability within a factor of 4.8.

Coates model (Eq. 18) was modified by changing its constant from 10^4 to 50^4. The error in permeability estimation is only slight reduced from 36.2 to 32.3 and the predicted permeabilities are still not satisfactory. Other models, which include formation factor, were also tested. The models tested are as follow[23-25]

$$k = 81\left(\frac{T_{2lm,750}}{F}\right)^2, \tag{21}$$

$$k = 9.5\left(\frac{T_{2lm}}{F}\right)^2, \tag{22}$$

$$k = 2.7\frac{T_{2lm,750}^{\ 2}}{F} \text{ and} \tag{23}$$

$$k = 2.7\frac{T_{2lm}^{\ 2}}{F}. \tag{24}$$

The predicted values are tabulated in **Table 12** and the results are not satisfactory since the error is about two order of magnitude.

Sample	$k_{measured}$ (mD)	k_{SDR} (mD)	k_{Chang} (mD)	k_{Coates} (mD)
1	0.023	0.46	0.0055	0.134
2A	0.022	13.5	0.08	3.8
2B	0.08	17	0.02	2.4
3	56	527	0.49	98
4A	140	206	6.6	58
4B	2,321	1523	20	448
Ratio*		43.6	142.5	36.2

* Ratio is the ratio of the predicted value to the measured value or vice versa.

Table 11. Predicted permeability from NMR correlation

Sample	Mod. Chang	Mod. Chang NMR	Mod. Coates	Eq. 21	Eq. 22	Eq. 23	Eq. 24
1	0.082	0.01	0.66	0.4	1	2.5	5.4
2A	0.56	0.43	19	10	18	102	158
2B	0.017	0.23	12	3	12.5	49.5	179
3	85	148	481	115	487	268	967
4A	116	77	285	422	269	771	418.5
4B	1,179	778	2,210	2,266	2,210	2050	1,702
Ratio	6.4	5.4	32.3	85.6	172.8	895.6	1,610

* Ratio is the ratio of the predicted value to the measured value or vice versa.

Table 12. Predicted permeability from the modified NMR correlation

5.3. Effective Medium Approximation

Effective medium approximations have been used to estimate the effective properties of heterogeneous materials. Many authors have applied EMA (Effective Medium Approximation) to estimate conductivity or permeabilitiy for carbonate formations. Myers (1989) used Hanai-Bruggeman equation to estimate conductivity for a bimodal porosity system.[26] Sen (1997) discussed the use of different approximations to calculate the resistivity of partially saturated carbonate rocks with microporosity.[27] Ramakrishnan et al. (2001) applied Bruggeman's symmetrical approximation to predict resistivity and permeability for Middle East carbonate reservoirs.[28]

We treat the matrix as the host and the vugs as the guest. Mode 1 and mode 2 are combined as the host, and mode 3 is served as the insertion. Hence, the host volume fraction f_{host} is given as:

$$f_{host} = \alpha_1 + \alpha_2 , \qquad (25)$$

where α_1 is the fraction of mode 1 and α_2 is the fraction of mode 2. The host porosity ϕ_{host} can be calculated from

$$\phi = \phi_{host} f_{host} + f_v \,, \tag{26}$$

where ϕ is the overall porosity, ϕ_{host} is the host porosity, f_{host} is host volume fraction (Eq. 25) and f_v is the vug or the insetion volume fraction (α_3). The effective permeability k_{eff} can be calculated by using Bruggeman's symmetrical approximation:[28,29]

$$f_v\left(\frac{k_v - k_{eff}}{k_v + 2k_{eff}}\right) + (1 - f_{host})\left(\frac{k_{host} - k_{eff}}{k_{host} + 2k_{eff}}\right) = 0\,. \tag{27}$$

The host permeability k_{host} is calculated by using Eq.1 using matrix porosity ϕ_{host} and $T_{2lm,host}$. If $k_v = \infty$, then k_{eff} becomes[28]

$$k_{eff} = \frac{k_{host}}{1 - 3f_v}\,. \tag{28}$$

This approximation shows a percolation threshold at f_v = ⅓.[27-29]

The predicted permeability using Eq. 28 is given in **Table 13**. It works better for the low permeability samples. This can be understood because the f_v is lower than ⅓ hence the Bruggeman's approximation treated the vugs as disconnected phase.

Higher permeability samples needs an approximation that implies more connectivity. Looyenga's approximation implies percolation at any volume fraction and is given as[30]

$$k_{eff}^{1/3} = f_v k_v^{1/3} + (1 - f_v) k_{host}^{1/3}\,. \tag{29}$$

The calculated permeability using this approximation is given in **Table 13**. The k_v is taken as 100,000 mD. This correlation gives a better estimate for higher permeability samples.

6. Discussion and Conclusion

The rock fabric differs significantly between different samples from different wells. This depicts the heterogeneity of the field at a macroscopic scale. The heterogeneity of West Texas carbonates at a smaller scale is clearly shown from the CT scan images. The porosity is significantly varies along the core length. The preferential flow path is determined from the tracer experiment and this path effects the oil recovery process. The tracer effluent concentration profiles for high permeability samples show early breakthrough followed by a long tail, which is the characteristic of carbonate system. Both pore throat size distribution and pore body distribution shows multimodal behavior. The pore throat and pore body sizes are better correlated in higher permeability samples. This different length scale of heterogeneity, from macroscopic to microscopic level, made the property prediction for carbonates very difficult.

Sample no. 1 has very fine grain size, hence the intergranular pore space is also very small. Although samples no. 2A and 2B have very big crystal size, the intergranular pore space is also very small because the crystals are grown very close to each other. Those three samples have very low permeability although they are vuggy samples. Sample no. 3 is rather unique. The intergranular pore space is very small, but the permeability is rather high. We think that the micro-fractures that connect the vugs play an important role here. If we neglect the T_2 signal above 750ms, we miss the fracture contribution to the flow. Samples no. 4A and 4B have large intergranular pore size, which interconnect the vugs. Again, if the T_2 signal above 750ms signal is neglected, a significant portion of intergranular porosity will not be used. For the last three samples, using 750ms cutoff predicts much lower permeability than actual.

Deconvoluting the multimodal NMR T_2 response into trimodal Weibull distribution gives a better insight on the actual contribution of each mode. It is found that the vuggy porosity estimated from the Myers's PCM model agrees very well with the value calculated from NMR using vugular 750 ms cutoff and from the fraction of the largest mode of trimodal Weibull distribution. Hence, the

formation factor or the tortuosity for fully saturated core can be estimated from NMR T_2 response.

The existing permeability correlations from capillary pressure curve were tested to estimate the West Texas samples permeability. The Winland-Pittman model gives the best prediction. A modified Chang's NMR model by including the tortuosity is proposed. It is observed that the tortuosity can be a good indicator whether the vugs are contributing to the flow or not. The new model operates between the SDR and Chang's model, depending on the tortuosity. The new proposed model is able to improve the permeability predicition for the West Texas samples studied and to allow the permeability prediction from NMR T_2 distribution alone.

Different effective medium approximations have to be used to estimate the permeability for less connected and better connected carbonates. All the parameters used in the approximation are also derived from NMR T_2 response.

Acknowledgments

This research is funded and supported by U.S. Department of Energy under contract DE-AC26-99BC15201 and Rice University Consortium members: Baker Atlas, Chevron, Deepstar, Exxon-Mobil, Norsk Hydro, Halliburton-NUMAR, Kerr-McGee, Marathon, Ondeo Nalco, Phillips, PTS, Schlumberger and Shell. Special thanks for Marathon, Shell and PTS for providing core samples and core analysis measurements. The authors also would like to acknowledge Dr. Charlotte Sullivan from Geosciences Dept., University of Houston, for assisting in the thin section analysis.

References

1. Chilingar, G. V., Mannon, R. W. and Rieke, H. H. III, *Oil and Gas Production from Carbonate Rocks*, Elsevier, New York, 1972.
2. Lucia, F. J., *Carbonate Reservoir Characterization*, Springer-Verlag, Berlin, 1999.
3. Roehl. P. O. and Choquette, P.W., *Carbonate Petroleum Reservoirs*, Springer-Verlag, New York, 1985.
4. Jennings, J. W. Jr and Lucia, F. J., "Predicting Permeability from Well logs in Carbonates with a Link to Geology for Interwell Permeability Mapping", paper SPE71336 presented at 2001 SPE Annual Technical Conference and Exhibition, New Orleans, 30 Sept – 3 Oct, 2001.
5. Chang, D., Vinegar, H., Morris, C. and Straley, C., "Effective Porosity, Producible Fluid, and Permeability in Carbonates from NMR Logging", *The Log Analyst*, 38, 60-72, 1997.
6. Crabtree, S. J., Jr., Erlich Robert and Prince, C., "Evaluation Strategies for Segmentation of Blue-dyed Pores in Thin Sections of Reservoir Rocks", *Computer Vision, Graphics, and Image Processing*, 28, 1-18, 1984.
7. Hicks, P. J. Jr., Deans, H. A., and Narayanan, K. R., "Distribution of Residual Oil in Heterogeneous Carbonate Cores using X-Ray CT", SPE21574, *SPEFE*, 1992.
8. Olea, R. A., *Geostatistics for Engineers and Earth Scientist*, Kluwer Academic Publisher, Boston, 1999.
9. Kenyon, W. E., "Petrophysical Principles of Applications of NMR Logging", *The Log Analyst*, 38, 21-43, 1997.
10. Dauba, C., Hamon, G., Quintard, M. and Cherblanc, F., "Identification of Parallel Heterogeneities with Miscible Displacement", *SCA*-9933, 1999.
11. Dauba, C., Hamon, G., Quintard, M. and Lasseux, D., "Stochastic Description of Experimental 3D Permeability Fields in Vuggy Reservoir Cores", *SCA*-9828. 1998.
12. Xu, B., Kamath, J., Yortsos, Y. C. and Lee, S. H., "Use of Pore Network Models to Simulate Laboratory Corefloods in a Heterogeneous Carbonate Sample", *SPE*57664 presented at 1997 SPE Annual Technical Conference and Exhibition, 1997.
13. Oshita, T. and Okabe, H., "Water Breakthrough in Carbonate Core Samples Visualized with X-Ray CT", *SCA*2000-18, 2000.
14. Coats, K. H. and Smith, B. D., "Dead-End Pore Volume and Dispersion in Porous Media", *SPEJ*, March, 73-84, 1964.
15. Brigham, W. E., "Mixing Equations in Short Laboratory Core", *SPE* 4256, 1974.

16. Salter, S. J. and Mohanty, K. K., "Multiphase Flow in Porous Media I: Macroscopic Observations and Modeling", *SPE11017,* presented at 1982 Annual Technical Conference and Exhibition, 1982.

17. Myers, M. T., "Pore Combination Modeling: A Technique for Modeling the Permeability and Resistivity Properties of Complex Pore Systems", *SPE22662*, presented at the 66th Annual Technical Conference and Exhibition, Dallas, 1991.

18. Kolodzie, S., "Analysis of Pore Throat Size and Use of Waxman-Smits Equation to Determine OOIP in Spindle Field, Colorado", *SPE9382*, presented at 1980 SPE Annual Technical Conference and Exhibition, Dallas, 1980.

19. Swanson, B. F., "A Simple Correlation between Permeabilities and Mercury Capillary Pressure", *JPT*, December, 2498-2504, 1981.

20. Katz, A. J. and Thompson, A. H., "Quantitative Prediction of Permeability in Porous Rock", *Phys. Rev. B*, 34, 11, 8179-8181, 1986.

21. Weibull, W., "A Statistical Distribution Function of Wide Applicability", *J. of Applied Mechanics*, 18, 293-297, 1951.

22. Coates, G. R. *et al*., "A New Characterization of Bulk-Volume Irreducible Using Magnetic Resonance", paper QQ, *38th Annual SPWLA Logging Symposium*, 1997.

23. Coates, G. R., Peveraro, R. C. A., Hardwick, A. and Roberts, D., "The Magnetic Resonance Imaging Log Characterized by Comparison with Petrophysical Properties and Laboratory Core Data", *SPE 22723*, presented at the 66th Annual Technical Conference and Exhibition, Dallas, 1991.

24. Kenyon, W. E., Takezaki, H., Straley, C., Sen, P. N., Herron, M., Matteson, A. and Petricola, M. J., "A Laboratory Study of Nuclear Magnetic Resonance Relaxation and its Relation to Depositional Texture and Petrophysical Properties – Carbonate Thamama Group, Mubarazz Field, Abu Dhabi", *SPE 29886,* presented at the SPE Middle East Oil Show, Bahrain, 1995.

25. Dunn, K. J., LaTorraca, G. A. and Bergman, D. J., "Permeability Relation with Other Petrophysical Parameters for Periodic Porous Media", *Geophysics*, 64, 2, 470-478, 1999.

26. Myers, M. T., "Pore Combination Modeling: Extending the Hanai-Bruggeman Equation", paper D, *13th Annual SPWLA Logging Symposium*, 1989.

27. Sen, P. N., "Resistivity of Partially Saturated Carbonate Rocks with Microporosity", *Geophysics*, 62, 415-425, 1997.

28. Ramakrishnan, T. S., Ramamoorthy, R., Fordham, E., Schwartz, L., Herron, M., Saito, N. and Rabaute, A., "A Model-Based Interpretation Methodology for Evaluating Carbonate Reservoirs', SPE71704 presented at 2001 SPE Annual Technical Conference and Exhibition, New Orleans, 30 Sept.-3 Oct, 2001.

29. Landauer, R., “Electrical Conductivity in Inhomogeneous Media”, in *Electrical Transport and Optical Properties of Inhomogeneous Media*, AIP Conference Proceedings No. 40, 1978.

30. Looyenga, H., “Dielectric Constants of Heterogeneous Mixtures”, *Physica*, 31, 401-406, 1965.